BLACK HOLES, GALAXY CLUSTERS AND GRAVITATIONAL WAVES

by

WALTER DEL POZZO

A thesis submitted to

The University of Birmingham

for the degree of

DOCTOR OF PHILOSOPHY (PHD)

Astrophysics and Space Research Group

School of Physics and Astronomy

The University of Birmingham

May 2010

fatti non foste a viver come bruti

ma per seguir virtute e canoscenza

Abstract

The Universe in general is well described by Einstein's General Relativity theory. However, the need to reconcile General Relativity (GR) with Quantum Mechanics implies that a more general theory is needed. Gravitational Waves (GW) offer the unique possibility of testing GR predictions in the strong field regime. As GWs are expected to be finally detected within the next decade, a rigorous framework to detect and analyse departures from GR is essential. In this thesis, we propose a Bayesian data analysis framework to compare alternative theories of gravity. We test the validity of our proposal by comparing GR predictions to the ones from a Massive Graviton theory. We demonstrate the capability of discriminating between the two competing theories and produce posterior probability distribution functions for the parameters on which the theories depend. We next quantify the bias that the assumption of an incorrect theory would introduce in the estimates. Finally, we devise a method to combine multiple observations which, applied to the Graviton Compton wavelength, substantially increases the amount of information that is possible to extract from GWs.

Active Galactic Nuclei (AGNs) are the second most energetic phenomen in the known Universe. As such, they have the power of deeply affecting their surroundings. Black Hole powered AGN's outflows are commonly invoked as the limiting factor in the cosmological growth of galaxies. Nevertheless, the mutual influence of environment and AGNs is still fertile ground for debate. Using current wide-field sky survey photometric data, in concert with the established Luminosity – Black Hole mass relation, we calculate the mass distribution of supermassive

massive black holes (SMBHs) in three different environments: field, groups and clusters of galaxies. We highlight a tendency for SMBHs to be concentrated in dense environments, as predicted from cosmological simulations. Moreover, we use wide-field radio band data to relate AGN activity and environment. We find that, within a dense environment, a SMBH has a higher-than-average probability of being a radio AGN. Furthermore, densest environments steepen the analytical relation between SMBH mass and the probability of being radio-actives where ram pressure striping is important.

The ΛCDM paradigm successfully explains the large scale observations of the Universe. However, the fine details of structure formation are yet to be fully understood. For instance, observers promote mergers as the mean by which the properties of the intracluster medium (ICM) are transformed although theorists refute them as a viable explanation. In particular, the observed distributions of metals in post-merger systems do not agree with what is produced in idealized simulations. According to their core entropy, clusters of galaxies are usually divided into two classes: “cool cores” (CC) and “non-cool cores” (NCC). To date, simulations considering exclusively collisions between CC failed to explain the observed metals distributions. Accordingly, we show that CC mergers cannot produce the observed flat metals profiles. However, mergers between NCC are able to reproduce observations because the high initial core entropy renders the ICM susceptible to buoyancy which, in turn, drives the mass mixing that erases the initial metal profiles.

Acknowledgements

I'd like to express my most sincere gratitude to my family, Mario, Teresa and Sara, for their perpetual and unconditioned support and to Stephanie.
You are the reason why I am writing this.

I would like to thank my supervisor, Dr. Somak Raychaudhury.

A special thank to Prof. Steven N. Shore for introducing me to the world of astrophysical research with his invaluable teachings.

During my PhD, I met a lot of extraordinary people. Among them, I am glad I was honored to learn from Dr. Alberto Vecchio and Dr. John Veitch that guided me in my first steps in the "valley of gravitational waves". I am grateful to Prof. Arif Babul whose deep insights always shook my (little) astrophysical knowledge to the basements. To Dr. Ian G. McCarthy for his kindness and profound understanding of hydrodynamics.

I'd like to thank then Prof. Trevor Ponman for all our fruitful discussions and for his enlightening comments. My thanks go to Dr. Andreas Freise and to our interesting discussions. Also, I'd like to acknoledge Dr. Ian Stevens for having followed me "on a road to nowhere".

I owe my thanks to the Montescudaio Hardcore Crew: ***never too far away from each other!***[1] Special thanks to Dr. Antonio Perreca and to his father's "Nocino" that warmed up our sad hearts during our first year in the City of the Future. Finally my gratitude goes to Dr. Giacomo Volpe, Dr. Miha Zakotnik and Sabina, Dr. Emilie Dasse, Dr. Vasilios "Bully" Bekiaris and Dr.

[1] Satanic Surfers, 1997, "Soothing" in *666 Motor Inn*, Burning Heart Records

Angeliki Marietou, to Dr. Eliza Vasilopulou and to all the people that I have met and I have cheered with and that accompanied me during this 3 and a half year long journey.

The financial support of the school of Physics and Astronomy, University of Birmingham is gratefully acknowledged.

Birmingham, England, 2010

Walter Del Pozzo

Statement of originality

The material in this thesis has not been submitted for a degree in any University. To the best of my knowledge contains no material previously published or written by another person except where due acknoledgment is made in the thesis itself.

- Chapter 3: the work presented in this chapter was made in collaboration with Dr. Ian G. McCarthy. My contribution to the work has been analysing and interpreting the outputs of the simulations produced by Dr. Ian G. McCarthy.

- Chapter 4: the work in this chapter was made in collaboration with Dr. Somak Raychaudhury and Prof. Arif Babul. My contribution consisted in obtaining, reducing, analysing and interpreting the data.

- Chapter 5: the work in this chapter was realised in collaboration with Dr. John Veitch and Dr. Alberto Vecchio. My contribution was the development of the subroutines relevant to the Massive Graviton theory and the analysis of the data.

Contents

List of Figures

List of Tables

1. A Snapshot of the Universe

Observed through the many windows in the electromagnetic spectrum the Universe renders an amazing and complicated picture. Since observations at different parts of the electromagnetic spectrum explore different energy regimes, multi-wavelength studies allow us to appreciate the intertwined physical processes in a global fashion. The Universe is indeed very complicated. Nevertheless in the past decades we have been able to understand and explain many of its features.

The Cosmic Microwave Background (CMB) radiation indicates that on the very large scales, $\sim 10^{28}$ m, the Universe is very homogeneous. The CMB is believed to be the thermal relic radiation from the primordial Universe. Essentially the universe is a black body in thermal equilibrium. On smaller scales, of the order of 10^{23-24} m, large sky surveys, such as 2MASS (2 Micron All-Sky Survey) (Cutri et al. 2003) and SDSS (Sloan Digital Sky Survey) (Adelman-McCarthy et al. 2008) show Superclusters of galaxies. Those are the largest known associations present in the Universe, figure 1.1. Around 10^{22} m we find *clusters* and *groups* of galaxies. A large fraction of galaxies live in groups (Eke et al. 2004; Merchán & Zandivarez 2005) and a small fraction of them reside within clusters.

Down to scales $\sim 10^{20}$ m we find galaxies. These are associations of billions of stars held together by their mutual gravitational attraction. Galaxies are classified according to their morphology into early-types, late-types, dwarfs and irregulars. The classification in early and late types is only for historical reasons as it was introduced by Hubble himself. It does not have

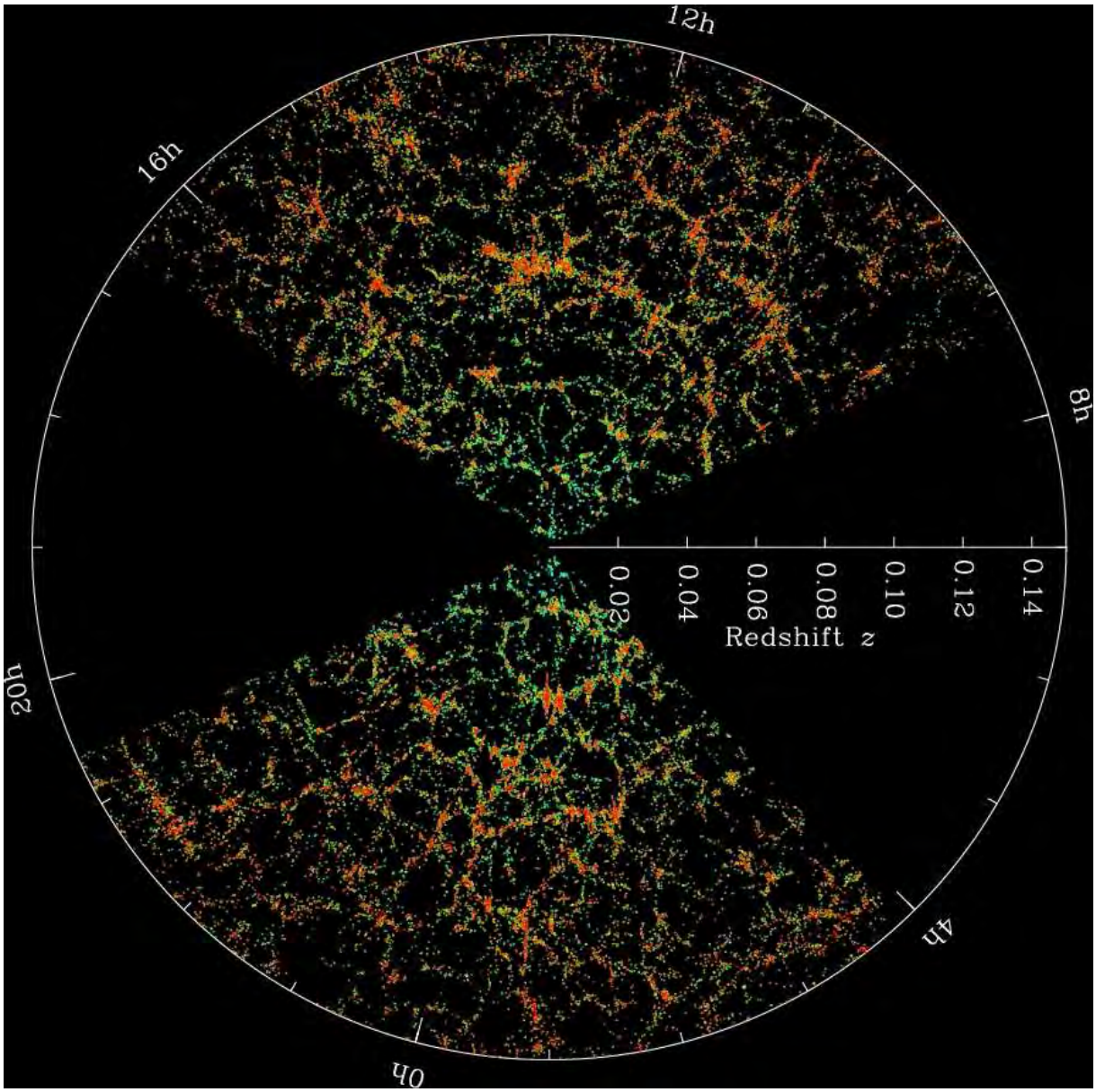

Figure 1.1: Pie Slice from SDSS galaxy catalogue showing the large scale structure of the local Universe. Image Credit: SDSS team.

any relation to any real evolutionary trend. Early-type, or elliptical, galaxies are spheroidal objects essentially pressure supported. They have masses up to $10^{13} M_{\odot}$ and typically have red colours. They are very poor in gas and dust content and the star formation activity is extremely low. Nevertheless early-types usually host very powerful and radio bright Active Galactic Nuclei (AGN). Ellipticals are found at the bottom of the big potential wells of clusters and groups of galaxies and are usually the dominant galaxy of the whole association. Late-type, or spiral, galaxies are spiral associations of stars rotationally supported. They are usually rich in gas and dust and star-forming. Usually the stellar component of a spiral galaxy consists of a disk and a bulge. The bulge often hosts an optically bright AGN.

Beside the bright Universe which we observe with telescopes, there is a dark one whose existence we can infer only indirectly. Early studies of galaxy motions in clusters (Smith 1936; Zwicky 1937) required a substantial amount of mass far in excess of that inferred from the optically luminous component. In time the evidence for the ”missing mass“ grew on extra-galactic (Faber & Gallagher 1979; Peterson 1985; Fabricant, Kent, & Kurtz 1989; Henry & Briel 1993; Mulchaey et al. 1993; Mulchaey 2000; Helsdon & Ponman 2003) and galactic (Begeman, Broeils, & Sanders 1991) scales. Today, Cold Dark Matter (CDM) is an accepted paradigm (Peebles 1982) and the basis for our models of galaxy formation. Alternatives to the CDM scenario have been proposed, such as the MOdified Newtonian Dynamics (MOND) (Milgrom 1983; Milgrom 2008), but they do not seem to be able to reproduce observations in the Solar System. In the CDM framework Dark Matter (DM) is taken to be made of non relativistic particles whose mass is approximately equal to or greater than 1 keV, are non-baryonic, non-collisional and non-dissipative: the ideal fluid. Evidences on the nature of DM come from various observations. Galaxy formation models require DM to be “cold” and “dark” to form structures compatible with large scale structure observations. Warm or hot (relativistic) DM implies a “top-down” galaxy formation scenario while cold DM leads to a “bottom-up” or hierarchical formation of structures in the Universe. Silk Damping (Silk 1968) (cfr. Sec. 2.2.1)

implies that DM does not interact with radiation, DM is therefore “dark”.

Future generation instruments are expected to open a new window on the “Dark Side of the Universe” by detecting gravitational waves. Gravitational waves are distortions of space-time propagating along space-time itself. They offer the possibility of observing a huge variety of systems directly (Cutler & Thorne 2002, for a review) without the complication of interlopers that in principle affect electromagnetic radiation. At this stage the prospects of gravitational waves detection are somewhat speculative, but we already know that ground based interferometers will observe neutron stars and black holes binaries to cosmological distances as well as core collapse supernovae in the local Universe (see Ott 2009 for a review). All these systems will constrain the latest stages of stellar evolution and provide ”standard sirens” for the determination of the distance ladder. Space based observatories, e.g. the Laser Interferometric Space Antenna (LISA) (Bender 1998), will observe the final stages of supermassive black holes coalescence. The implications ot these potential observations on our knowledge of the galaxy formation process are potentially very remarkable. Gravitational waves are also expected to probe gravity in the strong field regime and therefore to provide decisive tests of General Relativity and possibly of Quantum Gravity.

In this thesis I touch various aspects of current astrophysical research. In the first introductory chapter I will outline the background for all the projects I have undertaken during my PhD, and attempt to forge the connections among them. I will start by briefly reviewing the accepted cosmogony and the process of galaxy formation. I will then move to introduce gravitational waves. The final part of the following chapter will be devoted to review the main techniques used in the following chapters:

- wide field sky surveys;
- hydrodynamical simulations;
- Bayesian data analysis.

On notation: Every time I will refer to General Relativity I will conform to the Einstein convention on repeated indexes. Repeated indices are summed. Greek indices indicate quadridimensional quantities and Latin indices refer to space dimensions:

$$A_\mu A^\mu \equiv \sum_{\mu=0}^{3} A_\mu A^\mu$$
$$A^\mu \equiv (A^0, A^1, A^2, A^3)$$
$$A^k \equiv (A^1, A^2, A^3)$$

Furthermore $\vec{A}$ is a three dimensional vector while A is a four-vector.

2. Introduction

2.1 A brief history of the Universe

The chance discovery by Penzias & Wilson (1965) that the Universe is permeated by a uniform microwave background, the *cosmic microwave background* or CMB, is considered the definitive proof that the hot Big Bang model is correct. At the time of Penzias & Wilson discovery, it was already known that the Universe is expanding (Hubble 1929). Going backwards in time this implied that at the beginning everything should have been concentrated at a single point (Lemaître 1931). During the following three decades many theories were proposed, most notably the "Steady-State" theory (e.g. Hoyle 1954) and the "Big Bang" theory (e.g. Alpher et al. 1948). Interestingly, the term "Big Bang" was coined by Hoyle as a derogatory comment describing the competing theory. The discovery of the CMB, one of the predictions of the Big Bang as well as the primordial nucleosynthesis, helped to establish the Big Bang as the accepted theory.

According to the current state of knowledge the Universe evolved from a point of, formally, infinite density and temperature. During the first moments the Universe went through a period of very fast expansion, the so-called *inflation* (e.g. Guth 1981), which erased any initial quantum fluctuations. The state of the Universe was probably a "sea" of particles and anti-particles continuously being created and annihilated, and all the known forces were unified. At that point, due to some yet unknown mechanism, the symmetry between particles and antiparticles

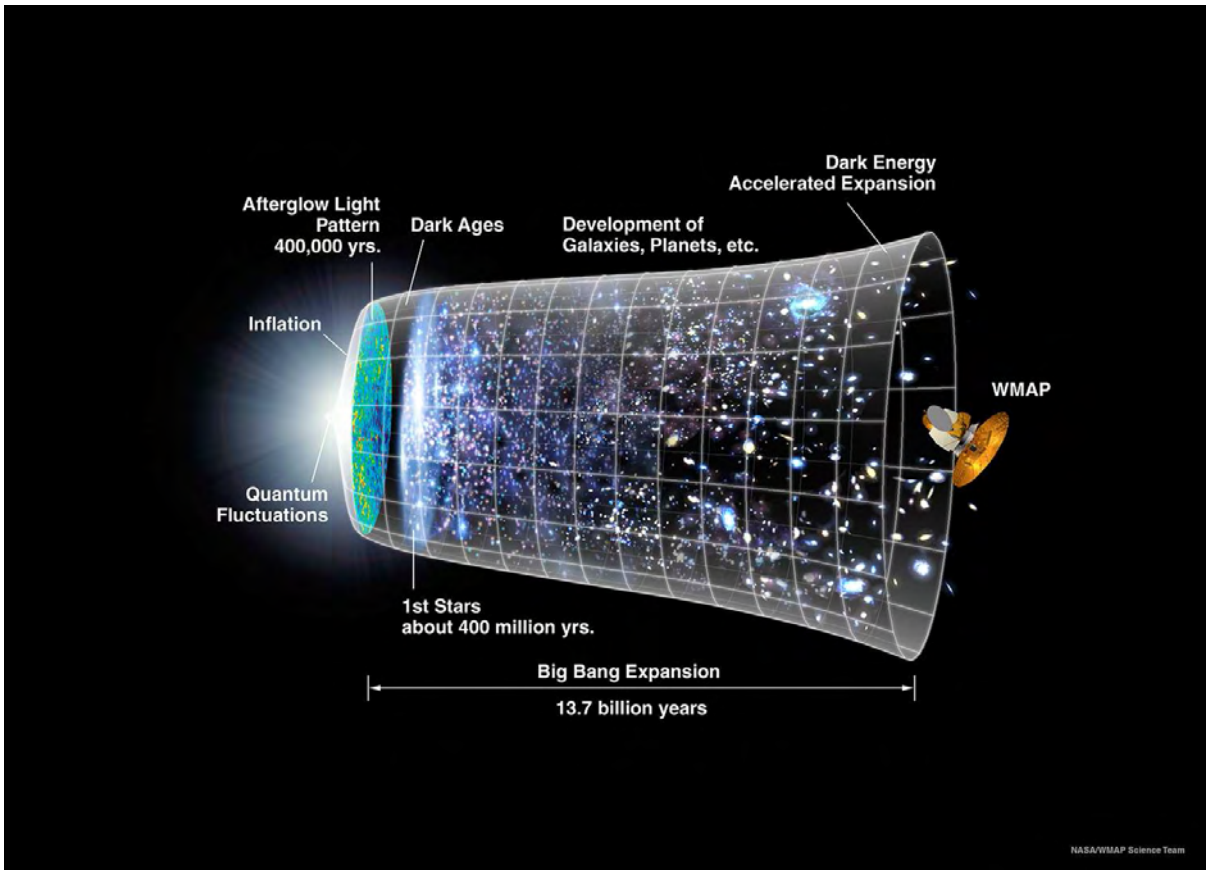

Figure 2.1: Sketch of the Universe history according to the Hot Big Bang model as accepted today. Image Credit: NASA.

was broken leaving a small excess of particles. Around 10^{-11} seconds after the Big Bang, the Universe enters the energy range that modern particle accelerators can probe. At that time the forces had already decoupled into the 4 fundamental interactions we know today. 10^{-6} seconds after the Big Bang quarks started binding to form the baryons. A few minutes later, the baryons started forming nuclei of hydrogen, helium and of a small amount of heavier elements (see Iocco et al. 2009 for a recent review about primordial nucleosynthesis). At this point the energy content of the Universe was dominated by photons. For the following $380,000$ years not much happened. The Universe kept expanding and cooling until the temperature reached $\sim 10^3$ K and electrons and baryons combined to form neutral atoms. The radiation effectively decoupled from matter. The CMB is the last "snapshot" of the radiation dominated era redshifted to longer wavelength because of the expansion of the Universe.

2.1.1 The Friedmann-Lemaître-Robertson-Walker solution

The dynamical evolution of the Universe is described by the Friedmann-Lemaître-Robertson-Walker metric (FLRW). This is an exact solution of Einstein's equations. The FLRW metric describes a simply connected, homogeneous and isotropic maximally symmetric Universe. The general metric obeying those requirements has a very simple form:

$$ds^2 = -c^2dt^2 + a(t)^2 d\Sigma^2 \tag{2.1}$$

where $d\Sigma$ encloses only the spatial coordinates and $a(t)$ is a scale factor that depends on time. Usually equation (2.1) is written in polar coordinates

$$d\Sigma^2 = \frac{dr^2}{1-kr^2} + r^2 d\Omega^2, \qquad d\Omega^2 = d\theta^2 + \sin^2\theta d\phi^2 \tag{2.2}$$

where $k = -1, 0, 1$ is the sign of the curvature radius thus describing a closed, $k = -1$, flat, $k = 0$, or open, $k = 1$, Universe. The state of the Universe is obtained by solving Einstein's

equations

$$G_{\mu\nu} - \Lambda g_{\mu\nu} = \frac{8\pi G}{c^4} T_{\mu\nu} \tag{2.3}$$

for $a(t)$. $G_{\mu\nu}$ is the Einstein tensor, Λ is the cosmological constant, the "Dark Energy", and $g_{\mu\nu}$ is the metric tensor. Homogeneity and isotropy imply a simple form for the stress-energy tensor $T_{\mu\nu} = \text{diag}(\rho, p, p, p)$. ρ is the density, in natural units where $c = 1$, and p is the pressure. Plugging equation (2.1) into (2.3) yields:

$$\left(\frac{\dot{a}}{a}\right)^2 + \frac{kc^2}{a^2} - \frac{\Lambda c^2}{3} = \frac{8\pi G}{3}\rho \tag{2.4}$$

$$2\frac{\ddot{a}}{a} + \left(\frac{\dot{a}}{a}\right)^2 + \frac{kc^2}{a^2} - \Lambda c^2 = -\frac{8\pi G}{3}p \tag{2.5}$$

known as the Friedman equations. The solution of (2.4) and (2.5) requires some prescription for the equation of state $\rho(t)$ to describe the global state of the Universe. Radiation dominated universes are described by $p = \rho/3$, pre-CMB era, while matter dominated universes by $p = \rho RT$, post-CMB era. The change of equation of state of the Universe at the surface of last scattering is the reason why usually this is identified with a phase transition of the Universe.

The Friedman's equations are commonly formulated in terms of the *Cosmological parameters* Ω_i and of the value of the *Hubble constant* H_0:

$$\begin{aligned}
&\mathrm{H}_0 \equiv \tfrac{\dot{a}}{a}|_{t=0} && \text{Hubble constant} \\
&\Omega_M \equiv \tfrac{8\pi G\rho}{3H_0^2} && \text{matter} \\
&\Omega_\Lambda \equiv \tfrac{\Lambda c^2}{3H_0^2} && \text{cosmological constant} \\
&\Omega_k \equiv \tfrac{kc^2}{a^2 H_0^2} && \text{curvature}
\end{aligned} \tag{2.6}$$

The expansion of the Universe is measured via the *cosmological redshift z*. For a photon, or any other form of radiation, emitted with wavelength λ_0 and detected at a longer wavelength λ, the

redshift z is defined as

$$z = \frac{\lambda - \lambda_0}{\lambda} \tag{2.7}$$

and is directly related to the ratio of the scale factor at the time of observation t_{obs} and emission t_{em}

$$1 + z = \frac{a(t_{obs})}{a(t_{em})} \tag{2.8}$$

For each given set of cosmological parameters it is possible to convert redshift into a measure of distance according to the FLRW metric. The *comoving distance* is the distance between two points in the Universe measured along a geodesic defined at the present cosmological time. In a flat universe its expression is given by (Hogg 1999):

$$\chi = \frac{c}{H_0} \int_0^z \frac{dz'}{\sqrt{\Omega_M (1+z')^3 + \Omega_k (1+z')^2 + \Omega_\Lambda}} \tag{2.9}$$

The most common distance measure used in this thesis is the *luminosity distance* D_L. It is defined by the relation between the flux S and the luminosity L of a given source

$$D_L^2 \equiv \frac{L}{4\pi S} \tag{2.10}$$

In an evolving universe, D_L is related to the comoving distance by

$$D_L = (1+z)\chi. \tag{2.11}$$

As H_0 is commonly measured in km·s^{-1}·Mpc^{-1}, in this last expression D_L is expressed in Mpc.

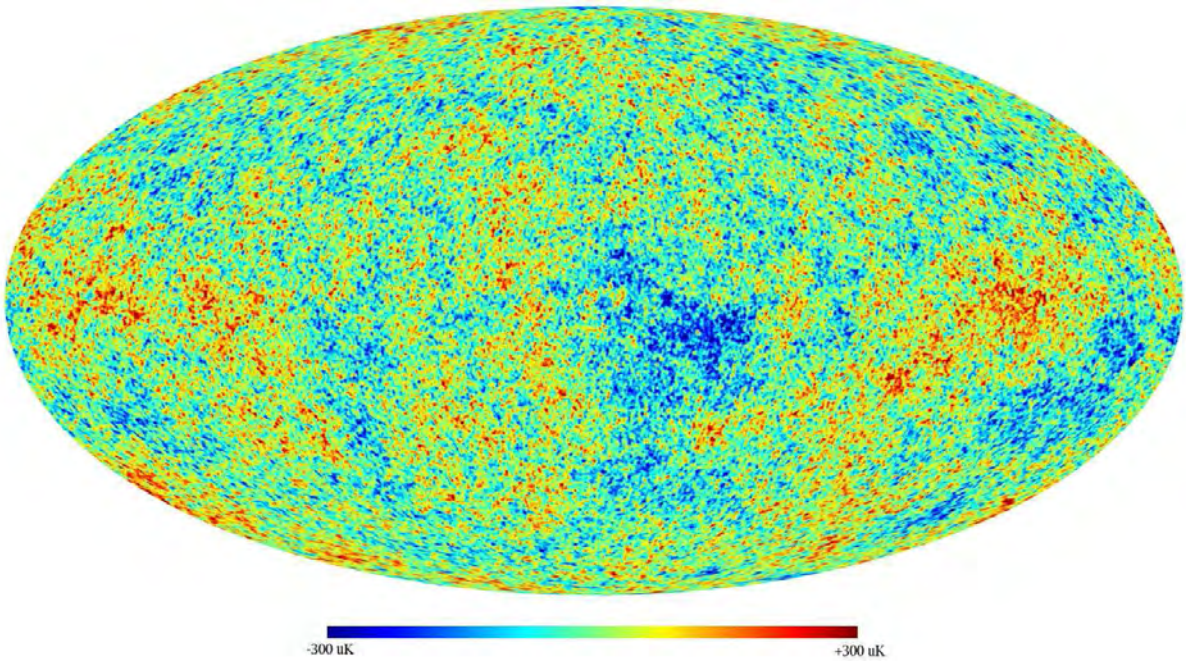

Figure 2.2: Cosmic microwave background (CMB) radiation as observed by the Wilkinson Microwave Anisotropy Probe (WMAP). The monopole and dipole momenta have been subtracted to show the temperature fluctuations. The typical temperature fluctuation on the sky is of the order of 10^{-5}.

2.2 Galaxy Formation Models

2.2.1 Spherical Collapse

The process of galaxy formation remains to date a large mystery. Much of the physics involved is understood, but the exact details are still very model dependent. Furthermore space missions like the Wilkinson Microwave Anisotropy Probe (WMAP) (Spergel et al. 2007) revealed that the energy content of our Universe is unknown. About 70% ot the total energy resides in an elusive form popularly named “Dark Energy”. The remaining 30% is in the form of matter. Of this only about 4% is in ordinary baryonic matter, the everyday atoms and molecules, while the rest is in the form of Dark Matter. Nevertheless current galaxy formation models successfully reproduce some of the key astronomical observations to date. Missions like COBE (Mather et al. 1994), BOOmerang (Crill et al. 2003) and WMAP (Spergel et al. 2007) have confirmed

that the CMB is characterised by a thermal black body spectrum with a temperature of ~ 2.73 K. Fluctuations are of the order of μK. Variations in the CMB temperature are related to density fluctuations at the time of decoupling (Sachs-Wolfe effect (Sachs & Wolfe 1967)). These small density (or gravitational potential) fluctuations are the seeds for the subsequent process of galaxy formation. Individual cloud collapse happens provided that the mass of the collapsing gas is enough to overcome the thermal pressure and the radiation pressure of the gas cloud itself (Jeans 1902). If the *free-fall* time $t_{ff} \propto (G\rho)^{-1/2}$ is much longer than the *sound crossing* time $t_s \propto (kT/m_p)^{1/2}$ the pressure responds fast enough to counter the gravitational force, and the system oscillates as sound waves. On the other hand if $t_{ff} << t_s$ the pressure does not respond fast enough to resist the gravitational collapse, and the system collapses on a free-fall time scale. The threshold is called the *Jeans length* λ_J and the collapse happens if the radius of the system R obeys to

$$R > \lambda_J \equiv \sqrt{\frac{\pi c^2}{G\rho}} \tag{2.12}$$

where c is the adiabatic speed of sound. The quantity $M_J \equiv 4\pi\rho\lambda_J^3/3$ is called the *Jeans mass*. At the time of decoupling, when the CMB formed, $M_J \simeq 10^5 M_\odot$. However at the time of decoupling, photon diffusion would have damped *any* perturbation with mass smaller than $\sim 10^{12} M_\odot$ (Silk 1968). This is one of the main requirements for the existence of excess matter not interacting electromagnetically, as otherwise only extremely massive structures would have emerged. With this caveat in mind, an overview of the process of gravitational collapse in an expanding background is given by the *spherical top-hat* model. Even though it is unrealistic, as growth of structure is expected to have happened by of merger events rathen than by spherical infall, the spherical model allows to assess useful quantities. In the formulation of Peebles (1980)[1] the basis of this model is a spherical region, which is overdense compared to the surroundings. At a time t_0 the sphere has a uniform density ρ_0 and radius R_0. The background

[1]Peebles solution applies to an Einstein-de Sitter universe. For example in an open universe the final overdensity of the virialized region can be substatially lower (Bryan & Norman 1998).

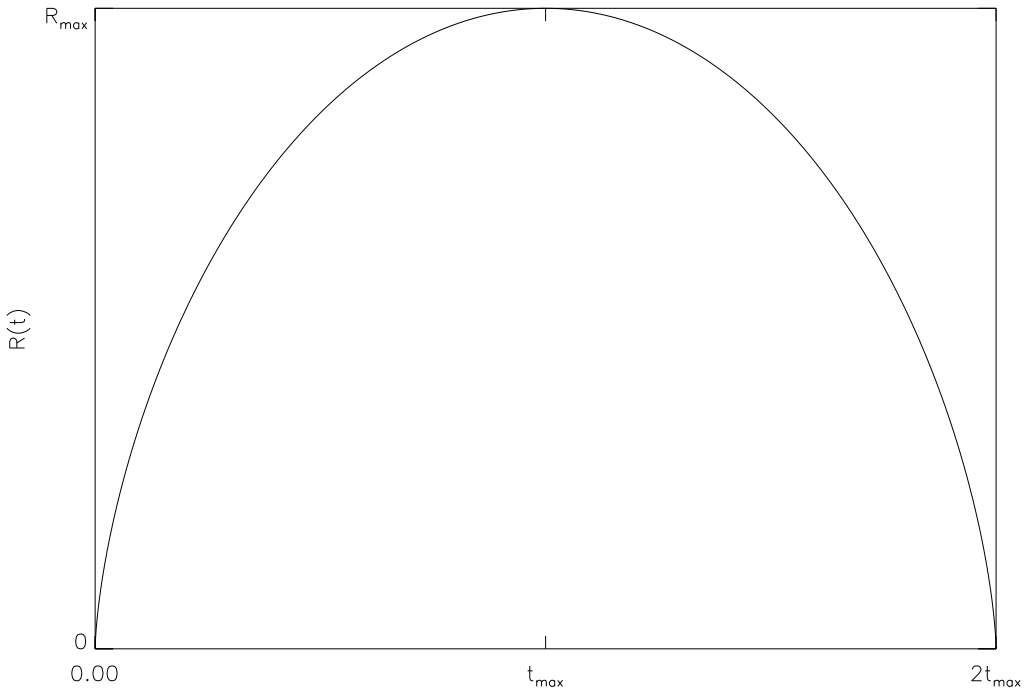

Figure 2.3: The evolution of a uniform overdense spherical region in an Einstein-de Sitter background universe.

universe has density $\overline{\rho}_0$ and Hubble parameter H_0 so that $\rho_0 > \overline{\rho}_0$. The density contrast at t_0 is defined as $\delta_0 = (\rho_0 - \overline{\rho}_0)/\overline{\rho}_0$. Solving parametrically the energy conservation equation it is possible to find the time evolution of the radius $R(t)$ of the sphere:

$$R(t) = \frac{R_{\rm max}}{2}(1 - \cos\theta) \qquad R_{\rm max} = R_0 \frac{1+\delta_0}{\delta_0} \tag{2.13}$$

$$t = \frac{t_{\rm max}}{\pi}(\theta - \sin\theta) \qquad t_{\rm max} = \frac{1}{H_0}\frac{1+\delta_0}{2\delta_0^{3/2}}\pi \tag{2.14}$$

$R_{max} \equiv R(t_{max})$ is the *turnaround radius*. Ideally at $t = 2t_{max}$ the system should collapse to a singular point. This cannot happen due to gas pressure. As the radius decreases, density and consequently pressure, will increase. Standing accretion shocks will form and the potential energy will be converted into heat and the system will approach an equilibrium state through *violent relaxation* (Lynden-Bell 1967). At last the system has *virialized*. For a system at equi-

librium the virial theorem states

$$2T + \Phi = 0 \tag{2.15}$$

where T is the time-averaged internal kinetic energy and Φ is the total gravitational potential energy. Conservation of energy implies that the virial radius is simply $r_{vir} = R_{max}/2$. The final density contrast at $t = 2t_{max}$ is about 178. In practice, this is taken to be 200 when defining structures both in observations or in N-body simulations (Evrard et al. 2002; Croton et al. 2006). Therefore r_{vir} is identified with r_{200}.

2.2.2 The hierarchical clustering model of galaxy formation

Spherical collapse is a useful model to understand the basic physics of the process of galaxy formation. However, in the ΛCDM paradigm, structure formation is believed to have happened through hierarchical merging of smaller structures (White & Rees 1978; Frenk et al. 1988; Peebles 1993). There is also considerable evidence for continuing hierarchical collapse for example by observations of galaxy mergers (Schweizer 1986) or cluster mergers (Forman & Jones 1982). The problem of understanding the nature of the hierarchical scenario can either be tackled analiticly (Press & Schechter 1974; Lacey & Cole 1993) using the so-called *Press-Schechter formalism*, or numerically using N-body simulations (Frenk et al. 1985; Efstathiou et al. 1988b; Evrard 1990; Mo, Mao, & White 1998; Lemson & Virgo Consortium 2006; Boylan-Kolchin et al. 2009, and many more). N-body simulations efficiently and accurately address dark matter physics and in the past decades have achieved a variety of theoretical results. Among these, some of the remarkable ones are the existence of a universal density profile for dark matter (Navarro, Frenk, & White 1996; Navarro, Frenk, & White 1997), the dynamics of dark matter substructures (Tormen 1997), halo abundances (Jenkins et al. 2001) and many more. Nevertheless the inclusion of gas physics has always been a major issue. This arises for many reasons:

(i) the limited resolution of all simulations to date does not allow to follow or model correctly the microphysics of the gas that affects its dynamics on large scale; (ii) the effects of feedback; (iii) difficulties in disentangling real physical processes from the effects of the particular implementation of gas physics.

An alternative approach is the one of *semianalytic* models (Kauffmann, White, & Guiderdoni 1993), where the full range of complex phenomena intervening in the process of galaxy formation are approximated by a set of simple rules. Semianalytic models are built around the merger trees (merging histories) of dark matter halos either obtained using the Press-Schecter formalism or directly from N-body simulations. Using simple prescriptions for complex processes like gas cooling, star formation, heating cooling suppression, reionisation, and galaxy mergers, they provide direct comparison with observative properties. These do not require immense computational power, and provide quick and deep exploration of the parameter space until a "best-fitting" solution is found.

2.2.3 Feedback

The concept of feedback was introduced when White & Rees (1978) recognized that in a hierarchical model, a simple cooling scheme for the gas would lead to a cooling catastrophe, since at early times the density is so high that all the gas would cool into subgalactic lumps where it would presumably turn into stars. As there is plenty of gas in the Universe today, this clearly has not happened. White & Rees solved this problem by introducing the idea of feedback, whereby the energy released by supernovae associated with an early generation of stars reheats some of the gas, before it has had a chance to condense into halos at high redshift, thus preventing the cooling catastrophe on the galactic scale. Years later, a similar problem arose in the context of galaxy cluster physics. X-ray observations of clusters of galaxies show that the emission from the diffuse Intra Cluster Medium (ICM) (see section 2.2.4) is sharply peaked around the central brightest galaxy. The inferred radiative cooling time of the gas in that peak, where the temper-

ature drops to the centre, is much shorter than the age of the system, suggesting the existence of a cooling flow there (Fabian 1994; Peterson & Fabian 2006, for a review). Nevertheless the central temperature of the gas never drops below a third of the virial temperature. This is seen as an indication that some sort of heating is taking place. The issues of cooling and heating of hot gas have broad relevance to the gaseous part of galaxy formation and evolution, and the truncation of the stellar mass distribution in massive galaxies is likely due to the process which stops cooling flows. The picture is further complicated by the existence of a bimodality in the cluster population (Sanderson, O'Sullivan, & Ponman 2009). Clusters are divided into *cool core* (CC) and *non cool core* (NCC) depending on their temperature profile. The prime suspects are Active Galactic Nuclei (AGN) (McNamara & Nulsen 2007, for a review). To understand these problems in the following sections I will review briefly the properties of the ICM and of AGNs.

2.2.4 The intracluster medium

The first detection of X-ray emission coming from outside the Galaxy dates from 1966. The emission was from the region surrounding M87 at the centre of the Virgo cluster (Byram et al. 1966). In the following years X-ray emission was detected also from the Coma and the Perseus clusters (Fritz et al. 1971; Gursky et al. 1971; Meekins et al. 1971). As a consequence, it was suggested that clusters of galaxies could be a general source of X-rays (Cavaliere et al. 1971). The *Uhuru* X-ray observatory allowed a full sky survey and established that this was the case, furthermore indicating that typical luminosities were in the range of 10^{44} erg·s^{-1}.

Several possible mechanisms were proposed to explain the observed X-ray brightness. Bremmstrahlung (free-free) emission from ionized gas was the most consistent with the X-ray spectra. This implied that the "empty" space between galaxies was filled with hot ($\simeq 10^8$K) and low density ($\simeq 10^{-3}$ cm^{-3}) gas, the *intracluster medium* (ICM). The level of understanding of the physics of the ICM went hand in hand with technological advance. Spatial X-ray surface bright-

ness profiles from the Röntgen Satellite (ROSAT) in the early 90s established the *cooling flow* paradigm. In this scenario, the radiative cooling time

$$t_{cool} = \frac{\frac{5}{2}nkT}{n^2\Lambda(T,Z)} \tag{2.16}$$

within tens of kpc radius in a cluster always exceeds the gravitational dynamical time

$$t_{ff} = \frac{1}{4}\sqrt{\frac{3\pi}{2G\rho}} \tag{2.17}$$

so cooling leads to a slow, subsonic inflow there. This is known as the cooling flow. The flow causes the density to rise and so maintain the pressure, which is determined by the weight of the overlying gas. The predicted temperature profile for a NFW halo is $T \sim r$ (Peterson & Fabian 2006). In equation (2.16) n is the gas number density, k is the Boltzmann constant, T is the gas temperature and $\Lambda(T,Z)$ is the cooling function for a given metallicity Z, in solar units, and temperature T. The predicted mass deposition rates from the cooling flow model are $\sim 10-1000 M_{\odot} yr^{-1}$. The cooling flow problem arises from two aspects of the model (Peterson et al. 2003):

- the soft X-ray cooling flow problem
- the mass sink cooling flow problem.

The former is due to the discrepancy between predictions and observations at low temperatures. The cooling flow model predicts arbitrary low temperatures toward the centre of the cluster, while observations show a plateau at around $T_{vir}/3$ in the inner regions. The latter refers to the absence of evidence of the predicted amount of cold gas mass that would also predict central galaxies far more massive and star forming than actually observed (Donahue & Voit 2004). A variety of possible solutions for the cooling flow problem has been proposed. The cooling could be stabilized by thermal conduction (Fabian, Voigt, & Morris 2002; Voigt et al. 2002),

heating from supernovae (Domainko et al. 2004), cluster mergers (Ricker & Sarazin 2001) or from AGNs (Binney & Tabor 1995; Churazov et al. 2002; Brüggen & Kaiser 2002; Brighenti & Mathews 2003; Hoeft & Brüggen 2004; Pizzolato & Soker 2005; Heinz & Churazov 2005; Cattaneo & Teyssier 2007; Shabala & Alexander 2009, and many more) (see McNamara & Nulsen (2007) for a review). Substantial evidence for a key role of AGNs in the ICM physics come from observations of large cavities in the ICM itself (Bîrzan et al. 2004; Dunn, Fabian, & Taylor 2005). Nevertheless, AGN heating suffers from a main problem: the energy must be deposited uniformly in radius and in time (e.g. Pope et al. (2006)). This can be solved either by a combination of AGN outbursts and convection (Chandran 2004; Chandran & Rasera 2007) or by the existence of a population of AGNs in the cluster of group volume (Nusser et al. 2006).

Cool Core and Non Cool Core Clusters

An important issue that is still relatively unexplored is the dichotomy between "cool core" (CC) and "non cool core" (NCC) clusters (see McCarthy et al. (2004) or Sanderson et al. (2006) for a definition). Studies based on previous generation X-ray satellites suggest that the cluster population might be evenly split between the two classes (Peres et al. 1998). What is the origin of such dichotomy?

Lensing observations show that stronger CCs are found preferentially in clusters showing relaxed morphologies and little substructure. This suggests that cluster mergers might play a decisive role in establishing and modifying the core properties (Richard et al. 2010). Mergers are also invoked to explain the observed distributions of metals[2] in the ICM (e.g. Leccardi, Rossetti, & Molendi (2010)). However, theoretical investigations suggest that mergers are unable to transform CCs in NCCs (Poole et al. 2008; Gómez et al. 2002). Cluster collisions, in fact, heavily disrupt CCs, but those are reestablished after few Gyrs. Nevertheless, during this transient phase the merger remnant resembles observed NCC systems. In this perspective, the

[2]As common practice in astrophysics, "metals" refer to anything with atomic number greater that two.

spread in observed cluster core properties can be interpreted in terms of the merger timescales. Poole et al. (2008) also show that the ICM metals distribution survives mergers between clusters. Moreover, the initial metallicity gradient is never disrupted, so it is difficult to explain The flat metallicities in post-merger NCC systems in terms of the merger timescales. All previous studies, however, are limited to the investigation of idealized mergers between CC systems. To date, no study explored the possibility of mergers between NCC systems. In Chapter 5, we explore the effects of such mergers, focusing our attention on the final and transient metallicity distribution.

2.2.5 Active Galactic Nuclei

Active Galactic Nuclei (AGN) are found in galaxies having a small core of emission embedded in an otherwise typical galaxy. The accepted model requires the presence of a super massive black hole lying at the centre of the galaxy. AGNs owe their brightness to the accretion of gas onto the central black hole. AGNs are classified in many ways: Seyferts, quasars, blazars and radio galaxies. Seyferts are usually found in late-type galaxies, quasars in galaxies with disturbed morphologies while radio galaxies are usually found in early-types. Seyferts are further classified into:

- Type 1 AGN if they show both broad and narrow emission lines in their optical spectra
- Type 2 AGN if they show only narrow emission lines

Differences in the spectral properties of these objects are explained as an orientation effect between the AGN and the observer (Antonucci 1993). AGNs can be radio loud or radio quiet depending on their level of radio emission. The observed spectral energy distribution of radio emission implies a non thermal origin; it comes in fact from synchrotron emission from ultra relativistic electrons spiraling in the accretion disc magnetic field. The size of jets in radio

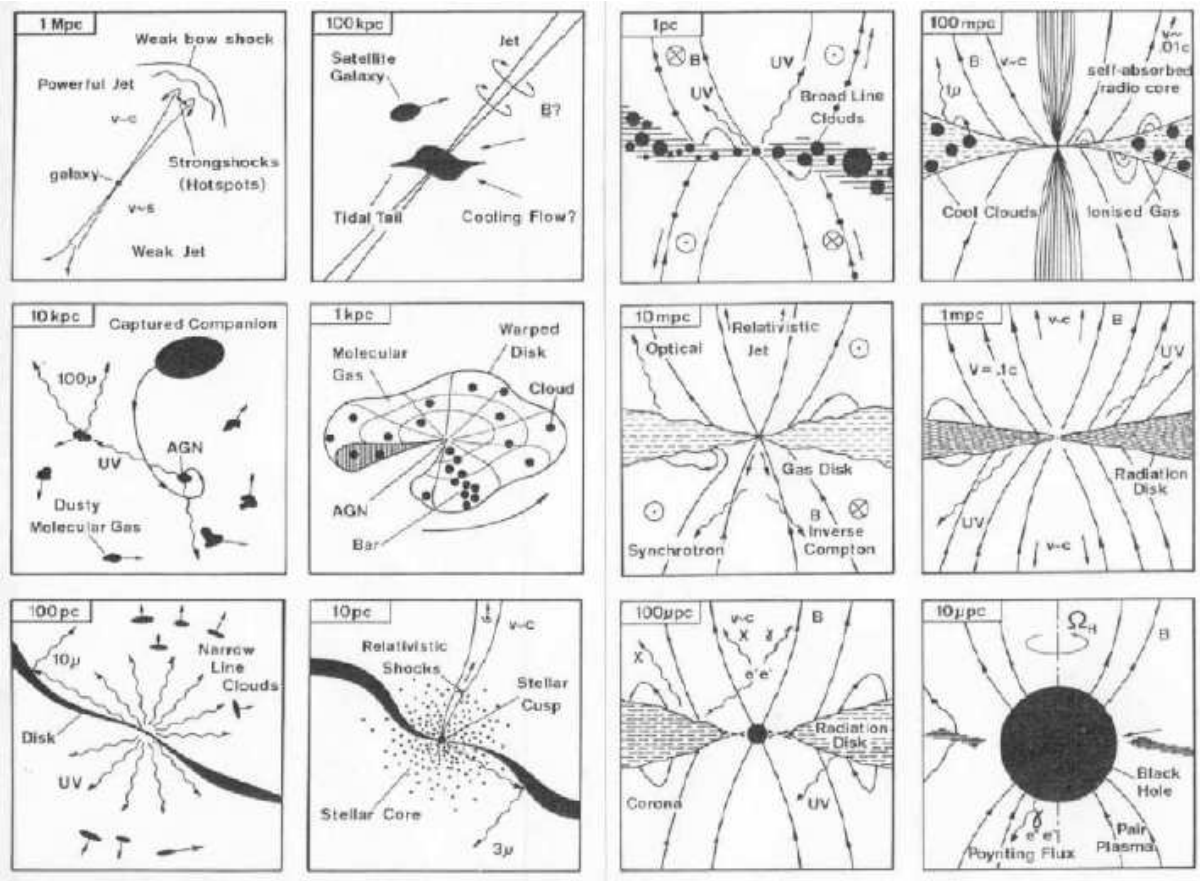

Figure 2.4: Summary of how AGNs affect their surroundings over 12 orders of magnitude in size: from relativistic radio jets at Mpc scales (upper left) to the supermassive black-hole (SMBH) and its surrounding accretion disk at AU or micro-pc scales (lower right). Starting from the upper left, each next panel is expanded by a factor of 10. The SMBH is well visible in the lower right two panels, and the inner accretion disk and torus in the right 6 panels (pc- AU scales). The outer AGN accretion disk and the escaping relativistic jet are well visible in the left 6 panels (mpc-μpc scales), with the galaxy itself shown in the 100-kpc panel (2nd from upper left). Figure from R. Blandford in Active Galactic Nuclei (1990; Springer Verlag, Berlin).

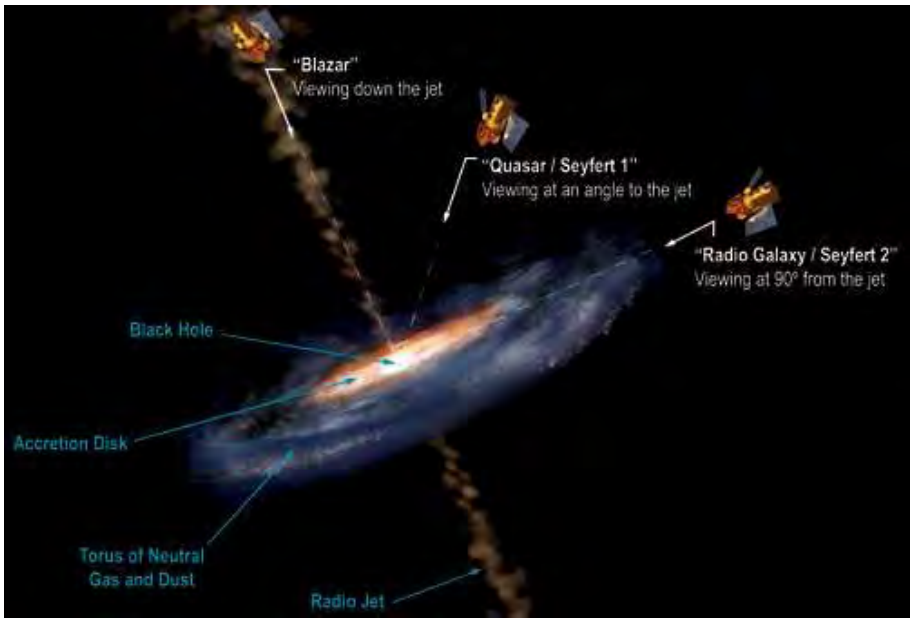

Figure 2.5: Illustration of AGN unification scheme. Type 2 AGNs are viewed edge on, type 1 AGNs are view at an angle $< 45^{\circ}$ and blazars are seen along the jet axis. [Image credit:NASA]

galaxies can be up to the Mpc scale. Radio galaxies are classified according to their morphology as Fanaroff-Riley (FR) type I and type II (Fanaroff & Riley 1974):

- FRI sources are brighter close to the nucleus of the galaxy, the jet is poorly collimated and disperses in extended emission. FRI sources have luminosities $\lesssim 10^{24}$ W Hz^{-1}.
- FRII sources are well collimated sources with very bright lobes and hot spots on their outer edges. They are the brightest radio sources in the Universe, $L \gtrsim 10^{24}$ W Hz^{-1}.

Figure 2.6 shows an example of both classes. Radio galaxies in the local Universe tend to be found in the densest environments like groups and clusters (Hill & Lilly 1991) and have clustering amplitudes in excess of normal galaxies (Peacock & Nicholson 1991; Magliocchetti et al. 2004; Brand et al. 2005). FR II are commonly found in the centre of cool core groups and clusters of galaxies (Eilek & Owen 2007). AGNs are believed to be powered by accretion onto supermassive black holes (SMBH), whose masses range between $M_{\bullet}/M_{\odot} \in [10^6, 10^{10}]$, inhabiting the centre of the host galaxy. If the infalling gas possesses angular momentum,

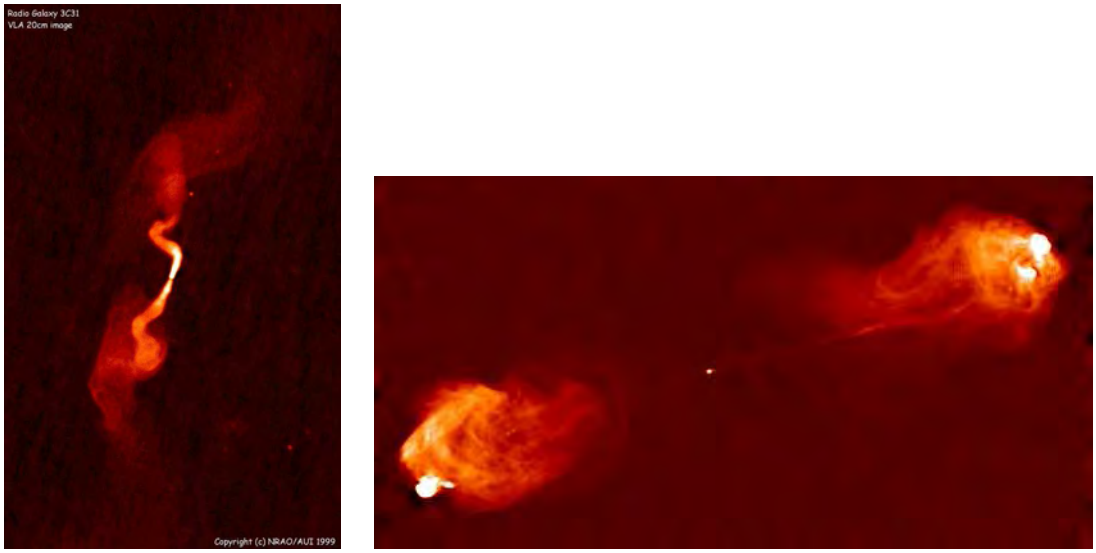

Figure 2.6: **Left**: radio image of the FR I galaxy 3C31. Note the well collimated jet emerging from a bright core that quickly disperse in a diffuse halo of radio emission. **Right**: the FR II galaxy Cygnus A. Two bright spots are clearly visible at the extremities of the radio lobes connected via a thin and well collimated jet. Both images were taken at the VLA. [Images credit: NRAO.]

accretion must ultimately proceed via a disc (Pringle & Rees 1972). The properties of the accretion disc depend on the dimensionless accretion rate $\dot{m} \equiv \dot{M}/\dot{M}_{Edd}$[3]:

1. $\dot{m} > \dot{m}_c$: the accretion flow is optically and geometrically thin. The flow is therefore radiatively efficient and energy is lost mostly via thermal radiation (Shakura & Sunyaev 1976);

2. $\dot{m} \leq \dot{m}_c$: the outer disc is truncated and the central part of the accretion flow is characterized by a very high optical depth. The central disk has a nearly spherical morphology and produces bipolar outflows (Narayan & Yi 1994; Narayan & Yi 1995; Narayan, Kato, & Honma 1997);

3. $\dot{m} < \dot{m}_c$: the disc is morphologically similar to the previous case but a weak inner disk can be sustained as a consequence of gas condensation from the ADAF downward into a

[3] $\dot{M}_{Edd} = L_{Edd}/\eta c^2, L_{Edd} = 4\pi GMc/\kappa,$ with κ electron scattering opacity and η radiation efficiency

cool disk (Liu, Meyer,& Meyer-Hofmeister 2006);

4. $\dot{m} << \dot{m}_c$: radiative cooling is very inefficient and the flow has the same characteristics as in cases (2) and (3), but most of it is in an advection dominated regime (Rees et al. 1982; Narayan & Yi 1994; Narayan & Yi 1995; Narayan, Kato, & Honma 1997).

The critical rate is defined as $\dot{m}_c \sim \alpha^2$ and α is the viscosity, usually taken ~ 0.1. In this scheme the different modes of AGN activity are seen as consequence of the different accretion regimes. Figure 2.7 summerises the various states of accretion.

The Black Hole Fundamental Plane

In recent years a correlation between radio and X ray emission from AGNs (and also from galactic black holes) has been discovered. The rate of accretion and the launch of a relativistic jet/outflow has been known to be correlated (Falcke & Biermann 1995; Begelman, Blandford, & Rees 1984; Rawlings & Saunders 1991). Furthermore, there have been claims of a correlation between radio luminosity of the AGN and SMBHs masses (Franceschini et al. 1998; McLure & Dunlop 2001). Others have reported a very weak or no correlation at all (Ho 2002; Woo et al. 2005). This is because of the difficulty of separating dependence of the radio power on the accretion rate from the mass dependence.

A breakthrough paper from Heinz & Sunyaev (2003) proved that assuming that the jet generation mechanism is independent of the BH mass, it is possible to derive a universal scaling relation between the radio luminosity, BH mass and accretion rate effectively, unifying the study of AGNs and galactic BHs. Furthermore, the relation is independent from the jet model. Following this study, Merloni et al. (2003) and Falcke et al. (2004) indipendently obtained a relation for low power BHs linking X ray luminosity, radio luminosity and BH mass:

$$L_X \propto L_R^m M_\bullet^{\alpha_X - m\alpha_R} \tag{2.18}$$

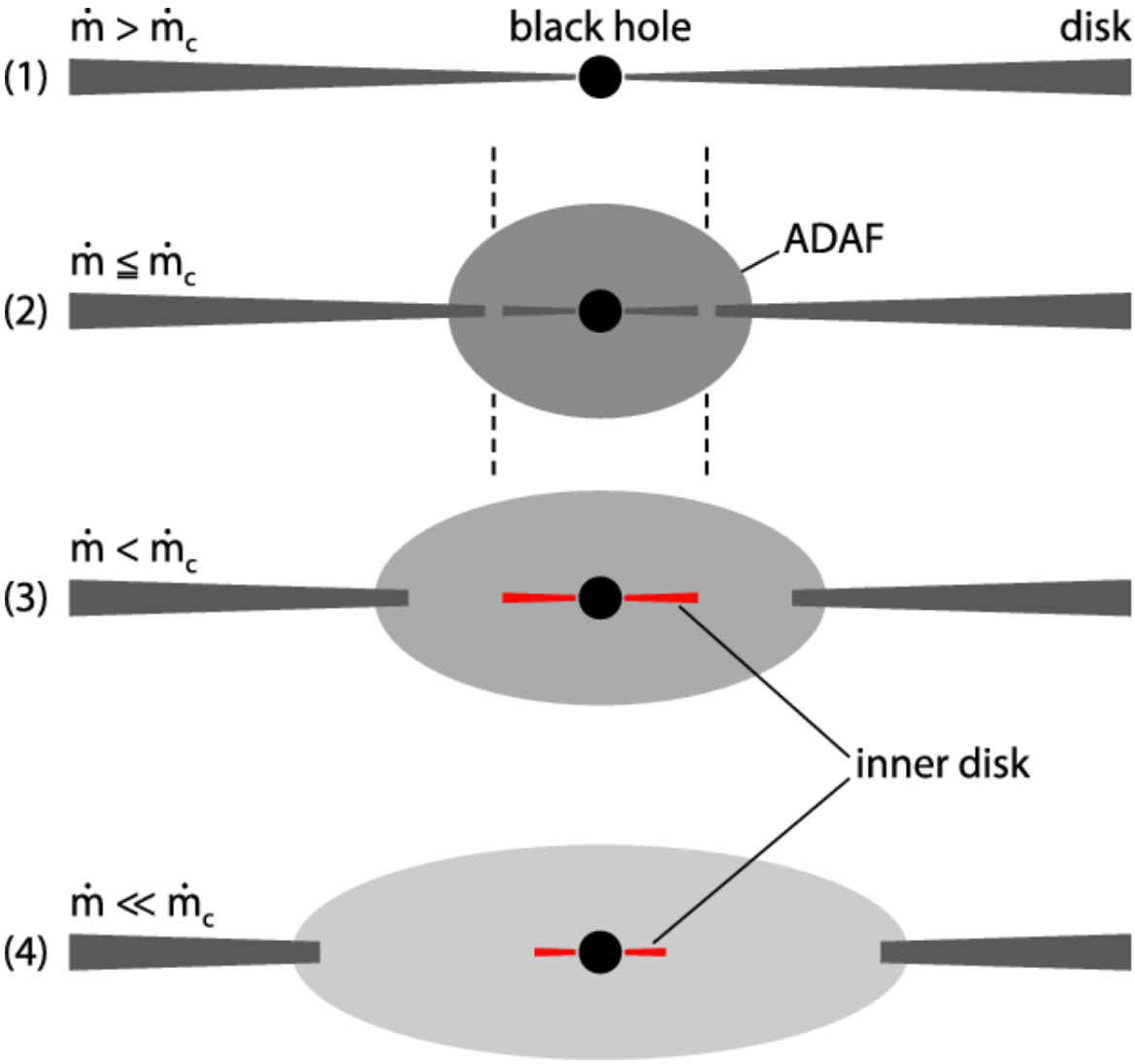

Figure 2.7: Geometry of the accretion flow as a function of the mass accretion rate scaled to the Eddington rate. The panels describe the transition from hard to soft state in a galactic black hole. (1) a soft state with high mass flow rate, (2) the formation of a gap separating the outer from the inner disk, (3) an inner disk, (4) beginning of the hard state. Thanks to the Ergodic theorem and the existence of a black hole fundamental plane, this time evolution is equivalent to the existance of different types of AGN activity. Reproduced from Meyer-Hofmeister, Liu,& Meyer (2009).

where the coefficients α_X and α_R are typical spectral indeces and m is given in Markoff et al. (2003). Equation (2.18) has been named the *black hole fundamental plane*. I have made use of this relation in Chapter 4 to predict the soft and the hard X ray luminosity functions from observed 1.4 GHz radio luminosities.

2.3 Gravitational Waves

Gravitational waves (GWs) are a class of solutions of the Einstein equations. The gravitational action S is the sum of the Einstein-Hilbert action S_E and the matter action S_M,

$$S = \frac{c^3}{16\pi G}\int d^4\sqrt{-g}R + S_M \tag{2.19}$$

where R is the Ricci scalar and $g = \det(g_{\mu\nu})$ is the determinant of the metric tensor $g_{\mu\nu}$. Taking the variation of S with respect to $g_{\mu\nu}$ we obtain the Einstein equations:

$$R_{\mu\nu} - \frac{1}{2}g_{\mu\nu}R = \frac{8\pi G}{c^4}T_{\mu\nu} \tag{2.20}$$

In equation (2.20) $R_{\mu\nu}$ is the Ricci tensor, $R = R_{\mu\nu}R^{\mu\nu}$ is the Ricci scalar and $T_{\mu\nu}$ is the stress-energy tensor. The quantity on the lefthand side of equation (2.20) is the Einsten Tensor $G_{\mu\nu} \equiv R_{\mu\nu} - \frac{1}{2}g_{\mu\nu}R$. By construction $\partial^\nu G_{\mu\nu} = 0$. At the same time, it implies that $G_{\mu\nu}$ is determined up to a null divergence function. The most general form for this function is $\Lambda g_{\mu\nu}$ where Λ is the Cosmological Constant or, as is fashionable these days, Dark Energy. This term is irrelevant in the following discussion.

Consider a flat background metric and a small fluctuation around it. The metric is given by:

$$g_{\mu\nu} = \eta_{\mu\nu} + h_{\mu\nu} \tag{2.21}$$

$\eta_{\mu\nu} = \text{diag}(-1, 1, 1, 1)$ is the Minkowski metric and $|h_{\mu\nu}| \ll 1$. After expanding to $O(h_{\mu\nu})$ equation (2.20) becomes:

$$\Box\bar{h}_{\mu\nu} + \eta_{\mu\nu}\partial^\rho\partial^\sigma\bar{h}_{\rho\sigma} - \partial^\rho\partial_\nu\bar{h}_{\mu\rho} - \partial^\rho\partial_\mu\bar{h}_{\nu\rho} = -\frac{16\pi G}{c^4}T_{\mu\nu}. \tag{2.22}$$

The operator $\Box$ is the flat space d'Alembertian, $\Box = \eta_{\mu\nu}\partial^\mu\partial^\nu = \partial_\mu\partial^\nu$ and $\bar{h}_{\mu\nu} \equiv h_{\mu\nu} - 1/2\eta_{\mu\nu}h$,

h is the trace of $h_{\mu\nu}$. Choosing the *Lorentz* or harmonic gauge,

$$\partial^\nu \bar{h}_{\mu\nu} = 0 \tag{2.23}$$

equation (2.22) simplifies to

$$\Box \bar{h}_{\mu\nu} = -\frac{16\pi G}{c^4} T_{\mu\nu} \tag{2.24}$$

In vacuum $T_{\mu\nu} = 0$, therefore we are left with the simple relation:

$$\Box \bar{h}_{\mu\nu} = 0. \tag{2.25}$$

Using the gauge invariance properties of the metric, it is possible to further simplify the Einstein equations, reducing the number of degrees of freedom from 10 to 2. In the *transverse-traceless gauge*, or TT gauge:

$$h^{0\mu} = 0, \qquad h^i_i = 0, \qquad \partial^j h_{ij} = 0 \tag{2.26}$$

the Einstein equations reduce to:

$$\left(\nabla^2 - \frac{1}{c^2} \frac{\partial^2}{\partial t^2} \right) h_{\mu\nu} = 0. \tag{2.27}$$

This last equation admits plane wave solutions $h^{TT}_{ij}(x) = e_{ij}(\vec{k}) e^{\imath k_\mu x^\mu}$. The tensor e_{ij} is called the polarization tensor and $k_\mu = (\omega/c, \vec{k})$. In case of propagation along the z axis, our plane wave reduces to:

$$h^{TT}(t,z) = \begin{pmatrix} h_+(t) & h_\times(t) & 0 \\ h_\times(t) & -h_+(t) & 0 \\ 0 & 0 & 0 \end{pmatrix} \tag{2.28}$$

where $h_+, h_\times$ are called the amplitudes of the “plus” and “cross” polarizations of the wave.

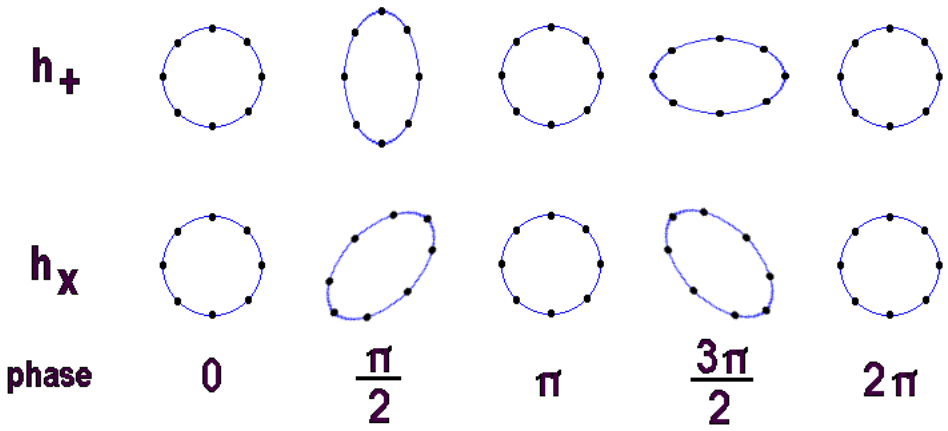

Figure 2.8: The response of a ring of matter to the passage of a gravitational wave is a squeezing and stretching in the reference frame that is in free fall with the center of mass of the ring. The upper row refers to the plus polarization while the second to the cross polarization. The strain is shown every quarter of period.

2.3.1 Generation of Gravitational Waves

Calculations of GW emission from any source in the weak field approximation require a solution of equation (2.22). Since this is linear it can be solved by the method of Green's functions. If $G(x-x')$ solves

$$\Box G(x-x') = \delta^4(x-x'), \tag{2.29}$$

the corresponding solution to equation (2.22) is

$$\bar{h}_{\mu\nu}(x) = -\frac{16\pi G}{c^4}\int d^4x' G(x-x')T_{\mu\nu}(x'). \tag{2.30}$$

In analogy to electromagnetism, the appropriate solution is a retarded Green's function (Jackson 1975)

$$G(x-x') = -\frac{1}{4\pi|\vec{x}-\vec{x}'|}\delta(x^0_{ret}-x'^0) \tag{2.31}$$

where $x'^0 = ct'$, $x^0_{ret} = ct_{ret}$ and $t_{ret} = t - c^{-1}|\vec{x} - \vec{x}'|$ is the retarded time. The solution to (2.22) is

$$\bar{h}_{\mu\nu}(x) = -\frac{4G}{c^4}\int d^3x' \frac{1}{4\pi|\vec{x} - \vec{x}'|} T_{\mu\nu}(t - c^{-1}|\vec{x} - \vec{x}'|, \vec{x}'). \tag{2.32}$$

In the TT gauge and in the low velocity and far field approximation, the gravitational field at first order can be expressed as (Misner, Thorne, & Wheeler 1973)

$$h_{\mu\nu}(\vec{r}, t) = \frac{2G}{c^4}\frac{1}{r}\left[\frac{d^2}{dt^2} I_{\mu\nu}\right]_{t-r/c} \tag{2.33}$$

where r is the distance from the source and

$$I_{\mu\nu} = \int d^3x \rho(\vec{x}, t)\left(x^\mu x^\nu - \frac{1}{3}x^2\eta_{\mu\nu}\right) \tag{2.34}$$

is the trace reduced quadrupole momentum associated with the energy density $\rho(\vec{x}, t)$ of the source. Conservation of the stress-energy tensor, that at the first order is equivalent to the conservation of linear momentum, implies that the first non-null contribution to GWs emission comes from the quadrupole term. In the case of compact binary systems equation (2.33) yields the formulae for GWs emission to the lowest quadrupole Newtonian order:

$$h_+(t) = \frac{1}{r}\frac{4G\mu\omega_s^2 R^2}{c^4}\left(\frac{1 + \cos^2\iota}{2}\right)\cos(2\omega_s t_{ret}) \tag{2.35}$$

$$h_\times(t) = \frac{1}{r}\frac{4G\mu\omega_s^2 R^2}{c^4}\cos\iota\sin(2\omega_s t_{ret}) \tag{2.36}$$

where $\mu = m_1 m_2/(m_1 + m_2)$ is the reduced mass, R is the separation of the binary, r is the distance to the binary, ι is the inclination of the binary orbital plane with respect to the celestial sphere and ω_s is the Kepler frequency. In the last orbits before the coalescence of the binary, the weak field approximation is not adequate to describe the dynamics of the system. Therefore one must resort to the full Einstein equations. The formidable task of fully solving these equations

has been only recently achieved numerically (e.g. Pretorius 2007 and references therein).

As the so-called *parametrized post-Newtonian* (PPN) framework is an adequate description of the inspiral phase of a coalescing binary system, it is common practice in GW data analysis to use PPN waveforms. The particular choice of the waveform I used here is specified in Chapter 3, Eqs. (3.12) and (3.8). A complete up-to-date description of the two body problem in the post-Newtonian approximation can be found in Blanchet (2006) or Blanchet (2009) and references therein.

2.4 Techniques

In this section I describe the main techniques I have used in the following chapters of this thesis. I start by briefly reviewing smoothed particle hydrodynamics (SPH) simulations focusing on GADGET-2 that is the SPH implementation used in Chapter 5. I then describe wide field sky surveys that are the core of the work I present in Chapter 4. Finally I give an overview of Bayesian data analysis in the context of gravitational waves especially concentrating on the novel Nested Sampling algorithm on which the material in Chapter 3 is based.

2.4.1 Smoothed Particle Hydrodynamics: GADGET-2

Computer simulations are nowadays an essential tool in the hands of any researcher. In section 2.2.2, I already introduced simulations as a fundamental and powerful instrument in the context of galaxy formation. Direct simulation is in fact the only available technique able to fully capture the dynamics of complex systems like clusters of galaxies. The physics of structure formation and evolution is fully determined by gravitational and hydrodynamical physics. Gravity can be solved for extremely efficiently using particle-based N-body simulations, while traditional mesh-based schemes to solve the Euler equations are extremely computationally expensive and their resolution is set by the grid size[4]. *Smoothed Particle Hydrodynamics* (SPH) (Monaghan (1992) for a review) is a method that solves Euler equations interpolating over a set of particles that trace the fluid motion. The particle nature of SPH allows direct integration of the most efficient gravity solvers with hydrodynamics. The core of the SPH idea is an interpolation method that allows any function to be expressed in terms of its values on a set of disordered points. The integral interpolant af any function $f(\vec{r})$ is

$$f(\vec{r}) = \int f(\vec{r}')W(\vec{r} - \vec{r}', h)d\vec{r}' \tag{2.37}$$

[4]Research to remove this limitation led to Adaptive Mesh Refinement (AMR) codes (Berger & Colella 1989), where the grid resolution is varied to use efficiently computing power.

where the integration is over the whole space, W is the kernel and h is the *smoothing length*. In terms of a discrete set of points (particles) equation (2.37) for each particle i becomes

$$f_i(\vec{r}) = \sum_j m_j \frac{f_j}{\rho_j} W(\vec{r}_i - \vec{r}_j, h) \tag{2.38}$$

where m_j is the mass of particle j, ρ_j is the density associated with particle j and the sum is over all particles. For example the density ρ_i associated with particle i is simply

$$\rho_i(\vec{r}) = \sum_j m_j W(\vec{r}_i - \vec{r}_j, h) \tag{2.39}$$

Spatial derivatives are simply obtained as

$$\nabla f_i(\vec{r}) = \sum_j m_j \frac{f_j}{\rho_j} \nabla W(\vec{r}_i - \vec{r}_j, h) \tag{2.40}$$

The kernel W has the following properties:

$$\int W(\vec{r} - \vec{r}', h) d\vec{r}' = 1 \tag{2.41}$$

$$\lim_{h \to 0} W(\vec{r} - \vec{r}', h) = \delta(\vec{r} - \vec{r}') \tag{2.42}$$

Usual choices are a Gaussian kernel or a spline kernel

$$W(\vec{r}, h) = \frac{8}{\pi h^3} \begin{cases} 1 + \frac{3}{2}q^2 + \frac{3}{4}q^3 & \text{if } 0 \leq \frac{r}{h} \leq 1/2 \\ \frac{1}{4}(2 - q^2) & \text{if } 1/2 \leq \frac{r}{h} \leq 1 \\ 0 & \text{otherwise} \end{cases} \tag{2.43}$$

where $q = r/h$. This is the particular choice in GADGET-2.

GADGET-2[5] is a TreeSPH code specifically designed for large volume cosmological simu-

[5]GADGET-2 is publicly available at the address http://www.mpa-garching.mpg.de/gadget.

lations (Springel 2005). It uses the "tree" method to solve for the gravitational potential. The way the tree algorithm operates is the following: particles are grouped into cells and the Poisson equation is solved through a multipole expansion. GADGET-2 uses the Barnes & Hut (1986) oct-tree algorithm. Starting from the whole simulation volume the particles are grouped into nodes. Each node is divided in 8 daughter nodes of half the side length each until the "leaf" level is reached where each node contains exactly one particle. The gravitational forces are calculated by "walking" the tree. Starting from the root at each node an octupole expansion is performed and a decision is made whether the accuracy of the calculation meets the requirements. If the answer is positive than the "branch" is abandoned otherwise the daughter nodes are opened and the algorithm continues. In this way, the gravitational force from a single particle can be computed with $O(\log(N))$ interactions instead of $O(N)$ from direct summation.

The hydrodynamics is solved by evolving the SPH version of Euler equations allowing each particle to have its own smoothing length h_i set by the requirement that the kernel volume contains a fixed mass. Time integration is performed using a leapfrog integration that garantees the Hamiltonian nature of the system. Furthermore adaptive time steps are implemented according to the particle velocity. Thus GADGET-2 is fully adaptive timewise and spacewise.

SPH vs AMR Both SPH and AMR are affected by fundamental problems (e.g. Springel (2010)) that affect them in particular regimes. SPH codes, for instance, do not resolve shocks effectively and any contact discontinuity is treated with low-order accuracy; SPH also seem to suppress fluid instabilities (Agertz et al. 2007) because of inaccurate gradient estimates across density jumps. Mitchell et al. (2009) also suggests that SPH might be underestimating the degree of mixing in simulations of cluster mergers because of Kelvin-Helmoltz instability suppression. The most serious problem affecting all AMR codes, or any Eulerian mesh-based code, is their lack of Galilean-invariance. Their results are sensitive to bulk velocities in the gas. Furthermore, entropy is implicitly produced when gas in different thermodynamic conditions

are mixed together in a single cell. Explicit entropy conserving schemes have been developed, but they come at the sacrifice of exact energy conservation (see §1 in Springel (2010)). The refinement itself is problematic as there is no criterion to "anticipate" the fluid dynamics to increase the resolution where actually needed. For the study presented in Chapter 5, GADGET-2 is the ideal choice. Because of its explicit entropy conservation scheme (Springel & Hernquist 2002) (that does not come at the cost of energy conservation), we are assured that any production of entropy is due to the physical processes intervening during a two-body idealized merger. The poor shock treatment will not be a concern as the typical Mach number we expect to observe is $M \sim 1-2$ (e.g. McCarthy et al. (2007)), therefore the difference in the gas density before and after the shock is ≈ 2. As we will investigate the degree of mixing during two-body idealized mergers, the result in Mitchell et al. (2009) might be a concern for our conclusions. Nevertheless, SPH *underestimates* mixing thus our conclusions will be strengthened.

2.4.2 Sky surveys

To study the demography of any population of galaxies is essential to have data over a large volume of the observable universe. In this thesis, I made use of wide field surveys in the optical, infrared and radio bands.

2MASS The Two Micron All-Sky Survey (2MASS)(Kleinmann et al. 1994) began in 1997 and was completed in 2001. The survey was carried out using two telescopes located in Mt. Hopkins, Arizona and Cerro Tololo/CTIO, Chile. This ensured coverage of the entire sky. The final data catalogue was released in 2003. The survey consists of all sky photometry in three wavebands in the near infrared: J (1.25 μ m), H (1.65 μ m), and Ks (2.17μ m). The completeness limit[6] is $K \sim 13.5$ for extended sources. More than 300 million point sources and 1 million extended sources were detected and catalogued. The full data release can be found

[6]The term "completeness limit" refers to the threshold apparent magnitude above which 100% of the sources are detected.

at: http://www.ipac.caltech.edu/2mass/.

SDSS The Sloan Digital Sky Survey (SDSS) (York et al. 2000) aimed to image an area of 10000 deg^2 in five different wavebands (u, g, i, r, z) to a depth of $g' \sim 23.5$. It uses a dedicated 2.5-m wide-angle optical telescope located in the Sacramento Mountains in Sunspot, New Mexico (USA). The current data release is the 7th in which the original goals of the project have been achieved and surpassed. In this thesis, I used the SDSS spectroscopic 6th data release (Adelman-McCarthy et al. 2008) in the version provided by the New York University Value-Added Galaxy Catalog (NYU-VAGC) (Blanton et al. 2003). The sky coverage is 7425 deg^2. The total number of galaxies identified is $790,860$ with petrosian magnitude limit $r \sim 17.77$.

SDSS uses a pair of spectrographs fed by optical fibres to measure 640 spectra simultaneously. The diameter of the fibres is $3''$, corresponding to 5.7 kpc at a redshift of 0.1; at this redshift the spectra are representative of a large fraction of light ($\sim 50\%$) from the target galaxy. For closer objects the emission is more dominated by nuclear emission. The minimum separation of the fibre centers is $55''$. Therefore each object lying within $55''$ will be missed by the spectroscopic survey. A solution to this problem is presented in the NYU-VAGC. They supplemented the original spectroscopic SDSS galaxy catalogue with the imaged galaxies that have been missed because of fiber collisions. The NYU-VAGC catalogue can be fully accessed at: http://sdss.physics.nyu.edu/vagc/.

In Chapter 4, I used the full galaxy sample comprising $790,860$ galaxies.

Radio Surveys The Faint Images of the Radio Sky at Twenty-one centimetres (FIRST) (Becker et al. 1995) and the NRAO VLA Sky Survey (NVSS) (Condon et al. 1998) are 1.4GHz sky surveys carried out at the VLA site in recent years. NVSS imaged the radio sky north of -40° with an angular resolution of $45''$ and flux sensitivity of 2.5mJy[7]. FIRST aims at covering the same sky area as SDSS with a flux sensitivity of 1mJy and angular resolution of $5''$. Because of

[7] 1Jy = 10^{-26}W·m^{-2}·Hz^{-1}.

the superior angular resolution of FIRST I used it in cross correlation with SDSS and 2MASS to identify radio counterparts of optically selected black holes. Furthermore, even if the high angular resolution "dilutes" the measured flux (Best 2004) compared to NVSS measurements, it guarantees that we are measuring the core radio luminosity to which the black hole fundamental plane relation is applicable.

Luminosity Function For Magnitude Limited Samples

Large surveys allow an accurate determination of the *luminosity function*. The luminosity function is represented by the comoving number of galaxies per absolute magnitude M bin:

$$dN = \Phi(M) dV dL \tag{2.44}$$

The determination of $\Phi(M)$ requires the availability of well defined samples whose selection criteria are well known and accountable for. Current surveys as described above are currently to be considered complete up to the nominal limiting apparent magnitude m_{lim}[8]. Even to this limit catalogues are incomplete for other reasons, for example the "Malmquist bias" for which more distant galaxies appear brighter on average because more and more faint galaxies are not detected. The incompleteness of the catalogue needs to be statistically compensated for. There are various methods (Binggeli, Sandage, & Tammann (1988) for a review) to calculate the statistical corrections to the luminosity function. The method I used in this thesis is the V/V_{max} technique (Schmidt 1968; Lynden-Bell 1971; Choloniewski 1987; Efstathiou et al. 1988). Here V is the sample volume between the galaxy and the observer and $V_{max} \equiv V(M)$ is maximum volume in which the galaxy could lie without dropping below m_{lim}. Calculating V_{max} requires the knowledge of the distance to each galaxy therefore of the redshift z. Once the absolute magnitude M has been calculated, one can estimate the luminosity function $\Phi(M)$ as

[8]The absolute and apparent magnitude are related by $M = m - 5(\log_{10}(D_L) - 1)$ where D_L is the luminosity distance defined in (2.11) and measured in pc.

(Choloniewski 1987; Schade 1991)

$$\Phi(M) = \sum_j \psi_j \delta(M - M_j) \tag{2.45}$$

$$\psi_j = \frac{1}{V^j} \tag{2.46}$$

that can be averaged over the magnitude bins to give:

$$\overline{\Phi(M)} = \frac{1}{\Delta M} \sum_j \frac{1}{V^j} \tag{2.47}$$

where V^j is the maximum volume accessible to object j given its absolute magnitude $M_j \in (M_1, M_2)$ and M_1, M_2 are the extremes of the bin under consideration, $\Delta M = M_1 - M_2$.

Surveys of emission line galaxies Survey of emission lines galaxies requires a different treatment. Schmidt et al. (1986) shows that in case the samples are selected according to the equivalent width, it is sufficient to modify the limiting magnitude in

$$m_{\rm lim} = r_{\rm lim} - 2.5 \log \left(\frac{\rm EW\,(1+z)}{\rm EW_{lim}} \right) + f\,(\lambda) \tag{2.48}$$

where $f\,(\lambda)$ is a tabulated function. I made use of these relations in Chapter 4 to calculate the supermassive black hole mass function in the local Universe. The V/V_{max} technique as introduced by Schmidt (1968) assumes uniform spatial density of galaxies. However, it has been used to determine the supermassive black hole mass function in clusters and groups of galaxies where the assumption of uniform distribution is obviously violated. Nevertheless, spatial uniformity breaks down when the luminosity function is calculated for regions with very different densities at the same time. In Chapter 4, overdense and underdense regions have been analysed separately and we assumed spatial uniformity separately in each environment.

2.4.3 Bayesian Data Analysis

The output of any GW detector is a time series made of the combination of the noise and the GW signal. As for many other systems a GW detector can be thought as a linear system so that

$$h(t) = D_{ij} h(t)^{ij} \tag{2.49}$$

the quantity D_{ij} is the *detector tensor* that describes the coupling between the detector itself and the GW. Since the GW can be written as $h_{ij}(x) = e_{ij}(\vec{k}) e^{\imath k_\mu x^\mu}$ it is convenient to define the *antenna pattern* as $F(\hat{n}) \equiv D_{ij} e^{ij}(\hat{n})$ where $\hat{n} = -\vec{k}/|\vec{k}| = (\theta, \phi)$ is the unit vector identifying the direction of propagation of the GW. In case of interferometric detector like GEO 600 (Willke 2004) LIGO (Barish & Weiss 1999) or Virgo (Acernese et al. 2004) and their upgraded versions

- Advanced LIGO[9],
- Advanced Virgo[10],

the response of the detector to the GW in a geocentric frame is (e.g. Anderson et al. 2001)

$$h(t) = h_+(t) F_+(\theta, \phi, \Psi) + h_\times(t) F_\times(\theta, \phi, \Psi) \tag{2.50}$$

$$F_+(\theta, \phi) = -\frac{1 + \cos^2\theta}{2} \cos 2\phi \cos 2\Psi - \cos\theta \sin 2\phi \sin 2\Psi \tag{2.51}$$

$$F_\times(\theta, \phi) = \frac{1 + \cos^2\theta}{2} \cos 2\phi \sin 2\Psi - \cos\theta \sin 2\phi \cos 2\Psi. \tag{2.52}$$

The GW signal, if any is present, is buried within the instrumental noise $n(t)$. The output of a detector is therefore $s(t) = h(t) + n(t)$, where $n(t)$ is the noise. The purpose of data analysis is to (i) test the hypothesis that the signal $h(t)$ is present in the detector output $s(t)$ and (ii) estimate the unknown parameters on which the model depends.

[9] http://www.ligo.caltech.edu/advLIGO/
[10] http://wwwcascina.virgo.infn.it/advirgo/

In the context of Bayesian inference, both aspects are simply tackled through an application of Bayes' theorem and the standard rules of probability theory. Bayesian approach is conceptually straightforward, but its practical implementation is challenging since one needs to explore large parameter spaces and compute high-dimensional integrals.

Given some data $\vec{d}$, a set of hypotheses H_i and all the prior information available I, Bayes' theorem states

$$P(H_i|\vec{d}, I) = \frac{P(H_i|I)P(\vec{d}|H_i, I)}{P(\vec{d}|I)}. \tag{2.53}$$

where $P(H_i|I)$ is the prior probability of H_i, $P(\vec{d}|H_i, I)$ is the *likelihood function* of the data, given that H_i is true, and

$$P(\vec{d}|I) = \sum_i P(\vec{d}|H_i, I) \tag{2.54}$$

is the marginal probability of the data set $\vec{d}$ which can only be calculated if there exists a complete set of independent hypotheses such that $\sum_j P(H_j|\vec{d}, I) = 1$. Even without the completeness condition stated above it is still possible to compare different hypotheses by defining the *odds ratio* O_{ij} between two of them,

$$O_{ij} = \frac{P(H_i|I)}{P(H_j|I)} \frac{P(\vec{d}|H_i, I)}{P(\vec{d}|H_j, I)} = \frac{P(H_i|I)}{P(H_j|I)} B_{ij}\,; \tag{2.55}$$

In the previous equation the normalisation factor $P(\vec{d}|I)$ cancels out, and

$$B_{ij} \equiv \frac{P(\vec{d}|H_i, I)}{P(\vec{d}|H_j, I)} \tag{2.56}$$

is known as the *Bayes Factor* or ratio of likelihoods. Since the gravitational wave signal we are modelling depends on a set of parameters, $\vec{\theta} \in \Theta$, described in Chapter 3, where Θ is the parameter space, the likelihood of the model H must be marginalised over all the parameters

weighted by their prior probability distribution, giving the *marginal likelihood* or *evidence*,

$$Z = P(\vec{d}|H, I) = \int_{\Theta} p(\vec{\theta}|H, I)p(\vec{d}|H, \vec{\theta}, I)d\vec{\theta}, \tag{2.57}$$

where $p(\vec{\theta}|H, I)$ is the prior probability distribution over the parameter space.

Assuming that the noise is a Gaussian and stationary process with zero mean and variance described through the one-sided noise spectral density $S_n(f)$:

$$\langle \tilde{n}(f) \rangle = 0\,, \tag{2.58}$$

$$\langle \tilde{n}(f)\, \tilde{n}^*(f') \rangle = \frac{1}{2}\delta(f - f')S(f)\,, \tag{2.59}$$

where $\langle . \rangle$ stands for the ensemble average. The likelihood of a given noise realisation $n = n_0$ is then given by a multivariate Gaussian distribution

$$p(n = n_0) \propto e^{-(n_0|n_0)/2}\,, \tag{2.60}$$

where $(.|.)$ stands for the inner product (e.g. Cutler & Flanagan (1994)):

$$(A|B) = 4\mathrm{Re}\int_0^{\infty} df \frac{\tilde{A}^*(f)\tilde{B}(f)}{S_n(f)} \tag{2.61}$$

that solves the variational problem of finding the optimal filter to maximise the signal-to-noise ratio (SNR). Given that for each particular realization of the noise n_0, the output of the detector will be $s = n_0 + h(\vec{\theta})$, $p(\vec{d}|H, \vec{\theta}, I)$ is identified with (2.60) and the evidence integral reduces to

$$Z = P(\vec{d}|H, I) \propto \int_{\Theta} p(\vec{\theta}|H, I)e^{-(s-h(\vec{\theta})|s-h(\vec{\theta}))/2}d\vec{\theta}. \tag{2.62}$$

For second Post-Newtonian order gravitational waves generated by binaries with negligible spins and eccentricity, the number of dimensions of the parameter space Θ is 9, and, to the

same PN order, for a generic binary system the total number of parameters increases up to 17.

For the case of a gravitational wave described by a theory whose Boson is massive, as considered in Chapter 3, the total number of parameters, neglecting spins, is 10 (Will 1998).

Model selection has been tackled through a number of techniques, including Reversible Jump MCMC (Green 1995) and thermodynamic integration (Gelman & Meng 1998). The technique used in this thesis to compute (2.62) is based on the Nested Sampling algorythm (Skilling 2004; Sivia & Skilling 2006). It is a powerful numerical technique to deal with multi-dimensional integrals. It differs from other Monte Carlo techniques such as Markov-Chain Monte-Carlo (MCMC) methods that are popular in applications of Bayesian inference, in that it is specifically designed to estimate the evidence integral itself with the PDFs

$$p(\vec{\theta}|\vec{d}, H, I) = \frac{p(\vec{\theta}|H, I)p(\vec{d}|\vec{\theta}, H, I)}{p(\vec{d}|H, I)} \tag{2.63}$$

of which the estimates of each parameter are optional by-products.

Nested Sampling and Parameter estimation

Nested Sampling (Skilling 2004; Sivia & Skilling 2006) has been already successfully applied to data from LISA, *e.g.* MultiNest (Feroz et al. 2009a; Feroz et al. 2009b) or to data sets primarily in the context of cosmology (Feroz et al. 2008; Feroz & Hobson 2008; Feroz, Hobson, & Bridges 2009). The version I used in Chapter 3 is the one presented in Veitch & Vecchio (2008a), Veitch & Vecchio (2008b) and Veitch & Vecchio (2010). I briefly review here its main features. The interested reader is referred to Veitch & Vecchio (2010) for a detailed description.

The evidence $Z = P(\vec{d}|H, I)$, given in equation (2.57) is given by the integral of the product of the prior distribution with the likelihood function. The relationship between the prior,

likelihood, posterior PDFs and the evidence is shown explicitly by the product rule:

$$p(\vec{\theta}|H,I) \times p(\vec{d}|\vec{\theta},H,I) = Z \times p(\vec{\theta}|\vec{d},H,I) \quad (2.64)$$

$$\text{Prior} \times \text{Likelihood} = \text{Evidence} \times \text{Posterior}. \quad (2.65)$$

As the prior and the posterior are, by definition, normalized, the magnitude of Z is set by the likelihood function. Z is evaluated by integration of the left side of equation (2.64) over the full parameter space Θ. Except in very simple cases, this integral cannot be performed analiticly and one must resort to suitable approximations. The basic idea of Nested Sampling is to consider a stochastic sampling of the prior distribution instead of a uniform grid on Θ and use this basket of N points, called *live points* (which will be denoted as $\vec{\theta}_i$, $i = 1, \ldots, N$), to evaluate the lefthand side of (2.64). The evidence integral (equation (2.57)) can then be expressed as

$$Z = \int_\Theta p(\vec{\theta}|H,I)p(\vec{d}|H,\vec{\theta},I)d\vec{\theta}\,, \quad (2.66)$$

$$\approx \sum_{i=1}^{N} p(\vec{d}|\vec{\theta}_i,H,I)w_i\,, \quad (2.67)$$

$$\approx \sum_{i=1}^{N} L_i w_i\,, \quad (2.68)$$

where the "weight"

$$w_i = p(\vec{\theta}_i|H,I)d\vec{\theta} \quad (2.69)$$

is the fraction of the prior distribution represented by the i-th sample, and $L_i \equiv p(\vec{d}|H,\vec{\theta}_i,I)$ is its likelihood.

To calculate the weight associated with each point $\vec{\theta}_i$, Skilling (2004) shows that it is useful to think of each point as lying on a contour surface of constant likelihood in the parameter space. Let's define the *prior mass* X_i as the fraction of the total prior volume enclosed by the i-th contour. As the likelihood is strongly peaked at the "true" values of the parameters $\vec{\bar{\theta}}$, there

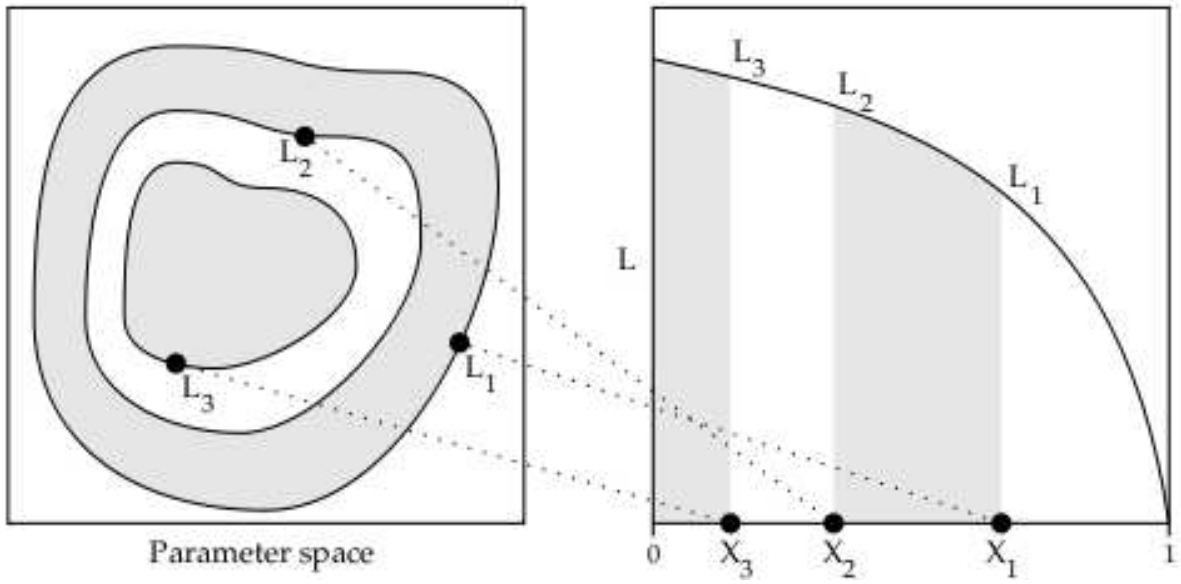

Figure 2.9: Each sample in the basket of live points can be thought of as lying on a contour line of equal likelihood value. Figure reproduced from Skilling 2004.

is monotonic map between X_i and likelihood contours; the larger X_i the smaller the value of the likelihood on whose contour the live point $\vec{\theta}_i$ lies, see Fig. 2.9.

Eq. (2.57) or (2.68) can then be expressed as the one-dimensional integral

$$Z = \int L(X)dX \leq \sum_i L(X_i)(X_i - X_{i-1})\,. \tag{2.70}$$

As the inverse mapping $\vec{\theta}(X)$ is not known, integral (2.70) cannot be solved analytically neither. However, the prior distribution is normalised to unity, so the unknown prior mass X_1 associated to the outermost likelihood contour L_1 is described by the same probability distribution $P(X_1)$ that characterises the maximum $t_1 \in [0,1]$ of N random numbers drawn from the uniform distribution $U(0,1)$. If we replace the point X_1 with a new point sampled from the prior volume lying at higher likelihood than L_1, $X(L > L_1)$, the process can be repeated so that $X_2 = t_2 X_1$. In general, $\ldots$,$X_i = t_i X_{i-1}$. By definition $t_i \equiv X_i/X_{i-1}$ is the shrinkage ratio. The probability of t_i is given by $P(t_i) = N t_i^{N-1}$. As the volume enclosed at each iteration shrinks geometrically,

we are ensured the convergence of the integral (2.70). At each iteration, the mean and variance of $\log t$ are

$$\mathrm{E}[\log t] = \int_0^1 dt p(t) \log t = -N^{-1} \tag{2.71}$$

$$\mathrm{var}[\log t] = \int_0^1 dt \left(\log t - \mathrm{E}[\log t]\right)^2 p(t) = N^{-2}\,. \tag{2.72}$$

Creating many realisations of the ts for each iteration in the algorithm and using the approximation of the mean, we can write the fractional prior volumes

$$\log X_i \approx \; -(i \pm \sqrt{i})/N. \tag{2.73}$$

We are now in the position of assigning a weight to each sample as $w_i = X_i - X_{i-1}$ and calculating the evidence (2.70). Finally, to fully determine the algorithm, we need a termination condition. Veitch & Vecchio (2010) adopt $L_{\max} w_i > Z_i e^{-5}$.

To summarise, the algorithm can be described as:

1. Draw N points $\vec{\theta}_a, a \in 1 \ldots N$ from prior $p(\vec{\theta})$, and calculate their L_a's.
2. Set $Z_0 = 0$, $i = 0$, $\log w_0 = 0$
3. While $L_{\max} w_i > Z_i e^{-5}$
   (a) i = i +1
   (b) $L_{\min} = \min(\{L_a\})$
   (c) $\log w_i = \log w_{i-1} - N^{-1}$
   (d) $Z_i = Z_{i-1} + L_{\min} w_i$
   (e) Replace $\vec{\theta}_{\min}$ with $\vec{\theta} \sim p(\vec{\theta}|H, I) : L(\vec{\theta}) > L_{\min}$
4. *Add the remaining points:* For all $a \in 1 \ldots N$, $Z_i = Z_i + L(\vec{\theta}_a) w_i$.

$\vec{\theta} \sim p(\vec{\theta}|H, I)$ means $\vec{\theta}$ is drawn from the distribution $p(\vec{\theta}|H, I)$. As an optional byproduct, Nested Sampling automatically gives posterior probability distribution functions (PDF)

$$p(\vec{\theta}|\vec{d}, H, I) = \frac{p(\vec{\theta}|H, I)p(\vec{d}|\vec{\theta}, H, I)}{p(\vec{d}|H, I)} \tag{2.74}$$

of all the parameters in the particular model used to evaluate the likelihood and the evidence. In fact as the nested sampling algorithm proceeds, the list of points used in approximating the evidence integral is stored, along with the likelihood values of each sample, the corresponding value of the parameter vector, and $\log X_i \approx i/N$. Since these samples are drawn from the prior distribution, limited by a likelihood contour to a fraction X_i of the full prior, they have a zero probability of lying outside the contour. Therefore, the density of the samples is boosted within the contour. The probability density of the i-th point from the nested sampling output is

$$p(\vec{\theta}_i|\mathrm{NS}) = \frac{p(\vec{\theta}_i|H, I)}{X_i}\,, \tag{2.75}$$

whereas samples from the posterior PDF, equation (2.63), have probability density

$$p(\vec{\theta}_i|\vec{d}, H, I) \propto p(\vec{\theta}_i|H, I)p(\vec{d}|\vec{\theta}_i, H, I)\,. \tag{2.76}$$

Since the nested sampling points are independent samples, they can be re-used to generate samples from the posterior PDF by re-sampling them. Substituting Eq. (2.75) into Eq. (2.76), it is easy to see that the probabilities are related by,

$$p(\vec{\theta}_i|\vec{d}, H, I) \propto p(\vec{\theta}_i|\mathrm{NS})p(\vec{d}|\vec{\theta}_i, H, I)X_i, \tag{2.77}$$

and so the resampling weight of each one is $\propto p(\vec{d}|\vec{\theta}_i, H, I)X_i$.

2.5 Outline of the Thesis

The rest of the thesis is organized as follows:

Chapter 3. In this chapter I present a method based on Bayesian inference to perform tests of General Relativity using gravitational waves observations. Using the massive graviton theory as a proof-of-principle case, I show how the computation of the evidence and of the Bayes factor among different hypothesis provides an absolute way of chosing between them. The bounds on the Compton wavelength of the Graviton that Advanced LIGO and ET will be able to provide are calculated and compared with previous non-Bayesian studies. I discuss then the bias introduced by mismodeling of the gravitational wave signal. Finally the importance of combining the information coming from independent observations is stressed and a practical application to the Graviton Compton wavelength is shown.

Chapter 4. In this chapter I investigate the effects of environment on AGN activity. The first part of the chapter is devoted to the investigation of the influence of the environment over the supermassive black hole mass function (SMBHMF) for quiescent and optically active BHs. I show that the SMBHMF depends on the environment. The second part of the Chapter is devoted to the study of the environmental dependence of AGN activity. In high density environments the fraction of radio-loud galaxies is substantially higher than the average. Starting from the BH masses estimates and 1.4GHz radio fluxes and using the Black Hole Fundamental Plane relation, I reproduce the observed hard and soft X-ray Luminosity Function. Finally, the results are summerized and discussed.

Chapter 5. In this chapter I use a large set of hydrodynamical simulation performed with the GADGET2 SPH code to address the importance of idealized two-body mergers in the context of clusters of galaxies physics. In particular, I compare the evolutions and final configurations of

mergers between clusters with and without an initial flat entropy core. Those are representative of the “cool core” (CC) and “non-cool core” (NCC) classes of observed clusters. The study is focused on the metals content of the ICM. In agreement with previous studies, I find that mergers between CC systems cannot produce the flat metals profiles observed in clusters. However, mergers between NCCs do reproduce observations because the high initial core entropy renders the ICM susceptible to bouyancy which, in turn, drives the mass mixing that erases the initial metal profiles.

Chapter 6. In this last chapter I discuss the future developments that each of the projects I presented in the previous chapters could undergo. I will stress especially the relevance of each of them in the general context of future astrophysical research.

Bibliography

Adelman-McCarthy, J. K., et al. 2008, ApJs, 175, 297

Acernese F., et al., 2004, CQGra, 21, 385

Agertz O., et al., 2007, MNRAS, 380, 963

Alpher, R. A., Bethe, H., & Gamow, G. 1948, Physical Review , 73, 803

Anderson W. G., Brady P. R., Creighton J. D., Flanagan É. É., 2001, PhRvD, 63, 042003

Antonucci R., 1993, ARA&A, 31, 473

Apostolatos T. A., Thorne K. S., 1992, PhRvD, 46, 2435

Barish B. C., Weiss R., 1999, PhT, 52, 44

Barnes J., Hut P., 1986, Natur, 324, 446

Becker R. H., White R. L., Helfand D. J., 1995, ApJ, 450, 559

Begelman M. C., Blandford R. D., Rees M. J., 1984, RvMP, 56, 255

Begeman K. G., Broeils A. H., Sanders R. H., 1991, MNRAS, 249, 523

Bender P. L., 1998, AAS, 30, 1326

Berger M. J., Colella P., 1989, JCoPh, 82, 64

Binggeli B., Sandage A., Tammann G. A., 1988, ARA&A, 26, 509

Binney J., Tabor G., 1995, MNRAS, 276, 663

Bîrzan L., Rafferty D. A., McNamara B. R., Wise M. W., Nulsen P. E. J., 2004, ApJ, 607, 800

Blanchet L., 2009, arXiv, arXiv:0907.3596

Blanchet L., 2006, LRR, 9, 4

Boylan-Kolchin M., Springel V., White S. D. M., Jenkins A., Lemson G., 2009, MNRAS, 398, 1150

Brand K., Rawlings S., Hill G. J., Tufts J. R., 2005, MNRAS, 357, 1231

Brighenti F., Mathews W. G., 2003, ApJ, 587, 580

Brüggen M., Kaiser C. R., 2002, Natur, 418, 301

Bryan, G.L. & Norman, M.L., 1998, ApJ, 495, 80

Byram, E. T., Chubb, T. A., & Friedman, H. 1966, AJ, 71, 379

Cattaneo A., Teyssier R., 2007, MNRAS, 376, 1547

Cavaliere, A. G., Gursky, H., & Tucker, W. H. 1971, Nature, 231, 437

Chandran B. D. G., 2004, ApJ, 616, 169

Chandran B. D. G., Rasera Y., 2007, ApJ, 671, 1413

Choloniewski, J. 1987, MNRAS, 226, 273

Choudhury T. R., Padmanabhan T., 2005, A&A, 429, 807

Churazov E., Sunyaev R., Forman W., Böhringer H., 2002, MNRAS, 332, 729

Condon J. J., Cotton W. D., Greisen E. W., Yin Q. F., Perley R. A., Taylor G. B., Broderick J. J., 1998, AJ, 115, 1693

Crill B. P., et al., 2003, ApJS, 148, 527

Croton, D.J., Springel, V., White, S.D.M., De Lucia, G., Frenk, C.S., Gao, L., Jenkins, A., Kauffmann, G., Navarro, J.F., Yoshida, N., 2006, MNRAS, 365, 11

C. Cutler and E. E. Flanagan, Phys. Rev. D **49**, 2658 (1994)

Cutler C., Thorne K. S., 2002, gr.qc, arXiv:gr-qc/0204090

Cutri, R. M., et al. 2003, The IRSA 2MASS All-Sky Point Source Catalog, NASA/IPAC Infrared Science Archive. http://irsa.ipac.caltech.edu/applications/Gator/,

Deng X.-F., He J.-Z., Jun S., Luo C.-H., Wu P., 2008, Ap, 51, 471

Domainko W., Gitti M., Schindler S., Kapferer W., 2004, A&A, 425, L21

Donahue M., Voit G. M., 2004, cgpc.symp, 143

Dunn R. J. H., Fabian A. C., Taylor G. B., 2005, MNRAS, 364, 1343

Efstathiou, G., Ellis, R. S., & Peterson, B. A. 1988, MNRAS, 232, 431

Efstathiou G., Frenk C. S., White S. D. M., Davis M., 1988, MNRAS, 235, 715

Eke, V.R., Baugh, C.M., Cole, S., Frenk, C.S., Norberg, P. et al., 2004, MNRAS, 348, 866

Eilek J. A., Owen F. N., 2007, hvcg.conf, 133

Evrard A. E., 1990, ApJ, 363, 349

Evrard, A.E., MacFarland, T.J., Couchman, H.M.P., Colberg, J.M., Yoshida, N., White, S.D.M., Jenkins, A., Frenk, C.S., Pearce, F.R., Peacock, J.A., Thomas, P.A., 2002, ApJ, 573, 7

Faber S. M., Gallagher J. S., 1979, ARA&A, 17, 135

Fabian A. C., 1994, ARA&A, 32, 277

Fabian A. C., Voigt L. M., Morris R. G., 2002, MNRAS, 335, L71

Fabricant D. G., Kent S. M., Kurtz M. J., 1989, ApJ, 336, 77

Falcke H., Biermann P. L., 1995, A&A, 293, 665

Falcke, H., Körding, E., & Markoff, S. 2004, A & A, 414, 895

Fanaroff B. L., Riley J. M., 1974, MNRAS, 167, 31P

Feroz F., Gair J. R., Graff P., Hobson M. P, Lasenby A., 2009, arXiv, arXiv:0911.0288

Feroz F., Gair J. R., Hobson M. P., Porter E. K., 2009, CQGra, 26, 215003

Feroz F., Hobson M. P., 2008, MNRAS, 384, 449

F. Feroz, M. P. Hobson and M. Bridges, arXiv:0809.3437 [astro-ph].

Feroz F., Hobson M. P., Bridges M., 2009, MNRAS, 398, 1601

Ferrarese L., Merritt D., 2000, ApJ, 539, L9

Forman W., Jones C., 1982, ARA&A, 20, 547

Franceschini A., Vercellone S., Fabian A. C., 1998, MNRAS, 297, 817

Frenk C. S., White S. D. M., Efstathiou G., Davis M., 1985, Nature, 317, 595

Frenk C. S., White S. D. M., Davis M., Efstathiou G., 1988, ApJ, 327, 507

Fritz, G., Davidsen, A., Meekins, J. F., & Friedman, H. 1971, ApJL, 164, L81

A. Gelman, J B. Carlin, H. Stern, and D. B. Rubin, *Bayesian data analysis*, (Chapman & Hall, 1997).

A. Gelman and X.-L. Meng, Statistical Science **13**, 163 (1998)

C. J. Geyer and E. A. Thompson, Journal of the American Statistical Association **90**, 909 (1995)

W. R. Gilks, S. Richardson, and D. J. Spiegelhalter, *Markov chain Monte Carlo in practice*, (Chapman & Hall / CRC, Boca Raton, 1996).

Gómez P. L., Loken C., Roettiger K., Burns J. O., 2002, ApJ, 569, 122

P. J. Green, Biometrika **82**, 711 (1995)

P. J. Green and A. Mira, Biometrika **88**, 1035 (2001)

Gursky, H., Kellogg, E., Murray, S., Leong, C., Tananbaum, H., & Giacconi, R. 1971, ApJL, 167, L81

Guth A. H., 1981, PhRvD, 23, 347

Heinz S., Sunyaev R. A., 2003, MNRAS, 343, L59

Heinz S., Churazov E., 2005, ApJ, 634, L141

Helsdon, S.F. & Ponman, T.J., 2003, MNRAS, 340, 485

Henry J. P., Briel U. G., 1993, AdSpR, 13, 191

Hill G. J., Lilly S. J., 1991, ApJ, 367, 1

Ho L. C., 2002, ApJ, 564, 120

Hoeft M., Brüggen M., 2004, ApJ, 617, 896

Hogg D. W., 1999, astro, arXiv:astro-ph/9905116

Hoyle, F. 1954, The Observatory, 74, 253

Hubble, E., 1929, Proceedings of the National Academy of Sciences of the United States of America, Volume 15, Issue 3, pp. 168-173

Kauffmann, G., White, S.D.M., Guiderdoni, B., 1993, MNRAS, 264, 201

Kleinmann S. G., et al., 1994, Ap&SS, 217, 11

Iocco, F., Mangano, G., Miele, G., Pisanti, O., & Serpico, P. D. 2009, Phys. Rep., 472, 1

Jackson J. D., 1975, ”Classical Electrodynamics”, 2nd edn, Wiley (1975)

Jeans, J. H. 1902, Royal Society of London Philosophical Transactions Series A, 199, 1

Jenkins A., Frenk C. S., White S. D. M., Colberg J. M., Cole S., Evrard A. E., Couchman H. M. P., Yoshida N., 2001, MNRAS, 321, 372

Lacey C., Cole S., 1993, MNRAS, 262, 627

Leccardi A., Rossetti M., Molendi S., 2010, A&A, 510, A82

Lemaître, G. 1931, Nature, 127, 706

Lemson G., Virgo Consortium t., 2006, astro, arXiv:astro-ph/0608019

Liu B. F., Meyer F., Meyer-Hofmeister E., 2006, A&A, 454, L9

Lynden-Bell, D., 1967, MNRAS, 136, 101

Lynden-Bell D., 1971, MNRAS, 155, 95

Magliocchetti M., et al., 2004, MNRAS, 350, 1485

Marconi A., Hunt L. K., 2003, ApJ, 589, L21

E. Marinari and G. Parisi, Europhysics Letters **19**, 451 (1992).

Markoff, S., Nowak, M., Corbel, S., Fender, R., & Falcke, H. 2003, New Astronomy Review, 47, 491

Mather J. C., et al., 1994, ApJ, 420, 439

McCarthy I. G., Balogh M. L., Babul A., Poole G. B., Horner D. J., 2004, ApJ, 613, 811

McLure R. J., Dunlop J. S., 2001, MNRAS, 327, 199

McNamara B. R., Nulsen P. E. J., 2007, ARA&A, 45, 117

Meekins, J. F., Fritz, G., Chubb, T. A., & Friedman, H. 1971, Nature, 231, 107

Mercha'n, M.E. & Zandivarez, A., 2005, ApJ, 630, 759

Merloni, A., Heinz, S., & di Matteo, T. 2003, MNRAS, 345, 1057

Meyer-Hofmeister E., Liu B. F., Meyer F., 2009, A&A, 508, 329

Mitchell N. L., McCarthy I. G., Bower R. G., Theuns T., Crain R. A., 2009, MNRAS, 395, 180

Milgrom M., 1983, ApJ, 270, 365

Milgrom M., 2008, arXiv, arXiv:0801.3133

A. Mira, Metron, **LIX** (3-4) 231 (2001)

Misner C. W., Thorne K. S., Wheeler J. A., 1973, ”Gravitation”, W. H. Freeman publisher (1973)

Mo H. J., Mao S., White S. D. M., 1998, MNRAS, 295, 319

Monaghan J. J., 1992, ARA&A, 30, 543

Mulchaey, J.S., 2000, ARA&A, 38, 289

Mulchaey, J.S., Davis, D.S., Mushotzky, R.F. and Burstein, D., 1993, ApJ, 404, L9

Narayan R., Yi I., 1994, ApJ, 428, L13

Narayan R., Yi I., 1995, ApJ, 444, 231

Narayan R., Kato S., Honma F., 1997, ApJ, 476, 49

Navarro, J.F., Frenk, C.S., White, S.D.M., 1996, ApJ, 462, 563

Navarro, J.F., Frenk, C.S., White, S.D.M., 1997, ApJ, 490, 493

Nusser A., Silk J., Babul A., 2006, MNRAS, 373, 739

Ott C. D, 2009, CQGra, 26, 063001

Peebles, P.J.E., *The large-scale structure of the universe*, 1980, Princeton, NJ: Princeton University Press., USA

Peebles P. J. E., 1982, ApJ, 263, L1

Peebles P. J. E., 1993, Principles of physical cosmology, Princeton Series in Physics, NJ, Princeton University Press

Penzias, A.A. & Wilson, R.W., 1965, ApJ, 142, 419

Peacock J. A., Nicholson D., 1991, MNRAS, 253, 307

Peres C. B., Fabian A. C., Edge A. C., Allen S. W., Johnstone R. M., White D. A., 1998, MNRAS, 298, 416

Peterson R. C., 1985, ApJ, 297, 309

Peterson J. R., Kahn S. M., Paerels F. B. S., Kaastra J. S., Tamura T., Bleeker J. A. M., Ferrigno C., Jernigan J. G., 2003, ApJ, 590, 207

Peterson J. R., Fabian A. C., 2006, PhR, 427, 1

Pizzolato F., Soker N., 2005, ApJ, 632, 821

Poole G. B., Babul A., McCarthy I. G., Sanderson A. J. R., Fardal M. A., 2008, MNRAS, 391, 1163

Pope E. C. D., Pavlovski G., Kaiser C. R., Fangohr H., 2006, MNRAS, 367, 1121

Press, W.H. & Schechter, P., 1974, ApJ, 187, 425

Pretorius F., 2007, arXiv, arXiv:0710.1338

Pringle J. E., Rees M. J., 1972, A&A, 21, 1

Rawlings S., Saunders R., 1991, Natur, 349, 138

Rees M. J., Begelman M. C., Blandford R. D., Phinney E. S., 1982, Natur, 295, 17

Richard J., et al., 2010, MNRAS, 404, 325

Ricker P. M., Sarazin C. L., 2001, ApJ, 561, 621

C. Röver, R. Meyer, and N. Christensen, Class. Quant. Grav. **23**, 4895 (2006).

C. Röver, R. Meyer, and N. Christensen, Phys. Rev. D **75**, 062004 (2007)

Sachs R. K., Wolfe A. M., 1967, ApJ, 147, 73

Sanderson A. J. R., O'Sullivan E., Ponman T. J., 2009, MNRAS, 395, 764

Schade, D. 1991, MNRAS, 251, 310

Schmidt M., 1968, ApJ, 151, 393

Schmidt, M., Schneider, D. P., & Gunn, J. E. 1986, ApJ, 306, 411

Schweizer F., 1986, Sci, 231, 227

Shabala S. S., Alexander P., 2009, MNRAS, 392, 1413

Shakura N. I., Sunyaev R. A., 1976, MNRAS, 175, 613

Silk, J. 1968, ApJ, 151, 459

D. S. Sivia with J. Skilling, *Data Analysis: A Bayesian Tutorial* (Second edition, Oxford University Press 2006)

J. Skilling, in *AIP Conference Proceedings: 24th International Workshop on Bayesian Inference and Maximum Entropy Methods in Science and Engineering*, Volume 735 pp. 395-405 (2004).

Smith S., 1936, ApJ, 83, 23

Spergel D. N., et al., 2007, ApJS, 170, 377

Springel V., 2005, MNRAS, 364, 1105

Springel V., Hernquist L., 2002, MNRAS, 333, 649

L. Tierney and A. Mira, Statistics in Medicine **18**, 2507 (1999)

Tormen G., 1997, MNRAS, 290, 411

M. Trias, A. Vecchio and J. Veitch, arXiv:0904.2207.

M. V. van der Sluys, C. Roever, A. Stroeer, N. Christensen, V. Kalogera, R. Meyer and A. Vecchio, arXiv:0710.1897 [astro-ph].

M. van der Sluys et al Class. Quant. Grav. **25**, 184011 (2008).

Veitch J., Vecchio A., 2008, CQGra, 25, 184010

Veitch J., Vecchio A., 2008, PhRvD, 78, 022001

Veitch J., Vecchio A., 2010, PhRvD, 81, 062003

Voigt L. M., Schmidt R. W., Fabian A. C., Allen S. W., Johnstone R. M., 2002, MNRAS, 335, L7

White S. D. M., Rees M. J., 1978, MNRAS, 183, 341

Will C. M., 1998, PhRvD, 57, 2061

B. Willke, et al. Class. Quant. Grav. **21**, 417 (2004)

Woo, J.-H., Urry, C. M., van der Marel, R. P., Lira, P., & Maza, J. 2005, ApJ, 631, 762

York D. G., et al., 2000, AJ, 120, 1579

Zwicky F., 1937, ApJ, 86, 217

3. Tests of General Relativity Using Bayesian Model Selection

Abstract

The second generation of interferometric gravitational wave detectors, including Advanced LIGO and Advanced Virgo, is expected to begin operation by 2015. One of the science drivers for the development of such instruments is to test General Relativity in the strong field regime and investigate departures from its predictions. Previous studies have focused on the calculation of the Fisher Information Matrix to assess the level of sensitivity required by the instruments to be able to detect parameters that describe deviations from General Relativity. However, it is important to build on this effort and develop a rigorous and systematic framework which is able to use gravitational-wave observations to discriminate between competing theories of gravity. Here we illustrate a method based on Bayesian inference and model selection that allows an objective comparison between different theories given a set of data. We apply our statistical scheme on the very simple alternative theory in which the gravitational force carrier has a non-zero mass. We concentrate our study on the calculation of the so-called *Bayes factor* between the two theories as a way to compare observations to the different predictions of the gravitational waveform and choose between them. We give examples of the bias that would be introduced in parameter estimates by assuming an incorrect theory and show how calculating the Bayes factor

for different models can help alleviate this problem. Finally, we develop a method to extract additional information from multiple independent observations of gravitational waves sources in a natural way. This work serves both as a testbed for our method and as a proof of principle of the way we propose that tests of General Relativity should be performed.

3.1 Introduction

General relativity (GR) has so far passed every experimental test with flying colours. Yet, a whole range of efforts is under way to put Einstein's theory under even more intense experimental scrutiny in the coming years (Will 2006). Amongst these, highly sensitive gravitational wave experiments are opening new means for probing gravity in the dynamical, strong-field regime (Sathyaprakash & Schutz 2009). Ground-based gravitational-wave laser interferometers, LIGO (Barish & Weiss 1999; Abbott et al. 2009) and Virgo (Acernese et al. 2004) have now reached a sensitivity that could plausibly lead to the first direct detection of gravitational waves. The upgrade of these instruments to the second generation (also known as advanced configuration) is already under way; Advanced LIGO [1] and Advanced Virgo [2] are expected to start science observations by 2015, and to provide a wealth of detections from a variety of sources (Cutler & Thorne 2002; Kokkotas 2008; Abadie et al. 2010). As soon as a positive detection is achieved, one can surely expect that gravitational-wave data will be used to test the predictions of General relativity, (see Will 2006; Sathyaprakash & Schutz 2009 for recent reviews). In the longer term future, very-high sensitivity laser interferometers, both space-based – such as the Laser Interferometer Space Antenna (LISA) (Bender et al. 2006) and Decigo (Kawamura et al. 2006) – and ground-based third-generation instruments, such as the Einstein gravitational-wave Telescope (ET) (Freise et al. 2009; Hild, Chelkowski,& Freise 2008; Punturo et al. 2010), will increase our ability to test alternative theories of gravity.

Tests of GR through the precise monitoring of the amplitude and phase evolution of gravitational waves have already been discussed in several studies (Will 1994; Ryan 1997; Will 1998; Will 2003; Will & Yunes 2004; Berti, Buonanno, & Will 2005; Glampedakis & Babak 2006; Kesden, Gair, & Kamionkowski 2005; Hughes 2006; Arun et al. 2006; Berti, Cardoso, & Will 2006; Barack & Cutler 2007; Alexander, Finn, & Yunes 2008; Gair, Li, & Mandel 2008; Yunes

[1] http://www.ligo.caltech.edu/advLIGO/
[2] http://wwwcascina.virgo.infn.it/advirgo/

& Finn 2009; Arun & Will 2009; Stavridis & Will 2009; Yunes & Sopuerta 2009; Yunes & Pretorius 2009; Apostolatos, Lukes-Gerakopoulos, & Contopoulos 2009; Schutz 2009; Keppel & Ajith 2010). Of particular interest are observations of the coalescence of binary systems, as they allow us to probe the dynamic, highly relativistic, strong-field regime, where radiation can theoretically be accurately modelled in GR, and alternative theories of gravity.

The key approach that all those studies have employed to investigate the ability to test GR is based on the computation of the expected accuracy of the measurements of the unknown parameters that characterise the radiation, including those introduced by alternative theories of gravity; moreover, the statistical errors are estimated using the inverse of the Fisher information matrix (Jaynes & Bretthorst 2003). These results are useful as approximate figures of merit for the constraints that can be expected to be derived from observations with future instruments. However, they suffer from several conceptual (and practical) limitations that we address in this chapter. The first is that at the conceptual level, those studies do not actually address whether observations will be able to discriminate an alternative theory of gravity from GR. They simply *assume* that the true theory of gravity is different from GR, and by computing the expected statistical errors on the unknown signal parameters (including those that encode deviations from GR) make some statements on whether or not the observations have sensitivity to the relevant parameter(s). This leaves aside the issue that the computation of the variance-covariance matrix simply provides a lower bound, the Cramer-Rao bound (Rao 1945; Cramer 1946), to the variance of the statistical errors, which is a meaningful bound on the accuracy of parameter estimation only in the limit of high signal-to-noise ratio (Nicholson & Vecchio 1998; Balasubramanian & Dhurandhar 1998; Vallisneri 2008; Zanolin, Vitale, & Makris 2009). Secondly, those studies ignore what would be the consequences of (small) deviations from GR, such that detections can still be achieved using GR waveforms when the actual theory of gravity differs from GR, but parameter estimation can be affected due to the use of the "wrong" waveform model; this issue has been recently raised in Yunes & Pretorius (2009) and termed "bias in

gravitational wave astronomy". Lastly, past studies do not take into account the fact that one can take advantage of the (hopefully) many detections to provide better constraints on alternative theories of gravity by combining the observations. In fact, although each astrophysical source will be characterised by different astrophysical parameters (such as masses and spins), if there is a deviation from GR described by some "global" fundamental parameters of the new theory that are the same for every system (*e.g.* the graviton has a mass different from zero, corresponding to a specific value), then one can *combine* all the observations and obtain better constraints. Finally, there has been no actual attempt to provide a method to address these issues in an analysis that can be implemented in practice.

In this chapter we tackle these specific issues by introducing a conceptual and practical approach within the framework of Bayesian inference to discriminate between different theories of gravity by performing model selection, and to estimate the unknown model parameters. The approach based on Bayesian inference is particularly simple and powerful as it provides both a statement on the relative probabilities of models (a given alternative theory of gravity versus General Relativity) and on the distribution of the unknown parameters that characterise the theory, the (marginalised) posterior probability density functions (PDFs). The conceptual simplicity of Bayes' theorem is balanced by the computationally expensive N-dimensional integral (where N, usually ≥ 10, is the total number of the unknown parameters) on which this theorem relies for the calculation of the evidence and the marginalised PDFs. Several integration techniques, such as (Reversible Jump) Markov-chain Monte Carlo methods (Gilks, Richardson, & Spiegelhalter 1996; Green 1995), thermodynamic integration (Gelman & Meng 1998) and Nested Sampling (Skilling 2004) have been explored in a range of fields to tackle this computational challenge. For our analysis we use a *nested sampling* algorithm that some of us have developed for applications of in the context of observations of coalescing binaries with ground-based instruments (Veitch & Vecchio 2010), and that has been shown to allow such N-dimensional integrals to be computed in an efficient and relatively computationally inexpensive

way (Veitch & Vecchio 2010; Veitch & Vecchio 2008a; Veitch & Vecchio 2008b; Aylott et al. 2009; Aylott, Veitch, & Vecchio 2009).

For the purpose of illustration of our method, in this chapter we focus specifically on the case of a "massive graviton" theory –*i.e.* a theory of gravity in which the boson mediating the gravitational interaction is characterised by a rest-mass m_g different from zero, and the corresponding Compton wavelength of the graviton λ_g is finite (the GR case corresponds to $m_g = 0$ and $\lambda_g \to \infty$) – and consider how one would go about testing in a statistically rigorous way GR against this alternative theory, by providing both a conceptual and practical (in the sense that is readily applicable to gravitational wave observations) approach to this problem. The reason for choosing a massive graviton theory for our proof-of-concept analysis is two-fold: (i) the gravitational radiation emitted by coalescing compact binaries in a massive graviton theory takes a particularly simple form characterised by only one additional unknown parameter – the Compton wavelength of the graviton λ_g – and therefore provides an ideal proof-of-concept case to study, and (ii) several studies have already explored the feasibility of placing new limits on the graviton mass using gravitational wave observations, and it is therefore useful to compare those expectations with actual results from a rigorous statistical analysis performed on mock data sets. Clearly the analysis that we show here can be applied to any other theory of gravity.

The chapter is organised as follows. In Section 3.2 we discuss the statistical method that we employ. In Section 3.3 we present the models we use as a test case for our study, and introduce the gravitational waveform generated by in-spiralling compact binaries in General Relativity, and in a "massive graviton" theory. Sections 3.4 and 3.5 contain the main results of the chapter: in Section 3.4 we show the results of our analysis for the observation of a single gravitational wave signal; in Section 3.5 we derive a method of combining multiple observations which are expected from advanced interferometers to further restrict the bounds on λ_g. Finally in Section 3.6 we summarise our work.

3.2 Method

Let us consider a set of theories of gravity $\{\mathcal{H}_j\}$, including General Relativity that we want to test using observations of gravitational waves emitted during the coalescence of binary systems of compact objects, either black holes or neutron stars. Each theory makes a prediction on the gravitational waveform $h(t;\vec{\theta})$, that depends on the specific theory $\mathcal{H}_j$ and a set of unknown parameters $\vec{\theta}$. The statements on the theories are based on a data set d (observations) and all the relevant prior information I that we hold.

Within the framework of Bayesian inference, the key quantity that one needs to compute is the posterior probability of a given theory (a "model" or hypothesis) $\mathcal{H}_j$. Applying Bayes' theorem we obtain

$$P(\mathcal{H}_j|d,I) = \frac{P(\mathcal{H}_j|I)\,P(d|\mathcal{H}_j,I)}{P(d|I)}\,, \tag{3.1}$$

where $P(\mathcal{H}_j|d,I)$ is the *posterior probability* of the model $\mathcal{H}_j$ given the data, $P(\mathcal{H}_j|I)$ is the *prior probability* of hypothesis $\mathcal{H}_j$ and $P(d|\mathcal{H}_j,I)$ is the *marginal likelihood* or *evidence* for $\mathcal{H}_j$ that can be written as:

$$\begin{aligned} P(d|\mathcal{H}_j,I) &= \mathcal{L}(\mathcal{H}_j) \\ &= \int d\vec{\theta}\, p(\vec{\theta}|\mathcal{H}_j,I)\, p(d|\vec{\theta},\mathcal{H}_j,I) \end{aligned} \tag{3.2}$$

In the previous expression $p(\vec{\theta}|\mathcal{H}_j,I)$ is the prior probability density of the unknown parameter vector $\vec{\theta}$ within the theory $\mathcal{H}_j$ and $p(d|\vec{\theta},\mathcal{H}_j,I)$ is the likelihood function of the observation d, assuming a given value of the parameters $\vec{\theta}$ and the theory $\mathcal{H}_j$.

If we want to compare different models – for this chapter, we concentrate on General Relativity versus an alternative theory of gravity – in light of the observations made, we can compute

the relative posterior probabilities, which is known as the *odds ratio*

$$\begin{aligned} O_{i,j} &= \frac{P(\mathcal{H}_i|d)}{P(\mathcal{H}_j|d)} \\ &= \frac{P(\mathcal{H}_j)}{P(\mathcal{H}_i)} \frac{P(d|\mathcal{H}_i)}{P(d|\mathcal{H}_j)} \\ &= \frac{P(\mathcal{H}_j)}{P(\mathcal{H}_i)} B_{i,j} \,, \end{aligned} \tag{3.3}$$

where $P(\mathcal{H}_j)/P(\mathcal{H}_i)$ is the *prior odds* of the two hypotheses, the confidence we assign to the models before any observation, and $B_{i,j}$ is the *Bayes factor*. Here, we are interested in what the data can tell us about the relative probabilities of two models, and so we will not involve the prior odds any further.

In addition to computing the relative probabilities of different theories, one usually wants to make inference on the unknown parameters, and therefore one needs to compute the joint posterior probability density function

$$p(\vec{\theta}|d, \mathcal{H}_j, I) = \frac{p(\vec{\theta}|\mathcal{H}_j, I) p(d|\vec{\theta}, \mathcal{H}_j, I)}{p(d|\mathcal{H}_j, I)} \,. \tag{3.4}$$

From the previous expression it is simple to compute the marginalised PDF on any given parameter, say θ_1 within a given theory of gravity $\mathcal{H}_j$

$$p(\theta_1|d, \mathcal{H}_j, I) = \int d\theta_2 \ldots \int d\theta_N p(\vec{\theta}|d, \mathcal{H}_j, I) \,. \tag{3.5}$$

The key quantities for Bayesian inference in Eq. (3.3), (3.4) and (3.5) can be efficiently computed using *e.g.* a nested sampling algorithm (Skilling 2004). In this chapter we used a specific implementation of this technique that we have developed for ground-based observations of coalescing binaries; we refer the reader to Veitch & Vecchio (2010) for details.

3.3 Models

In this Section we review the gravitational waveform approximations that we consider in this study and we spell out the model or hypotheses that consider in this analysis. We apply the method to the in-spiral phase of the coalescence of compact binary systems. We also make the additional simplifying assumption (that has however no consequence on any of the conceptual points) that there are no spins.

3.3.1 Gravitational waveforms

In General relativity, gravitational waves from the in-spiral of compact binary systems are accurately modeled via the post-Newtonian, (e.g. Blanchet 2006 for a review). Here we use the standard restricted post-Newtonian approximation, computing directly the waveform in the frequency domain by taking advantage of the stationary phase approximation. The amplitude of the radiation contains therefore only the leading order Newtonian contribution and higher order post-Newtonian terms are retained only in the phase. We further consider the expansion to post^2-Newtonian order and we assume that the compact objects have no spins. In summary, the frequency domain GW signal is given by

$$h(f) = \mathcal{A} f^{-7/6} e^{i\Psi(f)} \,, \tag{3.6}$$

where

$$\mathcal{A} = \frac{1}{\sqrt{30}\pi^{2/3}} \frac{\mathcal{M}^{5/6}}{D_L} \,, \tag{3.7}$$

is the amplitude of the signal and the phase $\Psi(f)$ at the relevant order is given by (Blanchet et al. 1995):

$$\begin{aligned}\Psi(f) &= 2\pi f t_c - \Phi_c + \frac{3}{128}(\pi M f)^{-5/3}\eta^{-1}\Big[1 - \\ &+ \left(\frac{3715}{756} + \frac{55}{9}\eta\right)(\pi M f)^{2/3} - 16\pi(\pi M f) + \\ &+ \left(\frac{15293365}{508032} + \frac{27145}{504}\eta + \frac{3085}{72}\eta^2\right)(\pi M f)^{4/3}\Big]\,. \end{aligned} \tag{3.8}$$

In the previous expressions f is the frequency of the GW dominant mode and D_L is the luminosity distance to the source. For a binary of component masses m_1 and m_2, we have also introduced the usual parametrization:

$$M = m_1 + m_2 \tag{3.9}$$

$$\eta = \frac{m_1 m_2}{M^2} \tag{3.10}$$

$$\mathcal{M} = \eta^{3/5} M\,; \tag{3.11}$$

They represent the total mass, the symmetric mass ratio and the "chirp" mass, respectively.

In a theory of gravity in which the graviton rest-mass is different from zero, the amplitude, phase and polarisation of the radiation would be affected. All these features could be exploited to test GR. One of the most notable effects, as derived by Will (1998), is that a massive graviton affects the dispersion relation of gravitational radiation, so that the propagation velocity $v_g \neq c$ of the waves depends on the frequency f as $(v_g/c)^2 = 1 - (c/f\lambda_g)^2$. In turn, this leads to an imprint on the phase of the radiation. In this chapter we therefore take the simplifying assumption in which the waveform is affected only in the phase (while the amplitude remains the same) and we model the radiation as we have done for the GR case as:

$$h_{\rm MG}(f) = \mathcal{A} f^{-7/6} e^{i\Psi_{\rm MG}(f)}\,, \tag{3.12}$$

where the amplitude is the same as for the GR case, Eq. (3.7), and the gravitational-wave phase becomes (e.g. Berti, Buonanno, & Will (2005))

$$\begin{aligned}\Psi(f) &= 2\pi f t_c - \Phi_c + \frac{3}{128}(\pi M f)^{-5/3}\eta^{-1}\Big[1 - \frac{128}{3}\frac{\pi^2 DM}{\lambda_g^2(1+z)}(\pi M f)^{2/3}\eta + \\ &+ \left(\frac{3715}{756} + \frac{55}{9}\eta\right)(\pi M f)^{2/3} - 16\pi(\pi M f) + \\ &+ \left(\frac{15293365}{508032} + \frac{27145}{504}\eta + \frac{3085}{72}\eta^2\right)(\pi M f)^{4/3}\Big]\,. \end{aligned} \tag{3.13}$$

The distance D that appears in the massive-graviton phase term (3.13) is given by (Will 1998):

$$D \equiv \frac{1+z}{H_0}\int_0^z \frac{dz'}{(1+z')\sqrt{\Omega_M(1+z'^3)+\Omega_\Lambda}}\,, \tag{3.14}$$

and in general differs from the luminosity distance D_L that enters into the GW amplitude, Eq. (3.7). The previous expression is correct under the assumption that the universe is flat, and H_0, Ω_M and Ω_Λ are the Hubble parameter, matter and cosmological constant parameter, today. In this chapter we concentrate on observations with ground-based laser interferometers, and in particular Advanced LIGO (although some limited results are also presented for third-generation instruments). As a consequence, we restrict in general to sources within 100 Mpc, $z < 0.025$. Therefore D differs from D_L by less than 5% and we will set the two numbers to be the same.

None of these assumptions have an impact on the conceptual approach that we propose in this chapter. However, some of the results on the specific cases considered here – an alternative theory characterised a massive graviton – are affected by the approximation. During the actual analysis of the data one would use the most accurate expression of the waveform available.

3.3.2 Models

We apply the method described in the previous section to the case of gravitational waves from the in-spiral of compact binary systems. Such systems are described by the well-known parameterised post-Newtonian formalism in the case of General Relativity, in which a Taylor expansion is performed on the amplitude and phase functions in terms of the orbital velocity, (see Blanchet 2006 for a review). In this chapter, we are interested in comparing standard GR with an alternative theory where the gravitational interaction is carried by a massive boson, with an unknown rest mass m_g or equivalently Compton wavelength $\lambda_g = h/m_g c$. The models we will consider are codified with the following notation,

- $\mathcal{H}_{GR}$: The data consists of (zero mean) Gaussian and stationary noise of known spectral density plus an inspiral signal of the form described by Eqs. (3.12)-(3.8) with $\lambda_g^{-1} = 0$.
- $\mathcal{H}_{MG}$: The data consists of (zero mean) Gaussian and stationary noise of known spectral density plus an inspiral signal of the form described by Eqs. (3.12)-(3.13), with λ_g as an additional unknown free parameter.

For both models $\mathcal{H}_i$ we compute the Bayes factors between the pure noise versus the noise plus a signal hypotheses. Those bayes factors will be indicated with $B_{\mathcal{H}_{\rm i},\rm noise}$. The Bayes factor between the MG and the GR models $B_{\rm MG,GR}$ is calculated simply as

$$B_{\rm MG,GR} = \frac{B_{\rm MG,noise}}{B_{\rm GR,noise}} \tag{3.15}$$

The gravitational wave described by Eqs. (3.12-3.8), was injected into simulated Gaussian stationary noise with a power spectral density equal to the Advanced LIGO design sensitivity.

Table 3.1: Number of inspiral cycles for different PN orders for 3 sample mass ratios used in our simulations. The f_{in} has been chosen to be 20 Hz for AdvancedLIGO instrument and 1 Hz for ET. f_{fin} has been chosen to be f_{ISCO}. λ_g is measured in meters. All the sources are at a distance of 20 Mpc for Advanced LIGO and 1 Gpc for ET.

PN order	$1.3M_\odot + 1.45M_\odot$		$5.5M_\odot + 6.0M_\odot$		$11M_\odot + 12M_\odot$	
	AdLIGO	ET	AdLIGO	ET	AdLIGO	ET
Newtonian	5181	763948	477	70805	148	22300
1PN	223	4505	51	1079	24	538
Tail	-33	-254	-12	-97	-7	-60
2PN	6	20	3	12	2	9
Massive Graviton	$-9(\frac{10^{15}m}{\lambda_g})^2$	$-9196(\frac{10^{15}m}{\lambda_g})^2$	$-9(\frac{10^{15}m}{\lambda_g})^2$	$-9177(\frac{10^{15}m}{\lambda_g})^2$	$-8(\frac{10^{15}m}{\lambda_g})^2$	$-9153(\frac{10^{15}m}{\lambda_g})^2$

A useful quantity to assess the relative contribution to the phase of the GW is the number of cycles contributed from each term of the expression within the frequency band of the detector in use. The contributions within the sensitive bands of each detector is presented in Table 3.1.

3.4 Results

In this Section we present the results pertinent to the analysis of simulated gravitational wave observations using single observations. In Section 3.5 we shall then generalise the results to *combining* multiple observations to produce more constraining limits on the massive graviton. The results are focused on observations with instruments corresponding to the Advanced LIGO design sensitivity, and contain an example of operations with the future Einstein gravitational-wave Telescope (ET). We start in Section 3.4.2 by investigating the capability of Advanced LIGO to distinguish between the MG and GR models. Thus, we inject in Gaussian and stationary noise for a range of massive graviton wavelengths coalescing binary signals and analyse the data using both MG and the GR waveforms to calculate the value of $\log B_{\rm MG,GR}$. In Section 3.4.3 we then discuss the effect of assuming the wrong theory of gravity (GR in this case) when performing parameter estimation of the detected signal (in this case assuming that the "true" theory of gravity contains a massive graviton as described in Eq. (3.8)). However, the value of the graviton wavelength λ_g is already bound by solar system tests and galaxy motions in clusters of galaxies (Will 2006) and one may have a theoretical bias that $\lambda_g \to \infty$. Therefore, in Section 3.4.4 we consider the situation in which the correct (classical) theory of gravity is General Relativity and investigate how tight the bounds on λ_g will be from future gravitational wave instruments. More specifically, we inject GR and analyze the data using the MG model and from the PDF of λ_g calculate the 95% lower limit on λ_g itself. We present the results of this experiment for Advanced LIGO and in a preliminary format for the Einstein Telescope.

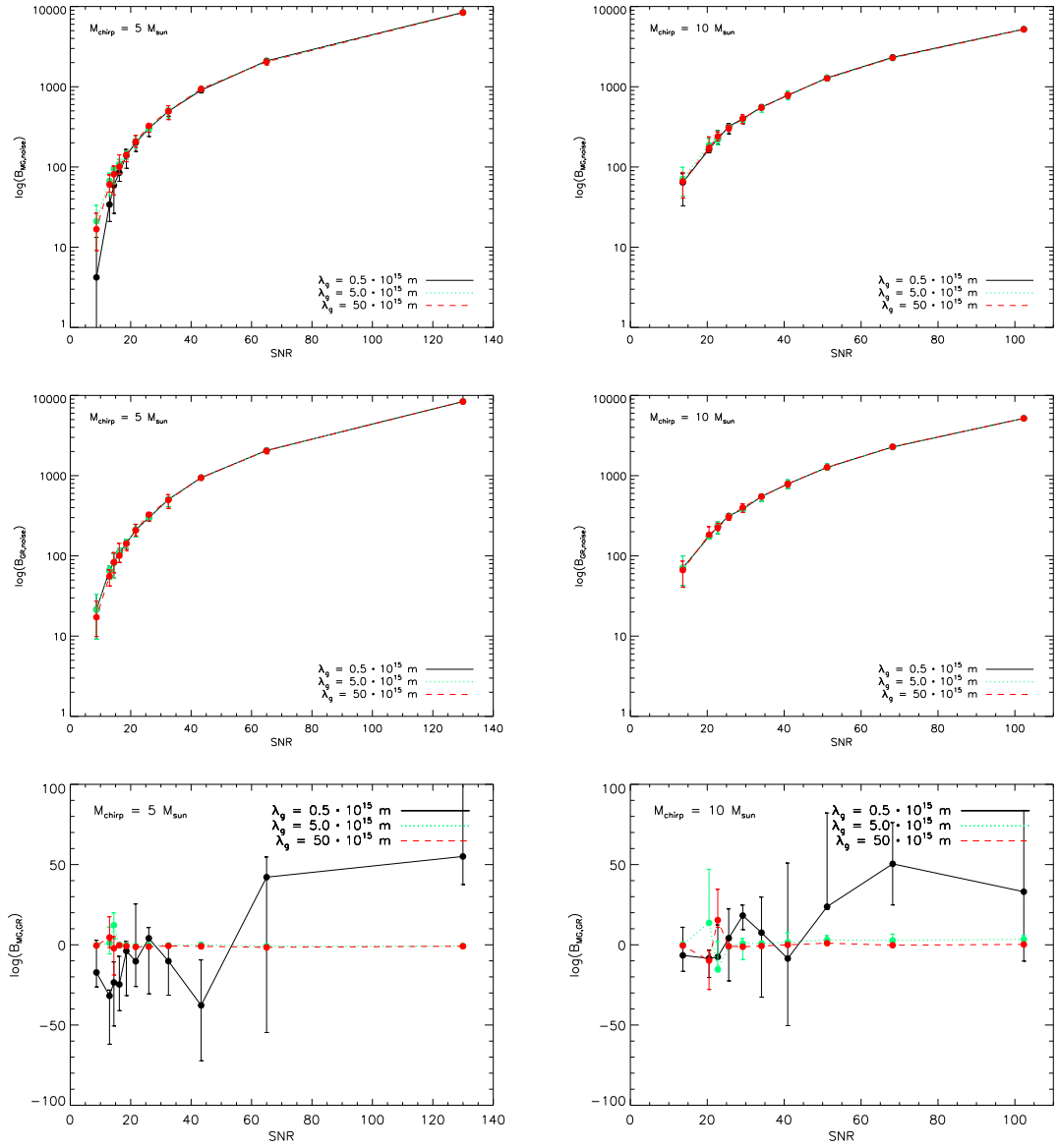

Figure 3.1: Logarithmic Bayes factors for the hypotheses MG vs noise only, GR vs noise only and MG vs GR, top, center and bottom panels respectively. The left column corresponds to $\mathcal{M} = 5M_\odot$ while the right one to $\mathcal{M} = 10M_\odot$. In each panel we show the result for a range of SNRs and for 3 values of λ_g: $\lambda_g = 0.5 \times 10^{15}$ m (solid line), $\lambda_g = 5 \times 10^{15}$ m (dotted line) and $\lambda_g = 50.0 \times 10^{15}$ m (dashed line). $\log B_{\rm MG,GR}$ favours the MG theory for high SNR and small value of λ_g. For $\lambda_g > 0.5 \times 10^{15}$ m the $\log$ Bayes factor tends to 1. Therefore there is no evidence in the data to favour the most complicated theory.

3.4.1 Details of the simulations

Our results are derived from a set of simulations on synthetic data sets. We generate Gaussian and stationary noise in the frequency domain with noise spectral density corresponding to the Advanced LIGO design sensitivity , as representative of the second-generation gravitational-wave instruments. Observations to set limits on the graviton mass require the use of at least three instruments at geographically separated locations to fully break the distance-source position determination. However, in order to reduce the computational costs of the simulations, we actually use a single instrument and assume the source sky location is known. As it is possible to recover the sky location when using a network of three or more interferometers, this constraint simulates the effect of using a network but with only one dataset to be analysed at a time.

We inject inspiral signals for a range of masses and values of the massive graviton into simulated noise. Unless otherwise stated, we use three values of the parameter $\lambda_g = 0.5,\ 5,\ 50\times 10^{15}$m [3] we generated a set of templates for two values of $\mathcal{M} = 5M_{\odot}, 10M_{\odot}$. In each template we assumed a near equal mass ratio, giving $\eta \approx 0.25$ and fixed the polarisation angle. In order to explore the results at different SNRs, for each mass we considered sources at different luminosity distances.

We performed a series of experiments in which we created mock Advanced LIGO datasets where we "injected" a gravitational wave described by the model in equations (3.12), with phase given by equation (3.8). For three values of the parameter $\lambda_g = 0.5,\ 5,\ 50 \times 10^{15}$m we generated a set of templates for two values of $\mathcal{M} = 5M_{\odot}, 10M_{\odot}$. In each template we assumed a near equal mass ratio, giving $\eta \approx 0.25$ and fixed the polarisation angle. In order to explore the results at different SNRs, for each mass we considered sources at different luminosity distances. We fixed the sky location in all different templates since the freedom in the angular parameters

[3] The purpose of this section is the investigation of our method's behaviour and its feasibility as an efficient way of performing tests of GR and so we have ignored the existing physical bound of the graviton Compton wavelength here. The magnitude of the non GR term in equation (3.8) is in fact $\propto \lambda_g^{-2}$, thus to have a significant contribution from this term we need to have small values of λ_g.

would introduce unnecessary complications for the purposes of this work. As it is possible to recover the sky location when using a network of three or more interferometers, this constraint simulates the effect of using a network but with only one dataset to be analysed at a time.

In the computation of the evidence integral, Eq. (3.2) we use a uniform prior on the chirp mass in the range $1 \leq \mathcal{M}/M_{\odot} \leq 15$, uniform prior in η over the range $0.1 - 0.25$, a prior in luminosity distance in the range $1 - 1500$ Mpc, and a uniform prior in ψ and $\cos\iota$ over the whole range. The fact that the signal position is reconstructed with a instrument network but we are performing simulations using a single instrument is captured into a prior for the source position parameters (right ascension and declination) that is flat and has a width of 0.1 radians around the actual value of the injection. When we analyse the data considering the MG model, we introduce an additional unknown parameter, λ_g. The prior we choose for λ_g is the scale invariant prior $p(\lambda_g) \propto \lambda_g^{-1}$, however λ_g is limited below and above to lie in the range $10^{14} \leq \lambda_g \leq 10^{28}$ m, where the lower bound is comfortably below that of 2.8×10^{15} m placed by Solar System experiments (Will 2006), and the higher by the size of the observable universe. This prior is effectively non-informative on the scale of λ_g between these bounds, and also implies that $p(\log\lambda_g) = const.$ We therefore use the parameterisation of $\log\lambda_g$ throughout the actual numerical computations, as it is more easily sampled over this large a range.

In the following section we present results coming from single simulated gravitational wave observations. In section 3.4.2 we investigate the capability of Advanced LIGO to distinguish between the MG and GR models. Thus, we generate in the frequency domain Gaussian stationary noise following the expected sensitivity curve of the Advanced LIGO instrument into which we inject our signals. We then analyse the data using both the MG and the GR models to calculate the value of $\log B_{\mathrm{MG,GR}}$. This requires a solution of integral 3.2, which is performed using the nested sampling algorithm with a total of 1 000 live points. The MG model introduces only one additional parameter, λ_g, compared to GR, and reduces to the GR waveform in the case that $\lambda_g \longrightarrow \infty$.

In section 3.4.3 we discuss a simple idealised example of the effect of assuming the wrong theory of gravity when performing parameter estimation. We investigate the bias over the estimated parameters by performing a series of MG injections and analysing the data using both the MG and the GR models. The value of λ_g is already very well bound from non-GW observations. In section 3.4.4 we investigate the more physically meaningful bounds that future interferometric antennae will put on λ_g. In this experiment we inject GR and analyze the data using the MG model and from the PDF of λ_g calculate the 95% lower limit on λ_g itself. We present the results of this experiment for Advanced LIGO and in a preliminary format for the Einstein Telescope. In section 3.5 we present the results coming from the combination of multiple independent observations. We obtain a general expression for the PDF of global parameters as a function of the PDFs from single observations. We illustrate our method on a simple analytic case of a sigmoid PDF, that well approximates our PDF on λ_g, in section 3.5.1. In section 3.5.2 we apply our findings to the realistic case of discrete sampled PDFs using the properties of the Dirichlet distribution.

3.4.2 Massive Graviton Injections

We first consider whether second-generation instruments, such as Advanced LIGO, would be able to discriminate between a theory in which the graviton is massive and General Relativity. In order to do so, we generate signals from binaries corresponding to two fiducial values of the chirp mass, $\mathcal{M} = 5M_\odot$ and $10M_\odot$ – we keep the symmetric mass ratio fixed to $\eta = 0.245$ (almost equal mass binaries) – and the three values of the Compton wavelength $\lambda_g = 0.5,\ 5,\ 50\times10^{15}$m, and we add them to Gaussian noise. The signal location and fixed orientation of the orbital plane is drawn randomly from a uniform distribution on the two-sphere. In order to explore the dependency of the results on the signal-to-noise ratio, we simply place the sources at different luminosity distances, to span the range $10 \leq \mathrm{SNR} \leq 100$. As we have discussed in Section 3.4.1 for each of the injections we perform the analysis on 10 different independent

noise realisations.

The Bayes factors $B_{\rm MG,GR}$, see Eq. (3.3), that the analysis yields are shown in Figure 3.1. The scatter of the values is due to the effect of the different realisation of the noise (which dominates the numerical fluctuations produced by the Monte Carlo integration of the evidence integral). The results clearly indicate that $\log B_{\rm MG,GR}$ favours the MG model only for $\lambda_g = 5 \times 10^{14}$ m – which is just below the Solar System bound 2.8×10^{15} m (Will 1998) – and for SNR ≥ 40.

A byproduct of our analysis are the marginalised PDFs, see Equation (3.5), of the parameters characterising the models in use. Figure 3.2 shows the PDFs for selected parameter for a specific injection with $D_L = 20$Mpc and $\lambda_g = 5 \times 10^{15}$m. For such system to total number of wave cycles produced by the massive graviton term in Eq. (3.8) from when the waveform enters the sensitivity band is 13.3 . The optimal signal to noise ratio in this case corresponds to 26, and for the specific noise realisation we obtained $\log B_{\rm MG,noise} = 302$ and the $\log B_{\rm GR,noise} = 291$ Bayes factor was 302 for the MG theory and 291 for the GR, which corresponds to $\log B_{\rm MG,GR} = 11$.

When the injected value of λ_g is too large to be "detected", or in the language of Bayesian inference the Bayes' factor does not favour the MG model, the posterior density function on λ_g *if one assumes the MG model* shows a characteristic behavior that is consistent with what one would expect intuitively: the algorithm excludes the region of the $\log(\lambda_g)$ prior that would give raise to an appreciable effect, ruling out the lower parts of the prior distribution. In these cases, given the particular nature of the two theories under consideration, the Bayes factor in equation (3.3) reduces to

$$B_{ij} \propto \frac{\log \lambda_g^{min} - \log \lambda_g^{max}}{\sigma_{\log \lambda_g}} \tag{3.16}$$

where $\log \lambda_g^{min}$ and $\log \lambda_g^{max}$ are the prior extremes and $\sigma_{\log \lambda_g}$ is the width of the posterior on $\log \lambda_g$, see figure 3.3. Therefore for large values of λ_g we expect the Bayes factor to tend to a constant. Behaviour that is verified in figure 3.1. In every simulation both theories manage to recover the injected parameters with good precision. Nevertheless GR shows a departure from

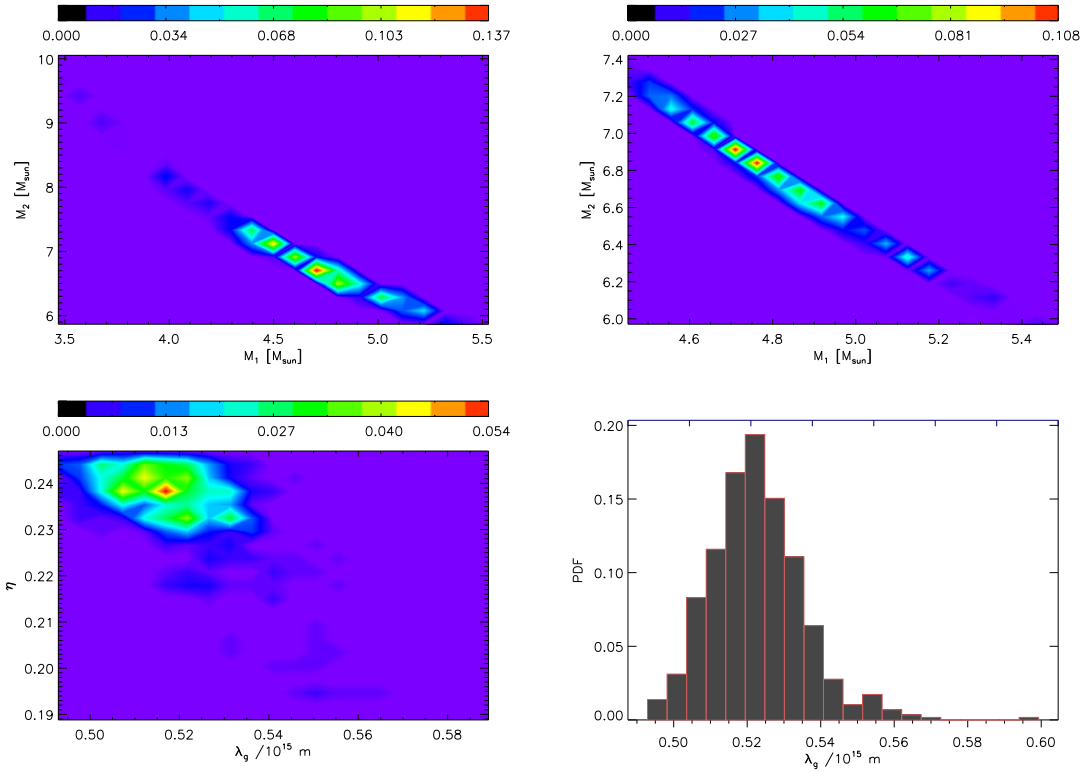

Figure 3.2: Posterior probability distributions obtained from our analysis. The MG waveform was injected with parameters $\mathcal{M} = 5.0M_{\odot}$, $\eta = 0.2495$ (giving $M_1 = 6.01M_{\odot}$ and $M_2 = 5.49M_{\odot}$), $D_L = 20$Mpc and $\lambda_g = 0.5 \times 10^{15}$m. The SNR was 26 and the $\log$ Bayes factor was 302 for the MG theory and 291 for the GR. The number of cycles from the massive graviton term was 13.3. **Top left panel**: two dimensional posterior distribution of the values of the inspiral masses recovered by the MG model. **Top right panel**: two dimensional posterior distribution of the values of the inspiral masses recovered by the GR model. **Bottom left panel**: two dimensional posterior distribution of η and λ_g as recovered by the MG model. **Bottom right panel**: posterior distribution of λ_g from the MG model.

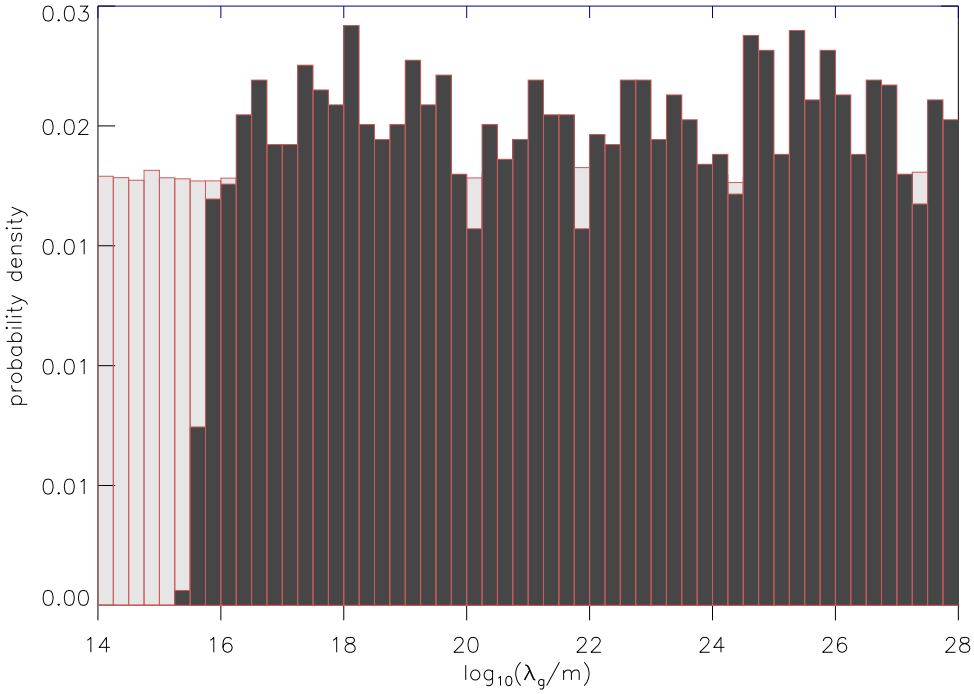

Figure 3.3: The charcoal histogram is an example PDF for $\log(\lambda_g)$ when $\log B_{\rm MG,GR}$ does not favor the MG model. The injected SNR was 17. The light grey histogram is the prior distribution in $\log(\lambda_g)$. When the injected model is GR the PDFs is excluding values of λ_g that would give an observable effect. For larger λ_g-s the phase contribution of the additional term in equation (3.8) is so small that does not affect the marginalization process.

the "real" parameters that is bigger than when using the MG model, regardless of having a comparable Bayes factor, as in the specific example in figure 3.2. This suggests that when the effect of unaccounted terms is of the same order of the modelled ones our parameter estimation might be *biased*. Therefore we devoted the rest of the work to understand the effects of neglecting additional terms in the GW phase evolution and possible ways around this problem.

3.4.3 Bias in Parameter Estimation

The assumption that General Relativity is the correct theory of gravity, may be a serious cause of bias in gravitational wave astronomy if the actual theory of gravity is different from GR (Yunes & Pretorius 2009). One might think that if a signal is detected with templates constructed using GR as the correct model of gravity, then the effects on the estimation of the parameters will be negligible. However, no quantification of this effect has ever been done, and in general this is not necessarily true as we are going to show here with a practical example, in which we take the MG theory as an example of deviation from GR. For the specific example of a MG theory, we note that the phase contribution of λ_g is proportional to $(\pi\mathcal{M}f)^{-1}$, see Eq. (3.8). The chirp mass and frequency dependency is exactly the same as the first Post-Newtonian term. Therefore we expect that the parameter that will be mostly affected by neglecting the effect of a massive graviton is the symmetric mass ratio η (and in turn the estimate of the individual mass components). The bottom-left panel of Figure 3.2 shows precisely the degeneracy (or correlation) between λ_g and η, clearly in the case in which the data are analysed assuming the model MG.

In order to explore this effect, we performed a set of numerical experiments to explore the dependence of the Bayes' factor $\log B_{\rm MG,GR}$ on the value of λ_g and to assess any eventual bias introduced by analysing the data assuming the wrong theory of gravity. We injected a family of MG waveforms according to Eq. (3.8) where we fixed the mass parameters to $\mathcal{M} = 5M_\odot$ and $\eta = 0.15$ and selected the distance and angular parameters to yield an optimal SNR $= 41$.

We then repeated the injections by varying only the the graviton Compton wavelength in the interval $10^{14} \leq \lambda_g \leq 10^{17}$ m, more specifically 13 different values that are reported in Table 3.2. In the table we also show the total number of wave cycles in the detection band (here the low-frequency cut-off is $f_{\rm low} = 20$ Hz) that the massive graviton term contributes for a signal with $\mathcal{M} = 5M_\odot$ and $\eta = 0.15$. Regardless of the signal-to-noise ratio, it is useful to notice that for $\lambda_g > 2.5 \times 10^{15}$ m the number of wavecycles produced by the graviton term drops below one. Figure 3.4 summarises the results, as a function of λ_g. For each set of 10 injections, we

Table 3.2: Total number of wave cycles from the massive graviton phase term as a function of λ_g for the mass parameter values use in the injections ($\mathcal{M} = 5M_\odot$ and $\eta = 0.15$) and a low-frequency cut-off $f_{\rm low} = 20$ Hz, to which results in Figure 3.4 refer.

λ_g [m]	Number of cycles
10^{14}	855
1.58×10^{14}	340
2.51×10^{14}	135
3.99×10^{14}	54
6.31×10^{14}	21
10^{15}	8
1.58×10^{15}	3
2.51×10^{15}	1
3.99×10^{15}	0.5
6.31×10^{15}	0.2
10^{16}	0.08
2×10^{16}	0.02
5×10^{16}	0.003
10^{17}	0.0008

computed $\log B_{\rm MG,noise}$ and $\log B_{\rm GR,noise}$. These quantities are always greater than unity and in general $\gg 1$ (although notice that for $\lambda_g = 10^{14}$ m, $\log B_{\rm GR,noise} \simeq 1.5$) and therefore for both model hypotheses the signal is clearly recovered. Notice however, that while $\log B_{\rm MG,noise}$ is essentially constant – as expected, considering that regardless of the value of λ_g the optimal SNR of the injection is always the same – and $\log B_{\rm MG,noise} \approx 730$, when one considers the GR model $\log B_{\rm GR,noise}$ increases from ≈ 1.5 for $\lambda_g = 10^{14}$ m to the same level of $\log B_{\rm MG,noise}$ by the time $\lambda_g \approx 10^{15}$ m. In fact for $\lambda_g \geq 10^{15}$ m (for this specific choice of masses and

signal-to-noise ratio) $\log B_{\rm MG,GR} \approx 1$ and there is no conclusive evidence from the data that the MG model should be preferred to the GR model. This behaviour is reflected in the value of η, figure 3.4 right panel. The bias introduced by neglecting additional effects in a GW template is potentially very severe. As long as the number of cycles (*c.f.* table 3.2) due to the mass of the graviton is less than one, the GR templates behave correctly and the systematic error that using the wrong template introduces is very small. When instead the number of cycles is greater than one the mismatch between the signal and the template is so big that even in case of a definite detection the estimated parameters can eventually be quite wrong. The Bayes factor for the GR hypothesis vs noise only is in fact *always* in favour of GR. One would then be inclined to believe that a successful detection has been made and that the PDFs of the parameters contain the "true" parameter, which may not necessarily be so.

The statistical properties of the sources that one would infer from the observation of GWs would be completely wrong, representing not our Universe, but merely reflecting our ignorance or the limitations of our models. A possible solution to this bias relies on the calculation of the Bayes factor between the different theories. As figure 3.4, right panel, is showing, $\log B_{\rm MG,GR}$ favours the MG model for small values of λ_g, where the bias is more severe. In a real situation the choice between the two models would depend critically on the priors that we assign to each theory. Nevertheless $\log B_{\rm MG,GR}$ would tell us what the actual *data* favour. As in figure 3.1, when the value of λ_g is large enough $\log B_{\rm MG,GR}$ converges to 1 therefore giving no reason to prefer the more complicated model. In this case the value of η recovered by both theories is consistent with the injected value.

This is, in our opinion, a real and serious issue that will require deep and thoughtful future investigations.

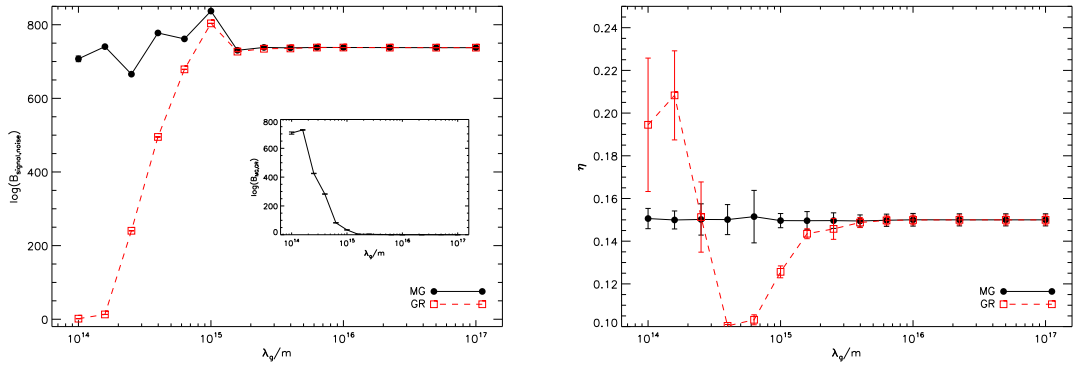

Figure 3.4: **Left panel**: The Bayes factor of the signal over noise-only hypotheses assuming the MG theory (solid circles) and GR (red open squares) as a function of the value of λ_g (in meters) of the injected signal. For any given value of λ_g, the difference between the values of two points yields $\log B_{\rm MG,GR}$, shown in the small inset. All the injections are carried out for a signal with $\mathcal{M} = 5M_\odot$ and $\eta = 0.15$, and distance and angular parameters selected in such a way to produce an optimal signal-to-noise ratio of 41. It is clear from the fact that $\log B_{\rm MG,noise}$ and $\log B_{\rm GR,noise}$ are $\gg 1$ (although notice that for $\lambda_g = 10^{14}$ m, $\log B^{\rm (GR)} = 1.5$ and therefore GR is just about able to recover the signal) that the signals are clearly detected. As expected the MG theory is (strongly) favoured for small values of λ_g, but for $\lambda_g \geq 10^{15}$ m (for this specific choice of masses and signal-to-noise ratio) $\log B_{\rm MG,GR} \approx 1$, thus the data do not provide any conclusive evidence in favour of the MG theory. **Right panel**: The median value of the maximum likelihood symmetric mass ratio η as recovered by the MG model (filled dots) and the GR model (empty squares). Each point is the average result of 10 independent runs. The error bars represent the combination of the 95% probability intervals from each run. Note that although $\log B_{\rm MG,GR} \approx 1$ for $\lambda_g \geq 10^{15}$ m, and therefore the MG model is not favorite over GR, the value of η recovered by the GR model is systematically biased to compensate for the additional phase shift due to the mass of the graviton that the GR model can not account for properly.

3.4.4 Bounds

In the previous Section we have just shown that even if a MG theory (in which the gravitational wave signal is of the form described in Eq. (3.8)) is the correct one, it is unlikely that in the near future gravitational wave observations will be able to tip the odds in favor of such a theory. On the other hand, even if the "correct" theory of gravity is characterised by a mass-less graviton, it interesting to investigate what limit on λ_g one could place experimentally. This can be addressed in straightforward way in Bayesian inference; it simply requires the evaluation of the marginalised posterior density function $p(\lambda_g|\vec{d}, \mathcal{H}_{\rm MG})$, from which one can compute a lower on λ_g corresponding to a given probability P:

$$\int_{\lambda_g^{(P)}}^{\infty} d\lambda_g \, p(\lambda_g|\vec{d}, \mathcal{H}_{\rm MG}) = P \, . \tag{3.17}$$

In our case we decide to set (arbitrarily) $P = 0.95$ and therefore compute the 95% lower limit on the graviton Compton's wavelength that we label $\lambda_g^{95\%}$. In order to explore this point, we first assume that the correct theory of gravity is one in which the graviton is zero-mass, and more specifically we consider GR. We then simulated 1000 independent observations for sources with the same physical parameters and at the same luminosity distance (that we fixed to $D_L = 20$) but different location/orientation in the sky (drawn uniformly on the two-sphere) so as to produce a range of optimal signal-to-noise ratios. We repeated the injections for three value of the chirp mass of the source, $\mathcal{M} = 1.2\, M_\odot \, , 5\, M_\odot$ and $10\, M_\odot$, keeping the symmetric mass ratio fixed to $\eta = 0.2495$. The inspiral waveform used to generate the injection is the GR waveform described by (3.8), and we analysed the data using the Massive Graviton model, Eq. (3.8) with a uniform prior on $\lambda_g/\mathrm{m} \in [10^{14},\ 10^{28}]$. From the marginalised PDF of λ_g we compute the 95% lower limit by setting $P = 0.95$ in Eq. (3.17). The results are shown in Figure 3.5.

Advanced LIGO will be able to put on the value of λ_g a much tighter constraint than the one currently accepted from the observation of the orbit of Mars. Since angular momentum contri-

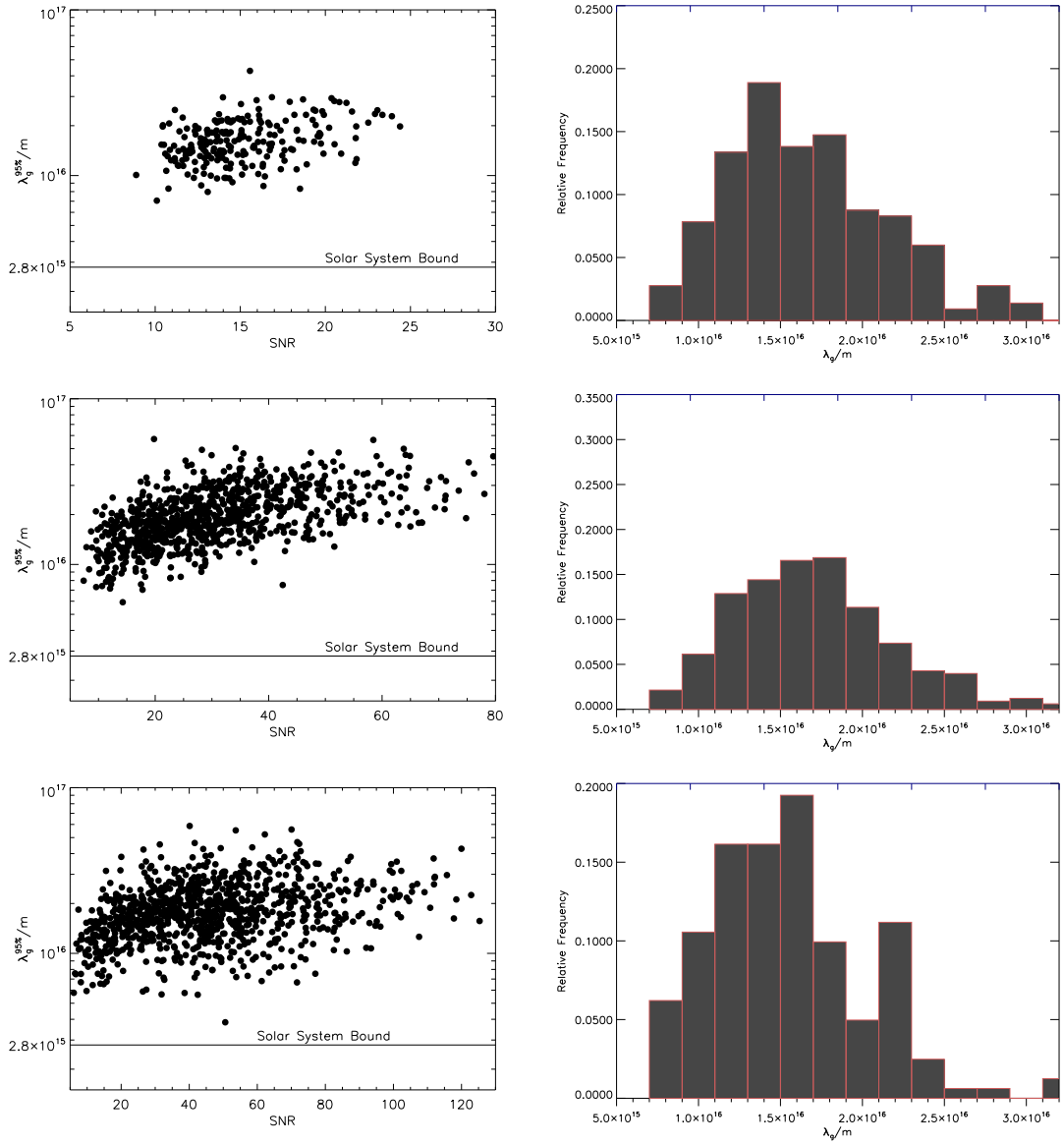

Figure 3.5: The 95% lower limit on the graviton Compton wavelength in observations with second generation ground-based instruments (the panels from top to bottom refer to inspiral signals from binaries with chirp mass $\mathcal{M} = 1.2\,M_\odot\,, 5\,M_\odot$ and $10\,M_\odot$, respectively, and $\eta = 0.2495$).**Left panels:** The value of $\lambda_g^{95\%}$ for each injection as a function of the optimal signal-to-noise ratio of the injected signal (plotted are only those value for which the Bayes' factor in the analysis yields $\log B^{(\mathrm{MG})}_{\mathrm{S,N}} \geq 3$ The solid line represents the Solar System bound, $\lambda_g = 2.8\times10^{15}$ m (Will 1998). **Right panels:** The histograms of $\lambda_g^{95\%}$ for each chirp mass for the injections for which $10 \leq \mathrm{SNR} \leq 25$.

butions could in principle increase the sensitivity to the Massive Graviton parameter (Stavridis & Will 2009) the results in figure 3.5 are to be considered lower limits. We note a very weak or no dependence at all from the value of $\mathcal{M}$ and from the SNR.

The Einstein gravitational-wave Telescope (ET) (Hild, Chelkowski,& Freise 2008; Hild et al. 2010) is a concept for a third generation gravitational wave instrument, that is currently under study. In short, the goal of ET is to increase the strain sensitivity by a factor ~ 10 with respect to advanced instruments and to push the low-frequency cut-off to ≈ 1 Hz. We used the sensitivity curve of ET in the single interferometer broadband configuration (Hild, Chelkowski,& Freise 2008). Because of the low frequency cut-off of 1Hz, the runtime of our ET based simulations is very long, as the templates can last up to 30 minutes. Therefore, in order to test the capabilities of a third generation instrument, we have been forced to reduce the accuracy of the nested sampling algorithm used in evaluation of the interval. Specifically, the number of live points used was reduced from 1 000 to 100, which allows a speed up of a factor of ten, but with the possibility of the nested sampling algorithm failing to locate the global maximum of the distribution, which will cause an early termination of the run.

In the following analysis we accounted for all these factors and did not include any chain that looked "unnaturally" truncated. This decision was taken by visual inspection of each simulation chain. We simulated 100 sources randomly distributed on the sky sphere. The mass parameters have been chosen by randomly drawing from uniform distributions, $1M_{\odot} \leq \mathcal{M} \leq 15M_{\odot}, 0.1 \leq \eta \leq 0.25$. Inclination and polarisation angles have been chosen from uniform distributions on the 2-sphere. The luminosity distance D_L has been fixed to 1Gpc. Using the parameters chosen as described above, we generated waveforms using the GR model and we analysed the data using the MG model. As in paragraph 3.4.4 we calculated the 95% confidence lower limit on λ_g. In our analysis we did not take into account the redshift dependence in equation (3.14) even if for $D_L = 1$ Gpc, corresponding to $z \sim 0.2$, cosmological corrections begin to become significant. Even in the poor precision conditions in which our experiments were performed,

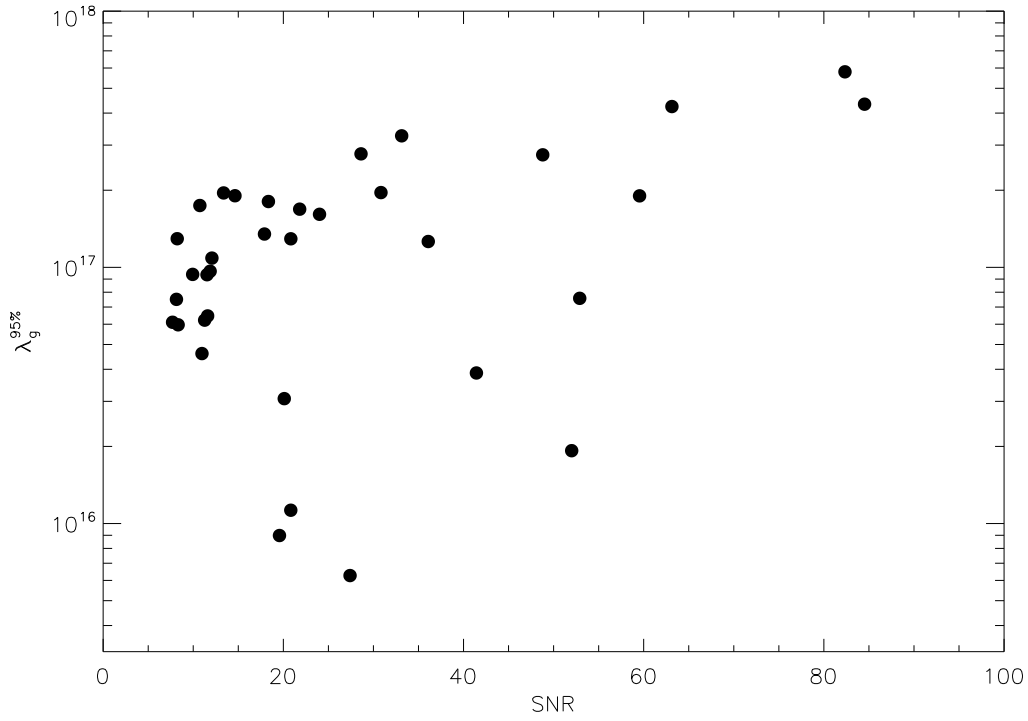

Figure 3.6: 95% lower limit on λ_g from 100 independent observations for values of $\mathcal{M}$ randomly sampled from a uniform distribution between $1 \leq \mathcal{M}/M_\odot \leq 15$ and $0.1 \leq \eta \leq 0.25$. Only those detections giving a $\log$ Bayes factor greater than 3 and that were not truncated before reaching the maximum of the likelihood are shown. See text for a discussion of the truncation effects.

the limits that the Einstein Telescope will be able to put on the value of λ_g are an order of magnitude better than what will be achieved by Advanced LIGO, figure 3.6. This result should anyway be treated as "preliminary". A proper analysis should be performed using a sufficient number of live points in the nested sampling run.

3.5 Multiple observations

Beyond the present challenge of directly detecting for the first time gravitational waves, second and third generation instruments are expected to detect an increasing number of sources in the coming years (Abadie et al. 2010; Cutler & Thorne 2002; Kokkotas 2008). Therefore, it is imperative that we exploit the information that multiple observations can bring in a statistical way. Bayes' theorem offers the possibility of combining the results from each individual observation in a straightforward and conceptually simple way. In the context of testing theories of gravity, this may be particularly powerful if a given theory is characterised by some "global parameters" – *e.g.* the Compton wavelength of gravitons – that are independent of the actual gravitational wave signal at hand. In this case one can construct posterior density functions that take into account of all the data available and therefore strengthen the inference process. For the specific case considered in this chapter, we will consider how one can set more stringent lower limits on the graviton's Compton wavelength using observations of a number of coalescing binaries each of which with different parameters. Specifically in our case we consider the example of inferring λ_g from the combined probability distribution from multiple, independent, observations..

Let us assume that we have a set of N independent observations, $d_1, \ldots, d_N$, in which a gravitational wave signal from a coalescing binary is detected. We want to estimate the marginal

PDF of λ_g from the joint set of observations. From Bayes' theorem we can write:

$$p(\lambda_g|d_1,\ldots,d_N) \propto p(\lambda_g)p(d_1,\ldots,d_N|\lambda_g)\,, \tag{3.18}$$

and from the chain rule,

$$p(d_1,\ldots,d_N|\lambda_g) = p(d_1|\lambda_g,d_2,\ldots,d_N)p(d_2,\ldots,d_N|\lambda_g)\,. \tag{3.19}$$

Since the observations are independent, Eq. (3.19) simplifies to

$$p(d_1|\lambda_g,d_2\ldots,d_N) \propto p(d_1|\lambda_g)\,, \tag{3.20}$$

and in general we can write

$$p(\lambda_g|d_1,\ldots,d_N) \propto p(\lambda_g)\prod_{i=1}^{N} p(d_i|\lambda_g)\,, \tag{3.21}$$

where

$$p(d_i|\lambda_g) = \int d\vec{\theta}\, p(\vec{\theta})\, p(d_i|\vec{\theta},\lambda_g) \tag{3.22}$$

is the marginalised likelihood for the ith observation.

3.5.1 A proof-of-concept example

One can first develop some intuition about the benefits and power of this approach by considering a simple case, in which the relevant functions that enter the computation of $p(\lambda_g|d_1,\ldots,d_N)$, Eq. (3.21), have simple analytical forms; this case is also useful to disentangle conceptual issues from practical ones related to the discrete nature of the functions with which one deals in practice, and that we shall address in the next Section.

Following the results of Section 3.4.2 in which we showed that in the case in which the

correct theory of gravity is general relativity, the posterior PDF $p(\log(\lambda_g)|d)$ is well approximated by a sigmoid function, see Figure 3.3. Let us therefore consider a set of $i = 1, \ldots, N$ observations each of which yields a posterior PDF is of the form

$$p(\log(\lambda_g)|d_i) \propto \frac{1}{1 + a_i e^{-b_i \log(\lambda_g)}}\,, \tag{3.23}$$

where a_i and b_i are real numbers that different from observation to observation. We can simulate the outcome of N observations on a range of binary systems by simply selecting the values of a_i and b_i and then combine the results by using Eq. (3.21). In fact, for the specific choice of prior on λ_g that we consider here, we have

$$p(d_i|\lambda_g) \propto \frac{p(\log(\lambda_g)|d_i)}{p(\lambda_g)} = p(\log(\lambda_g)|d_i) \tag{3.24}$$

As an example, we can assume that we have, say, 50 detections of coalescing binaries, each of which coming from a different source and a different SNR, that leads to a 95% lower limit on the graviton's Compton wavelength $\lambda_g^{95\%}$, by randomly drawing values of a and b to construct the PDFs (3.23) . We have generated 50 distributions according to Eq. (3.23). For each of them we compute the 95% lower limit on λ_g, based on a single observation, and the same quantity using the combining set of observations, from Eq. (3.21). Figure 3.7 summarises the results. It shows a monotonic increase in the value of the 95% lower limit calculated from the combined PDF, solid line, compared to each single 95% lower limit, dashed line. Interestingly, the amount of knowledge, quantified by the 95% limit, never decreases. Adding "bad" observations at most leaves the 95% limit constant.

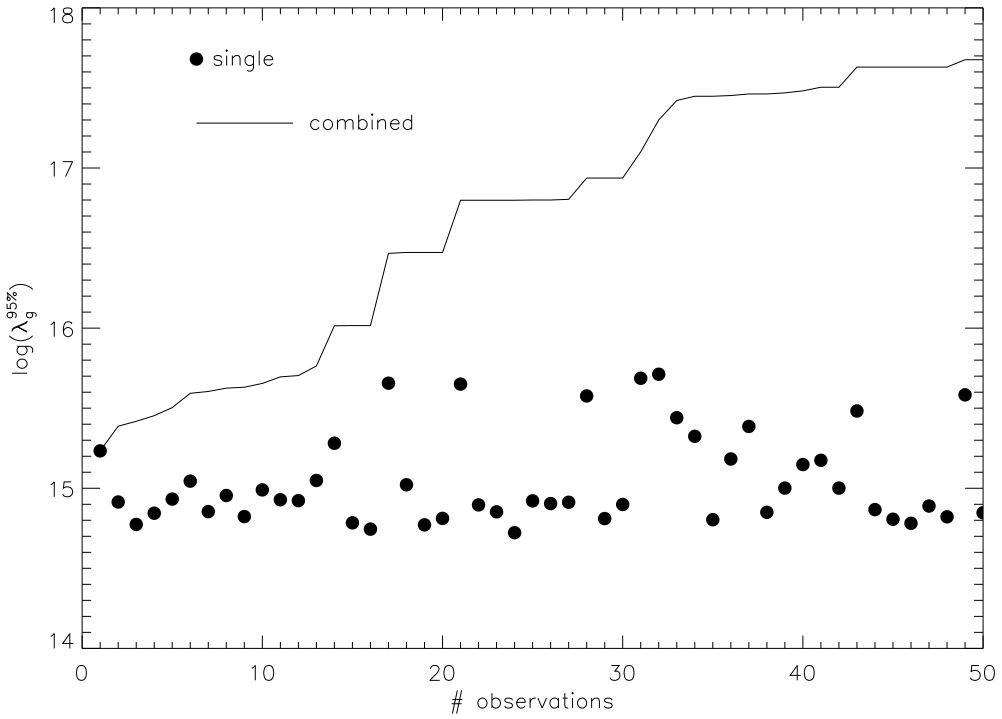

Figure 3.7: The limit on λ_g for an example of individual and combined (independent) observations of inspiral binaries. The plot shows the 95% lower limit on the graviton Compton wavelength $\lambda_g^{95\%}$ for each individual observation (solid circle) and for the combined set of observations (solid line), following Eq. (3.21). The posterior PDF on λ_g from which the single and combined result are obtained is assumed to be of the form (3.23), with random a and b coefficients.

3.5.2 Combining independent observations

In practice, we are dealing with a finite number of samples from the posterior distribution of each run, rather than with an analytical function. This introduces certain complications when producing the combined PDF on the λ_g parameter, which we have tackled using the following procedure.

To state the problem, we wish to find an appropriate approximation to the posterior PDF for each observation which we can multiply together in order to get the combined PDF, Eq. (3.21), through Eq. (3.24). A typical approach is to categorise the samples into a series of bins, creating a histogram which approximates the underlying PDF. A histogram $\mathbf{m}$ is a set of k integers, $\mathbf{m} = (m_1, \ldots, m_k)$, which register the number of samples falling into k independent categories. As our histogram approximates a probability distribution, which we know is normalised, we can approximate the probability in each bin by dividing each count by $n = \sum_{i=1}^{k} m_i$. This process can introduce a large amount of noise to the distributions, as there are likely to be very few posterior samples falling into the bins of low probability density, which occurs near the region of the 95% limit (or any other large probability interval) in which we are interested. A naïve approach to combining these histograms would be to multiply the (normalised) results in each bin, but if one of the histograms contains zero samples in a bin, then all combined results produced from this distribution will also register zero in that bin no matter how many samples may appear there in the other histograms used in the combination.

This problem arises because of the treatment of the normalised count in each bin as if it were the actual probability in that bin. In fact, given a particular histogram, we can calculate the actual probability distribution for the probability in each bin, using the Dirichlet distribution. This allows us to avoid the probability in any one bin going to zero, although that may still be the most likely value given the histograms.

The probability of getting a given histogram of k bins from a set of n items is governed by

a multinomial distribution:

$$p(\mathbf{m};\mathbf{p}) = \frac{n!}{m_1!\cdots m_k!}\prod_{i=1}^{k} p_i^{m_i}\,, \tag{3.25}$$

$$n = \sum_{i=1}^{k} m_i\,. \tag{3.26}$$

Thus we can alternatively describe an histogram using the probabilities $\mathbf{p} = (p_1,\ldots,p_k)$ associated with each bin of the histogram itself. The probability distribution of the probabilities entering the definition of the multinomial distribution is described by the Dirichlet distribution. In fact the probability density for the variables $\mathbf{p} = (p_1,\ldots,p_k)$ given the histogram $\mathbf{m} = (m_1,\ldots,m_k)$ is

$$p(\mathbf{p};\mathbf{m}) = \frac{1}{Z(\mathbf{m})}\prod_{i=1}^{k} p_i^{m_i-1} \tag{3.27}$$

where $p_1,\ldots,p_k \geq 0$, $\sum_{i=1}^{k} p_i = 1$ and $m_1,\ldots,m_i > 0$. The parameters m_i can in this context be interpreted as "prior observation counts" for events governed by p_i. Furthermore, in the limit $m_i = 0$ the Dirichlet distribution is a conjugate non-informative prior for the multinomial distribution. The normalisation constant $Z(m)$ is given by

$$Z(\mathbf{m}) = \frac{\prod_{i=1}^{k}\Gamma(m_i)}{\Gamma(\sum_{i=1}^{k} m_i)}. \tag{3.28}$$

We use the Dirichlet distribution to calculate the probability $p_1,\ldots,p_k$ associated to each of the k bins given the current histogram $\mathbf{m}$. Thanks to this procedure no bin is ever assigned a zero probability. Therefore, to calculate the combined PDF, Eqs.(3.21), we multiply not the multinomial distributions corresponding to each histogram, but the "probability histograms", the Dirichlet distributions, describing the probabilities associated with each bin given each histogram. The combined PDF can also be thought as the joint probability distribution of the probability that each bin has to receive a future point, given all the previous observations.

We applied the above method to a set of 50 mock datasets from the Advanced LIGO instrument. We chose all the relevant parameters in a random way except the luminosity distance D_L that has been fixed to 20 Mpc. All the parameters have been chosen by sampling a uniform distribution in the appropriate metric. After generating the corresponding inspiral waveforms using the GR template we analysed our data using the MG model. In this particular instance we analyse the data using 10 parallel runs of our algorithm over each dataset varying the seed of the MCMC. The independence of the MCMC chains implies that we can combine all the chains, effectively using 10000 Live points. Figure 3.8 shows the 95% lower limit on λ_g obtained by applying equation (3.21), black dots, 95% lower limits corresponding to the single $i-$th equation. The occasional drops in the 95% lower limit on $\log(\lambda_g)$, *c.f.* Fig. 3.8, are caused by the

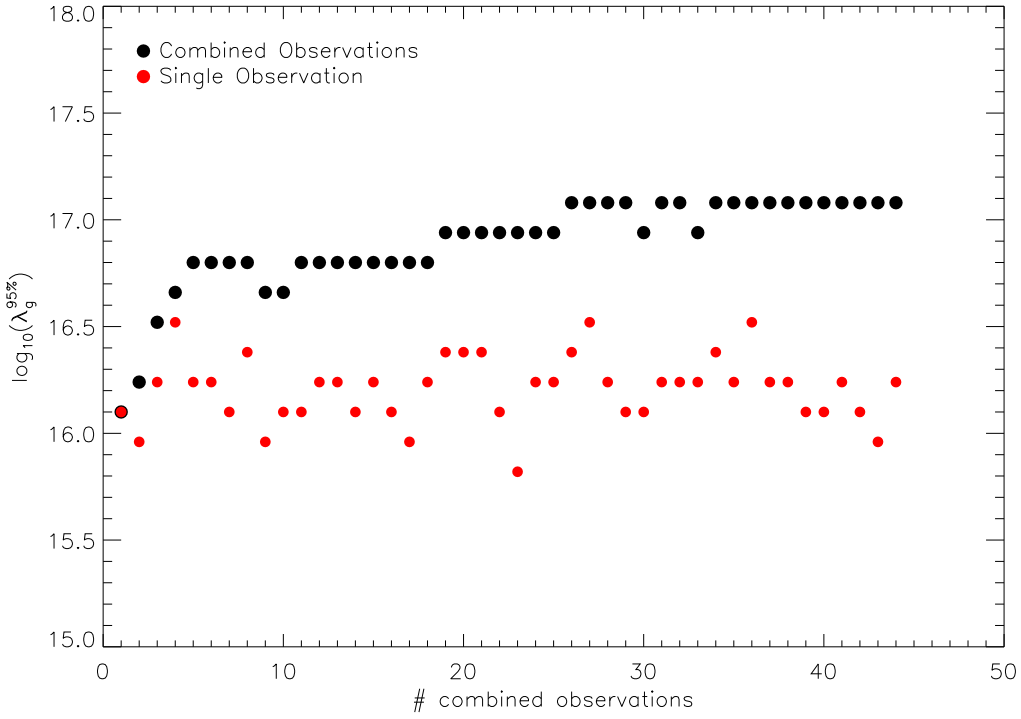

Figure 3.8: 95% lower limit on $\log(\lambda_g)$ resulting from the combination of 50 simulated sources. Only the succesful detections are shown. The black dots are the combined limits while the red dots are the 95% lower limit on $\log(\lambda_g)$ from the single corresponding observation.

discretization induced by the binning processes. Figure 3.7 in fact shows that in the ideal case

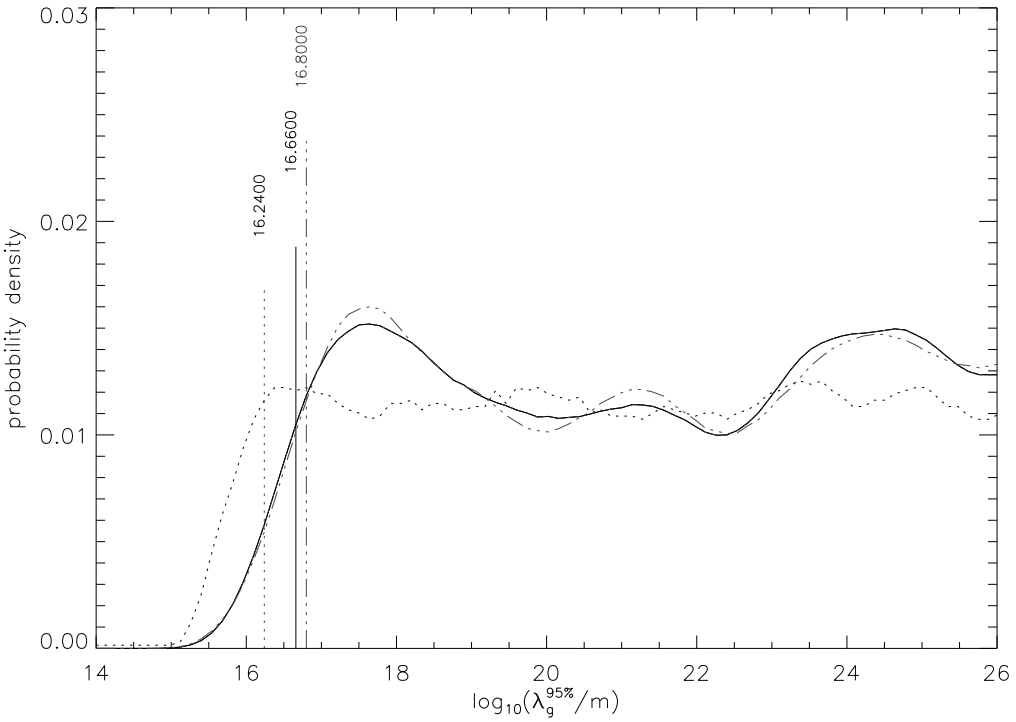

Figure 3.9: A practical example showing how the 95% limit calculated from the combined PDF can decrease. In black the combined (solid line) PDFs for step n, the charcoal dot dashed line is the $n+1$-th PDF obtained multiplying the n-th combined PDF and the n-th single PDF (charcoal dotted line). The vertical lines are the corresponding 95% lower limits that are also indicated in the figure.

the combined PDF never yields a decrease in the 95% limit. Each bin is indeed a closed box, either it contains a sample or it does not. When calculating $\lambda_g^{95\%}$, the integral in (3.17) becomes a finite sum over each of the k bins defining the histogram $\mathbf{p} = (p_1, \ldots, p_k)$:

$$\sum_{i=\lambda_g^{95\%}}^{k} p_i = 0.95 \tag{3.29}$$

where, with an abuse of notation, we identified the index i labeling the bins with their corresponding value of λ_g. Consider now a single PDF, or better its histogram, $\mathbf{s} = (s_1, \ldots, s_k)$, and a combined PDF $\mathbf{c} = (c_1, \ldots, c_k)$. We absorbed the normalization constant inside their definitions. The result of updating $\mathbf{c}$ with $\mathbf{s}$ is simply

$$\mathbf{s} \times \mathbf{c} = (s_1 c_1, \ldots, s_k c_k) \equiv \mathbf{c}' \tag{3.30}$$

and the new value of $\lambda_g'^{95\%}$ is

$$\sum_{i=\lambda_g'^{95\%}}^{k} s_i c_i = 0.95 \tag{3.31}$$

The conditions for which $\lambda_g'^{95\%} < \lambda_g^{95\%}$ from the histograms can be found immediately:

$$\sum_{i=\lambda_g'^{95\%}}^{k} s_i c_i = \sum_{i=\lambda_g^{95\%}}^{k} c_i \tag{3.32}$$

Using the normalization conditions $\sum_{i=0}^{k} p_i = 1$ we can write:

$$\sum_{i=0}^{\lambda_g'^{95\%}} s_i c_i = \sum_{i=0}^{\lambda_g^{95\%}} c_i \tag{3.33}$$

$\lambda_g'^{95\%} < \lambda_g^{95\%}$ implies that $\mathbf{s}$ must bear as much elements to the left side of $\lambda_g'^{95\%}$ as the original $\mathbf{c}$ does leftward of $\lambda_g^{95\%}$. Therefore when multiplying by a "bad" PDF, the resulting PDF could

have a higher count in the leftmost bins and consequently give a worse $\lambda_g^{95\%}$. Figure 3.9 shows an example of the situation described above. We can quantify the overall influence of this effect in a simple way. Since this "back shift" is purely due to a discrete process, the details of the end PDF might depend on 2 factors:

- the sampling of the original PDFs;
- the order in which we combine observations.

These two issues are only of practical relevance since theoretically none of them influence the final PDF. Therefore we assured the robust character of the result presented in figure 3.8 with 2 simple experiments.

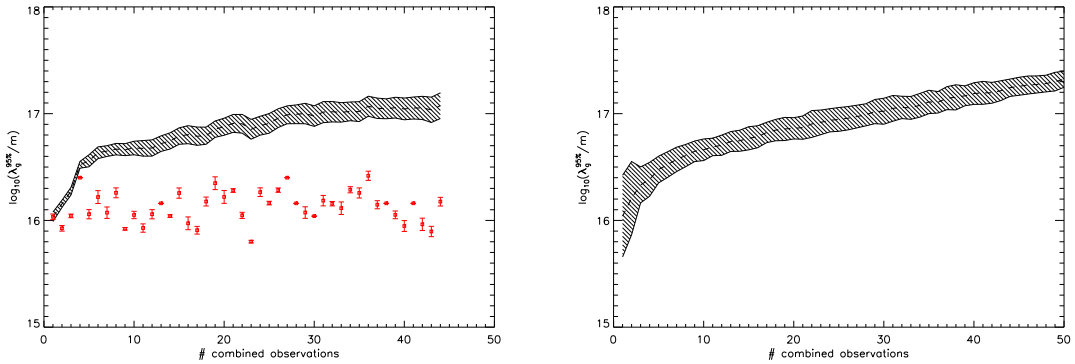

Figure 3.10: **Left Panel**: the shaded region is the 1σ confidence region over the 95% lower limit on $\log(\lambda_g)$ obtained combining 100 realisations of the single observation PDFs. The order of the observations is held fixed. The squares are the 95% lower limits on $\log(\lambda_g)$ for each single observations. The error bars are the 1σ confidence interval of each point. **Right Panel**: the shaded region is the 1σ confidence region over the 95% lower limit on $\log(\lambda_g)$ coming from combining 100 random permutations of the datasets. The mean trend, the dashed line in both panels, is consistent in both cases. Depending on the particular realisation the value of $\log(\lambda_g^{95\%})$ obtained from the combined PDF can vary up the ~ 0.1.

In the first one, left panel on Fig 3.10 , we computed the mean and 1σ interval of $\log(\lambda_g^{95\%})$ for 100 different realisations of the single observations PDFs. In the second one, right panel on Fig. 3.10 , we computed again the mean and 1σ interval of $\log(\lambda_g^{95\%})$ for 100 random permutations of the datasets. In both cases we note a statistical spread in the value of $\log(\lambda_g^{95\%})$ that is as

high as ~ 0.1, but the mean trend, the dashed line in both panels, is clearly consistent between the two and with what presented both in figure 3.7 and in figure 3.8. We are therefore confident that combination of independent observations is a powerful tool to be applied to any experiment able to detect even few, ~ 10, GW events. Our study shows a significant improvement on the value of $\lambda_g^{95\%}$ already after the combination of 5 PDFs $\lambda_g^{95\%}$. The latter is in fact larger than any single experiment is able to give.

3.6 Conclusions

In this work we have developed a rigorous framework to systematically compare alternative theories of gravity. Our approach is based on the Bayesian model selection method. In this framework we are able to compute Bayes factors between alternative theories which tell us the factor by which the data prefers the hypotheses. As a proof-of-principle, this formalism has been applied to the emission of gravitational waves from non-spinning compact binary systems inspiral in two competing theories:

- 2nd order Post-Newtonian General Relativity;
- 2nd order Post-Newtonian General Relativity plus the additional contribution of a massive graviton.

We calculated the Bayes factor between these two models using simulated data from Advanced LIGO and showed examples of parameter estimations for both theories.

We investigated the potential bias that might be introduced by using non correct models to analyse gravitational waves data. We found that, even in case of a clear detection using the GR model, the value of the parameters that are inferred are biased. This is a serious issue as it could mislead the knowledge of the Universe derived from GW astronomy. Deeper investigations are ongoing to study the effects of more general family of parametrised post Einstein waveforms (Yunes & Pretorius 2009).

We investigated the bounds that Advanced LIGO and the Einstein Telescope should be able to put on the Compton wavelength of the graviton. We found that Advanced LIGO will be able to put bounds on λ_g that are an order of magnitude better than Solar System based estimates, with a value of $\sim 10^{16}$ m, which appears to be a slight improvement compared to previous studies based on the Fisher information matrix. We expect the greater sensitivity of ET will push the boundaries at least another order of magnitude further.

We also developed an algorithm to combine multiple sets of results which are samples from independent PDFs. We have demonstrated a simple analytical example and an implementation on simulated multiple observations such as may actually be observed. We showed that by using this process to combine multiple observations may lead to significant improvements in the lower bound of the graviton Compton wavelength.

Bibliography

Abadie J., et al., 2010, arXiv:1003.2480.

Abbott B. P., et al., 2009, RPPh, 72, 076901

Acernese F., et al., 2004, CQGra, 21, 385

Alexander S., Finn L. S., Yunes N., 2008, PhRvD, 78, 066005

Apostolatos T. A., Lukes-Gerakopoulos G., Contopoulos G., 2009, PhRvL, 103, 111101

Arun K. G., Iyer B. R., Qusailah M. S. S., Sathyaprakash B. S., 2006, PhRvD, 74, 024006

Arun K. G., Will C. M., 2009, CQGra, 26, 155002

Aylott B., et al., 2009, CQGra, 26, 165008

Aylott B., Veitch J., Vecchio A., 2009, CQGra, 26, 114011

Balasubramanian R., Dhurandhar S. V., 1998, PhRvD, 57, 3408

Barack L., Cutler C., 2007, PhRvD, 75, 042003

Barish B. C., Weiss R., 1999, PhT, 52, 44

P. Bender P. et al., LISA Pre-Phase A Report; Second Edition, MPQ 233 (2006)

Berti E., Buonanno A., Will C. M., 2005, PhRvD, 71, 084025

Berti E., Cardoso V., Will C. M., 2006, PhRvD, 73, 064030

Blanchet L., 2006, LRR, 9, 4

Blanchet L., Damour T., Iyer B. R., Will C. M., Wiseman A. G., 1995, PhRvL, 74, 3515

Cramer H., 1946, Mathematical Methods of Statistics. Pergamon Press, Princeton University Press, New Jork

Cutler C., Thorne K. S., 2002, in *General Relativity and Gravitation* Ed N. T. Bishop and D. M. Sunil (Singapore: World Scientific) p 72 (2002). arXiv:gr-qc/0204090.

Dilkes F. A., Duff M. J., Liu J. T., Sati H., 2001, PhRvL, 87, 041301

Freise A., Chelkowski S., Hild S., Del Pozzo W., Perreca A., Vecchio A., 2009, CQGra, 26, 085012

Gair J. R., Li C., Mandel I., 2008, PhRvD, 77, 024035

Gelman A. & Meng X.-L., 1998, Statistical Science 13, 163

Gilks W. R., Richardson S., & Spiegelhalter D. J., 1996, ”Markov chain Monte Carlo in practice”, Chapman & Hall CRC, Boca Raton

Glampedakis K., Babak S., 2006, CQGra, 23, 4167

Green P. J., 1995, Biometrika 82, 711

Hild S., Chelkowski S., Freise A., 2008, arXiv, arXiv:0810.0604

Hild S., Chelkowski S., Freise A., Franc J., Morgado N., Flaminio R., DeSalvo R., 2010, CQGra, 27, 015003

Hughes S. A., 2006, AIP Conf. Proc. 873, 233

Jaynes E. T., Bretthorst G. L., 2003, “Probability Theory: The Logic of Science”, Cambridge University Press, Cambridge, England

Kawamura S., et al, 2006, CQGra, 23, S125

Keppel D., Ajith P., 2010, arXiv, arXiv:1004.0284

Kesden M., Gair J., Kamionkowski M., 2005, PhRvD, 71, 044015

Kokkotas K. D., 2008, RvMA, 20, 140

Nicholson D., Vecchio A., 1998, PhRvD, 57, 4588

Punturo M., et al., 2010, CQGra, 27, 084007

Rao C., Bullet. Calcutta Math. Soc, 1945 37, 81

Ryan F. D., 1997, PhRvD, 56, 1845

Sathyaprakash B. S., Schutz B. F., 2009, LRR, 12, 2

Schutz B. F., 2009, CQGra, 26, 094020

Skilling J., 2004, AIPC, 735, 395

Stavridis A., Will C. M., 2009, PhRvD, 80, 044002

Vallisneri M., 2008, PhRvD, 77, 042001

Veitch J., Vecchio A., 2008, PhRvD, 78, 022001

Veitch J., Vecchio A., 2008, CQGra, 25, 184010

Veitch J., Vecchio A., 2010, PhRvD, 81, 062003

Will C. M., 1994, PhRvD, 50, 6058

Will C. M., 1998, PhRvD, 57, 2061

Will C. M., 2003, CQGra, 20, 219

Will C. M., Yunes N., 2004, CQGra, 21, 4367

Will C. M., 2006, LRR, 9, 3

Yunes N., Finn L. S., 2009, JPhCS, 154, 012041

Yunes N., Pretorius F., 2009, PhRvD, 80, 122003

Yunes N., Sopuerta C. F., 2009, arXiv, arXiv:0909.3636

Zanolin M., Vitale S., Makris N., 2009, arXiv, arXiv:0912.0065

4. The Distribution of Black Holes in the Local Universe: Links to AGN Activity

Abstract

From galaxies observed in the Sloan Digital Sky Survey (SDSS), we calculated and investigated the dependence on the environment of the Super Massive Black Holes Mass Function (SMBHMF). High mass BHs live preferentially in high density environments as expected from cosmological simulations. By cross-correlating SDSS and the Faint Images of the Radio Sky at Twenty-one centimetres (FIRST), we measured the fraction of radio-loud AGN (RAF) in the group, cluster and field environment. We find evidence for an increased fraction of radio AGNs in red galaxies orbiting the groups and clusters potential. We investigated the BH mass, $M_{\bullet}$, dependence of the RAF and found $f_{\rm radio-loud} \sim M_{\bullet}^{1.6}$ in all environments, except in non-central galaxies in clusters of galaxies, where $f_{\rm radio-loud} \sim M_{\bullet}^{2.3}$. We interpret this result as an effect of ram pressure stripping being more efficient in the cluster environment. Using the *black hole fundamental plane* we use our BH masses and 1.4 GHz fluxes to construct X-ray luminosity functions that are in agreement with observations. This allows us to infer the distribution of accretion rates in the local Universe from the number of observed sources.

4.1 Introduction

Active galactic nuclei (AGN) are believed to play a prominent role in shaping the bright end of the luminosity function of galaxies (e.g. Benson et al. 2003), and in tempering radiative cooling of the intra-cluster (ICM) of galaxy clusters and groups (e.g. McNamara & Nulsen 2007 for a review, and also Bildfell et al. 2008; Pipino et al. 2009). There are two principal types of AGN activity: optical/quasar mode and radio-loud/jet mode. Which of these is responsible for quenching galaxy formation and which is responsible for moderating cluster and group cooling flows is not well understood, and neither are the physical determinants that give rise to these two modes. Given that AGN feedback is now increasingly invoked as an essential feature of galaxy formation and incorporated in corresponding numerical simulations (Sijacki et al. 2007; Bower et al. 2006; Lagos et al. 2008), it is critically important to identify the parameters that govern the nature and the duration of AGN activity.

Two physical parameters that are often cited as being relevant are the black hole mass and the local environment of the host galaxy. For example, in a breakthrough series of studies, Best and collaborators (Best 2004; Best et al. 2005a; Best et al. 2005b) found that the probability that a supermassive black hole is radio loud scales with black hole mass as $M_{\bullet}^{1.6}$. Whether this relationship is modulated by the local environment and if so, how, is not well known. There are, however, indications that suggest an environmental dependence. The brightest cluster (and group) galaxies (BCGs and BGGs respectively) are more likely to host powerful radio sources (Eilek & Owen 2007 and many others) and even the satellite galaxies in group and cluster environments are more likely to be active in the X-rays (Martini et al. 2006; Martini et al. 2007) and in the radio (Best 2004; Best et al. 2005a; Lin & Mohr 2007). These results, however, are not unambiguous and may simply be a manifestation of the mass dependence. After all, the massive galaxies are often found in dense, gas-rich environments. Our aim is to try and determine if the environment is, in and of itself, a relevant factor.

Let us consider the mass distribution of supermassive black holes (hereafter, the supermas-

sive black hole mass function or SMBHMF) in the nearby Universe. If the nature of the AGN activity is a function only of the black hole mass, we would expect variations in the fraction of "radio active" galaxies (hereafter, the radio active fraction) to correlate straightforwardly with variations in the SMBHMF across all environments. Therefore, a systematic determination of the SMBHMF and the radio active fraction in different regimes is warranted. With the exception of Colberg & Di Matteo (2008), this issue has received little attention. This then is our aim. The key issues that we wish to address in this chapter are:

- Does the distribution of supermassive black holes in cluster and group galaxies differ from those in field galaxies?
- What is the relationship between the SMBHMF and the nature of AGN activity in different environments?

Pursuing such an agenda requires assembling statistically homogeneous samples of galaxies in different environments. Several determinations of the SMBHMF in the nearby Universe have been attempted. These studies have usually involved a limited number of galaxies (Benson et al. 2007), or covered survey volumes of limited size (Marconi et al. 2004), or examined only active BHs with spectral signatures in optical spectra (Greene & Ho 2007). Our plan is to take advantage of the volume-limited surveys, such as the SDSS (Adelman-McCarthy et al. 2008), FIRST (Becker et al. 1995) and 2MASS (Cutri et al. 2003), covering a large fraction of the sky at various wavelengths to carry out our programme.

We have organized the chapter as follows: In §2 we describe and compare of galaxy samples. In §3 we describe the construction of SMBHMF in the field as well as in the galaxy group and cluster environment. In §4 we compare the SMBHMF in the different environments. In §5 we calculated the fraction of AGN that are active at radio wavelengths in these different environments. In §6 we use the observed fundamental plane of black holes to relate the radio luminosities and BH masses of AGNs to their putative X-ray luminosities, compute the corre-

sponding X-ray luminosity function and compare it to recent observational results. In §6, we conclude with a discussion and interpretation of the various results. Throughout the chapter we have adopted a concordance cosmology: $H_0 = 70$ km s^{-1} Mpc^{-1}, $\Omega_\Lambda = 0.7$, $\Omega_M = 0.3$.

4.2 Sample Selection

To construct the distribution of masses of supermassive black holes in the nearby Universe, we start by assembling a well-defined sample of galaxies with optical photometry and spectroscopy from the Sloan Digital Sky Survey data release 6 (SDSS DR6) (Adelman-McCarthy et al. 2008). Specifically, we use the version of SDSS DR6 referred to as the NYU Value-Added Galaxy Catalog (Blanton et al. 2005), which attempts to account for galaxies missing from the SDSS spectroscopic sample due to fibre collisions that poses a serious concern when studying galaxies in high density cluster cores.

Our master sample comprises all galaxies brighter than the spectroscopic completeness limit, $r = 17.77$ with redshift of $z \leq 0.1$. The total number of galaxies included in this master sample is 348,528. The r-band magnitude limit of $r = 17.77$ corresponds to an absolute magnitude limit of $M_r = -20.4$ at the redshift limit of $z = 0.1$. Based on the scaling relationships reported in §3, we expect should be able to probe the SMBHMF to a lower mass limit of roughly $M_\bullet \sim 10^7 M_\odot$.

The FIRST survey has an angular resolution of $5.4''$ and covers almost exactly the same area of the sky as the SDSS so we can use the FIRST 1.4 GHz radio survey (Becker et al. 1995) to obtain 1.4 GHz radio fluxes for our optically-selected galaxies. We do so by associating our optical galaxies with radio sources that lie within a projected search radius of $10''$ (Best 2004). We are able to find radio fluxes for ∼9.5% of our SDSS sample. Best et al. (2005a) has published the results of a similar exercise using radio fluxes from the NVSS 1.4 GHz continuum survey (Condon et al. 1998). We discuss our choice to use the FIRST survey instead of NVSS

in §4.5.2.

The various colours discussed in this chapter are calculated in the galaxy rest frame. In the NYU Value-Added Galaxy Catalog, the fluxes are given in nano-maggies (nMgy). These quantities are related to standard apparent magnitudes via

$$m = 22.5 - 2.5 \log_{10} f \tag{4.1}$$

where f is the total flux in nMgy. The characteristic radii are given in pixels[1]. For the purpose of comparison with the literature, the colours presented in figures 4.2 and 4.3 are calculated at a standard redshift of 0.1. The K-corrections have been calculated using a modified version of the IDL routines described in Blanton & Roweis (2007). It is worth noting that, for the redshift limit of 0.1 that we chose, the average value of the K-correction is ≈ 0.1mag in all bands (see Fig. 15 of Blanton & Roweis (2007)).

4.2.1 Three samples of black hole hosts

We identify potential host galaxies of the SMBHs using three different approaches. The first two take advantage of the known correspondence between stellar mass in the spheroidal component of a galaxy and the embedded SMBH (e.g. McLure & Dunlop 2002; Marconi & Hunt 2003). The third one use an alternative approach based on emission lines (Greene & Ho 2005).

- **Sample A:** We apply a threshold in the global colour $u-r \geq 2.2$ (Strateva et al. 2001). This colour cut is expected to generate a spheroid dominated subsample of galaxies and is commonly used to generate a sample of AGN host galaxies. The total number of galaxies in this sample is $140,153$, or approximately 40% of the galaxies in the master sample. 6241 (5%) of these galaxies have a radio counterpart in the FIRST survey. *Sample A* is obviously biased toward red galaxies and will miss systems with an appreciable spheroidal

[1] One SDSS pixel is approximately $0.396''$.

component but whose global colours are altered by recent or ongoing star formation. For example, approximately 25% of all the brightest cluster galaxies, i.e. nearly all of the brightest cluster galaxies residing at the centres of cool-core clusters, have appreciably bluer cores due to ongoing star formation (Bildfell et al. 2008; Pipino et al. 2009) fuelled by the accumulation of cooling gas. Bluer than typical colours have also been observed in early type systems showing signs of star formation following recent minor mergers (Kaviraj et al. 2009; Kannappan et al. 2009) with gas rich companions, as well as in systems in which star formation has only recently been truncated (Nolan et al. 2007; Mahajan & Raychaudhury 2009). Such systems will be missed by colour-based studies (Mahajan & Raychaudhury 2009).

- **Sample B:** To capture the missing galaxies with appreciable spheroids that do not satisfy the colour cut for *Sample A*, we construct another sample of galaxies where we select spheroid-dominated galaxies using a morphological criterion. Given a strong correlation between the concentration parameter $C = R_{50}/R_{90}$, we extracted from our master sample all galaxies with $C \leq 0.33$ as is appropriate for early-type galaxies (Shimasaku et al. 2001). We apply a further selection criterion and require the galaxies to also have best-fitting Sersic index $n \geq 2.5$. Both C and n are computed from the surface brightness fits provided by Blanton et al. (2005). Our threshold value for the Sersic index is somewhat lower than normal because as Blanton et al. (2003) have shown, even for pure de Vaucouleurs profiles, the recovered index from these NYU-VAGC fits is 3.5 instead of 4. The total number of galaxies in *Sample B* is $142,649$, or approximately 40% of the galaxies in the master sample, and 6736 (5%) of these galaxies are matched with a radio counterpart in the FIRST survey.

- **Sample C:** The above two samples represent attempts to compile a sample of black hole hosts regardless of whether these BHs are dormant, active in the kinetic mode, and/or

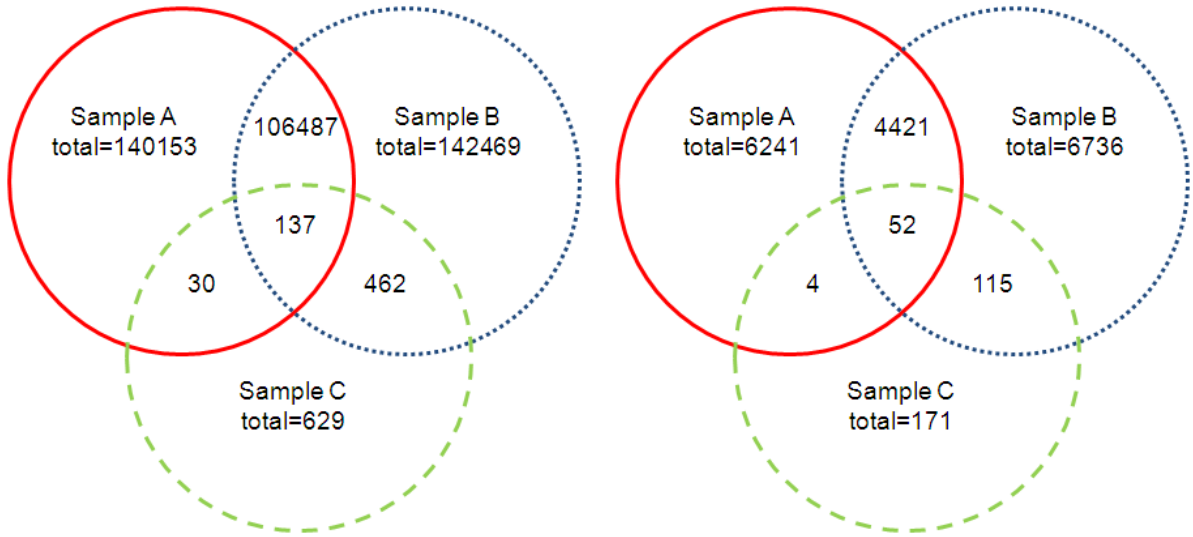

Figure 4.1: **Left panel:** The total number of galaxies in each of the three samples A, B & C used in this chapter is 140,153, 142,469 and 629 respectively. The Venn diagram shows the extent of overlap between the three. **Right panel:** Same as above, but only the galaxies that are matched with a 1.4 GHz radio source in the FIRST catalogue.

active in the optical mode. To construct our third sample, we change tack and look for systems that show evidence of AGN activity in the form of broad H_α emission line. To distinguish systems in which the H_α emission is due to AGN activity as opposed to start formation, we follow (Greene & Ho 2007) and require the H_α emission line to be such that FWHM$_{H_\alpha} \geq 1000$, equivalent width (EW) ≥ 30Å, and S/N > 10 in the relevant pixels. This last choice assures us that the detection of the H_α emission in the SDSS spectra is reliable. A value of the H_α EW≥ 30 Åis very rarely measured from star-forming galaxies (Kennicutt 1998) while the criterion of FWHM$_{H_\alpha} \geq 1000$ is chosen to specifically select broad line emitters (Greene & Ho 2007). We recognize that the use of criteria based on the H_α emission line will bias the sample in favour of host galaxies hosting optically active SMBHs. The total number of galaxies in *Sample C* is 629, or every one out of every 500 galaxies in our master sample. 171 (27%) of these galaxies have a radio counterpart in the FIRST survey.

Fig. 4.1 graphically summarises the relative numbers of galaxies in the three samples, and shows the extent of overlap between them. The left panel shows the total number of galaxies in each sample, as selected from the SDSS DR6 catalogue. The right panel shows the subset of each sample having a radio counterpart in the FIRST catalogue.

A comparison of the sample properties reveals several interesting features. The left panels of Fig. 4.2 shows the distribution of $g-r$ colour as a function of r-band absolute magnitude derived from SDSS photometry. The grey scale contours shows the properties of *all* galaxies in the SDSS NYU-VAGC catalogue that satisfy our redshift and magnitude cuts. The red contours show the distribution of galaxies in our Sample A (top row), Sample B (middle row) and Sample C (bottom row). Galaxies in these samples that are matched to 1.4 GHz sources in the FIRST catalogue are plotted in blue. The right panels show the associated histograms for $g-r$ colour: black solid curve traces the histogram for *all* galaxies, the red dashed lines map out the distribution for Samples A (top panel), B (middle panel) and C (bottom panel), and the blue dotted lines show the $g-r$ distribution of galaxies matched to a radio source.

As expected, the red sequence features prominently in the colour-magnitude plots for Sample A and B and overall, the galaxies in these samples span similar range in M_r: $-23 \leq M_r \leq -20$. The color-based Sample A, however, misses a substantial population of galaxies whose morphological parameters are consistent with early-type bulge-dominated galaxies but which do not have the red global colour normally expected of early-type galaxies, cfr. the numbers presented in figure 4.1. Not surprisingly, the host galaxies of radio loud AGNs in both samples share the overall characteristics of the underlying parent population from which they were drawn. Radio loud AGNs (from both Samples A and B) reside in high luminosity (high mass) systems ($-23 \leq M_r \leq -20.5$) that are on the redder ($\langle g-r \rangle \sim 0.95$).

The galaxies in Sample C, however, are very different. The host galaxies of the optically bright (optically active) AGNs are preferentially intermediate luminosities (and by extension, masses) ($-21 \leq M_r \leq -20$) and have bluer colour (a relatively flat colour distribution with

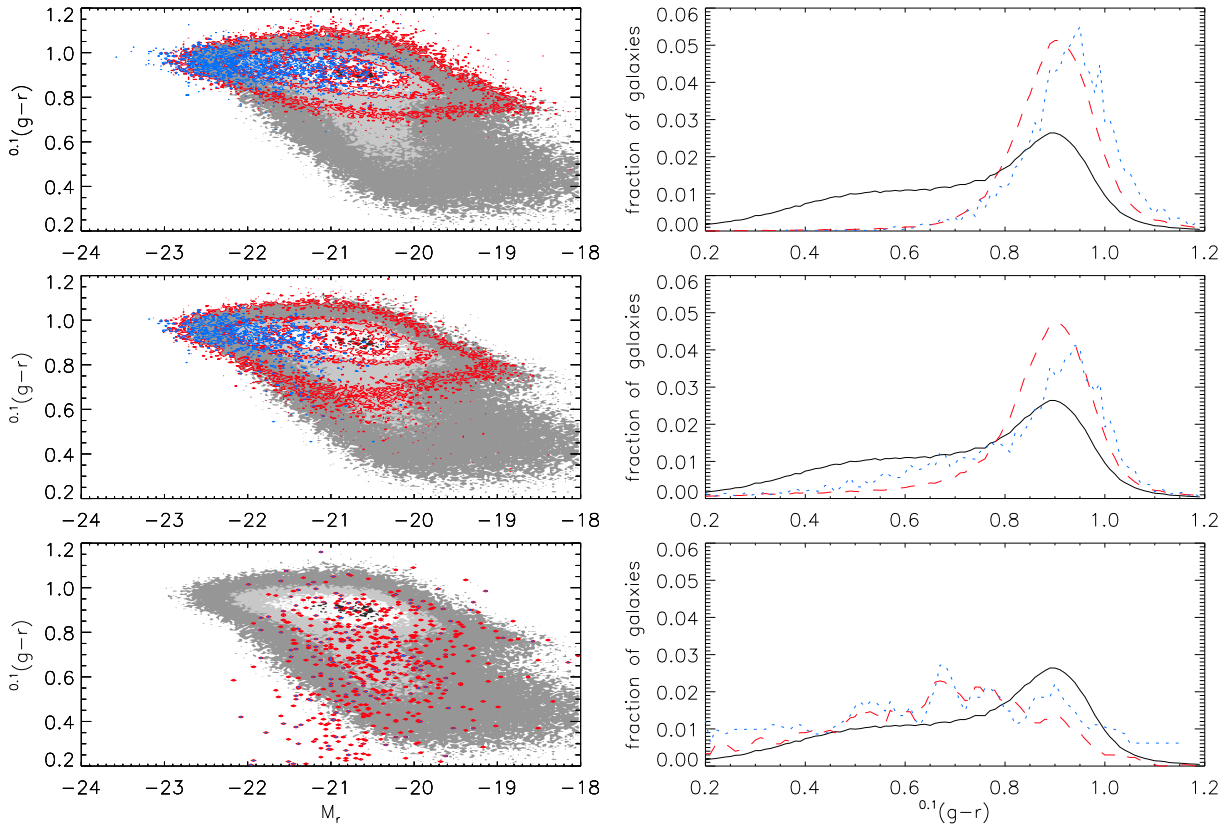

Figure 4.2: **Left panels**: $g-r$ colour plotted against the r-band absolute magnitude for (i) all the galaxies in the SDSS NYU-VAGC catalogue that satisfy our redshift and apparent magnitude limits (grey scale map in the top, middle and bottom panels), (ii) galaxies in Sample A (red contours in the top panel), Sample B (red contours in the middle panel) and Sample C (red contours in bottom panel), and (iii) galaxies in each of the samples with radio counterpart in the FIRST catalogue (blue contours). **Right panels**: The $g-r$ color distribution of (i) *all* galaxies (black solid curve in all three panels), (ii) galaxies in Samples A, B and C (red dashed curves in the top, middle and bottom panels respectively), and (iii) galaxies matched to radio sources (blue dotted curves). The contours in all lefthandside plots show the 25, 50 and 75 percentiles.

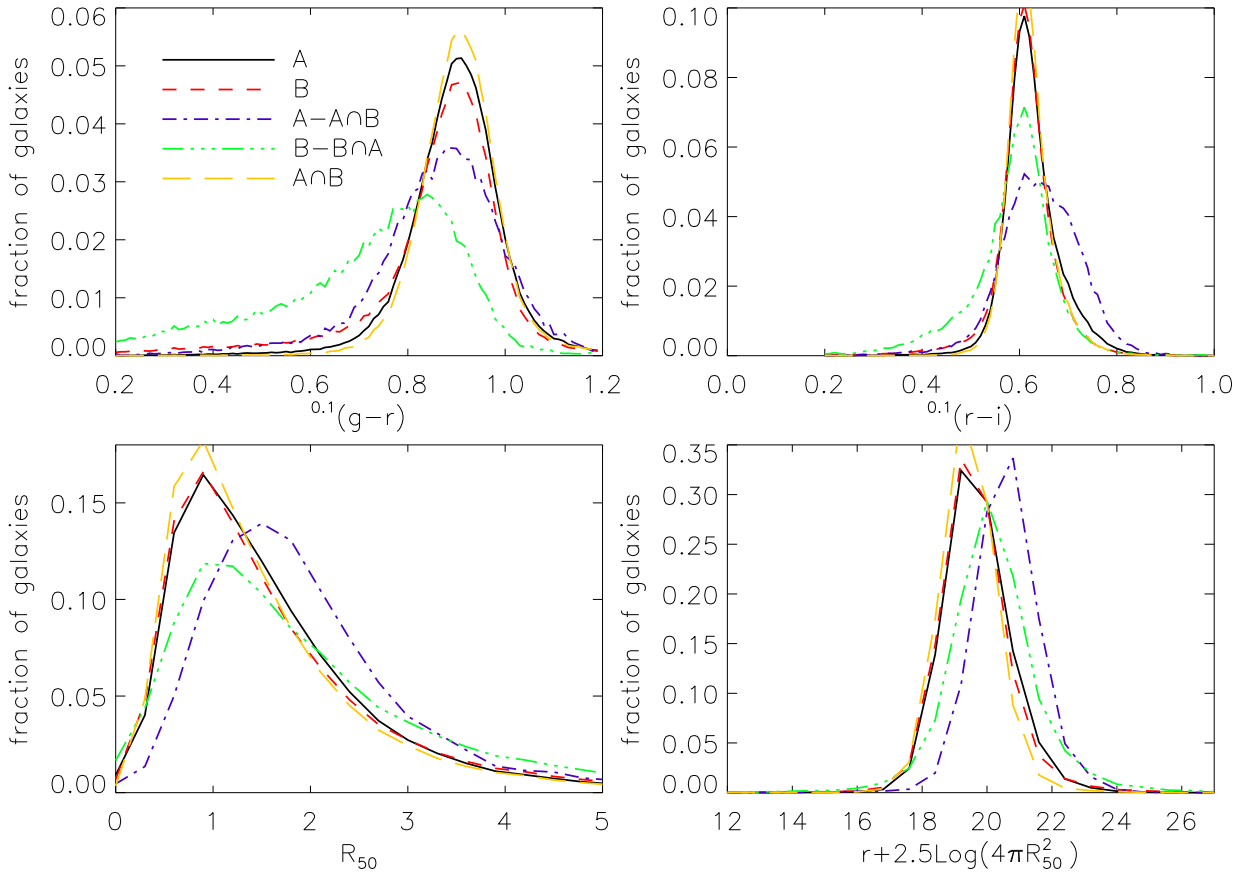

Figure 4.3: **Top row**: $g - r$ and $r - i$ colours for galaxies in sample A, B, and the various intersections among the samples. **Bottom row**: R_{50} and $r + 2.5\log(4\pi R_{50}^2)$ distributions for samples A, B and intersections. In all panels the lines are the same.

$g - r0.7$). Radio loud AGNs belonging to Sample C share the same features as the overall distribution.

4.2.2 Blue Ellipticals and Red Spirals

Looking at our samples, 4.1, we notice about $40,000$ galaxies in Sample B that are consistent with being early-types but whose colour is substantially bluer than $u-r \leq 2.2$. At the same time there about $40,000$ galaxies in Sample A which have red colour but not early-type morphology. We define the first class of objects, blue coloured and morphologically early-types, as $B-A\cap B$ and the second, red coloured but morphologically *not* early-types, as $A-A\cap B$. In figure 4.3 we compare these two classes of systems with Sample A and Sample B. For completeness on the plot is shows also the intersection $A \cap B$ between the two samples. In the top row we compare the fibre colours $g-r$ and $r-i$. As expected, the distributions have their maxima at $g-r = 0.9$ with the exception of $B - A \cap B$. In this case the distribution peaks at $g-r = 0.8$ and has a broad tail towards bluer colours. The $r-i$ distributions show the same behaviour. The bottom left panel in figure 4.3 shows the distributions of R_{50}, the radius enclosing 50% of the petrosian magnitude. The mode of the half-light radius distribution is $\approx 1''$ for all classes except for $A - A \cap B$ where it is $\approx 1.5''$. The bottom right panel shows a proxy for the surface brightness $r+2.5\log(4\pi R_{50}^2)$. This quantity is the apparent magnitude per square arcsecond. All classes of galaxies behave similarly except $A - A \cap B$ that has lower typical surface brightness compared to the other classes. This is the kind of behaviour that we would expect from an extended, disk-like object. In summary, we deduce that: (i) $B - A \cap B$ systems show bluer colours but morphological properties consistent with "normal" early-type galaxies; (ii) $A - A \cap B$ systems show colours consistent with early-type galaxies, but low surface brightness more typical of late-types. We are therefore tempted to identify galaxies in $B - A \cap B$ with early-types that are experiencing an active star-forming phase (Mahajan & Raychaudhury 2009; Kaviraj et al. 2009). At the same time we identify galaxies in $A - A \cap B$ with red, bulge-dominated spirals

of the kind observed in Masters et al. (2010).

4.2.3 Black Holes Hosts in Field, Group and Cluster Environments

To explore the variation of the BHMF as a function of host galaxy environment, we classify each of the optical galaxies in our three samples as *field*, *group* or *cluster* galaxy based on their local neighbourhood. We identify the neighbourhood as follows.

- **Rich Cluster Environment:** We start by identifying all the rich clusters in the Abell catalogue abell89 with redshifts $z \leq 0.1$ that are located in the area of the sky covered by SDSS DR6. We then classify an SDSS galaxy as a potential cluster member if it lies within a projected radius of $3\,h_{70}^{-1}$ Mpc of a cluster centre and within ± 3000 in velocity space. We then use the galaxies selected to belong to a given cluster to estimate the cluster's velocity dispersion $\sigma_{r,clus}$ as well as its overdensity radius r_{200} using the relationship

$$r_{200} = \frac{\sqrt{3}}{10}\frac{\sigma_r}{H(z)} \tag{4.2}$$

  from Carlberg et al. (1997). We use the derived velocity dispersion and r_{200} to revise the galaxy membership of each cluster. Specifically, the cut-off for the projected distance is updated to the newly calculated r_{200} and we require that the galaxy's radial velocity, $V_{r,gal}$, falls within the range $V_{r,clus} - 2\sigma_{r,clus} \leq V_{r,gal} \leq V_{r,clus} + 2\sigma_{r,clus}$, where $V_{r,clus}$ is the mean radial velocity of the cluster and $\sigma_{r,clus}$ is its radial velocity dispersion. We repeat the process and continue iterating until the value of $\sigma_{r,clus}$ remains unchanged to within 5%. In order to ensure that we are able to estimate the cluster velocity dispersion reliably, we do not consider further any cluster whose galaxy membership falls below 10. In the SDSS DR6 region, there are 314 Abell clusters with $z < 0.1$. The total number of clusters satisfying our "richness" requirement is 287. The $\sigma_{r,clus}$ distribution is shown on the left panel in Fig. 4.4. Of all the SDSS galaxies that satisfy our redshift and limiting

magnitude cuts, a total of $44,987$ (13%) are members of clusters that meet our richness criterion. Of the three samples we have constructed, $28,956$ galaxies (21%) from Sample A are cluster galaxies, $27,974$ (20%) of Sample B galaxies are cluster galaxies, and 65 Sample C galaxies (10%) are cluster galaxies. And of these, $1,358$ ($\sim$4%) of the Sample A systems, $1,362$ ($\sim$5%) of the Sample B systems, and 17 (26%) of the Sample C systems are radio loud.

- **Poor Group Environment:**

  To identify galaxies that are in groups, we start with a list of groups extracted from the Berlind (in preparation) group catalogue, which is itself derived from the SDSS DR7 catalogue. The total number of groups with $z < 0.1$ is $17,580$. We start by removing all "groups" lying within 3 Mpc in projected radius and 3000 in velocity space of any of the clusters defined as described in the previous paragraph. We then identify all galaxies within the projected distance of 1.5 Mpc of a group center as a putative group galaxy and retain only those groups for which there are at least 4 spectroscopically confirmed members. Our final list consists of $7,147$ groups.

  We use the same iterative scheme described previously to establish galaxy membership and the velocity dispersion of each of these groups. We compute the velocity dispersion $\sigma_{r,grp}$ in groups using the relationship

$$\sigma_{r,grp} = \sqrt{\frac{\sum_i (\nu_i - \overline{\nu})}{N - \frac{3}{2}}}, \tag{4.3}$$

  which gives a better estimate of the velocity dispersion when the number of galaxies is small (Osmond & Ponman 2004). We use the same relationship between r_{200} and σ_r to determine radius of the groups. In the case that a galaxy is placed in more than one group, membership is decided on the basis of the galaxy projected distance from each group centroid by selecting the host group as the one whose distance is smaller. The

$\sigma_{r,grp}$ distribution is shown on the right panel in Fig. 4.4.

Of *all* the SDSS galaxies that satisfy our redshift and limiting magnitude cuts, a total of $154,744$ (44%) reside in groups with more than 4 members. Group galaxies in our Sample A, B and C number $39,098$ (28%), $38,385$ (27%) and 116 (18%) respectively. And of these, $2,152$ (5%) of the Sample A group galaxies, $2,307$ (6%) of the Sample B group galaxies, and 32 (28%) of the Sample C group galaxies are radio loud.

- **Brightest Galaxies**

  For each of the groups and of the clusters we also identify the Brightest Cluster/Group Galaxies (BCG and BGG respectively). These are selected by taking the brightest galaxy in the r band within 0.25 r_{200}. We chose this distance threshold as $\sim$95% of all brightest galaxies in each association fall within this limit.

- **Field Environment:**

  We identify all galaxies that are not associated with groups or clusters as "field" systems. To ensure that our field sample is not contaminated by galaxies belonging to groups and clusters that fall below our richness threshold, we excluded all galaxies potentially associated with an Abell cluster or a Berlind group. This subset comprises $72,099(52\%)$, $76,110$ (53%) and 448 (71%) galaxies in Sample A, B and C respectively. Of these 2321 $(\sim 4\%)$, 2545 $(\sim 4\%)$ and 122 (27%) have radio counterparts identified with FIRST.

The present definition of "environment" cannot be considered a quantification of the effective density of galaxies. Richness based criteria like the ones used here can be thought as effective means of exploring the impact of the parent halo mass on the properties of the dwelling galaxies. The use of a better density estimator, such as Σ_5, is required in order to quantify what the dependence on the local density is on the relevant properties. Nevertheless, our subsamples are representative of different typical halo masses (see Fig. 4.4).

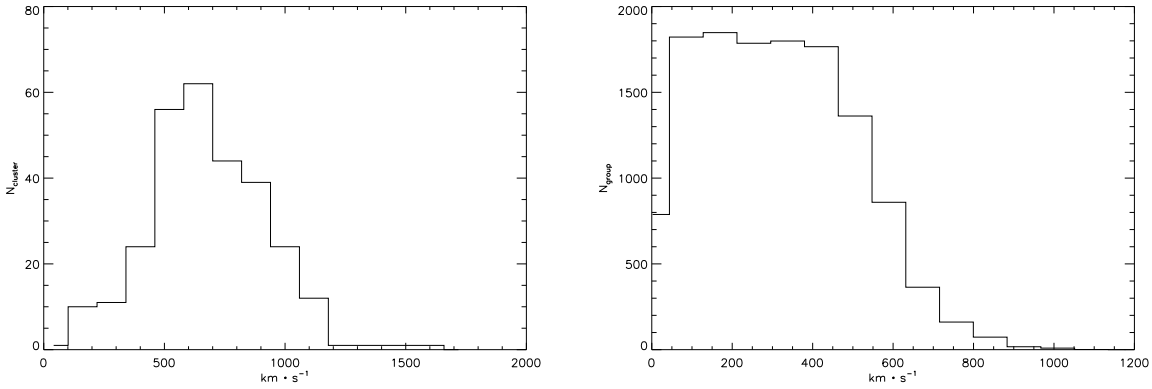

Figure 4.4: **Left panel:** $\sigma_{r,clus}$ distributions for the cluster in our sample. The single σ are obtained as described in the text. **Right panel:** Same as left, but for $\sigma_{r,grp}$.

4.3 The Supermassive Black Hole Mass Function

Having categorized the galaxies in our three samples as either cluster, group, or field galaxy, we now proceeded to determine the supermassive black hole mass function (SMBHMF) in these different environments. In order to do so, we first need to estimate the mass of the black holes hosted by the galaxies.

4.3.1 Black hole masses

For galaxies belonging to samples A and B, we derive the mass $M_\bullet$ of the embedded supermassive black hole using the following relationship between the K-band luminosity of the bulge and the black hole mass (Marconi & Hunt 2003):

$$\log\left(\frac{M_\bullet}{M_\odot}\right) = -(0.39 \pm 0.05)(M_K + 24) + (8.33 \pm 0.08), \tag{4.4}$$

where M_K is the K-band absolute magnitude of the system in question. The above relation is valid for E galaxies as well as for S0, and Sa/b with minor changes (e.g. Graham 2007) that are of minor relevance for our purposes here.

Nearly 70% of the galaxies in our samples have K-band photometry available from the

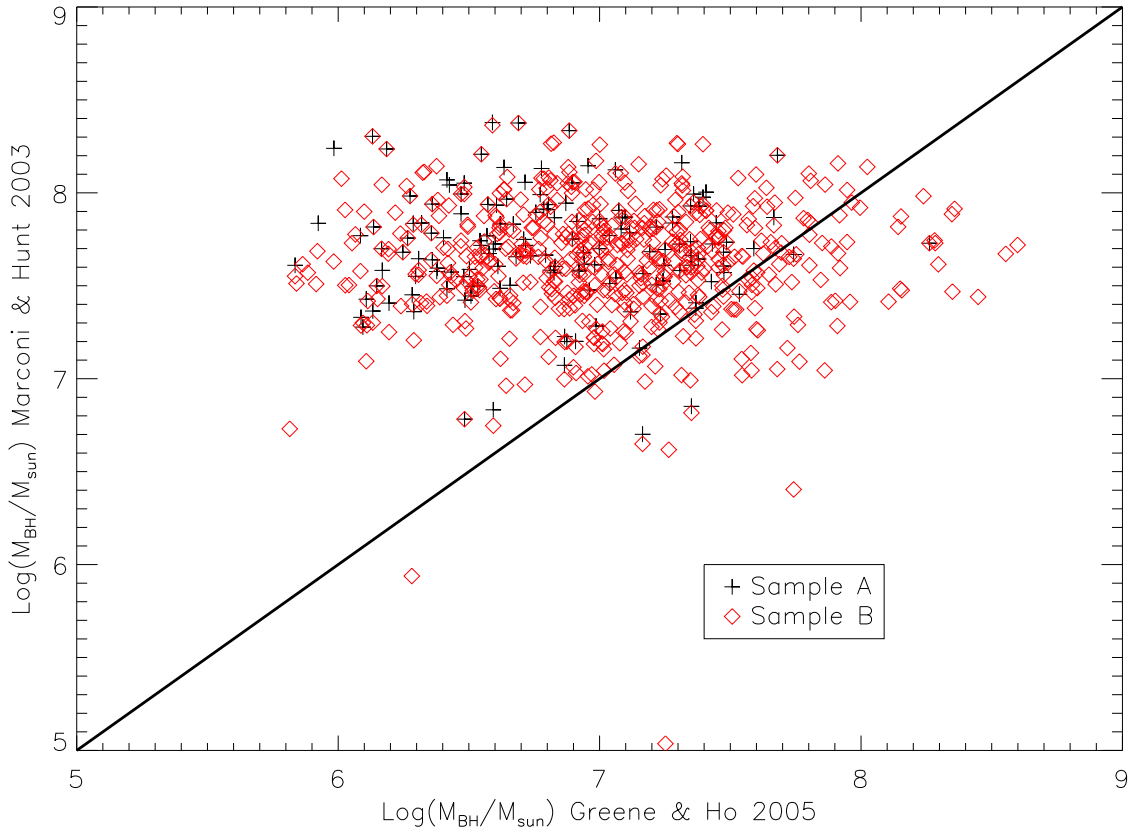

Figure 4.5: Comparison of $M_\bullet$ derived using the Greene-Ho approach based on width of the H_α emission line (see Eq. 4.7) and the Marconi-Hunt scheme based on the K-band luminosity (see Eq. 4.4) for all the objects in sample C. The black crosses are the galaxies at the intersection between sample A and sample C, while the red diamonds are the galaxies at the intersection between Sample B and sample C. The line represents equality.

2 micron all-sky survey(2MASS) (Cutri et al. 2003), which has a magnitude limit of $m_K \leq 13.5$. For the remaining galaxies, we estimated their K-band magnitude from their SDSS r-band magnitudes, using a conversion derived from the galaxies with both K-band and r-band photometry:

- Sample A : $M_K = (1.14 \pm 0.01)\, M_r + (1.80 \pm 0.03)$,
  $\langle M_K - M_r \rangle = -1.26$;
- sample B : $M_K = (1.09 \pm 0.01)\, M_r + (0.94 \pm 0.03)$,
  $\langle M_K - M_r \rangle = -1.19$;
- sample C : $M_K = (1.10 \pm 0.03)\, M_r + (0.97 \pm 0.58)$,
  $\langle M_K - M_r \rangle = -1.24$.

The optical r-band luminosity of the galaxy spheroid is calculated by directly integrating the best fitting Sersic profile from the optical photometry of Blanton et al. (2005)

$$I(r) = A \exp\left[-\left(\frac{r}{r_0}\right)^{1/n}\right], \tag{4.5}$$

yielding for the luminosity

$$L(r) = 2\pi A r_0^2 n \Gamma(2n-1). \tag{4.6}$$

For galaxies in Sample C, we can estimate the black hole mass $M_\bullet$ using the Marconi & Hunt (2003) relation (Eq. 4.4), or the width of the H_α emission line, as suggested by Greene & Ho (2005):

$$\frac{M_\bullet}{M_\odot} \approx 2 \times 10^6 \left(\frac{\mathrm{L}_{H_\alpha}}{10^{42} erg\ s^{-1}}\right)^{0.55} \left(\frac{\mathrm{FWHM}_{H_\alpha}}{10^3 \mathrm{km\ s^{-1}}}\right)^{2.06} \tag{4.7}$$

To use this relation, we de-redden the H_α fluxes using the approach described by Fitzpatrick (1999) before computing the L_{H_α} luminosity. In Fig. 4.5, we compare the black hole mass masses resulting from the two approaches. Surprisingly, there does not appear to be any corre-

lation between the two $M_\bullet$ estimates. The "Marconi-Hunt" masses are much more tightly distributed between $\sim 10^7$ and $\sim 10^8\ M_\odot$ while the "Greene-Ho" black hole masses span nearly three orders of magnitude. In the absence of an agreement, we chose to adopt the Marconi & Hunt (2003) relation both because it is more widely accepted and used and for consistency — the black hole masses for galaxies in Samples A and B are computed using the Marconi & Hunt (2003) scheme. Furthermore, the "Greene-Ho" relation is based on the assumption that the broad line region, where the lines are emitted, is in virial equilibrium (e.g. Kaspi et al. (2005)). This assumption allows to calculate $M_\bullet$ but might be regarded as simplistic. Neglecting radiation pressure, for instance, leads to systematic underestimates of $M_\bullet$ (e.g. Marconi et al. (2008)).

4.3.2 SMBHMF in different environments

Having estimated the BH masses for the galaxies in the three samples A, B and C, we now construct the SMBHMF in the field, group and cluster environments.

- **The Field SMBH Mass Function:** In Fig. 4.6, we show the SMBH mass function for black holes hosted by "field" galaxies as black curves. There are three curves corresponding to our three samples: Sample A, B and C. To account for the effect of the apparent magnitude limits used to define these subsamples, we used the V/V_{max} weighting method (Lynden-Bell 1971; Choloniewski 1987; Efstathiou et al. 1988) to compute the mass function. According to this formalism, the maximum volume out to which each galaxy would be included in our sample, given our flux limits, is calculated in order to compensate for the galaxies excluded by these limits.

  Samples A and B are defined solely by optical cut $r \leq 17.77$ applied to the SDSS catalogue and the associated V/V_{max} correction is straightforward. The V/V_{max} correction for Sample C requires a bit more of attention since we need to account for the additional

spectroscopic selection criterion that we applied, namely that the equivalent width of the H_α line EW$\geq 30\mathring{A}$. We consider the joint probability of detecting a galaxy whose r- band magnitude is ≤ 17.7 *and* whose EW is $\geq 30\mathring{A}$. We do this using the approach proposed by Schmidt et al. (1986), where the combined limiting magnitude is taken to be

$$m_{\rm lim} = r_{\rm lim} - 2.5 \log \left(\frac{\rm EW\,(1+z)}{\rm EW_{lim}} \right) + f\,(\lambda)\,, \tag{4.8}$$

where $f\,(\lambda)$ is a tabulated function given in Schmidt et al. (1986).

We calculate the uncertainty on the BHMF by generating 100 Monte Carlo samples of each $M_\bullet$, with a stochastic component consistent with the dispersion about the mean built-in to account for the intrinsic scatter of 0.3 dex in the $L_{bulge} - M_\bullet$ relation of Marconi & Hunt (2003). Since the number of galaxies is very large, particularly in Samples A and B, the resulting uncertainty is small except in the highest mass bins.

- **Group and Cluster SMBH Mass Function:**

  Fig. 4.6 also shows the composite SMBH mass function in groups and clusters (blue and red curves, respectively). The procedure used to construct the SMBHMF is that same as that described above. To correct for the incompleteness introduced by the magnitude limit, we made use of the V/V_{max} formalism, normalising to the fractional volume occupied by the clusters and groups compared to the whole SDSS volume. The factor of ~ 200 in normalization between the group/cluster SMBHMF and that in the field is due to the overdensity threshold of 200 that we used to define the radii of the groups/clusters. For completeness, we note that mass function for groups and clusters includes black holes hosted by the BGGs/BCGs. The plot of the SMBHMF excluding BGGs/BCGs is shown in Fig. 4.7. We also show, in the insert panel in Fig. 4.6, the distribution of black hole masses associated with the BGGs and BCGs. We note here that, regardless of the different selection criteria used to select galaxies, Sample A and Sample B SMBHMFs agree

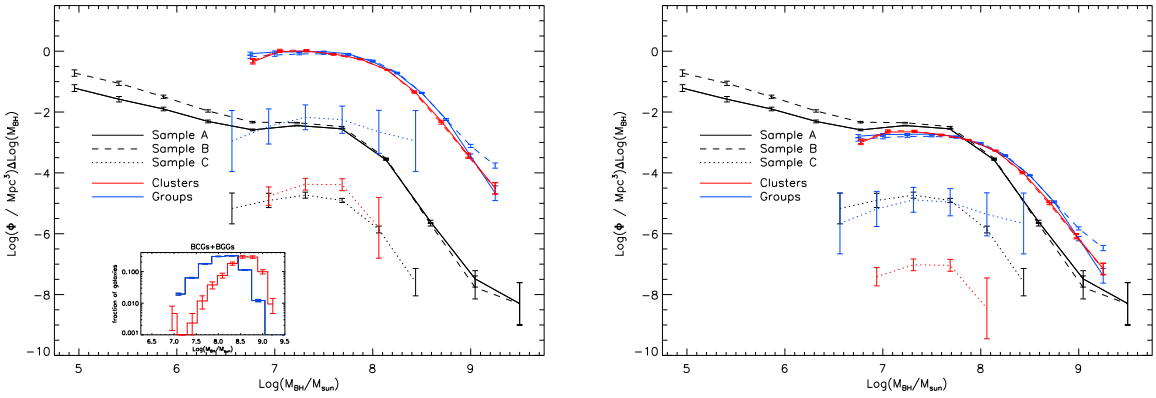

Figure 4.6: The supermassive black hole mass function (SMBHMF) for the three samples used in this work. The different line styles indicate the sample, as noted in the legend. For each sample, the field sample is plotted in black, the group sample in blue, and the cluster sample in red. In the left panel the SMBHMF are plotted taking into account the different normalizations between the SMBHMF in groups/clusters and in the field. This difference in normalization is due to the definition of r_{200} that enters in the calculation of V_{max} for the SMBHMF in groups/clusters. The right panel shows the same SMBHMF but without this additional normalization factor. In both panels, the SMBHMF for groups and clusters includes the BGGs and BCGs respectively. (We show the SMBHMF in groups and clusters computed by excluding BGGs/BCGs in Fig. 4.7.) The distribution of $M_\bullet$ in the BGGs/BCGs is shown in the insert in the left panel. There is no appreciable difference between the SMBHMF of galaxies in groups and in clusters identified in samples A and B (blue and red lines respectively). Very different is the situation for sample C. The density of SMBHs for optically active BHs in groups (blue dotted line) is *two* orders of magnitude higher than in clusters (red dotted line). The right plot shows the same SMBHMFs but without the overdensity renormalization to facilitate the comparison among different environments.

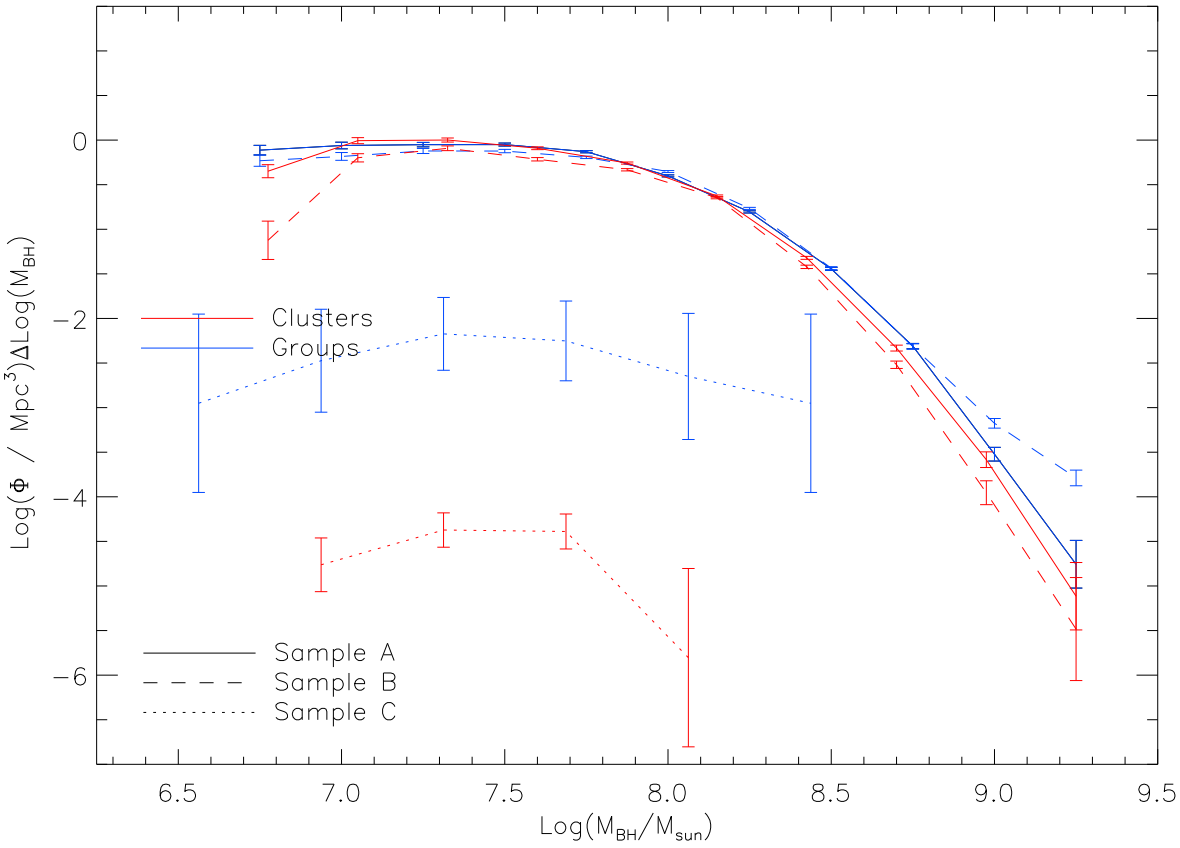

Figure 4.7: The SMBH mass function for groups (blue) and clusters (red) from sample A (solid line) and sample B(dashed line), where the black holes associated with the brightest group and cluster galaxies have been excluded. A comparison with Fig. 4.6 shows that the BHMFs do not depend on the presence/absence of the brightest galaxies: a Kolmogorov-Smirnov test confirms that the two mass functions are consistent with being drawn from the same underlying parent distribution.

very well in all environments. Differences emerge in the field MFs for $M_\bullet \leq 10^{6.5} M_\odot$. Below this mass the MFs are essentially dominated by the statistical corrections introduced by the V/V_{max} method. Therefore can not quantify the reliability of neither MFs below $M_\bullet \leq 10^{6.5} M_\odot$.

We discuss the above mass functions in the next section.

4.4 The environmental dependence of the black hole mass function

At a first glance, the SMBHMF behaves differently according to the environment. In the right panel in figure 4.6, we show the SMBHMF in the three environments under consideration. Differently from the left panel, the correction to V_{max} because of the volume of clusters/groups compared to DR6 is not taken into account. Without this additional normalization, all the curves overlap.

As a first step towards quantitatively discussing the SMBH mass function in the three environments under consideration, we attempt to characterize the distribution using a analytic functional form. Of different possibilities — a Schechter function, a lognormal function and a broken power law — the broken power law,

$$\Phi(M_\bullet) = \Phi_0 \left[\left(\frac{M_\bullet}{M_\bullet^*} \right)^{\alpha} + \left(\frac{M_\bullet}{M_\bullet^*} \right)^{\beta} \right]^{-1}, \tag{4.9}$$

is the most appropriate. We fit the derived mass functions for Samples A and B using two different thresholds: $M_\bullet \geq 10^7 M_\odot$ and $M_\bullet \geq 10^6 M_\odot$. The first cut corresponds to a mass threshold above which we expect the BHMF to be complete. The latter results are more likely to be affected by incompleteness and we present them with this caveat. We also provide a fit for the optically active SMBHMF. Those results are to be considered with precaution: the large errors on the group MF poorly constraint the fit that consequently is consistent with a constant MF. In the cluster case, the number of parameters is equal to the number of data points therefore our solution did not converge. The numbers presented in this case are the output of the last integration iteration before failure of the fitting algorithm. With those caveats, we present the results of our fits in Table 4.1.

Table 4.1: Best parameters for the broken power-law fit (Eq. 4.9) to various BHMFs. The fits for the clusters and groups Sample C are reported only for completeness as they are very poorly constrained, see text.

	Φ_0 (Mpc^{-3})	$M^*_\bullet/10^7 M_\odot$	α	β
Field A [$M_\bullet \geq 10^7 M_\odot$]	$(3.30 \pm 0.05) \times 10^{-3}$	8.3 ± 0.1	4.5 ± 0.1	0.16 ± 0.01
Field A [$M_\bullet \geq 10^6 M_\odot$]	$(3.70 \pm 0.05) \times 10^{-3}$	8.0 ± 0.1	4.5 ± 0.1	0.03 ± 0.01
Field B [$M_\bullet \geq 10^7 M_\odot$]	$(3.2 \pm 0.1) \times 10^{-3}$	8.7 ± 0.1	4.9 ± 0.1	0.22 ± 0.01
Field B [$M_\bullet \geq 10^6 M_\odot$]	$(3.1 \pm 0.1) \times 10^{-3}$	8.7 ± 0.6	4.9 ± 0.1	0.21 ± 0.01
Field C	$(1.0 \pm 0.6) \times 10^{-6}$	2.6 ± 0.2	1.5 ± 0.1	-0.4 ± 0.1
Cluster A	$(5.0 \pm 0.1) \times 10^{-1}$	13 ± 1	3.8 ± 0.1	0.18 ± 0.01
Cluster B	$(5.0 \pm 0.1) \times 10^{-1}$	12 ± 1	4.0 ± 0.1	-0.14 ± 0.02
Cluster C	$(1.0 \pm 0.3) \times 10^{-6}$	4.4 ± 0.7	4.1 ± 1.1	-1.1 ± 0.4
Group A	$(5.4 \pm 0.1) \times 10^{-1}$	14 ± 2	3.6 ± 0.1	0.23 ± 0.01
Group B	$(6.4 \pm 0.1) \times 10^{-1}$	13 ± 2	3.3 ± 0.2	0.05 ± 0.02
Group C	$(0.14 \pm 0.01) \times 10^{-3}$	2.3 ± 2.3	1.1 ± 0.8	-1.4 ± 1.0

4.4.1 SMBHMF in the field

The mass functions for field SMBHs derived from Samples A (color selection) and B (morphology selection) are qualitatively similar, and they also agree with results presented in previous studies. The mean BH mass density in the local Universe implied by our mass functions is $\rho_\bullet = (2.59 \pm 0.04) \times 10^5\, M_\odot$ Mpc^{-3} (Sample A) and $\rho_\bullet = (3.56 \pm 0.07) \times 10^5\, M_\odot$ Mpc^{-3} (Sample B). These numbers are also in reasonable agreement with values that have appeared in the literature: $\rho_\bullet \sim 4.6 \times 10^5\, M_\odot$ Mpc^{-3} (Marconi et al. 2004), $\rho_\bullet \sim 3.2 \times 10^5\, M_\odot$ Mpc^{-3} (Yu & Tremaine 2002), $\rho_\bullet \sim 2.9 \times 10^5\, M_\odot$ Mpc^{-3} (Aller & Richstone 2002) and $\rho_\bullet \sim 3.3 \times 10^5\, M_\odot$ Mpc^{-3} (Franceschini et al. 1998). We have scaled the cited results to our adopted cosmology.

The SMBHF for Sample C stands is stark contrast to those derived from Samples A and B. This is not a surprise given that Sample C comprises SMBHs that are optically active whereas Samples A and B encompass all supermassive blacks holes, whether they are optically active, radio-active or plain dormant. A straightforward comparison of the three mass functions suggests that typically 1 out of every 10^2 black holes in the Universe is optically active. The mass density of optically active SMBHs is $\rho_\bullet^{\rm active} = (55 \pm 12) M_\odot$ Mpc^{-3}. As we are likely missing

the more massive systems, this mass density estimate should be viewed as a lower limit.

4.4.2 SMBHMF in groups & clusters

Focusing first on Samples A and B, the SMBH masses in our group and cluster subsamples are primarily in the mass range: $6.5 \leq \log(M_\bullet/M_\odot) \leq 9.25$. An examination of the mass functions reveals that there is no appreciable difference between the group mass functions for Samples A and B, no appreciable difference between the cluster mass functions for Samples A and B, and no appreciable difference between the mass functions in groups and in clusters. Moreover, these results remain unchanged whether the brightest cluster/group galaxies are included or excluded, cfr. figure 4.6 and 4.7.

As discussed in section 4.2.3, we are defining the cluster or group environments according to parent halo mass rather than local galaxy density. Therefore, the observation that the SMBHMF is very similar in both environments could be a consequence of our definition. If clusters and groups have, on average, the same typical number density of galaxies and the growth history of a BH depends only on its neighbourhood, naturally the SMBHMF will be the same regardless of the parent halo mass. Therefore, we verified this conjecture by calculating both the average number density and the projected local density Σ_5 of galaxies in the two environments. Σ_5 has been calculated from the distance to the fifth nearest neighbour and assuming for each galaxy the cluster/group redshift. The results are shown in Figure 4.8. Group galaxies tend to live in denser environments, both globally and locally. As the group and cluster SMBHMF is very similar, to this level of detail we are incline to believe that the SMBHMF depends very weakly on the local density.

The black holes found in group and cluster environments are not outrightly more massive that those in the field as evidenced by the values of the characteristic masses: $M^*_\bullet \sim 1.3 \times 10^8 M_\odot$ in clusters and groups, and $M^*_\bullet \sim 8.5 \times 10^7 M_\odot$ in the field. These characteristic masses are equal within 3σ thus statistically their difference is marginally significant.

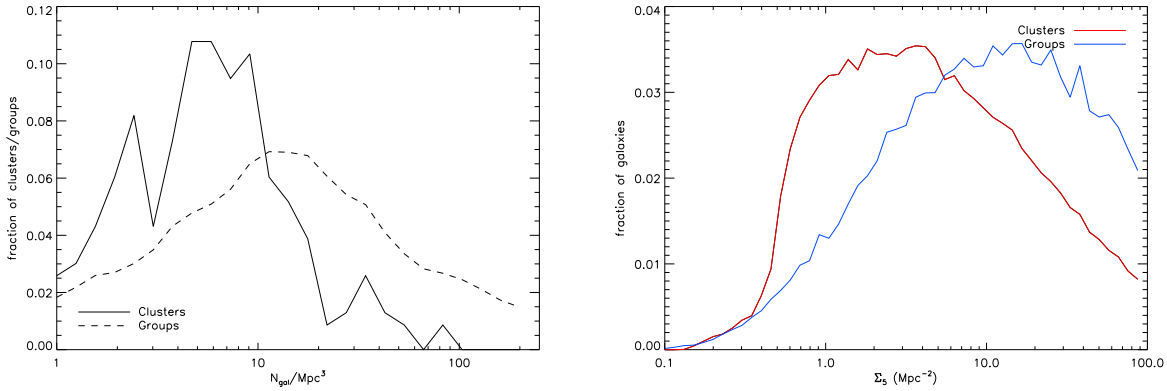

Figure 4.8: **Left panel:** average number density of galaxies in groups (dashed line) and clusters (solid line). **Right panel:** projected local densities, Σ_5, in groups (blue line) and clusters (red line). Groups appear denser both globally and locally.

The SMBHMFs are sensitive to the environment of their host galaxies. This argues against the view that a black hole's primary growth period occurs during the early phases of galaxy formation, before the external environment becomes established and impacts the galaxy's evolutionary trajectory. This is precisely what a number of semi-analytic models of structure formation (e.g. Lagos et al. 2008; Bower et al. 2006) indicate. The clusters/groups MF is biased toward higher masses compared to the field. This behaviour is consistent with the findings of Colberg & Di Matteo (2008). Using direct simulation to investigate the growth of BH seeds in a cosmological context, the authors report that the most massive BHs are preferentially found in overdensities. Our inactive SMBHMF qualitatively agrees with their predictions.

Turning to our mass function of optically active systems in groups and clusters, Sample C BHs are found preferentially in intermediate mass BHs, $10^{6.5} M_{\odot} \leq M_{\bullet} \leq 10^{8.5} M_{\odot}$ and equally common in the field and in groups of galaxies.

The scarcity of H_{α} emitters in the cluster environment is an interesting issue. Comparing the group and cluster SMBH mass functions for Samples A and B to that for group/cluster mass function for Sample C over the mass range $6.5 \leq \log\left(M_{\bullet}/M_{\odot}\right) \leq 8$, we note that roughly 1 in 10^4 black holes in clusters are optically active while 1 in 10^2 in groups. To the extent that we

can discern, this is consistent with the fraction of optically active AGNs in the field.

The scarcity of H_α emitters in the densest environments can have two possible origins: (a) ram pressure stripping (b) strangulation (McCarthy et al. 2008b). In fact, for an AGN to be an optical system, its accretion rate must be greater than $\sim 0.03\dot{M}_{Edd}$ (Narayan & Yi 1994). The reduced density of optically bright AGNs is then due to the absence of gas to be accreted. A galaxy infalling into the cluster gas might be stripped away of its gas, thus cutting the supply of fuel for the AGN. Even if the galaxy manages to retain its gas supply during the infall, this gas is consumed by star formation or optical AGN activity. Once the gas runs out, no further cold gas will be available as the hot intracluster gas cannot condense in the galaxy potential. Remarkably, H_α emitters in groups are far common than in clusters and the relative fraction between optically bright and optically dim BHs is the same as in the field environment. In other words, optically active quasars are not strongly suppressed in group environments. They are $\sim$ 100 times more likely to be optically active than a cluster BH of the same mass. This suggests that processes like ram pressure stripping may not be important for quenching AGN activity in groups. This is not entirely surprising. Typically a galaxy will be stripped only when it falls to the very center of the group and since the infall timescales are long, it is quite possible that AGNs may cease to be optically active well before ram pressure becomes important simply because all the available fuel has been consumed. Indeed the optical AGNs radial distribution, figure 4.9, is consistent with this picture. We note the absence of H_α emitters within $0.1r_{200}$ where stripping is important. Outside this radius, both in clusters, red histogram, and groups, blue histogram, optical AGNs are distributed approximately in an uniform manner. Furthermore, a KS test suggests that the two populations are drawn from the same parent distribution with a confidence level of 74%.

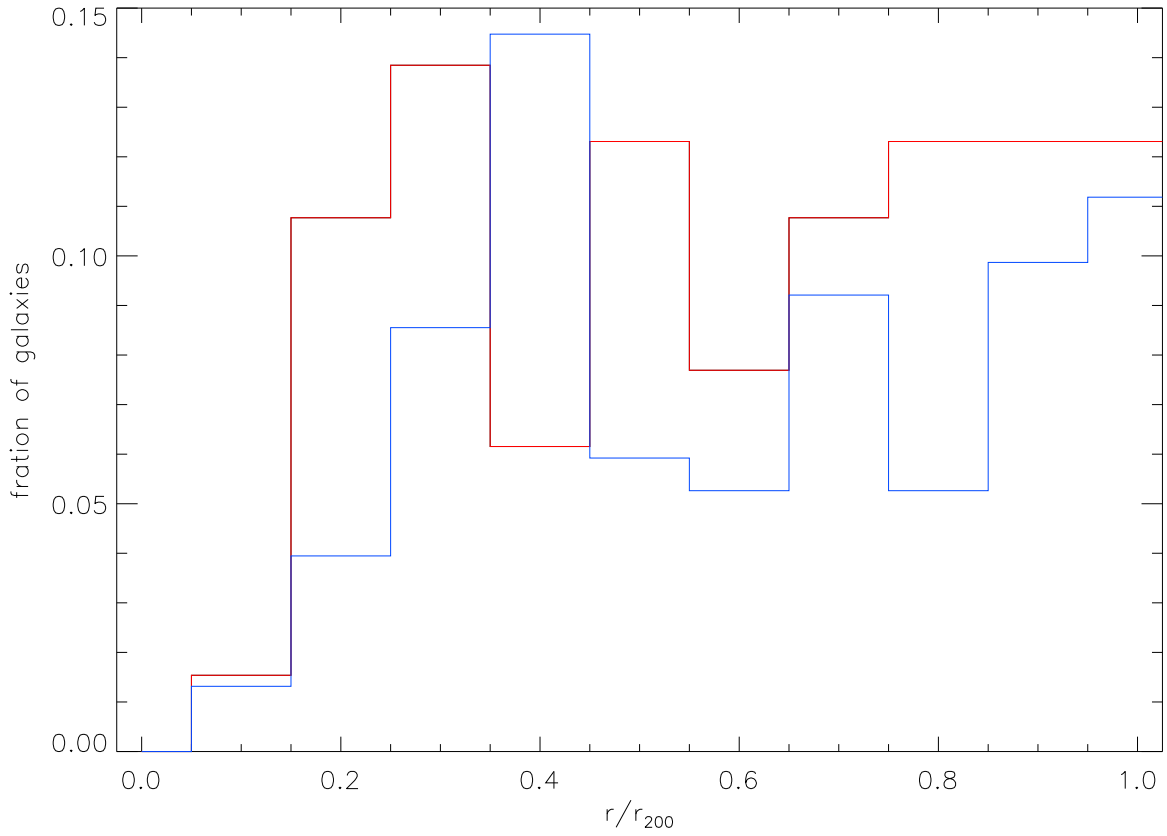

Figure 4.9: The radial distribution of H_α emitters in clusters, red histogram, and groups, blue histogram. A two tailed KS test implies that the two populations come from the same distribution with 74% confidence level.

Brightest galaxies

The small panel in figure 4.6 reveals an interesting feature. Brightest galaxies tend to be more massive in clusters than in groups. The modes of the two distributions are located at $M_\bullet \approx 10^8 M_\odot$ in groups and at $M_\bullet \approx 10^{8.5} M_\odot$ in clusters. This result could have been anticipated on the basis of the observed $M_{200} - M_{BCG}$ relation (e.g. Lin & Mohr 2007).

4.5 The relation between Black Hole mass and AGN activity

In this section we investigate the relation between $M_\bullet$ and AGN activity. We start by studying the correlation between the 1.4 GHz power and $M_\bullet$. We then devote our attention to the mass dependence of the Radio-Active Fraction (RAF) of galaxies as a function of $M_\bullet$.

4.5.1 The dependence of radio power on black hole mass

For the galaxies in our main sample, matched to radio sources in the FIRST 1.4 GHz catalogue, we checked for a possible correlation between their radio power and black hole mass $M_\bullet$. A simple least-squares fit gives:

$$P_{1.4\ GHz} = (16 \pm 6) \left(\frac{M_\bullet}{M_\odot} \right)^{0.8 \pm 0.3}, \tag{4.10}$$

where the uncertainties account for the large scatter in the data.

The dependence of radio power on $M_\bullet$ is a controversial issue. For instance, Franceschini et al. (1998) finds $P \propto M_\bullet^{2.5}$, Lacy et al. (2001) reports $L \propto M_\bullet^{1.9}$, but these findings are likely driven by limited statistics. Bigger samples, in fact, tend to indicate no correlation at all (Woo et al. 2005). Theoretical studies also disagree; for instance in Nemmen et al. (2007) scenario the jet power P scales as $\propto \dot{M}_{bondi} \sim M_\bullet^2$. Shabala et al. (2008) instead proposes a much weaker dependence, $P \propto M_\bullet^{0.7 \pm 0.5}$, consistent with (4.10).

As radio sources in dense environments tend to be more powerful than their field counterparts, we repeated the same study for galaxies in our groups and clusters catalogues. The correlation we find is completely consistent with (4.10).

4.5.2 The fraction of radio-loud AGN

The fraction of galaxies with radio-loud AGN (1.4 GHz radio power $P \geq 10^{23}$ W Hz^{-1}) is known as the radio active fraction (RAF). Best et al. (2005a) have determined this by matching SDSS-selected galaxies with the NVSS 1.4 GHz continuum survey (Condon et al. 1998). We repeat this exercise for our samples of galaxies, but use the FIRST survey instead.

There are important differences, between the NVSS and FIRST surveys, that are relevant to our study, even though both were conducted at $\lambda = 21$ cm with the Very Large Array. The FIRST survey, designed to coincide with the area of sky covered by the SDSS, goes fainter (source detection threshold of 1 mJy, as opposed to 2.5 mJy for NVSS), and the angular resolution is higher (beam of $5.4''$, as opposed to $45''$ for the NVSS). The higher resolution of FIRST means that it distinguishes small scale structures and yields accurate positions, bur underestimates flux for sources much larger than the beam (Kimball & Ivezić 2008). Hence, at the bright end, our radio luminosities are likely to be lower than those for the same sources picked by Best et al. (2005a). Indeed, for radio galaxies for which both NVSS and FIRST fluzes are present, about 30% of the fluxes from FIRST are found to be a factor of 3 lower than fluxes from NVSS. (Best et al. 2005b).

Fig. 4.10 shows the the fraction of radio-loud AGN (radio active fraction, RAF) for the "field" samples, as a function of black hole mass $M_\bullet$. On the plot the three samples A, B and C are represented by the asterisks, diamonds and triangles respectively. The squares on the same plot show the equivalent curve obtained by Best et al. (2005a) from NVSS matches, for comparison.

The radio active fractions (RAFs) we thus obtain for the field samples are in agreement with

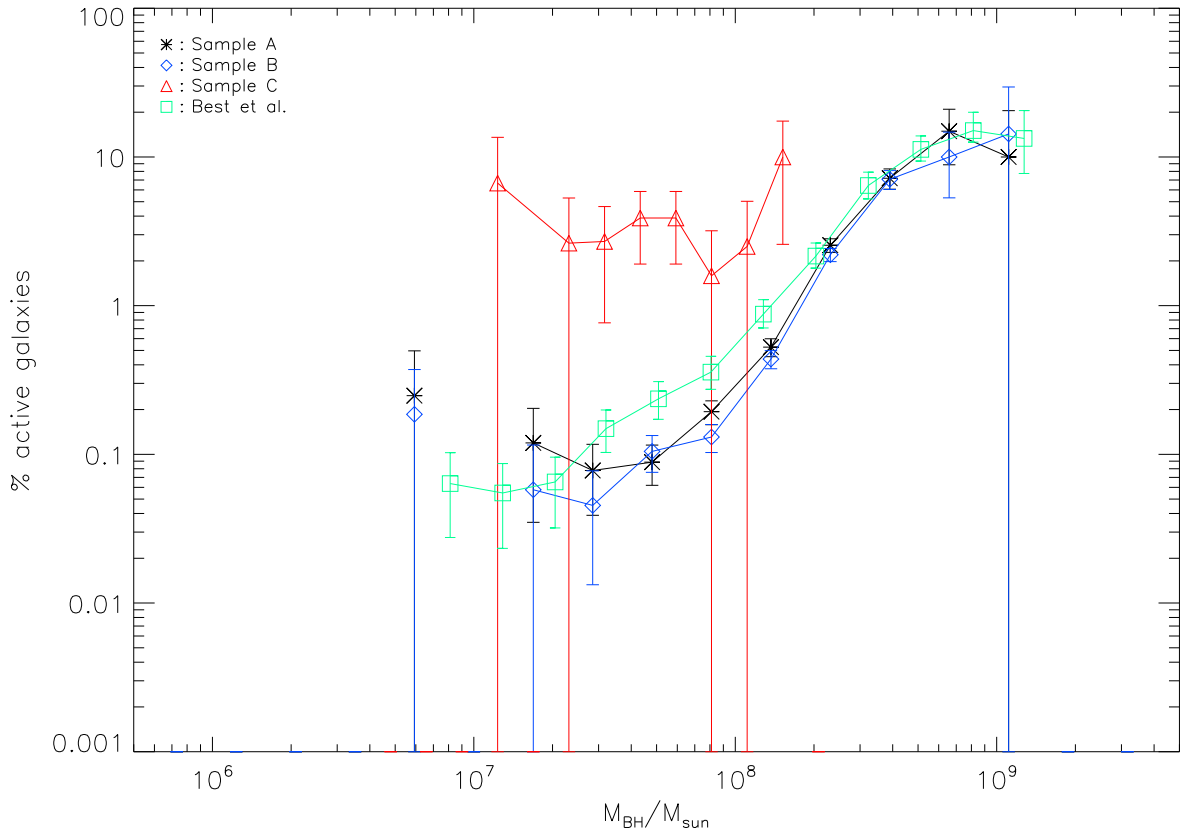

Figure 4.10: The fraction of radio-loud AGN (RAF, 1.4 GHz radio power $P \geq 10^{23}$ W Hz^{-1}) for the "field" samples, as a function of black hole mass $M_\bullet$. The various symbols represent: (i) black asterisks: Sample A, (ii) blue diamonds: Sample B, (iii) red triangles: Sample C, (iv) green squares, Best et al. (2005a). The latter use NVSS data.

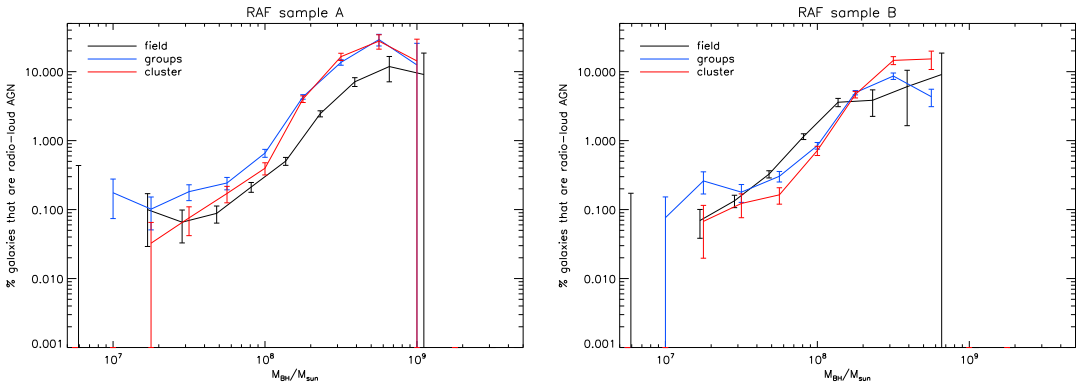

Figure 4.11: **Left:** The radio active fraction (RAF) for all galaxies in the cluster (red solid line) and group (blue solid line) subsample of our Sample A, as a function of black hole mass $M_\bullet$. At a given BH mass, group and cluster galaxies have a higher probability of being radio-loud compared to the field. The RAFs for the galaxies in clusters (red line) shows a stronger dependence on $M_\bullet$ than for galaxies in the field (black line) or groups (blue line). **Right:** The same for Sample B. In this case, per given BH mass, group and cluster galaxies have a slightly smaller probability of being radio-loud compared to the field. Nevertheless, the RAF is again steeper in clusters.

what already found by Best et al. (2005a) who found $f_{\rm radio-loud} \sim M_\bullet^{1.6}$. The best fits to our field RAFs are:

$$f^A_{\rm radio-loud} = 10^{-0.24\pm0.10}\left(\frac{M_\bullet}{10^8 M_\odot}\right)^{1.63\pm0.18} \quad (4.11)$$

$$f^B_{\rm radio-loud} = 10^{0.03\pm0.07}\left(\frac{M_\bullet}{10^8 M_\odot}\right)^{1.46\pm0.11}, \quad (4.12)$$

which, within the uncertainties, agree with Best et al. (2005a).

For the optically active Sample C, the RAF yields $f_{\rm radio-loud} \sim M_\bullet^{0.2\pm0.9}$, which is consistent with being constant.

Cluster and group environments

We calculated the RAFs of galaxies in our group and cluster samples and compared them to the galaxies in the field. These are shown for Samples A and B in Fig. 4.11. The RAFs are calculated excluding the BCG/BGG. Those are examined separately. Sample A galaxies have

Table 4.2: Summary of all power law fits of the RAFs relative to Samples A and B in the three environments.

	RAF
Field A	$10^{-0.24\pm0.10}\left(\frac{M_\bullet}{10^8 M_\odot}\right)^{1.63\pm0.18}$
Field B	$10^{0.03\pm0.07}\left(\frac{M_\bullet}{10^8 M_\odot}\right)^{1.46\pm0.11}$
Cluster A	$10^{-0.20\pm0.04}\left(\frac{M_\bullet}{10^8 M_\odot}\right)^{2.23\pm0.07}$
Cluster B	$10^{-0.20\pm0.07}\left(\frac{M_\bullet}{10^8 M_\odot}\right)^{2.53\pm0.02}$
Group A	$10^{-0.02\pm0.08}\left(\frac{M_\bullet}{10^8 M_\odot}\right)^{1.68\pm0.22}$
Group B	$10^{-0.19\pm0.17}\left(\frac{M_\bullet}{10^8 M_\odot}\right)^{1.27\pm0.33}$

a higher probability of being radio-loud per $M_\bullet$ bin compared to field galaxies. On the contrary Sample B galaxies have a comparable, or slightly smaller, probability compared to field galaxies. In both panels, the cluster RAF, red curves, shows a stronger dependence on $M_\bullet$ than both the group and field RAF. Analytic fits for the RAFs both for samples A and B are summarized in Table 4.2. Cluster galaxies indeed show an increased RAF. The average dependence on $M_\bullet$ for field and group galaxies is in fact $f_{\rm radio-loud} \sim M_\bullet^{1.5}$, while cluster galaxies obey to $f_{\rm radio-loud} \sim M_\bullet^{2.3}$. We examine the possible reasons for this different behaviour in 4.7.

The stronger dependence on $M_\bullet$ of the RAF in clusters of galaxies might be due to an explicit effect of the size dependence of FIRST fluxes Radio sources in dense environments are known to be smaller on average (Feretti & Giovannini 1994). If this is the case, the same source observed by FIRST and NVSS should measure a higher flux in the first case because of FIRST smaller beam size. We tested this hypothesis by evaluating the FIRST bias with respect to NVSS in the field and cluster environments. We do not find any difference in the two cases. We therefore conclude that our results are robust in this respect and are not an artefact of the particular nature of the survey used.

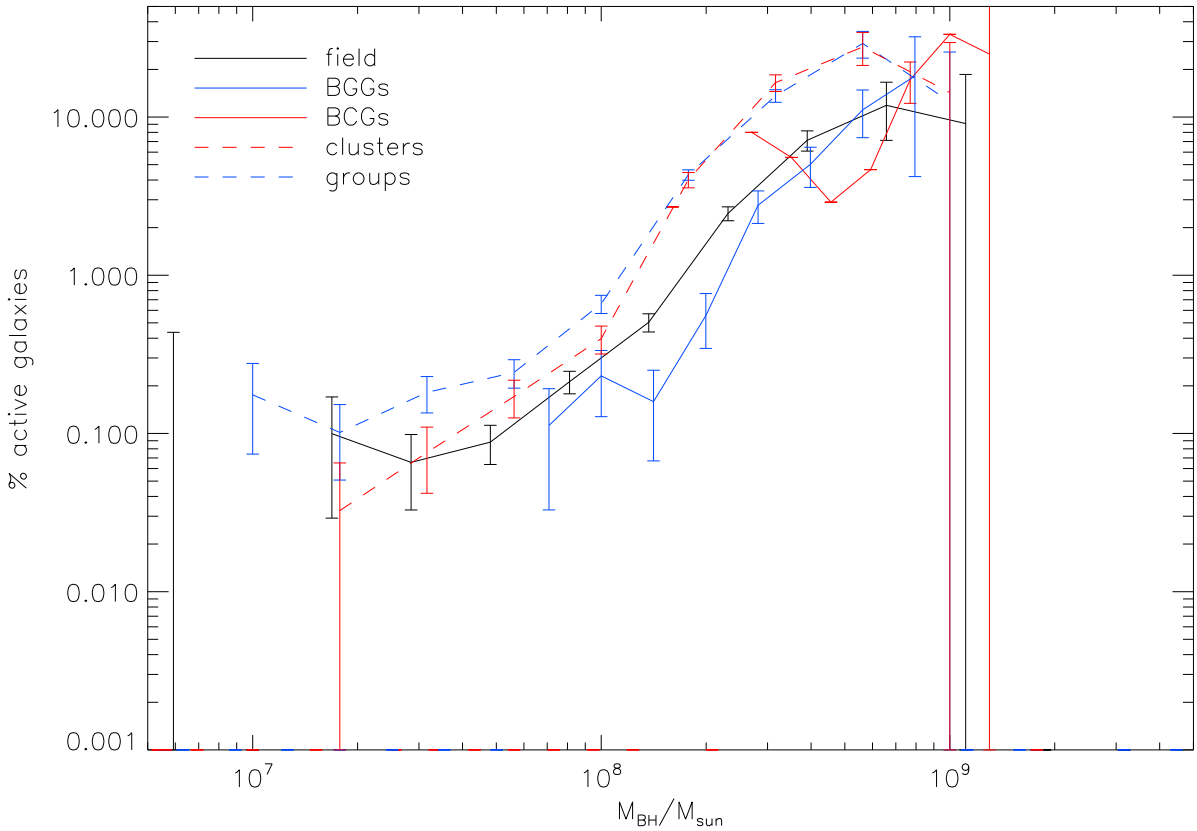

Figure 4.12: The radio active fraction (RAF) of brightest cluster (red solid line) and group (blue solid line) galaxies, as a function of black hole mass $M_\bullet$, compared to the RAF for the field (black) and for all galaxies in clusters (dashed red line) and groups (dashed blue line). This comparison is shown for galaxies in Sample A, which should be more complete at the brighter end for early-type galaxies. BCGs/BGGs have probabilities of being radio-loud that are comparable to field galaxies.

4.5.3 The brightest galaxies in clusters and groups

We evaluated the RAFs for the brightest galaxies in the clusters and groups in our samples (BCGs and BGGs) alone, shown in Fig. 4.12. Central galaxies have similar probability of being radio-loud compared to field galaxies. We also find that $f_{\rm radio-loud} \propto M_\bullet^{1.5}$ in both cases, even if the BCG result should be taken with care given the oscillatory nature of the data.

Previous studies (Croft et al. 2007; von der Linden et al. 2007) found that the probability of a central galaxy to be radio-loud is higher compared to that of a field galaxy. This enhancement in the RAF was found to be higher for lower stellar masses. We do not see this increase in Fig. 4.12.

Given our observations, we are conclude that the cluster environment increases the RAF only for the non-central galaxies, while the BCGs/BGGs follow the field trend. The substantial fraction of radio-loud central galaxies (e.g. Burns 1990) is then not due to the special environment where they live, but to their high $M_\bullet$.

4.6 X-ray Luminous AGN

The existence of a fundamental plane between measurable properties of black holes, across the electromagnetic spectrum (e.g. Heinz & Sunyaev 2003; Merloni et al. 2003; Falcke et al. 2004), allows us to find a relation between the radio and X-ray luminosities of the nuclei of the galaxies in our sample. For low-power AGN assuming that distinctly sub-Eddington BHs are jet-dominated (as opposed to near-Eddington BHs, which are disk-dominated), Falcke et al. (2004) suggests

$$L_X \propto L_R^m M_\bullet^{\alpha_X - m\alpha_R} \tag{4.13}$$

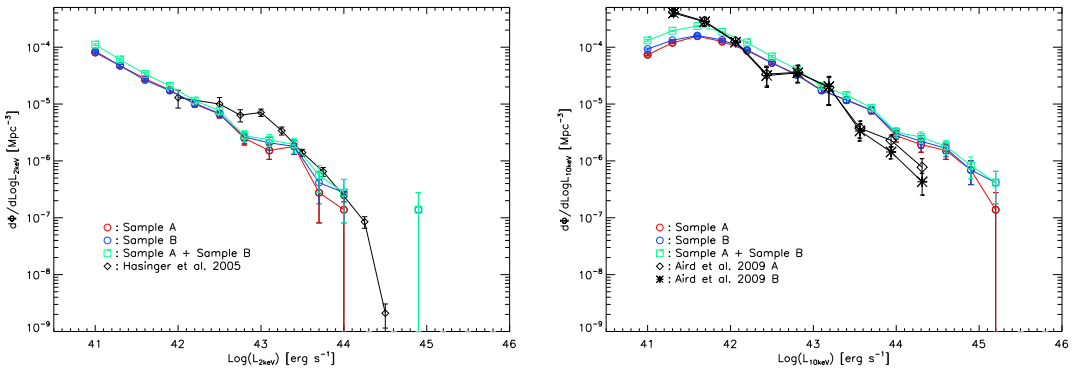

Figure 4.13: **Left:** The X-ray 0.5–2 keV luminosity function (XLF) of AGN in galaxies belonging to Sample A (red), Sample B (blue) and Sample A+Sample B (green) where the intersection between the two samples has been removed from Sample B. The X-ray luminosities are calculated from the optical properties of the AGN employing a series of scaling relations discussed in the §4.6. These predicted luminosity functions are compared with the observed luminosity function (black) of X-ray bright AGN in deep X-ray surveys (Hasinger et al. 2005). **Right:** The X-ray 2–10 keV luminosity function (XLF) for the same samples as in the left panel, compared to the observed XLF from Aird et al. (2009): open diamonds corresponding to their LDDE model, while the black asterisks correspond to their LADE model.

where $\alpha_X \simeq -0.6$ and $\alpha_R \simeq 0.15$ are typical values for the optically thin and optically thick spectral indices. The value of the coefficient m is

$$m = \frac{\frac{17}{12} - \frac{2}{3}\alpha_X}{\frac{17}{12} - \frac{2}{3}\alpha_R} \tag{4.14}$$

(e.g. Markoff et al. 2003). Observationally such a relation has been shown to work, albeit with a large scatter (e.g. Gültekin et al. 2009). We use Eq. (4.13) to assign a 0.2–2 keV X-ray luminosity to each of our radio detected BHs.

After assigning 0.2–2 keV luminosity to each BH in sample A, B and C(using Eq. 4.13), we constructed an X-ray luminosity function (XLF) at 0.2–2 keV for the BHs in our samples (Figs. 4.13 and 4.14). We compare this predicted XLF to the observed XLF of point sources from various surveys conducted in different energy ranges:

1. **Comparison with Hasinger et al. (0.2-2 keV):** From deep X-ray surveys at various parts

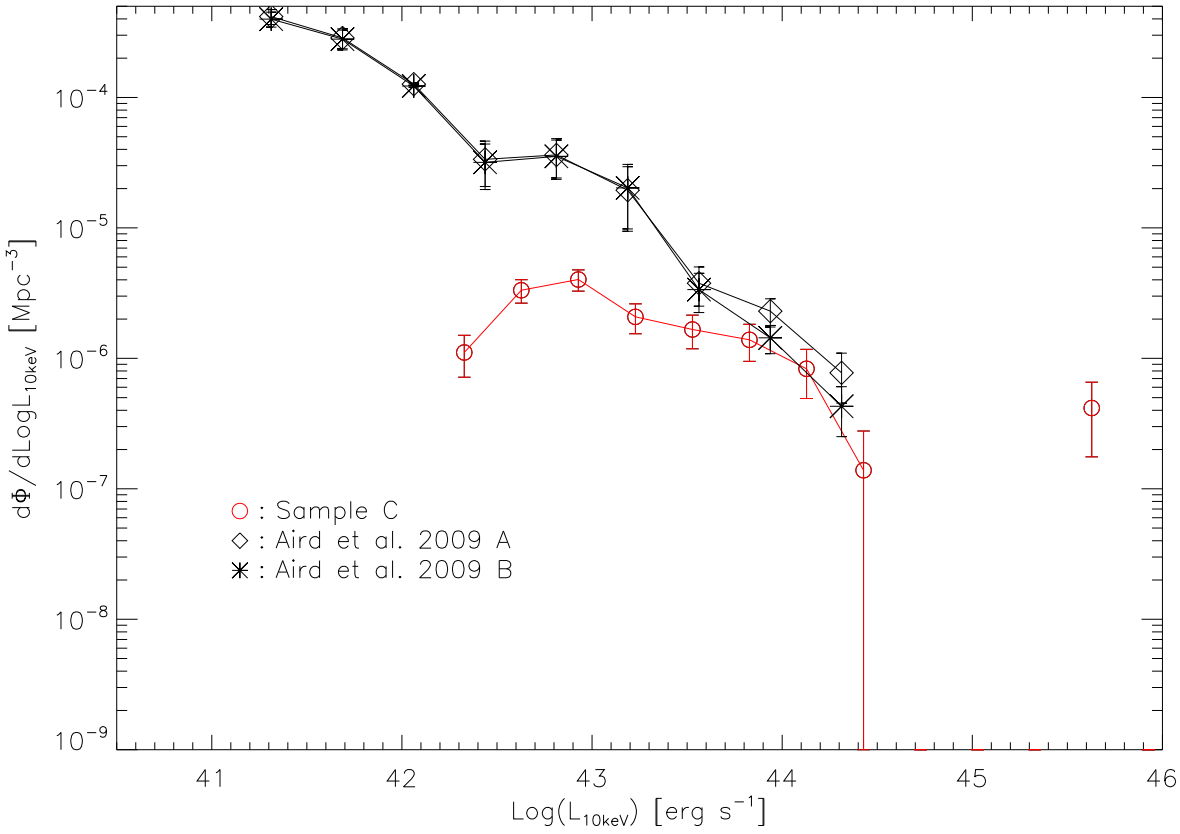

Figure 4.14: The XLF in the 2–10 keV band from Sample C (red). This is compared with the observed XLF from Aird et al. (2009): open diamonds corresponding to their LDDE model, while the black asterisks correspond to their LADE model. Sample C galaxies populate the bright end of the XLF.

of the sky, Hasinger et al. (2005) have compiled a luminosity function of flux limited X-ray point sources, mostly representing AGNs. the 0.2–2 keV energy range. This is plotted as the black curve in the left panel of Fig. 4.13. Despite the inherent scatter in the series of relations we used to derive X-ray luminosities from BH mass, our predicted luminosity function compares well with the observed XLF.

2. **Comparison with Aird et al. (2-10 keV):** It has been pointed out, from large multiwavelength surveys such as the GOODS field, that a significant fraction of AGN are obscured, even in the soft X-rays (e.g. Treister et al. 2009). Thus the soft X-ray energy range might not be ideal for such a comparison. We therefore repeat the above exercise, computing the 2–10 keV XLF, from the 0.2–2 keV values obtained above, assuming a spectral slope of 1.9 (Aird et al. 2009). These values are plotted in the right panel of Fig. 4.13, for the samples A, B and Fig. 4.14 for sample C. The total luminosity function obtained from summing sample A and sample B is shown in purple. In the summation, galaxies in their intersection have been counted only once.

   The black points in the right panel of Fig. 4.13 represent the 2–10 keV luminosities of observed AGN from the deep Chandra survey of the AEGIS field (Aird et al. 2009) ($z < 0.2$). The open diamonds correspond to their luminosity-dependent density evolution (LDDE) model, while the black asterisks correspond to their luminosity and density evolution (LADE) model. Starting from a model of luminosity evolution, modelled as a power law with L_* changing with redshift, the LDDE and LADE models differ by the nature of the evolutionary corrections to the luminosity function. In the former, this correction is both redshift and luminosity dependent, while in the LADE model, only the normalization constant varies with the redshift. Fig. 4.13 shows excellent agreement, between this observed sample and our modelled values, except at the very faint end where the discrepancy can be accounted for by not having applied any completeness correction. We emphasise that in obtaining the modelled XLF, we do not apply any arbitrary normal-

isation, so here we are reproducing the observed XLF in both slope and in normalisation. Interestingly, Sample C accounts for the very bright end of the XLF.

3. **Comparison with Martini et al. (0.5-8 keV):** Instead of determining the XLF, Martini et al. (2007) and Sivakoff et al. (2008) find the the average fraction of galaxies, in their sample of clusters and groups, that are optically brighter than absolute magnitude $R < -20$ and more luminous in 0.5–8 keV X-rays than 10^{41} erg s^{-1} to be $f\,(R < -20,$ $L_X > 10^{41}$ erg s^{-1}) $= 5 \pm 1.5\%$. For sources brighter than 10^{42} erg s^{-1}, the corresponding fraction is $f\,(R < -20,\, L_X > 10^{42}$ erg s^{-1}) $\simeq 1\%$.

   In order to directly compare, we convert our estimated 0.2–2 keV X-ray luminosities to their energy range (0.5–8 keV), by assuming a hard X-ray spectral index of 1.9 (Aird et al. 2009). Our estimates for the corresponding average fraction of X-ray luminous AGN at 0.5–8 keV are: $f\,(R < -20,\, L_X > 10^{41}$ erg s^{-1}) $= 3.4 \pm 0.1\%$, and $f\,(R < -20,$ $L_X > 10^{42}$ erg s^{-1}) $= 1.3 \pm 0.1\%$, where the uncertainties account only for the Poisson errors. These are very similar to the Martini et al. (2007) observations.

   The corresponding X-ray active fractions for galaxies in groups from our sample are also similar: $f\,(R < -20,\, L_X > 10^{41}$ erg s^{-1}) $= 3.8 \pm 0.1\%$, and $f\,(R < -20,\, L_X > 10^{42}$ erg s^{-1}) $= 1.5 \pm 0.1\%$.

4.7 Discussion

Semi-analytical cosmological simulations show that SMBHs grow mostly because of dynamical instabilities inside the host galaxy (e.g. Lagos et al. 2008; Bower et al. 2006). This observation predicts that the SMBHMF should vary very little with the environment. This is in contrast with results from direct simulation of BH growth in cosmological context (Colberg & Di Matteo 2008) where massive BHs are preferentially found in dense environments. Fig. 4.6 shows that groups and clusters host a population of BHs that is more massive than the field environment.

This picture is also confirmed by the characteristic value of $M^*_\bullet$, $\sim 8.5 \times 10^7 M_\odot$ in the field and $\sim 1.2 \times 10^8 M^*_\odot$ in groups and clusters. Furthermore, it is well known that most massive systems are highly clustered. This is reflected, for instance, in the Luminosity Function of early-type galaxies that in clusters is brighter than its field counterpart (e.g. De Propris et al. 2003). So it is not surprising to find more massive BHs in dense environments. At the same time, clustering could be the explanation of the absence of low mass BHs in clusters and groups. Nevertheless, in the context of volume-limited surveys like the ones considered in this work, the probability of detecting very faint objects (low mass BHs) is a strong function of the volume under consideration. Therefore we are inclined to attribute the absence of low $M_\bullet$ in cluster or groups environments to selection effects related to the small volume that these objects occupy compared to the whole survey volume.

If, as Colberg & Di Matteo (2008) suggest, the high concentration of massive BHs in dense environment is due to enhanced accretion rates, looking in those environments we should register an increased level of AGN activity compared to lesser overdensities. This is indeed shown in figure 4.11: at a given $M_\bullet$, BHs in red galaxies (Sample A) are twice as likely to be radio galaxies compared to the field. At the same time, morphologically selected galaxies (Sample B) (that are not necessarily red, cfr. 4.2.2) have the same probability as field galaxies to be radio-loud. Given that Sample B systems could be substantially bluer than Sample A, we are tempted to conclude that the reduced RAF in the former case is due to star-formation that, for a fixed amount of gas condensing onto the host galaxy, deprives the central SMBH of its fuel.

Turning to the optically active BHMF (Sample C), we are affected by low number statistics. As such, the results relative to Sample C presented in table 4.1 should be treated with extreme caution. Nevertheless, from a comparison among the SMBHFs in the three environments, we can derive some important facts. In general, roughly 1 out of every 10^2 BHs in the Universe is optically active. This is also the fraction of optically active BHs in groups. Turning to clusters, this fraction goes down by a factor of at least a 100. Furthermore, a comparison between the

active and inactive MFs gives a very rough estimate of the duty cycle t_{duty} of optical AGNs in the different environments:

- field: $t_{duty} \approx \times 10^8$ yr;
- groups: $t_{duty} \approx \times 10^8$ yr;
- clusters: $t_{duty} \approx \times 10^6$ yr.

The field and groups figures are not unreasonable.

Sample C BHs live in mid-sized galaxies and, as such, they are, in principle, deeply affected by ram pressure stripping and strangulation. Ram pressure stripping is mostly efficient in the cores of clusters where the Intra Cluster Medium (ICM) density is higher. Indeed, no optical AGNs are found within $0.1r_{200}$, cfr. Fig. 4.9. In the same figure, we also note that in groups as well no optical AGN is found within the same radius. Ram pressure stripping is just as important in the cores of groups. So why do groups and clusters show such difference in the density of optically active systems? The most reasonable explanation is the different efficiency of ram pressure in stripping the gas from a galaxy. For ram pressure to have an impact, this condition must be met

$$P_{\rm ram} \sim \rho_{\rm ICM} v_{\rm gal}^2 > \sigma^2 \rho_{\rm gas}/3, \tag{4.15}$$

where $v_{\rm gal}$ is the galaxy orbital velocity, $\rho_{\rm ICM}$ is the ICM density and σ and ρ_{gas} are the galaxy velocity dispersion and gas density respectively. For a given galaxy (and central BH), the ratio of $P_{\rm ram}$ in a group and a cluster is given by

$$\frac{P_{\rm ram}^{GR}}{P_{\rm ram}^{CL}} \sim \frac{\rho_{\rm ICM}^{GR} v_{GR}^2}{\rho_{\rm ICM}^{CL} v_{CL}^2}. \tag{4.16}$$

Roughly $\rho_{\rm ICM} \sim M/R^3$ and the orbital velocity $v^2 \sim M/R$. Substituting, we have

$$\frac{P_{\rm ram}^{GR}}{P_{\rm ram}^{CL}} \sim \left(\frac{M_{GR}}{M_{CL}}\right)^2 \left(\frac{R_{GR}}{R_{CL}}\right)^4 \tag{4.17}$$

Typical values are $M_{GR} \sim 10^{14} M_{\odot}$, $M_{CL} \sim 10^{15} M_{\odot}$, $R_{GR} \sim 1.5$ Mpc and $R_{CL} \sim 2$ Mpc. These numbers imply that

$$\frac{P_{\rm ram}^{GR}}{P_{\rm ram}^{CL}} \sim \text{few} \times 10^{-3} \tag{4.18}$$

So the effects of ram pressure are thousands of times higher in clusters compared to groups. Consequently, for a given BH mass, the probability that a galaxy retains its gas and feeds its central BH is a thousand smaller. The observed density of optical AGNs in clusters must then be a thousand times smaller.

The existence of a Black Hole Fundamental Plane (BHFP) (Heinz & Sunyaev 2003; Merloni et al. 2003; Falcke et al. 2004) is a remarkable discovery. The BHFP effectively unifies the study of BH physics on the galactic (X-ray Binaries) and on the extragalactic (AGNs) scales. We tentatively used the relation from Falcke et al. (2004) to predict X-rays luminosity functions and compared with available observations in the soft (Hasinger et al. 2005) and hard (Aird et al. 2009) bands. Remarkably our BH masses and radio luminosities combine in exact the right way to reproduce reasonably well the observed X-ray Luminosity Functions, cfr. Fig 4.13.

As the BHFP applies to low power BHs, we can deduce that *most* of the radio-loud AGNs are in this state. So per given BH mass, most systems will also have low X-ray luminosity. The lower limit of the BHMF determines the lower cutoff in the X-ray luminosity function. However, as the X-ray luminosity increases, we observe an excess, due to the small number of systems that are active in the optical mode, cfr. Fig 4.14, and, as a result, are brighter than the "low-luminosity" systems of the same mass. At the very brightest end of the X-ray luminosity, we are dominated by optical mode systems. Since the rate of accretion determines the X-ray luminosity and the mode of AGN activity, we can effectively unify the three different aspects of AGN activity we examined. Along the XLF, we therefore observe three distinct regimes of accretion rate. In analogy to galactic X-Ray Binaries (Meyer-Hofmeister, Liu,& Meyer 2009) we can classify our galaxies according to their accretion rate $\dot{m} \equiv \dot{M}/\dot{M}_{Edd}$:

1. $\dot{m} << \dot{m}_{crit}$: Sub-Eddington accretion rates, where the AGN radiates in radio mode and has low X-ray luminosity. These AGN are characterised by low or no optical activity, have an optically thick disk, and are in a jet dominated state;

2. $\dot{m} \leq \dot{m}_{crit}$: Eddington accretion rates, which is the regime of optically active AGN (broad emission lines, notably H_α). These systems are disk dominated and have high X luminosity;

3. $\dot{m} \geq \dot{m}_{crit}$: Super-Eddington rate, where all of the above coexist.

$\dot{m}_{crit}$ is critical accretion rate for which the disc becomes optically thin to optically thick, $\dot{m}_{crit} \sim \alpha^2$ and α is viscosity coefficient (e.g. Narayan & Yi 1994). For $\alpha \sim 0.1$ the transition happens at $\dot{m}_{crit} \sim 0.01\dot{M}_{Edd}$.

There are indeed very few systems in the super-Eddington state, but we can still quantify the fraction of systems expected in that state. Comparing the numbers from Fig. 4.1, which show the numbers of galaxies involved in the radio and optical AGN phases, we can determine the fractions of BHs in the different accretion states to be:

- Samples A or B: Sub-Eddington rate, 5%
- Sample C: Eddington rate, 0.3%
- Sample A $\cap$ B $\cap$ C: Super-Eddington rate, 0.01%

Interestingly, the fraction of AGN predicted in the sub-Eddington state is not very different from the estimates of the jet production efficiency of 3% in the local Universe (Heinz et al. 2007).

4.7.1 The Mass dependence of $f_{radio-loud}$

The radio-active fraction (RAF) we measured in field galaxies $f_{\rm radio-loud} \sim M_\bullet^{1.5}$ is in agreement with what was found by Best et al. (2005a) by matching a similar SDSS catalogue with

a different radio survey (NVSS). The differences between the two studies can be understood in terms of the characteristics of the radio surveys used.

If we exclude the central galaxies, in clusters we find a much stronger dependence of the RAF on $M_\bullet$, $f_{\rm radio-loud} \sim M_\bullet^{2.3}$. The group RAF is instead consistent with what found in the field, $f_{\rm radio-loud} \sim M_\bullet^{1.5}$.

Central galaxies are very likely to host powerful radio AGNs (e.g. Burns 1990; Magliocchetti & Brüggen 2007). Croft et al. (2007) and von der Linden et al. (2007) in fact measure an enhanced probability of finding radio AGNs in BCGs/BGGs compared to other cluster/group galaxies. Our findings disagree as BCGS and BGGs behave similarly to field galaxies with respect to the probability of being radio-loud. As these two classes of galaxies tend to host very massive BHs, typical values are $10^8 M_\odot$ and $10^{8.5} M_\odot$, these masses alone are responsible for the large fraction of radio AGNs in the cores of groups and clusters. From (4.10), we deduce typical fractions $\sim 50\%$.

Sample C RAF is independent of $M_\bullet$. The constancy of optical AGNs radio-loud fraction has been noticed already in Best et al. (2005a). The authors suggest that this is indicative of the fact that optical and radio activity are independent of each other. As the mode of AGN activity depends on the accretion rate, this statement is not very clear. An optical AGN to be also radio-loud requires a very high accretion rate. High accretion episodes are likely related to extraordinary events, such as mergers, that are unrelated to the BH mass. Optical and, simultaneously, radio AGNs are probably systems that are experiencing or just experienced a merger.

The fraction of radio-loud galaxies: an effect of gas cooling?

Best et al. (2005a) interprets the dependence of $f_{\rm radio-loud}$ on $M_\bullet$ as a consequence of the cooling of hot gas in the extended envelopes of elliptical galaxies. This is physically well-motivated, but their calculation relies on the assumption that the velocity dispersion of the

hot gas in the extended atmosphere and the one of the stars in the galaxy are the same is not necessarily true.

Here we propose an alternative scenario, without making such an assumption. Let us consider an elliptical galaxy (central or non-central) having a hot gaseous ISM. The temperature of this hot ISM depends on the gravitational potential of the dark halo of the galaxy. The cooling time of this gas will be given by $t_{cool} \sim M_{gas}T/L_X$. In elliptical galaxies, the temperature of the hot ISM is related the their X ray luminosity by the empirical mean relation $L_X \sim T^5$ (O'Sullivan et al. 2003). Thus, the cooling time scales as $t_{cool} \sim M_{gas}/T^4$. The accretion rate will then simply scale as $\dot{M} \sim M_{gas}/t_{cool} \sim T^4$.

The temperature T of the hot ISM is found to be related to the stellar velocity dispersion of the galaxy through the empirical relation $T \sim \sigma_{star}^{1.5}$ (Mahdavi & Geller 2001). This translates into the dependence of the accretion rate on the stellar velocity dispersion as $\dot{M} \sim \sigma_{\rm star}^{6}$. Since the black hole mass is found to scale as $M_\bullet \sim \sigma_{star}^{4.4}$ (Graham & Li 2009), we finally get a relation between the accretion rate and the black hole mass $\dot{M} \sim M_\bullet^{1.6}$. Assuming that $f_{\rm radio-loud} \sim \dot{M}$, we end with the scaling relation $f_{\rm radio-loud} \sim M_\bullet^{1.6}$. This scaling relation is in reasonable agreement with what we and Best et al. (2005a) observe in isolated (field) or central galaxies in groups and clusters.

Why do clusters satellite galaxies have high RAFs?

The principal difference between central and non-central galaxies is that the former are at the bottom of the gravitational potential of the dark halo of the group or cluster, while the galaxies in the latter category orbit in the spatially varying potential of the cluster. Cosmological simulations (Gnedin 2003) show that non-central galaxies are subject to multiple strong tidal interactions during their lifetime. The tidal stress thus experienced are not necessarily maximal at the pericentre of the orbit of a non-central galaxy, but could occur at distances of up to 1 Mpc from the cluster centre.

Tidal forces on galaxies have been often invoked as an explanation for the triggering of Seyfert galaxies (Byrd et al. 1986; Byrd et al. 1987). Studies have focussed on the effect of the tidal field due to a close companion, but it is not unreasonable to assume that the net effect of a tidal field on a galaxy would be the same, regardless of the details of the field itself. The timescale and the magnitude of the tidal shocks in an extended potential is of the same order as that due to a close companion, the timescale being around $\sim 10^8 yr$ (Gnedin 2003; Byrd et al. 1986). The effect of a tidal field is to distort the galactic shape (Miller 1986) and to induce the formation of spiral arms or bars (Valluri 1993) in late-type galaxies. The inflows arising from the interaction with a tidal field are $\sim 3M_\odot$ yr^{-1} for disk galaxies and 10^{-2} times smaller for spherical systems (Byrd et al. 1986). Byrd et al. (1987) invoke this induced inflow as an explanation for the triggering of Seyferts in close encounters between galaxy pairs. Therefore tidal interactions could in principle trigger low power AGN activity in non-central galaxies *only* if the non-central galaxies (or satellites) are able to retain a substantial fraction of their gas against ram pressure stripping. Since this process is not important in groups, except in their very core, the RAF dependence on $M_\bullet$ is not modified compared to field galaxies.

Ram Pressure stripping and Steep RAF in Cluster Satellite Galaxies

stripping is able to remove a substantial fraction of gas from galaxies orbiting the cluster potential (e.g. Abadi, Moore, & Bower 1999; Mori & Burkert 2000; Schindler et al. 2005). For a galaxy with mass $M_{\rm gal}$ the condition for the ram pressure exerted by the ICM to be able to efficiently strip the galaxy itself is given in (4.15). To first order, $\sigma^2 \sim M_{\rm gal}$ and $\rho_{\rm gas} \sim M_{\rm gal}$, so the condition for ram pressure stripping to be efficient is $P_{\rm ram} > M_{\rm gal}^2$.

Furthermore, a galaxy spends most of its orbital period near the apocenter, where $\rho_{\rm ICM}$ and $v_{\rm gal}$ are at their minimum. An additional process, namely the accretion of gas from the ICM itself, competes with the gas stripping. The accretion of ICM from a galaxy approximately follows the relation $\dot{M} = 8\pi G^2 M_{\rm gal}^2 \rho_{\rm ICM} (v_{\rm gal} + c_s)^{-3}$ (Bondi & Hoyle 1944). At the apocenter,

$v_{\rm gal} \sim 0$, so the maximum accretion rate for a $10^{10} M_{\odot}$ galaxy and typical values for $\rho_{\rm ICM} \sim 10^{-27}$ g cm^{-3} and $c_s \sim 1000$ is of $\dot{M} \sim 6 \times 10^{-2} M_{\odot}$ yr^{-1}. Assuming that *all* the gas is accreted onto the central BH, having a mass $\sim 10^7 M_{\odot}$, this corresponds to an accretion rate $\approx 0.01 \dot{M}_{Edd}$. These accretion rates are of the order of $\dot{m}_{crit}$ for which the flow around the BH becomes radiatively inefficient (Narayan & Yi 1994).

If we can assume that the mass of gas in each satellite is roughly $\propto M_{gal}^2$, we may repeat the same argument as in 4.7.1, and obtain the observed relation $f_{\rm radio-loud} \sim M_{\bullet}^{1.9-2.4}$ if and only if $L_X \sim \sigma_{\rm star}^{10-12}$ holds. The latter relation is what Mahdavi & Geller (2001) claim is the correct scaling for ellipticals. Therefore if our results and their interpretations are correct, an observable effect of stripping would be to steepen the $L_X \sim \sigma_{\rm star}$ relation. This traces the capacity of the most massive galaxies to retain their gas. Less massive systems will instead lose a larger fraction of their gas. Ram pressure should therefore leads to a *steepening* not only of the $L_X - \sigma_{\rm star}$ relation, but consequently of the $f_{\rm radio-loud} - M_{\bullet}$ as well. At any given stellar velocity dispersion $\sigma_{\rm star}$, we expect that the $L_X - \sigma_{\rm star}$ for BCGs and isolated ellipticals would trace $L_X \sim \sigma_{\rm star}^7$, while satellite ellipticals in clusters should tend towards $L_X \sim \sigma_{\rm star}^{10}$.

In other words, tidal interaction with the cluster or group potential triggers instabilities that drive gas accreted from the ICM onto the central SMBH. The accretion powers the radio AGN. Consequently, because of the higher accretion rates compared to galaxies in the field, the overall probability of being radio-loud for a satellite galaxy is higher in dense environments than in the field. In clusters of galaxies ram pressure stripping is important. Since the capability to retain gas and to accrete from the ICM is a strong function of the orbiting galaxy mass, $f_{radio-loud}$ is a strong function of $M_{gal} \propto M_{\bullet}$. BCGs and BGGs do not show this kind of behaviour because they do not experience the "tidal kicks" that satellites do. Their BHs rely on cooling only. Being at the bottom of the cluster/group gravitational well, they have at their disposal a huge amount of gas to feed and grow the central BHs. Given the dependence of $f_{radio-loud}$ on $M_{\bullet}$, they spend a large fraction of their lives in a radio-active phase.

Table 4.3: Total 1.4 GHz energy input from BCGs, BGGs and satellite galaxies

	1.4 GHz energy
BCGs	$\sim 9 \times 10^{55}$ erg
BGGs	$\sim 3 \times 10^{55}$ erg
Non-Central galaxies:	
Clusters A	$\sim 6 \times 10^{55}$ erg
Clusters B	$\sim 9 \times 10^{53}$ erg
Groups A	$\sim 1 \times 10^{54}$ erg
Groups B	$\sim 2 \times 10^{53}$ erg

4.7.2 Energy contributions to the ICM

Satellite (non-central) galaxies, due to their high probability of being radio-active, could have a significant impact to the total energy balance of the ICM. A distributed population of AGNs could solve the "cooling flow" problem (Nusser et al. 2006). However, the energy output from satellites needs to be at least comparable to the output of the central galaxy. From our data it is a simple exercise to estimate the total energy output of the BCGs/BGGs and compare with the same quantity calculated for non-central galaxies. We calculate the total energy in the 1.4 GHz band from each BH simply by multiplying the AGNs lifetime derived from the RAFs by the corresponding radio power. This is a very estimate and cannot be in any way considered a conclusive proof of the impact of satellite galaxies on the energy balance of the ICM. Furthermore, only a small fraction of the cluster/group volume is affected by radiative cooling. Thus, for this calculation we restrict to satellite galaxies within $\approx 0.1\, r_{200}$.

Our estimates, summarized in table 4.3, imply that in cluster the diffuse population of red radio-active galaxies can affect the ICM as much as the BCGs. This is in stark contrast with Best et al. (2007). The authors find in fact that the contribution from non-central galaxies is not significant compared to the BCGs. The contribution from galaxies belonging to Sample B is instead negligible. This happens because of the difference in the RAFs between the two samples. Similarly, in groups the contribution of Sample B galaxies is one order of magnitude smaller that Sample A's. In the group case though, the BGGs dominate the energy output.

Based on these numbers, we conclude that, differently from groups, clusters non-central AGNs can work in concert with the BCGs to balance radiative cooling.

4.8 Summary

We summarize briefly our work as follows:

- We used SDSS DR6 in concert with 2MASS and FIRST to identify potential BH hosts using a colour based scheme (Sample A), a morphology based scheme (Sample B) and the width of the H_α line (Sample C). We investigated the main colour and morphology properties of the samples. We discovered a substantial fraction of Sample A galaxies not classified morphologically as early types. At the same time, we identified an analogous fraction of Sample B galaxies not characterised by red colours. We interpreted these as "red spirals" (Masters et al. 2010) and "blue ellipticals" (e.g. Mahajan & Raychaudhury 2009).

- We constructed the BHMF for the whole SDSS DR6 galaxy catalogue both for the inactive and the optically active population of BHs. Our findings are consistent with previous studies while extending the mass range over which the BHMF is sampled down to $10^5 M_\odot$. The density we obtain from our BHMF for the 2 optically dim samples are $\rho_\bullet = (2.59 \pm 0.04) \times 10^5\ M_\odot$ Mpc^{-3} and $\rho_\bullet = (3.65 \pm 0.07) \times 10^5\ M_\odot$ Mpc^{-3} for Samples A and B respectively.

- We constructed the BHMF in clusters and groups both for the inactive and the optically active population of BHs. We find an excess of massive BHs compared to the field. We interpret this as a manifestation of the hierarchical assembly of structures leading to enhanced accretion rates onto BHs living in high density environments. The optical active population in clusters is suppressed by a factor ~ 100 compared to the field and to groups.

This is likely an effect of ram pressure stripping.

- We investigated the link between BH mass, environment and AGN activity. We found a correlation between 1.4 GHz radio power and $M_\bullet$, $P_{1.4\ GHz} \sim M_\bullet^{0.8\pm0.3}$.

- Using FIRST radio power measurements, we calculated the radio-active fraction for field and group/cluster galaxies. In the first case, we find a dependence on $M_\bullet^{1.6}$ in agreement with Best et al. (2005a). Field Sample C galaxies show a constant RAF with $M_\bullet$. Sample A group and cluster galaxies have a probability of being radio-loud that is a factor of two higher than their field counterparts. Sample B group and cluster galaxies do not show this increased probability. We interpret the RAF as evidence for increased accretion rates in dense environment, in accordance to cosmological simulations (Colberg & Di Matteo 2008). Sample B galaxies do not show increased probability because their are likely going through a star-forming phase that decreases the amount of fuel available for the central BH.

- As a result of ram pressure stripping, satellite galaxies in clusters show a RAF that depends on $M_\bullet$ stronger than their field and group counterparts; $f_{radio-loud} \sim M_\bullet^{2.3}$. This predicts that satellite galaxies should obey to $L_X \sim \sigma_{\rm star}^{10}$ in contrast to isolated and central galaxies where $L_X \sim \sigma_{\rm star}^{7}$.

- Using the BH fundamental plane relation of Falcke et al. (2004), we obtain a X-ray Luminosity Functions (XLFs) in the soft and hard bands. We compare our predictions with Hasinger et al. (2005) and Aird et al. (2009) and find excellent agreement. We also infer the fraction X-ray bright AGNs in clusters and in groups. Our fractions agree very well with what found by Martini et al. (2006),Martini et al. (2007) and Sivakoff et al. (2008).

- We interpret the different modes of AGN activity as a direct manifestation of the accretion

rate distribution. From the number of galaxies in our radio samples, we estimate the fraction of systems in each accretion state: (i) Sub-Eddington rate, 5%; (ii) Eddington rate, 0.3%; (iii) Super-Eddington rate, 0.01%.

- We estimate the total energy output from clusters/groups radio AGNs. We provide indications that in clusters the diffuse red galaxy population has an energy output that is comparable to the central galaxy. This does not hold in groups of galaxies, where the central galaxy AGN dominates over the satellites.

Bibliography

Abadi M. G., Moore B., Bower R. G., 1999, MNRAS, 308, 947

Abell, G. O., Corwin, H. G., Jr., & Olowin, R. P. 1989, ApJS, 70, 1

Adelman-McCarthy, J. K., et al. 2006, ApJs, 162, 38

Adelman-McCarthy, J. K., et al. 2008, ApJs, 175, 297

Aird, J., et al. 2009, arXiv:0910.1141

Aller, M. C., & Richstone, D. 2002, AJ, 124, 3035

Becker, R. H., White, R. L., & Helfand, D. J. 1995, ApJ, 450, 559

Benson A. J., Bower R. G., Frenk C. S., Lacey C. G., Baugh C. M., Cole S., 2003, ApJ, 599, 38

Benson, A. J., Džanović, D., Frenk, C. S., & Sharples, R. 2007, MNRAS, 379, 841

Berlind et al., in preparation

Best, P. N. 2004, MNRAS, 351, 70

Best, P. N., Kauffmann, G., Heckman, T. M., Brinchmann, J., Charlot, S., Ivezić, Ž., & White, S. D. M. 2005, MNRAS, 362, 25

Best, P. N., Kauffmann, G., Heckman, T. M., & Ivezić, Ž. 2005, MNRAS, 362, 9

Best, P. N., Kaiser, C. R., Heckman, T. M., & Kauffmann, G. 2006, MNRAS, 368, L67

Best, P. N., von der Linden, A., Kauffmann, G., Heckman, T. M., & Kaiser, C. R. 2007, MNRAS, 379, 894

Bianchi, S., Guainazzi, M., Matt, G., Fonseca Bonilla, N., & Ponti, G. 2009, A & A, 495, 421

Bildfell C., Hoekstra H., Babul A., Mahdavi A., 2008, MNRAS, 389, 1637

Bîrzan, L., McNamara, B. R., Nulsen, P. E. J., Carilli, C. L., & Wise, M. W. 2008, ApJ, 686, 859

Blanton, M. R., et al. 2003, ApJ, 592, 819

Blanton, M. R., et al. 2005, AJ, 129, 2562

Blanton M. R., Roweis S., 2007, AJ, 133, 734

Bondi, H., & Hoyle, F. 1944, MNRAS, 104, 273

Bower, R. G., Benson, A. J., Malbon, R., Helly, J. C., Frenk, C. S., Baugh, C. M., Cole, S., & Lacey, C. G. 2006, MNRAS, 370, 645

Burns J. O., 1990, AJ, 99, 14

Byrd, G. G., Valtonen, M. J., Valtaoja, L., & Sundelius, B. 1986, A & A, 166, 75

Byrd, G. G., Sundelius, B., & Valtonen, M. 1987, A & A, 171, 16

Buzzoni, A. 2005, MNRAS, 361, 725

Carlberg, R. G., et al. 1997, ApJl, 485, L13

Choloniewski, J. 1987, MNRAS, 226, 273

Churazov, E., Gilfanov, M., & Revnivtsev, M. 2001, MNRAS, 321, 759

Colberg, J. M., & Di Matteo, T. 2008, ArXiv e-prints, 804, arXiv:0804.1756

Colless, M. 1989, MNRAS, 237, 799

Condon J. J., Cotton W. D., Greisen E. W., Yin Q. F., Perley R. A., Taylor G. B., Broderick J. J., 1998, AJ, 115, 1693

Croft, S., de Vries, W., & Becker, R. H. 2007, ApJl, 667, L13

Cutri, R. M., et al. 2003, The IRSA 2MASS All-Sky Point Source Catalog, NASA/IPAC Infrared Science Archive. http://irsa.ipac.caltech.edu/applications/Gator/

De Propris, R., et al. 2003, MNRAS, 342, 725

Dressler, A. 1980, ApJ, 236, 351

Dressler, A., Thompson, I. B., & Shectman, S. A. 1985, ApJ, 288, 481

Efstathiou, G., Ellis, R. S., & Peterson, B. A. 1988, MNRAS, 232, 431

Eilek, J. A., & Owen, F. N. 2007, in *Heating versus Cooling in Galaxies and Clusters of Galaxies*, ESO astrophysics Symp, p133

Fabian, A. C. 1994, ARA & A, 32 ,277

Fabian, A. C., Reynolds, C. S., Taylor, G. B., & Dunn, R. J. H. 2005, MNRAS, 363, 891

Falcke, H., Körding, E., & Markoff, S. 2004, A & A, 414, 895

Feretti L., Giovannini G., 1994, A&A, 281, 375

Fitzpatrick, E. L. 1999, PASP, 111, 63

Franceschini, A., Vercellone, S., & Fabian, A. C. 1998, MNRAS, 297, 817

Giacintucci S., et al., 2008, ApJ, 682, 186

Gnedin, O. Y. 2003, ApJ, 582, 141

Graham, A. W. 2007, MNRAS, 379, 711

Graham, A. W., & Li, I.-h. 2009, ApJ, 698, 812

Greene, J. E., & Ho, L. C. 2005, ApJ, 630, 122

Greene, J. E., & Ho, L. C. 2007, ApJ, 667, 131

Gültekin K., Cackett E. M., Miller J. M., Di Matteo T., Markoff S., Richstone D. O., 2009, ApJ, 706, 404

Hasinger, G., Miyaji, T., & Schmidt, M. 2005, A & A, 441, 417

Heinz, S., & Sunyaev, R. A. 2003, MNRAS, 343, L59

Heinz, S., Merloni, A., & Schwab, J. 2007, ApJl, 658, L9

Kannappan S. J., Guie J. M., Baker A. J., 2009, AJ, 138, 579

Kennicutt, R. C., Jr. 1998, ApJ, 498, 541

Kaspi S., Maoz D., Netzer H., Peterson B. M., Vestergaard M., Jannuzi B. T., 2005, ApJ, 629, 61

Kaviraj S., Peirani S., Khochfar S., Silk J., Kay S., 2009, MNRAS, 394, 1713

Kimball A. E., Ivezić Ž., 2008, AJ, 136, 684

Lacy M., Laurent-Muehleisen S. A., Ridgway S. E., Becker R. H., White R. L., 2001, ApJ, 551, L17

Lagos, C. D. P., Cora, S. A., & Padilla, N. D. 2008, MNRAS, 736

Lin, Y.-T., & Mohr, J. J. 2007, ApJs, 170, 71

Lin, Y.-T., Mohr, J. J., & Stanford, S. A. 2004, ApJ, 610, 745

Lynden-Bell D., 1971, MNRAS, 155, 95

Magliocchetti, M., & Brüggen, M. 2007, MNRAS, 379, 260

Mahajan S. and Raychaudhury S., 2009, MNRAS, 400, 687

Mahdavi, A., & Geller, M. J. 2001, ApJl, 554, L129

Marconi, A., & Hunt, L. K. 2003, ApJl, 589, L21

Marconi, A., Risaliti, G., Gilli, R., Hunt, L. K., Maiolino, R., & Salvati, M. 2004, MNRAS, 351, 169

Marconi A., Axon D. J., Maiolino R., Nagao T., Pastorini G., Pietrini P., Robinson A., Torricelli G., 2008, ApJ, 678, 693

Markoff, S., Nowak, M., Corbel, S., Fender, R., & Falcke, H. 2003, New Astronomy Review, 47, 491

Masters K. L., et al., 2010, MNRAS, 487

Merloni, A., Heinz, S., & di Matteo, T. 2003, MNRAS, 345, 1057

Martini, P., Kelson, D. D., Kim, E., Mulchaey, J. S., & Athey, A. A. 2006, ApJ, 644, 116

Martini, P., Mulchaey, J. S., & Kelson, D. D. 2007, ApJ, 664, 761

Meyer-Hofmeister E., Liu B. F., Meyer F., 2009, A&A, 508, 329

McCarthy I. G., Balogh M. L., Babul A., Poole G. B., Horner D. J., 2004, ApJ, 613, 811

McCarthy I. G., Babul A., Bower R. G., Balogh M. L., 2008, MNRAS, 386, 1309

McCarthy I. G., Frenk C. S., Font A. S., Lacey C. G., Bower R. G., Mitchell N. L., Balogh M. L., Theuns T., 2008, MNRAS, 383, 593

McLure R. J., Dunlop J. S., 2002, MNRAS, 331, 795

McNamara, B. R., & Nulsen, P. E. J. 2007, ARA & A, 45, 117

Miller, R. H. 1986, A & A, 167, 41

Mori, M., & Burkert, A. 2000, ApJ, 538, 559

Narayan, R., & Yi, I. 1994, ApJl, 428, L13

Narayan, R. 1996, ApJ, 462, 136

Narayan, R., & Medvedev, M. V. 2001, ApJl, 562, L129

Nath, B. B. 2008, MNRAS, 387, L50

Navarro, J. F., Frenk, C. S., & White, S. D. M. 1997, ApJ, 490, 493

Nemmen, R. S., Bower, R. G., Babul, A., & Storchi-Bergmann, T. 2007, MNRAS, 377, 1652

Nolan L. A., Raychaudhury S., Kabán A., 2007, MNRAS, 375, 381

Nusser, A., Silk, J., & Babul, A. 2006, MNRAS, 373, 739

O'Sullivan, E., Ponman, T. J., & Collins, R. S. 2003, MNRAS, 340, 1375

Osmond, J. P. F., & Ponman, T. J. 2004, MNRAS, 350, 1511

Peterson, J. R., & Fabian, A. C. 2006, PhR, 427, 1

Pipino, A., Kaviraj, S., Bildfell, C., Babul, A., Hoekstra, H., Silk, J. 2009, MNRAS, 395, 462

Poole G. B., Fardal M. A., Babul A., McCarthy I. G., Quinn T., Wadsley J., 2006, MNRAS, 373, 881

Rasmussen J., Ponman T. J., Mulchaey J. S., Miles T. A., Raychaudhury S., 2006, MNRAS, 373, 653

Sadler, E. M., et al. 2002, MNRAS, 329, 227

Sanderson, A. J. R., Ponman, T. J., & O'Sullivan, E. 2006, MNRAS, 372, 1496

Schade, D. 1991, MNRAS, 251, 310

Schindler, S., et al. 2005, A & A, 435, L25

Schmidt, M., Schneider, D. P., & Gunn, J. E. 1986, ApJ, 306, 411

Shabala, S. S., Ash, S. A., Alexander, P., & Riley, J. M. 2008, MNRAS, 388, 625

Shakura, N. I., & Sunyaev, R. A. 1973, A & A, 24, 337

Shimasaku, K., et al. 2001, AJ, 122, 1238

Sijacki, D., Springel, V., di Matteo, T., & Hernquist, L. 2007, MNRAS, 380, 877

Sivakoff, G. R., Martini, P., Zabludoff, A. I., Kelson, D. D., & Mulchaey, J. S. 2008, ApJ, 682, 803

Soltan, A. 1982, MNRAS, 200, 115

Snowden, S. L., Mushotzky, R. F., Kuntz, K. D., & Davis, D. S. 2008, A & A, 478, 615

Strateva, I., et al. 2001, AJ, 122, 1861

Strateva, I. V., Brandt, W. N., Schneider, D. P., Vanden Berk, D. G., & Vignali, C. 2005, AJ, 130, 387

Treister E., et al., 2009, ApJ, 706, 535

Tremaine, S., et al. 2002, ApJ, 574, 740

Vanden Berk, D. E., et al. 2001, AJ, 122, 549

Valluri, M. 1993, ApJ, 408, 57

Vikhlinin, A., Markevitch, M., Murray, S. S., Jones, C., Forman, W., & Van Speybroeck, L. 2005, ApJ, 628, 655

von der Linden, A., Best, P. N., Kauffmann, G., & White, S. D. M. 2007, MNRAS, 379, 867

Woo, J.-H., Urry, C. M., van der Marel, R. P., Lira, P., & Maza, J. 2005, ApJ, 631, 762

Yang, X., Mo, H. J., van den Bosch, F. C., Pasquali, A., Li, C., & Barden, M. 2007, ApJ, 671, 153

Yu, Q., & Tremaine, S. 2002, MNRAS, 335, 965

5. Metallicity Evolution in Mergers of Clusters of Galaxies

Abstract

In this chapter we present a set of idealized two-body simulations specifically designed to investigate the effects of varying initial conditions on the merger remnant. After presenting the numerical methods employed and describing in detail our set up, we present results for equal mass ratio cluster mergers. For the purpose of this chapter we consider two different orbital initial conditions and two different initial entropy states of the Intra Cluster Medium (ICM). The clusters we consider are representative of the two main classes identified observationally. We consider pure power law entropy cores (PL) and constant entropy cores (300). Those can be identified with "cool core" (CC) and "non cool core" (NCC) clusters. From the kinematic point of view, we study head on mergers and off axis mergers. After summarizing the main features of the merger using the two dimensional surface brightness maps, we concentrate on the effects over two dimensional emission weighted metal distributions. We observe substantial differences between the two classes of clusters, with the 300 class showing very complex features resulting in flat one dimensional metal profiles. We interpret these features as the effect of mixing induced by shock heating. NCC clusters are prone to enhanced mixing because of their longer buoyancy timescales. CC clusters are more resilient to merger induced mixing,

re-establishing their original metal gradients after the transients. We therefore reproduce the results already presented in Poole et al. (2008) while at the same time explaining the measured flat metal profiles in post merger NCC clusters as a consequence of the progenitor's thermodynamical state.

5.1 Introduction

In a ΛCDM scenario, the growth of structures is driven by hierarchical mergers. As the most massive associations in the Universe, clusters of galaxies are the last structures to form. *Chandra* and XMM observations support this idea. There is, in fact, compelling evidence of ongoing mergers from the observations of a variety of complicated transient structures as cold fronts (Markevitch et al. 2000) or shock fronts (Markevitch & Vikhlinin 2001). These observations triggered a variety of theoretical investigations devoted to understanding the observed features. Understanding a single merger event in a cosmological context is complicated by the presence of larger structures, smooth accretion processes and, last but not least, the necessarily limited resolution. Therefore, the study of idealized two-body mergers is an appealing alternative. Structures indeed grow mostly by major merger episodes (Cohn & White 2005). Two-body simulations also allow initial conditions to be under control and therefore to characterise their impact on short and long term transients. Several groups have devoted their efforts to this kind of study. Ricker & Sarazin (2001) considered impact parameters between 0 and 5 times the dark matter scale radius and mass ratios of 1:1 and 1:3 to study the effects of a merger on the luminosity and temperature "boosts". In their simulations they found that the gas is preferentially heated in the outskirts of the remnant and that dark matter oscillations are a prominent source of turbulence and mixing of the IntraCluster Medium (ICM). Gómez et al. (2002) concentrated on 4:1 and 16:1 mergers between realistic "cooling flow" clusters and studied whether the core would survive the impact without reaching conclusive results. In a series of papers, Poole and collaborators performed the largest set of idealized mergers simulations to date. They used mass ratios of 1:1, 3:1 and 10:1 and three different initial orbital configurations, face on and off-axis. The clusters were all set to obey a power law entropy configuration, adequate to describe "cooling flow" systems. With this set up they studied the dynamical evolution and transient structures (Poole et al. 2006), quantified the effects on scaling relations and on the Sunyaev-Zeldovich effect (Poole et al. 2007) and the stability of resilience of "cooling flows" systems (Poole et al.

2008). McCarthy et al. (2007) used equal mass "cooling flow" systems to quantify the amount of entropy generated by shock heating. They established a two stage scenario for the injection of energy into the ICM, resulting in improved recipes for semi-analytical models.

Clusters of galaxies seem to follow a show a bimodal distribution when classified according to their central entropy (Sanderson, O'Sullivan, & Ponman 2009; Cavagnolo et al. 2009). Clusters whose entropy declines monotonically with radius are classified as "cool core" (CC), while clusters where the entropy levels to a constant value in the core are indicated as "non cool-core" (NCC). There are evidences that core entropy properties are a key ingredient for star-formation and AGN activity of the central cD galaxy (e.g. Rafferty, McNamara, & Nulsen 2008). The origin of the bimodality is not clear. It could be a consequence of "preheating" (McCarthy et al. 2004; McCarthy et al. 2008), AGN heating (e.g. McNamara & Nulsen 2007) or a consequence of mergers. This latter possibility, though, seems to be excluded (Gómez et al. 2002; Poole et al. 2008).

Metal abundances in the ICM seem to be correlated to the core entropy level; in CCs, metal abundances increase toward the center of the cluster, while in NCCs they tend flatten (De Grandi & Molendi 2001; Leccardi & Molendi 2008; Sivanandam et al. 2009; Leccardi, Rossetti, & Molendi 2010), (but also see Sanderson, O'Sullivan, & Ponman (2009) for different conclusions). Also, CC systems have central metallicities that might exceed solar values while, on the other hand, NCC clusters central metallicities that are a fraction of the solar value (Cavagnolo et al. 2009). The metals content of the ICM is established by galactic winds driven by supernovae explosions (White 1991), ram pressure stripping (Mori & Burkert 2000), early enrichment by population type III stars (Loewenstein 2001) and intracluster stars (Zaritsky, Gonzalez, & Zabludoff 2004). Given that the processes responsible for establishing the metals distribution are the same for all clusters, what differentiates the two populations? A possible solution relies on the turbulence and mixing driven by AGN activity (Rasera et al. 2008). Leccardi, Rossetti, & Molendi (2010) instead, explains the different profiles in CCs and NCCs as

a record of recent mergers. Similarly, high resolution observations of merging clusters show indeed very complicated morphologies and substructures in the metals distribution (Sauvageot, Belsole, & Pratt 2005; Lovisari et al. 2009). Cluster mergers are known to be an effective source of turbulence and mixing (Gómez et al. 2002) but simulations argue against mergers as the origin of flat metals profiles in NCC (Poole et al. 2008). As the entropy profile is what sets the efficiency of buoyancy, we believe that appropriate initial conditions could lead to different conclusions. To our knowledge in fact, all previous studies focused on a particular initial gas configuration, *e.g.* a power law entropy profile or an observed cooling flow configuration. None of them has investigated the effects on metals distribution for different core properties of the progenitors. In this chapter we devote our attention to fill this gap and give precise observational signatures concentrating especially on metal profiles and maps. The rest of the chapter is organised as follows: Section 2 describes the set up we adopted for our simulations. Section 3 will be concerned with the description of the merger process. In section 4 metallicity maps will be presented and discussed. Section 5 will deal with entropy and mixing. Finally in section 6 the main results will be summarized and discussed.

5.2 Simulation set up

The idealized non-radiative cluster mergers simulations have been produced using the public version of the the parallel TREESPH code GADGET-2 (Springel, Yoshida, & White 2001; Springel 2005). Lagrangian in nature, the GADGET-2 code is the ideal choice for tracking the entropy evolution of any particle ensemble. Furthermore, thanks to its explicit entropy conserving scheme (Springel & Hernquist 2002), we are guaranteed that any change in this quantity is related to physical phenomena and not to any spurious numerical effect. We performed a series of cluster collision simulations between systems whose virial masses range from $10^{14}M_{\odot} \leq M_{200} \leq 10^{15}M_{\odot}$. We set the mass of the heaviest system to $M_{200} = 10^{15}M_{\odot}$ in all

simulations (M_{200} will be defined later). We explore mergers with mass ratios of $1:1$, $3:1$ and $10:1$. For the sake of clarity we will refer to the most massive system as the "primary" and to the less massive as the "secondary". The initial orbital parameters have been chosen referring to the result of the large N-body cosmological simulation (Benson 2005). For this particular choice the relative velocity of v the 2 system is chosen as $v = (v_r^2 + v_t^2)^{1/2} \simeq 1.1 v_c(r_{vir})$ where v_r and v_t are the radial and tangential velocity, relative to the center of mass of the binary system and $v_c(r_{vir})$ is the circular velocity at the virial radius. Given the masses in consideration we fixed the total relative velocity to $\simeq 1444$ km·s^{-1}. We considered 3 different initial configurations for each mass ratio, corresponding to $v_t = 0$, $v_t = v_r/4$ and $v_t = v_r/2$. We refer to these cases as "head on", "small impact parameter" and "large impact parameter", respectively. The initial relative distance between the components is chosen such that the gaseous components of each cluster is barely touching, therefore it's just equal to the sum of r_{200} for the 2 components. In each simulation the total number of particles used to describe the primary system was held fixed to 10^6. Of these, 500000 particles describe the DM component and the rest describe the gas component. This choice yields a mass per particle of $1.76 \times 10^9 M_\odot$ for the DM and of $0.24 \times 10^9 M_\odot$ for the gas, assuming a baryon fraction $f_b = 0.141$. The particle masses were held fixed, therefore less massive systems were modelled using a smaller number of particles. The gravitational softening length has been fixed to 10 kpc. We adopt a SPH viscosity parameter $\alpha_c = 0.8$ and a Courant number of 0.1. Finally each simulation is run for 13 Gyr, approximately an Hubble time. Snapshots are taken out regularly every 1 Gyr. Table 5.1 summarizes the simulations that have been produced.

5.2.1 Initial conditions

Here we briefly describe the initial conditions we adopted to describe each cluster. The reader is referred to McCarthy et al. (2007) for a more detailed description.

Dark Matter set up

All our systems are constructed assuming that they are structural copies of each other. The DM initial density profiles follow a NFW (Navarro, Frenk, & White 1997) profile:

$$\rho(r) = \frac{\rho_s}{(r/r_s)(1+r/r_s)^2} \tag{5.1}$$

where

$$\rho_s = M_s/4\pi r_s^3 \tag{5.2}$$

$$M_s = \frac{M_{200}}{\ln(1+r_{200}/r_s) - (r_{200}/r_s)/(1+r_{200}/r_s)}. \tag{5.3}$$

In the above equations we defined r_{200} as the radius within which the cluster mean density is 200 times the critical density of the Universe, ρ_{crit}, and $M_{200} = (4/3)\pi r_{200}^3 \times 200\rho_{crit}$. The concentration parameter $c = r_{200}/r_s$ has been fixed to 4, typical values extracted from cosmological simulations for the masses that we considered in this work. We ignored any dependence on M_{200} of c since this has been shown to be very weak. Since the DM component lacks any kind of thermal pressure, in order to keep our chosen profile steady we have to assign appropriate velocity to the DM particles. This has been achieved by solving the Jeans equation for the radial velocity profile for a spherical and isotropic halo. To avoid particle runaway and so insure that the mass remained constant throughout the simulation time the DM density profiles has been extended out to r_{25} and embedded inside a confining medium with constant density equal to ρ_{25}.

Gas set up

Following Mitchell et al. (2009), the gaseous component has been initially distributed to follow an entropy[1] power law configuration

$$\frac{S(r)}{S_{200}} = 1.47 \left(\frac{r}{r_{200}} \right)^{1.22} \tag{5.4}$$

plus eventually an entropy floor in the inner core of the cluster, $r = 0.1 r_{200}$. The "virial entropy", S_{200}, is given by

$$S_{200} = \frac{GM_{200}}{2r_{200}} \frac{1}{(200\rho_{crit})^{2/3}} \tag{5.5}$$

Equation (5.4) matches the entropy profiles of groups and clusters formed in non-radiative cosmological simulations (Voit, Kay, & Bryan 2005). We setup our clusters in 4 different core entropy states:

1. pure power low (PL). We assume that relation (5.4) holds at every radius. This case corresponds to a "cool core" (CC) cluster;
2. 100keV·cm^2 entropy floor (100);
3. 200keV·cm^2 entropy floor (200);
4. 300keV·cm^2 entropy floor (300).

The last three cases are representative of "non cool core" (NCC) clusters. The density and pressure profiles are set by simultaneously solving the hydrostatic equilibrium and continuity

[1]As common in X-ray astronomy we define the entropy S not as the thermodynamical entropy but as $S = P\rho_{gas}^{-5/3}$. These two quantities are related simply by $S_{therm} \propto \ln S^{3/2}$.

equations:

$$\frac{d\log P}{d\log M_{gas}} = -\frac{GM_{tot}M_{gas}}{4\pi r^4 P} \tag{5.6}$$

$$\frac{d\log r}{d\log M_{gas}} = \frac{M_{gas}}{4\pi r^3}\left(\frac{S}{P}\right)^{3/5} \tag{5.7}$$

The temperature profile is obtained then from the gas equation of state. Equations (5.6) and (5.7) are solved imposing as boundary conditions $r(M_{gas} = 0) = 0$ and that the total mass of gas within r_{200} yields a realistic baryon fraction $M_{gas}/M_{tot} = 0.141$.

Initial Metallicity Profile

Once all the DM and the gas particles have been distributed following the procedure described above, to each gas particle was assigned an initial metallicity according to (Sanderson, O'Sullivan, & Ponman 2009)

$$Z(r) = \begin{cases} 10^{0.313\log(\frac{r}{r_{500}}+0.634)} & \text{if } \log(\frac{r}{r_{500}}) \leq -1.85 \\ 10^{-0.333\log(\frac{r}{r_{500}}-0.554)} & \text{if } \log(\frac{r}{r_{500}}) \geq -1.85 \end{cases} \tag{5.8}$$

where r is the distance relative to the center of each cluster. In practice to each particle sitting on a shell with distance r from the center of the cluster is assigned a metallicity as given by equation (5.8). The value of $Z(r)$ of each particle is unique and never allowed to change throughout the simulation. The metallicity is in fact linked to the ID number that is univocally assigned by GADGET-2 to each particle in the simulation. In reality what is measured from X-ray observations is a luminosity-weighted metallicity. This because the value of $Z(r)$ is inferred by spectral modelling over shells centred around the maximum of the surface brightness. Therefore to allow a direct comparison with observations a similar procedure has been implemented.

Metallicity Maps and Profiles

In each snapshot of every simulation luminosity-weighted metallicities are calculated using the following procedure. The simulation volume is covered with a 3D mesh of 256^3 cells. This mesh also defines a Cartesian reference system $\{x, y, z\}$. In each cell, having a size of 10kpc^3, average densities, temperatures and metallicities are calculated simply taking the mean over all the particles inside each cell. The X-ray luminosity for each cell is then:

$$L(x,y,z) = \left(\frac{\rho(x,y,z)X_e}{(X_e+X_i)\mu m_p}\right)^2 \frac{\Lambda\left(T(x,y,z), Z(x,y,z)\right)}{X_e} \tag{5.9}$$

where $\rho(x, y, z)$ is the cell density, $T(x, y, z)$ is the cell temperature, $Z(x, y, z)$ is the cell metallicity, X_e is the number of electrons per hydrogen atom, X_i is the number of ions per hydrogen atom, μ is the mean molecular weight, m_p is the proton mass, and $\Lambda\left(T(x, y, z), Z(x, y, z)\right)$ is the cooling function. $\Lambda\left(T(x, y, z), Z(x, y, z)\right)$ is calculated using the appropriate MEKAL (Mewe, Gronenschild, & van den Oord 1985; Liedahl, Osterheld, & Goldstein 1995) model cooling function for the temperature and metallicity of each cell. Once I obtained luminosities for each cell using equation (5.9) these are projected onto the $x - y$ plane to obtain the surface brightness as

$$Sb(x,y) = \int dz L(x,y,z) \tag{5.10}$$

The centre of the cluster is then identified with the cell corresponding to the maximum of the surface brightness. In the early stages of the merger process, when the primary and the secondary are still well defined detached systems, is not trivial to define a cluster centre. Nevertheless in the final stages of the process, after the cores of the clusters have merged, a single system is well defined, therefore it is possible to construct radial profiles relative to this centre. Keeping those caveats in mind, each cell is then assigned a radial distance from the newly identified center of

the cluster. Emission-weighted metallicity maps are calculated as

$$Z(x,y) = \frac{\int L(x,y,z)Z(x,y,z)dz}{\int L(x,y,z)dz}. \tag{5.11}$$

From equation (5.11), emission-weighted metallicity profiles $Z(r)$ are calculated directly using a change of coordinates from the Cartesian $\{x, y\}$ system to the polar system $\{r, \theta\}$ and summing over the angle θ. The origin of the polar system is taken as described above.

Table 5.1: Summary of all galaxy cluster merger that have been simulated for this work. The entropy cores refer to the list defined in 5.2.1. The total number of simulations performed is 90.

Mass Ratio	Orbit	Entropy Cores: secondary–primary			
1:1	Head on	PL–PL	100–100	200–200	300–300
	Small b	PL–PL	100–100	200–200	300–300
	Large b	PL–PL	100–100	200–200	300–300
3:1	Head on	PL–PL	PL–100	PL–200	PL–300
		100–PL	100–100	100–200	100–300
	Small b	PL–PL	PL–100	PL–200	PL–300
		100–PL	100–100	100–200	100–300
	Large b	PL–PL	PL–100	PL–200	PL–300
		100–PL	100–100	100–200	100–300
10:1	Head on	PL–PL	PL–100	PL–200	PL–300
		100–PL	100–100	100–200	100–300
	Small b	PL–PL	PL–100	PL–200	PL–300
		100–PL	100–100	100–200	100–300
	Large b	PL–PL	PL–100	PL–200	PL–300
		100–PL	100–100	100–200	100–300

5.3 Qualitative Merger Evolution

As summarized in table 5.1, the total number of simulations performed is 90. In each case output is produced every Gyr for a total of 14 snapshots. This yields a total of 1260 outputs. Therefore, to illustrate the physics of the merger, here only a small subset will be presented. In particular we will concentrate on the 1:1 mass ratio and compare the evolutions of the PL and

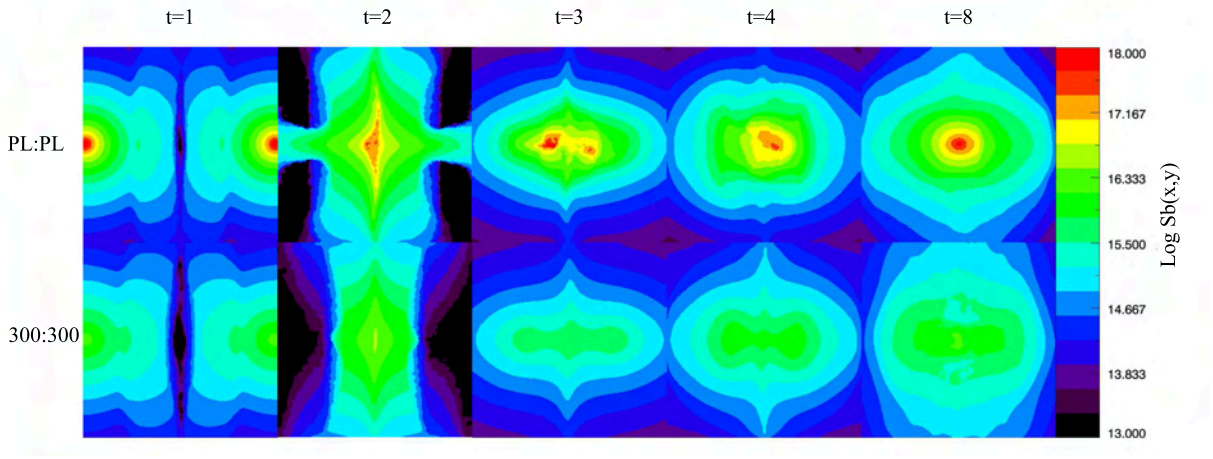

Figure 5.1: Surface brightness maps snapshots of the central 2 Mpc for the head on $1:1$ merger. From top to bottom: (i) PL:PL, (ii) 300:300. In each row from left to right $t = 1, t = 2, t = 3, t = 4, t = 8$ Gyr. In all cases by $t = 8$ Gyr the PL:PL remnant appear relaxed and with a well defined core. The 300:300 still shows plume-like structures. These can be taken as a signature of buoyant oscillations of the gas.

300 cases. Furthermore only the head-on and the small impact parameter cases will be shown.

All the simulations proceed through a common evolutionary sequence as already noted in Poole et al. 2006: pre-interaction phase, first core interaction, apocentric passage, second core interaction and relaxation. The exact values of the timescales depend on the value of the core entropy but in general the above phases are well identifiable. At the beginning of each simulation the two systems start in contact at a distance equal to the sum of the respective r_{200}s. In the following sections we describe the merger evolution from the surface brightness point of view. Refer to Figs 5.1 and 5.2 for a pictorial representation of the main evolutionary phases.

5.3.1 Head on Merger

The simulation starts with the systems in contact and on a direct on axis impact course with a relative velocity equal to ≈ 1444 km·s^{-1}. At $t = 1$ Gyr a shock has developed at the interface of the two atmospheres. The systems surface brightness increases sharply and the outer layers of the atmospheres are distorted because of the tidal interactions and the collision induced

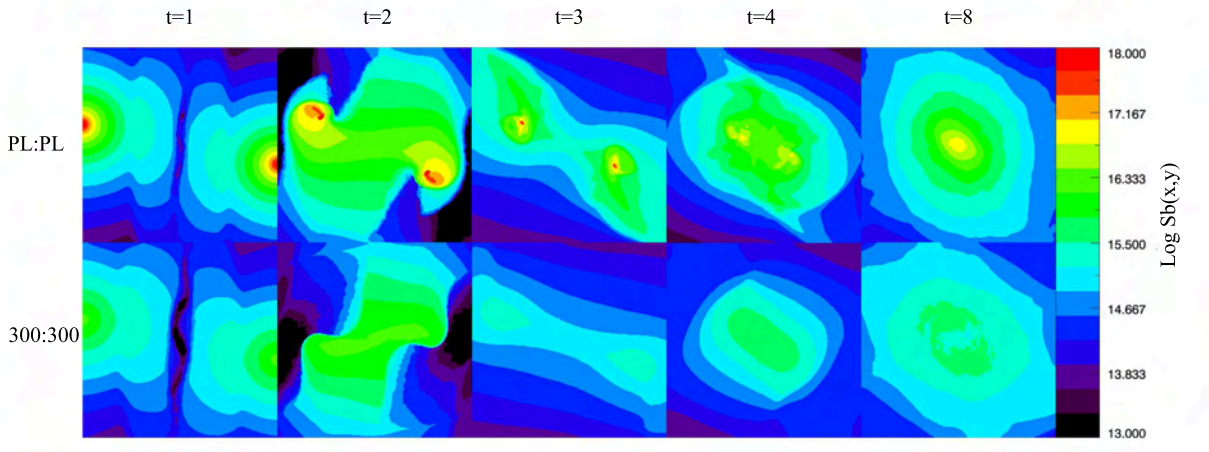

Figure 5.2: Surface brightness maps snapshots of the central 2 Mpc for the small impact parameter $1:1$ merger. From top to bottom: (i) PL:PL, (ii) 300:300. In each row from left to right $t = 1, t = 2, t = 3, t = 4, t = 8$ Gyr. In all cases by $t = 8$ Gyr the 2 systems have merged and relaxed and no substructure is present in the surface brightness.

compression. The two cores are still very well defined as no interaction has taken place yet. The emission at the interface between the two atmosphere is strongly depressed. At $t = 2$ Gyr the cores have gone through their first close encounter and have interacted with the contact shock. In the PL:PL case the cores are disrupted and small parcels of bright gas are visible in an elongated high emission area extending perpendicularly to the direction of motion, following a moderate shock. In the 300:300 case no substructure is visible. The emissivity is maximum in the very centre of the shock. In general the atmospheres are elongated and surrounded by areas of very low emissivity. At $t = 3$ Gyr the cores reach their apocentre and begin to bounce back. In the PL:PL case the two cores are well defined and rich in substructure. In the 300:300 merger no definite core is visible, but plume-like structures extend on the left and the right of the standing shock. In both cases, the shock is still clearly visible perpendicular to the direction of motion. At $t = 4$ Gyr the secondary accretion episode takes place. In the PL:PL merger only one defined core of emission is present. In the 300:300 case the plume-like structures are still visible. The extreme right panels in Fig. 5.1 show the systems after $t = 8$ Gyr in simulation time. The PL:PL remnant appears already relaxed and resembles the progenitors. The

300:300 remnant is instead still showing the plumes suggesting that the gas is still undergoing oscillations around the equilibrium point.

5.3.2 Off Axis Merger

The simulation starts with the systems in contact. The modulus of the relative velocity is ≈ 1444 km·s^{-1}. The radial and tangent velocities are $v_r \approx 1400$ km·s^{-1} and $v_t \approx 350$ km·s^{-1}. At $t = 1$ Gyr, as in the head on case, a shock at the interface of the colliding atmospheres has developed. In this location the surface brightness is minimum and the two atmospheres appear distorted as a result of compression and tidal interactions. At $t = 2$ Gyr the cores have gone through their pericentres and reached the apocentres. The strong tidal interaction experienced by the cores has distorted them and at least in the PL:PL case the typical features of this interaction are visible: tidal tails and a bridge connecting the two still well defined cores. Those features are not evident in the 300:300 case except for the development of a spiral like structure. At $t = 3$ Gyr the cores are falling back toward the common centre of mass. They are well defined as well as the bridge of dimmer gas connecting them. At $t = 4$ Gyr the second close encounter has taken place. Consequently a secondary shock is visible and the cores have lost much of their luminosity because of shock heating that reduced their density further. Nevertheless in the PL:PL case they are still distinguishable even if they appear seriously disrupted by the interaction. The extreme right panels in Fig. 5.2 show the systems after $t = 8$ Gyr in simulation time. The PL:PL remnant appear relaxed and with a well defined core. As a consequence of shock heating the density of the newly formed core is lower than the progenitors and the core itself appear dimmer than the original ones. The 300:300 remnant core instead still shows two substructures. As in the head on merger, these are the signatures of buoyant oscillations. We note here that off axis mergers induce an overall rotation on the ICM as a consequence of the conservation of angular momentum.

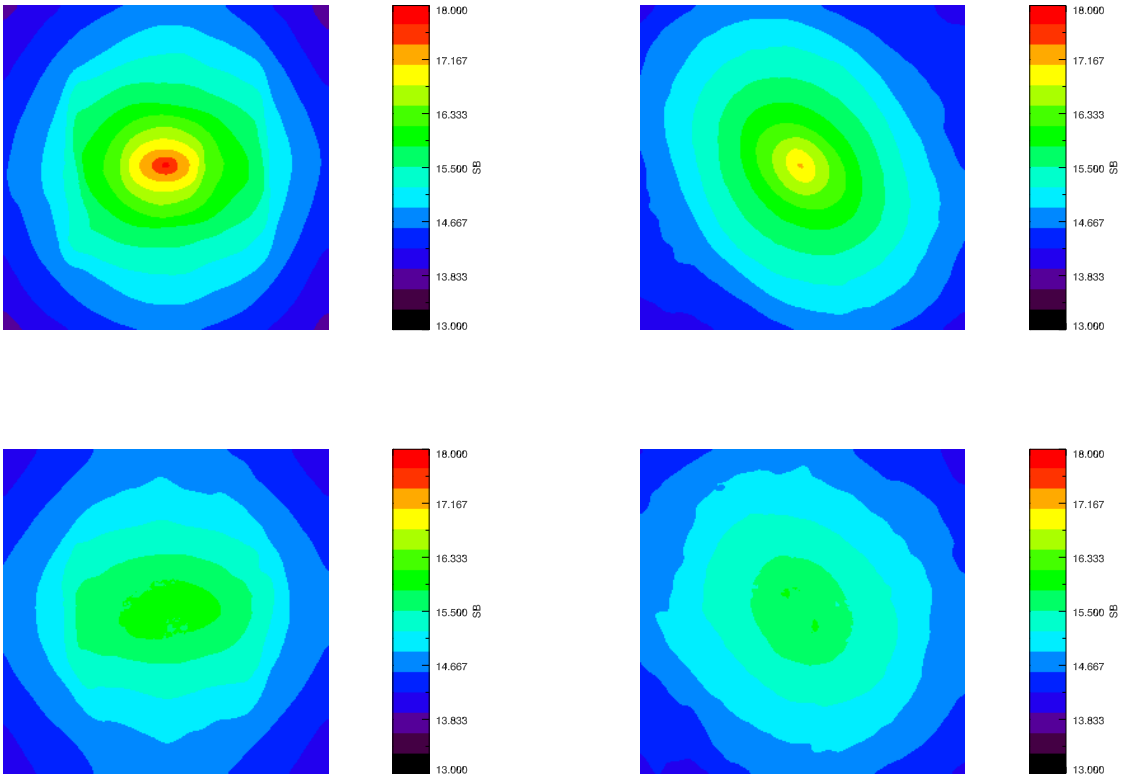

Figure 5.3: Surface brightness maps of the central 2 Mpc of the simulation volume for the 1:1 mergers after 13Gyr. Top line: $Sb(x, y)$ for the PL:PL merger. Bottom line: $Sb(x, y)$ for the 300:300 merger. Left column: $Sb(x, y)$ for the head on merger. Right: $Sb(x, y)$ for the small impact parameter merger.

5.3.3 End Configurations

At the end of the simulation, after 13 Gyr, all the surface brightness maps, see Fig. 5.3, show relaxed systems. In the PL:PL cases a high luminosity core is present; the CC has reformed. The ICM appears approximately spherical in the head on case and elliptical in the small impact parameter case. This is a consequence of the global rotation acquired by the remnant to conserve angular momentum. The 300:300 remnant does not show a strongly peaked emission in the core, but the remnant resembles the progenitors very closely. In no case appreciable substructure is present.

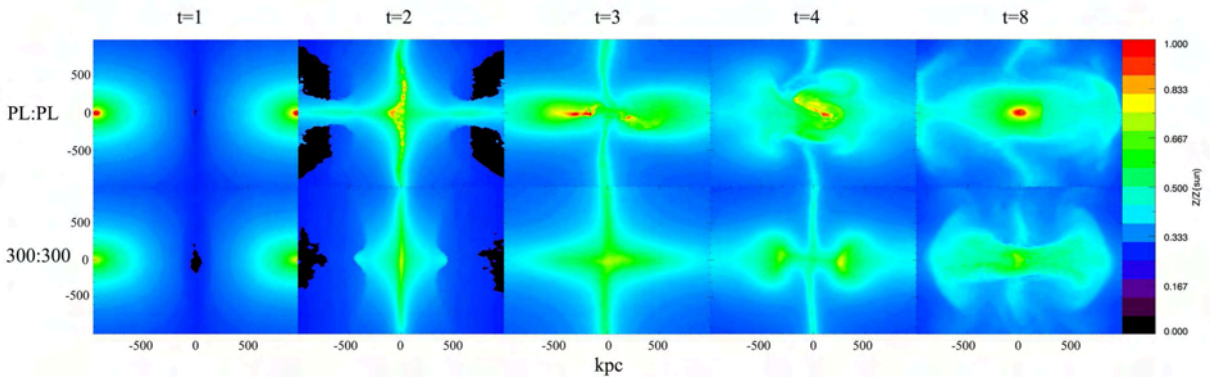

Figure 5.4: Emission weighted projected metallicity maps of the central 2 Mpc of the simulation volume during the head on $1:1$ merger. From top to bottom: (i) PL:PL, (ii) 300:300. In each row from left to right $t = 1, t = 2, t = 3, t = 4, t = 8$ Gyr.

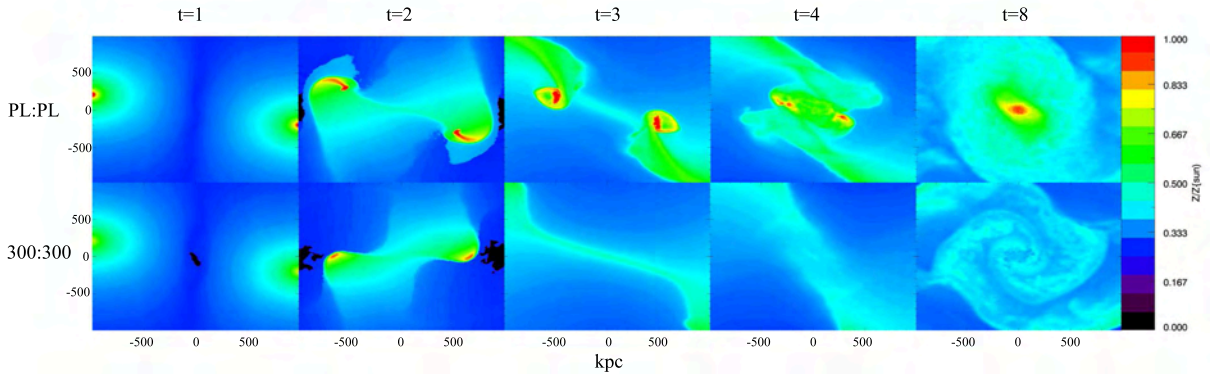

Figure 5.5: Emission weighted projected metallicity maps of the central 2 Mpc of the simulation volume during the small impact parameter $1:1$ merger. From top to bottom: (i) PL:PL, (ii) 300:300. In each row from left to right $t = 1, t = 2, t = 3, t = 4, t = 8$ Gyr.

5.4 Metallicity evolution

The emission weighted metallicity maps tell a different story. Figures 5.4 and 5.5 show the maps at 1, 2, 3, 4 and 8 Gyr for the head-on and small impact parameter cases respectively. The initial metallicities are set by equation (5.8). The measured $Z(r)$ is very different for the PL and the 300 case already in the first snapshots before any interaction actually took place. This is clear as $L \sim \rho^2$ and the two classes of clusters have different densities in the cores, $\rho_{PL} \sim r^{-4}$ and $\rho_{300} \sim r^{-3/2}$, because of the different initial entropy profiles. As in the previous section, we

describe now the merger evolution from the metals distribution point of view. Refer to figures 5.4 and 5.5 for a pictorial representation of the main evolutionary phases.

5.4.1 Head On Merger

At $t = 1$ Gyr the newly developed contact shock that is visible in the surface brightness maps had no consequence on $Z(x, y)$. The first, dramatic, effects of the merger process are evident at $t = 2$ Gyr. When the cores collide and interact with the standing shock the original metal core is seriously disrupted. High metallicity parcels of gas follow closely the high surface brightness gas identified in Fig. 5.1, second panels. High metallicity gas is "squeezed" along the direction of the standing shock and of the motion in the shape of a cross. This structure is evident both in the PL:PL and in the 300:300 cases. At $t = 3$ Gyr the cores have reached their apocentre. In the PL:PL case the small parcels of metals that were defined in the previous snapshot have merged together. Two well defined metal cores are in fact visible but severely distorted. The 300:300 merger does not show the same richness in substructure. At $t = 4$ Gyr, when the secondary accretion episode takes place, the PL:PL and the 300:300 mergers appear extremely different. In the first case a core has almost reformed. Parcels of high metallicity gas are still merging and in general they show a complex and irregular morphology. At intermediate radii complex structures are present. Plumes of gas with $Z \sim 0.5Z_{\odot}$ is concentrated in plumes embedded in low metallicity, $Z \sim 0.3Z_{\odot}$, gas. The gas that was concentrated along the standing shock is starting to break up and to fall onto the central regions of the newly formed cluster. The 300:300 case show two lobes of gas with $Z \sim 0.5Z_{\odot}$. Within the lobes there are small parcels with $Z \sim 0.8Z_{\odot}$ in arc-like structures. The stripes of metals along the shock are still well defined. The extreme right panels in Fig. 5.4 show the systems after $t = 8$ Gyr in simulation time. Contrary to the surface brightness, none of the systems appear relaxed yet. In general the metals are not distributed spherically. In the PL:PL remnant a central core with $Z \sim Z_{\odot}$ has finally formed. Nevertheless, two side lobes with $Z \sim 0.5Z_{\odot}$ are still well defined and

the outskirts of the atmosphere show parcels of gas still being re-accreted onto the core. The 300:300 remnant present a very elongated morphology along the original direction of motion. A small $Z \sim 0.8Z_{\odot}$ core is barely visible. The two side lobes follow the surface brightness lobes visible in the lower rightmost panel in Fig. 5.1.

5.4.2 Off Axis Merger

The differences in the evolution of metals between the PL:PL and the 300:300 mergers that we put in evidence in the previous section are exacerbated by the presence of an initial angular momentum. As in the head on case, at $t = 1$ Gyr the newly developed contact shock that is visible in the surface brightness maps has no consequence on $Z(x, y)$. At $t = 2$ Gyr the cores have experienced a strong tidal interaction because of the pericentric passage. The tidal compression increases the metallicities even in the 300:300 case. In this case, $Z \sim Z_{\odot}$ is higher than the initial one. The high metal cores appear distorted and the effects of the induced rotation begin to be evident. Furthermore, the cores are connected by a bridge of gas with $Z \sim 0.5Z_{\odot}$. Tidal tails with $Z \sim 0.6Z_{\odot}$ are also very well defined. At $t = 3$ Gyr the cores are falling back toward the common centre of mass. The differences between the PL:PL and the 300:300 become striking. In the PL:PL merger there are two well defined high metallicity core showing the effects of rotation and connected through a bridge with $Z \sim 0.5Z_{\odot}$. In the 300:300 case no structure is visible, except the bridge with $Z \sim 0.5Z_{\odot}$ connecting two lumpy structures just on the edge of 2 Mpc volume presented in Fig. 5.5. It is interesting to compare with the corresponding surface brightness map. The two structures do not correlate at all at this stage. At $t = 4$ Gyr the second close encounter has taken place. The PL:PL case shows two distorted cores with $Z \sim Z_{\odot}$ embedded in a common envelope with $Z \sim 0.6Z_{\odot}$. Tidal tails with the same metal content are still visible. In the 300:300 case a core structure with $Z \sim 0.4Z_{\odot}$ is being formed by the central parts of the tidal tails. Again there is no correlation with the observed structures in the surface brightness maps. After $t = 8$ Gyr in simulation time

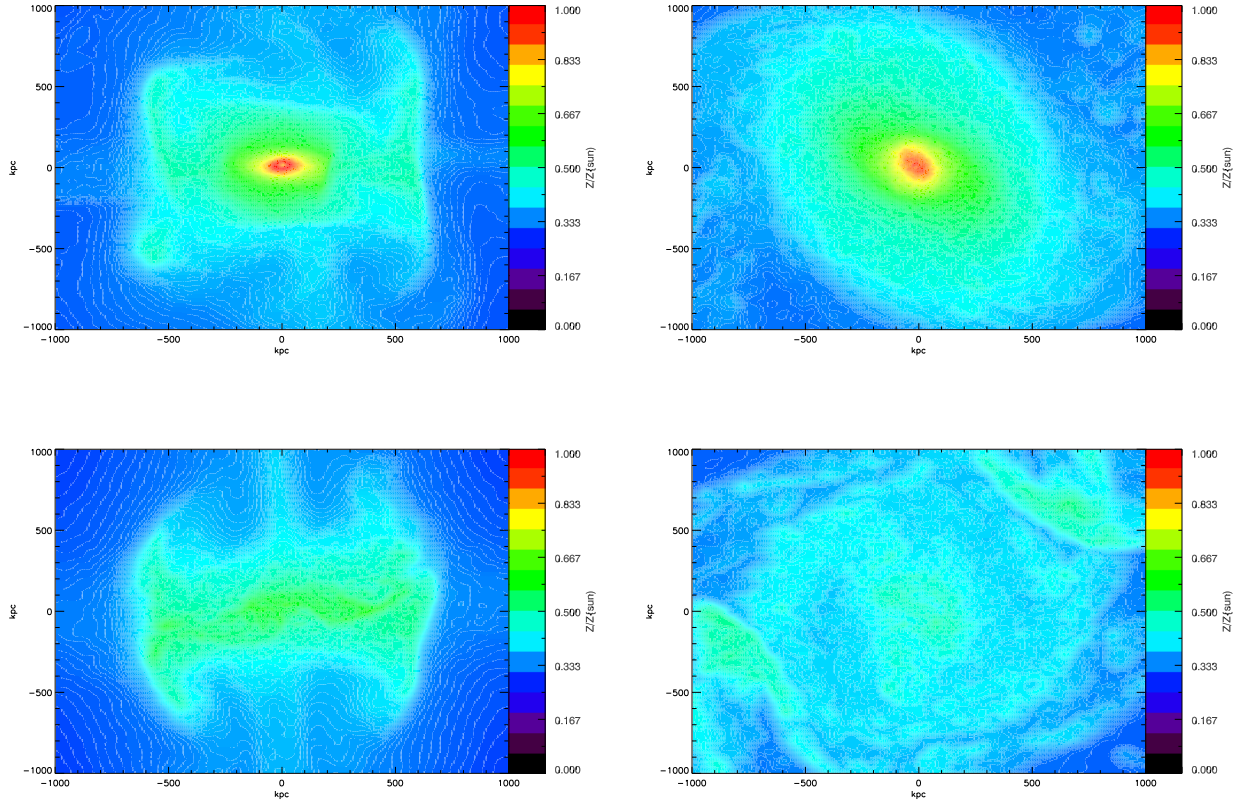

Figure 5.6: The end luminosity weighted metallicity maps for the 1:1 merger. Top line: $Z(r)$ for the PL:PL merger. Bottom line: $Z(r)$ for the 300:300 merger. Left column: $Z(r)$ for the head on merger. Right: $Z(r)$ for the small impact parameter merger.

the PL:PL remnant appear relaxed and with a well defined $Z \sim Z_{\odot}$ core. The outer parts of the atmosphere still show some parcels of gas in the process of being accreted onto the core. The 300:300 remnant core is far from equilibrium. Metals are distributed in an irregular spiral structure whose $Z \sim 0.4Z_{\odot}$. Two lumps of $Z \sim 0.5Z_{\odot}$ are visible on the edge of the 2 Mpc map.

5.4.3 End Configurations

The metal distributions at the end of each simulation, Fig. 5.6, picture a different situation compared to the surface brightness, Fig. 5.3. In the PL:PL cases, top row in Fig. 5.6, a central

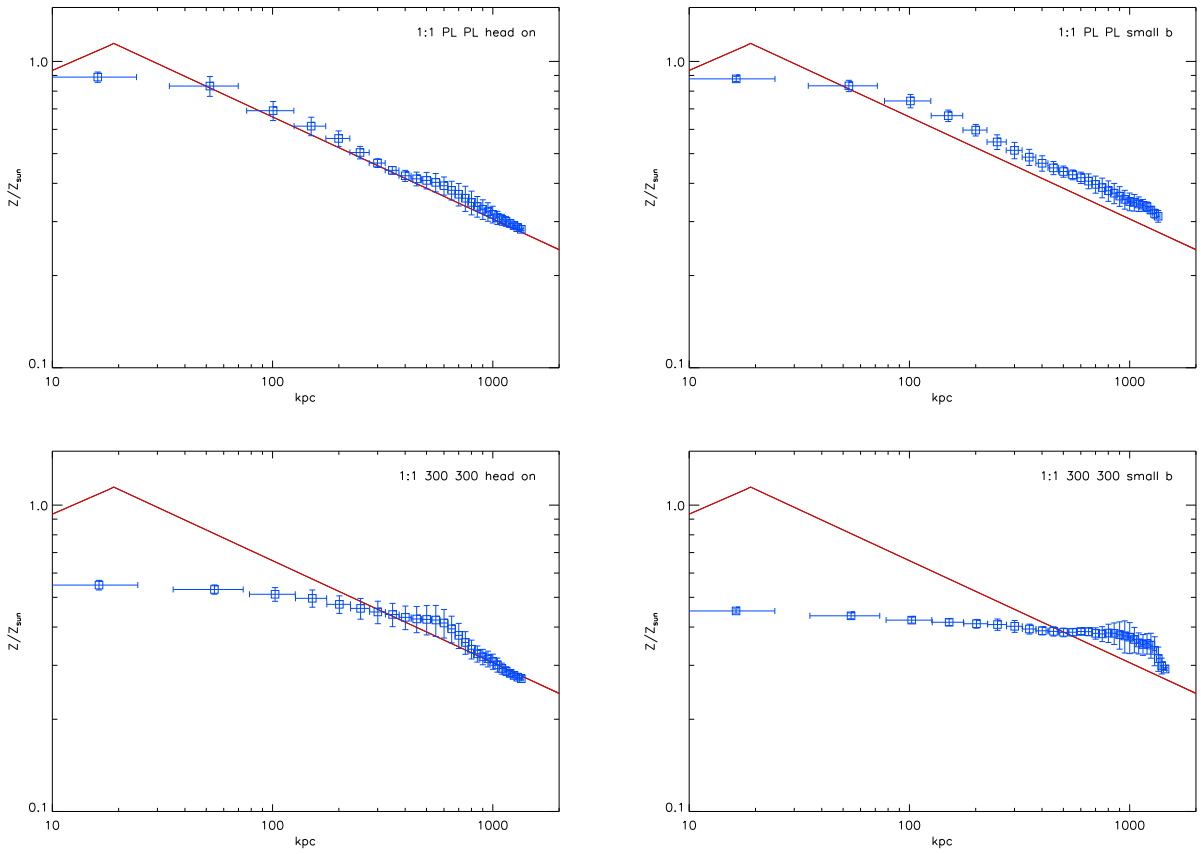

Figure 5.7: The luminosity weighted metallicity profiles for the 1:1 mergers after 13Gyr. In all panels the red solid line is the initial metallicity in the primary clusters, equation (5.8). Top line: $Z(r)$ for the PL:PL merger. Bottom line: $Z(r)$ for the 300:300 merger. Left column: $Z(r)$ for the head on merger. Right: $Z(r)$ for the small impact parameter merger.

$Z \sim Z_{\odot}$ core is evident and coincides with the maximum of the surface brightness, top row in Fig. 5.3. We deduce that the central core is re established after the merger transients. Nevertheless the head on mergers leave some signatures in the metal distribution. At intermediate radii, $r \sim 500$ kpc, substructures are present. Two almost symmetric $Z \sim 0.6Z_{\odot}$ fronts lay perpendicular to the initial direction of motion. In the small impact parameter case instead no substructure is present. Considering that in nature most of the mergers are off axis, we expect that, in general, observations of CC remnants will not show appreciable substructures. The 300:300 head on case is similar to the PL:PL one. The main difference is the absence of a well defined central high Z core. Instead we observe an elongated structure with almost constant $Z \sim 0.6Z_{\odot}$. At intermediate radii, $r \sim 500$ kpc,there are two almost symmetric $Z \sim 0.5Z_{\odot}$ fronts. In case of initial angular momentum, the 300:300 remnant is clearly not in a relaxed state yet. In the core the spiral structure with $Z \sim 0.4Z_{\odot}$ is still clear and in the corners of the panel there are parcels of high Z gas still in the process of being accreted onto the newly formed cluster. The metal distribution is complex and far from reaching an equilibrium state even after 13 Gyr. Thus we deduce that observations of NCC merger remnants will most likely reveal this level of complexity and substructures. In this scenario the degree of substructure could be in principle used as a probe of the initial conditions of the progenitors ICM. Hot progenitors will give birth to complex and unrelaxed metal morphologies while cold progenitors will give birth to smoother progenies.

Most observational studies concentrate on the determination of one dimensional profiles. Therefore it is useful to compare the predictions from our simulations to observed $Z(r)$ profiles. Fig. 5.6 shows the emission weighted emission maps after 13 Gyr in simulation time. Consistently with what already observed in idealized two-body merger simulations, mergers between CC clusters, top line in Fig. 5.7, do not manage to destroy metal profiles (Poole et al. 2008). This is true for both the orbital configurations we considered in this work. Mergers between NCC clusters tell instead a different story, bottom row Fig. 5.7. At the end of the

simulations metal gradients are strongly suppressed, more if the initial angular momentum is different from zero, and our synthetic profiles are consistent with observations in post merger NCC systems (De Grandi & Molendi 2001; Leccardi & Molendi 2008; Leccardi, Rossetti, & Molendi 2010). In view of our observation, would be extremely interesting to have a large set of high resolution metal maps of the ICM for these flat $Z(r)$ systems. Firstly, the comparison between Fig. 5.11 and Fig. 5.7 shows how the process of averaging over the angles to obtain a one dimensional profile flushes away the amount of substructure that could be observed. Secondly, and most important in our opinion, high resolution maps could allow to probe the initial state of the ICM of the progenitors by comparing with a large set of simulations like the one we produced.

Since the amount of kinetic energy available to the two classes of mergers we are considering in this chapter is the same, what drives the substantial differences we observed? To understand their physical causes we devoted the rest of our investigation to the amount of entropy generated during the merger and to the correspondent amount of mass mixing taking place in the process.

5.5 Entropy Generation and Mixing

The issue of entropy generation during lumpy accretion has been already tackled in McCarthy et al. (2007). As a result of their study of idealized mergers, the authors improved our understanding of shock heating by proposing a two stage heating model that properly describes their observations. From the definition of entropy $S = P\rho_{gas}^{-5/3} \propto T\rho_{gas}^{-2/3}$. Self-similarity means that all systems are structural copies of each other, therefore the characteristic entropy depends only on the temperature of the system. From the virial theorem $M \propto T^{3/2}$ so finally $S \propto M^{2/3}$. Figures 5.8 and 5.9 show the entropy generated during the merger process in the head on and in the small impact parameter cases as a function of the mass enclosed by each particle. In

both plots the top row shows the PL:PL while the bottom row shows the 300:300 case and at the evolutionary stages identified in section 5.3. In the PL:PL case clear episodes of entropy generation can be identified; these correspond to the main merger evolution phases as described in section 5.3. As noted in McCarthy et al. (2007), the bulk of the entropy generation happens in two stages. At $t = 2$ Gyr when the colliding cores start their interaction and at $t = 4$ Gyr when the cores finally merge. The resulting system has an entropy that approximately agrees with the self-similar prediction. The main deviations from self-similarity are registered at the core, $M_{gas} < 0.1 M_{gas,tot}$, and at the outskirts, see the top row of Fig. 5.10. The core of remnant is substantially heated by the merger, its final entropy is several factors higher than the original entropies of the progenitors, contrary to what found in Ricker & Sarazin (2001). Nonetheless the transferred heat is not enough to destroy the core as the top row in Fig. 5.3 shows. Our simulations confirm that mergers between CC systems do not erase the cool core. Consistently with what found by Gómez et al. (2002) and Poole et al. (2008), the cool core is in fact effectively disrupted by the merger, but quickly reestablished after few Gyr. In case of initial angular momentum, the amount of entropy generated is higher. This is related to viscous dissipation of angular momentum. In the head on 300:300 merger, no entropy is produced in excess of the self-similar prediction. In the small impact parameter case instead the remnant is slightly heated in excess of the self-similar expectation but only for $\sim 1\%$ in mass. In all panels is evident an excess entropy generation at large masses (or, equivalently, at large radii). This is artificial and due to poor density estimates near the edges of the idealized systems (McCarthy et al. 2007).

Examination of the entropy generation during a merger event, see figures 5.8, 5.9 and 5.10, demonstrates that heating takes place preferentially in the lowest entropy gas. In fact we find the highest increases in entropy in the core of the remnant of the PL:PL merger, while the already hot 300:300 is only moderately heated. In both cases we observe a large scatter in the final entropy. This large scatter implies that mixing is taking place. In Fig. 5.11 the enclosed gas mass at the end of each simulation, corresponding to $t = 13$ Gyr, is plotted. The enclosed gas

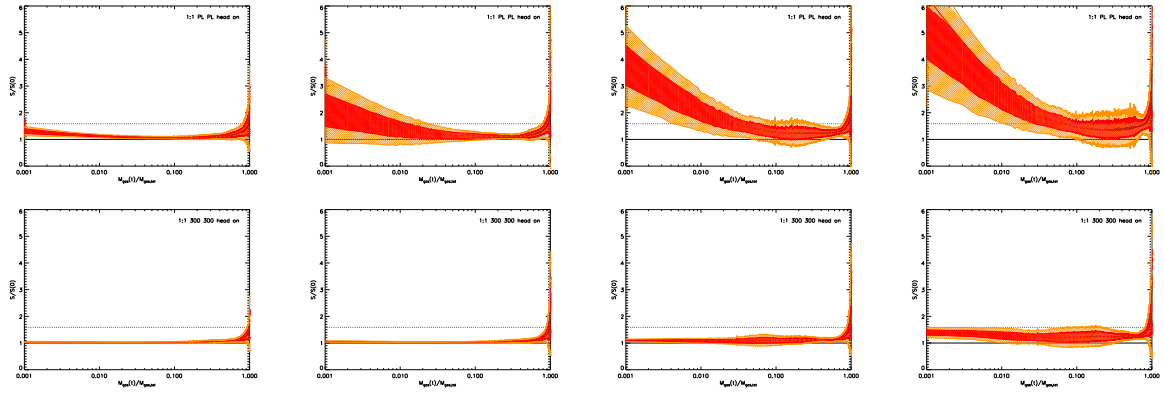

Figure 5.8: Entropy generation during the head on $1:1$ merger as a function of the enclosed gas mass. The enclosed gas mass for each particle is calculated by summing the masses of all other particles with entropies lower than the particle under consideration. The dashed line is the self similar prediction $S \propto M^{2/3}$. From top to bottom: (i) PL:PL, (ii) 300:300. In each row from left to right $t = 2, t = 3, t = 4, t = 8$ Gyr. The red contours represent 68% of the particles while the yellow contours represent 94%.

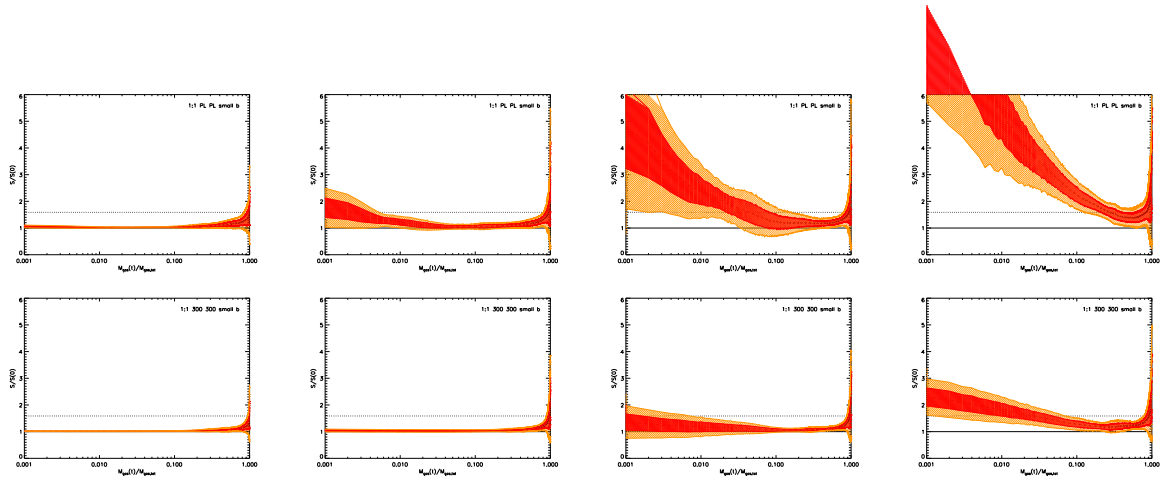

Figure 5.9: Entropy generation during the small impact parameter $1:1$ merger as a function of the enclosed gas mass. The dashed line is the self similar prediction $S \propto M^{2/3}$. From top to bottom: (i) PL:PL, (ii) 300:300. In each row from left to right $t = 2, t = 3, t = 4, t = 8$ Gyr. Lines and colours as in Fig. 5.8.

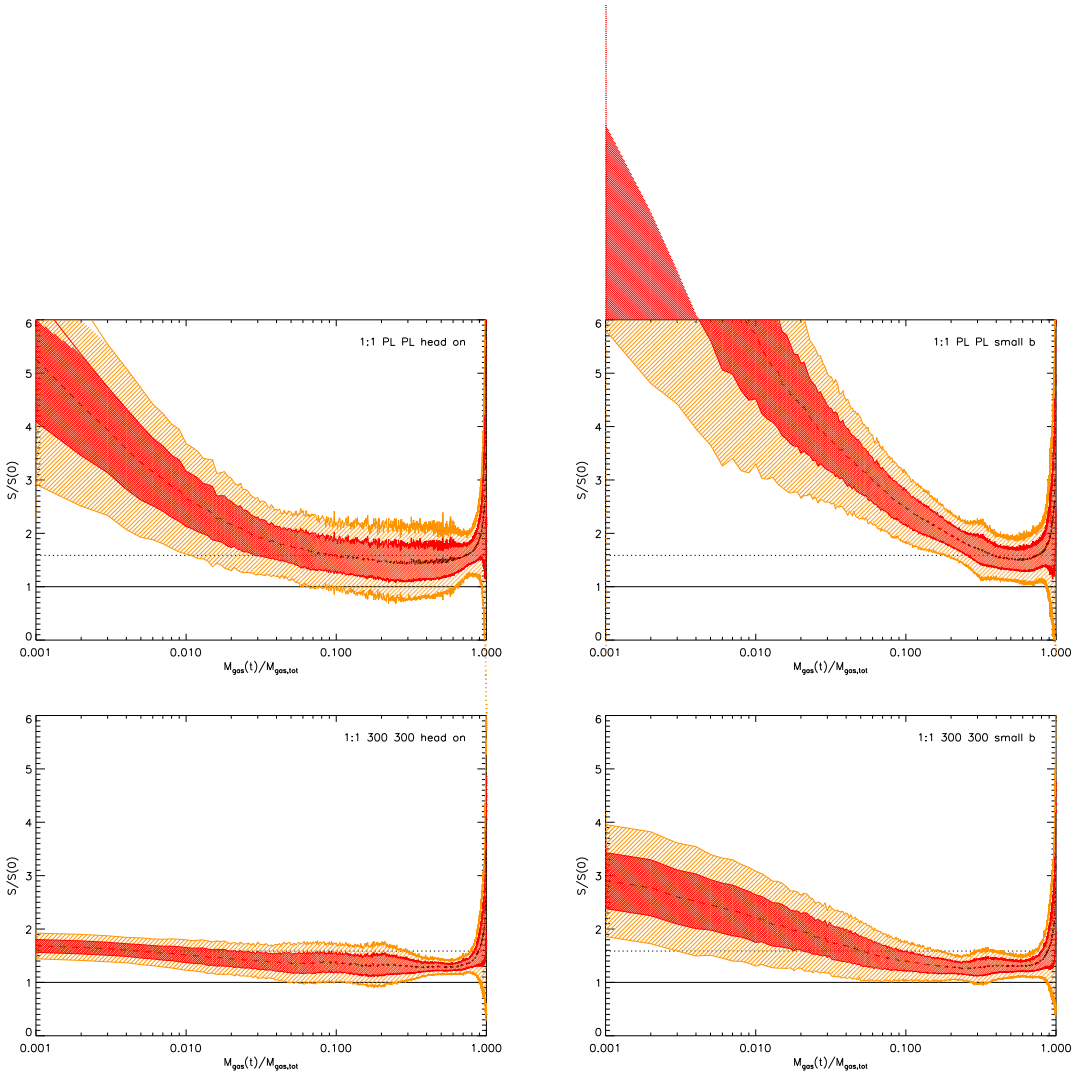

Figure 5.10: The entropy jump as a function of the cumulative mass at the end of the 1:1 merger simulations. From top to bottom: entropy jumps for increasing initial central entropy. From left to right: entropy jumps for increasing initial impact parameter. In each panel the dotted line represents the self similar prediction. The dashed line is the mean value. The red contours show the entropy jump for the 68% percent of the particles while the yellow contours show the 94%. The entropy jump in the outer boundary is artificial.

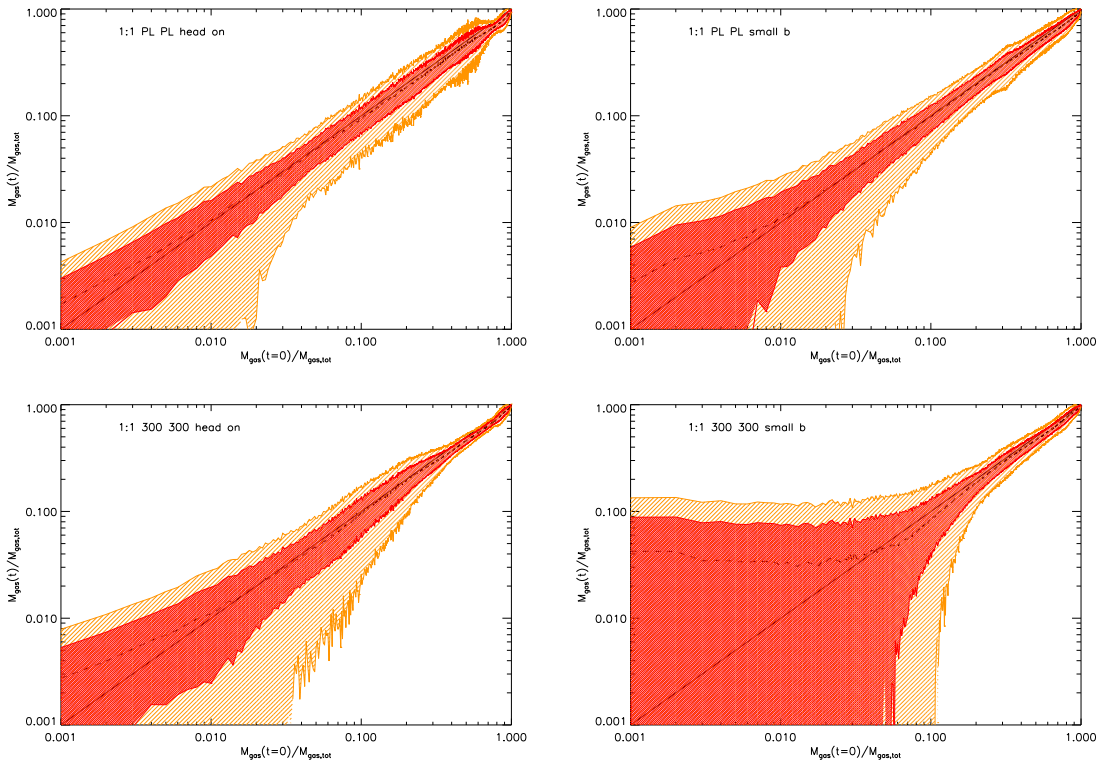

Figure 5.11: The enclosed gas mass of particles at the end of the 1:1 merger simulations as a function of the initial enclosed gas mass. The enclosed gas mass is calculated by summing the masses of all the particles having entropy less than the particle under consideration. Top row: PL:PL merger. Bottom row: 300:300 merger. The left panels show the head on merger while the right panels show the small impact parameter case. The red contours show the mass enclosure for the 68% percent of the particles while the yellow contours show the 94%. The dashed line is the mean value. The 300:300 merger induce a much higher degree of mixing compared to the PL:PL case.

mass of each particle is calculated by summing the masses of all other particles with entropies lower than the particle under consideration. This plots shows that a substantial amount of gas mixing takes place especially in the small impact parameter and high initial core entropy case, bottom right panel in Fig. 5.11.

In the PL:PL cases only $\sim 1\%$ of the mass experience a substantial mixing. This agrees with the expectation that CC systems are in general more relaxed and closer to an equilibrium state. In the 300:300 cases up to $\sim 10\%$ in the small impact parameter merger is efficiently mixed. This is the reason why in this extreme case the measured metallicity profile, Fig. 5.7, appears

approximately flat and the two dimensional maps, Fig. 5.6, shows a complex morphology.

5.6 Discussion

In this section we discuss our main results and interpret them in view of possible observational signatures and predictions. We start by identifying what drives the mixing responsible for the metallicities we observe in our simulations. We then discuss the effects of neglecting radiative cooling in our simulations.

5.6.1 What drives the mixing?

The recent study from Mitchell et al. (2009) about differences between SPH and AMR codes suggests that our observations are not an artefact induced by the details of the numerical scheme implemented to solve Euler equations. In reality SPH tends to underestimate mixing (Springel 2010) as a consequence of suppression of fluid instabilities (Agertz et al. 2007). With these considerations, the results presented here should be treated as a lower limit to the actual amount of mixing taking place.

High entropy gas is more susceptible to fluid instabilities as buoyancy and convection. In a stratified atmosphere the bulk buoyancy properties of the gas are described by the Brunt-Väisälä (BV) frequency. In general the BV frequency ω^2_{BV}, assuming pressure equilibrium between the buoyant parcel of fluid and the surrounding medium and spherical symmetry, is (Mihalas & Mihalas 1984)

$$\omega^2_{BV} = \frac{g}{c_s^2 \rho}\left[\frac{\partial P}{\partial r} - c_s^2 \frac{\partial \rho}{\partial r}\right] \tag{5.12}$$

where g is the gravitational acceleration and P, ρ and c_s are the pressure, density and sound speed of the ambient atmosphere respectively. Given the definition of entropy, we can rewrite the Brunt-Väisälä frequency as

$$\omega^2_{BV} = \frac{3g}{5}\frac{\partial \log S}{\partial r} \tag{5.13}$$

where we also assumed a mono atomic ideal gas to describe the ICM. Given that $\partial \log S/\partial r > 0$ in all configurations, the ICM results convectively stable and only harmonic buoyant oscillations of parcels of gas are possible. The PL and the 300 cases differ for the timescale of those oscillations. The buoyancy timescale $t_{buoy} \approx 1/\omega_{BV}$ is therefore

$$t_{buoy} \approx \sqrt{\frac{5}{3g}\left[\frac{\partial \log S}{\partial r}\right]^{-1}} \tag{5.14}$$

Since in the 300keV·cm^2 core $\partial \log S/\partial r << 1$, once a parcel of gas is displaced the time required to perform a whole oscillation is very long. This simple considerations explain the longer timescales observed in the 300:300 merger compared to the PL:PL.

In all the simulations we have performed, the effects of radiative cooling have been neglected. Potentially a particle could radiate the entropy it gained through heating before the gas has a chance to expand and settle to its new radius. It is therefore important to assess the magnitude of the impact that cooling will have on our result. The easiest way to do so is to compare the cooling time, the time to radiate the entropy away, with the sound crossing time, the time to expand and settle to the new radius. The cooling time (Peterson & Fabian 2006) is given by

$$t_{cool} \equiv \frac{\frac{5}{2}nkT}{n^2\Lambda} \tag{5.15}$$

$$\propto Sn^{-1/3}\Lambda^{-1} \tag{5.16}$$

where Λ is the cooling function and n is the number density. In a very crude approximation, we can take $\Lambda \approx 10^{-23}$ erg·s^{-1}·cm^3 and $n \approx 10^{-2}$ cm^{-3}. In this case t_{cool} becomes

$$t_{cool} \approx 0.1\frac{S}{\text{keV}\cdot\text{cm}^2}\text{Gyr} \tag{5.17}$$

We have already seen that the sound crossing time is given by

$$t_{cross} \equiv r/c_s \tag{5.18}$$

$$\propto r\left[S^{-1/2}n^{-1/3}\right] \tag{5.19}$$

In the same crude approximation as before, $n \approx 10^{-2}$ cm^{-3}, t_{cross} becomes

$$t_{cross} \approx 0.1\frac{r}{\text{kpc}}\left[\frac{S}{\text{keV}\cdot\text{cm}^2}\right]^{-1/2}\text{Gyr} \tag{5.20}$$

The radius of the core of the merger remnant is of the order of 200 kpc. Within this distance the amount of entropy gained in the core of the remnant is approximately a factor of 1.6 the entropy of the progenitors for the 300:300 case while ≈ 10 in the PL:PL case. This factor means that in the PL:PL case it would be radiated away in approximately 2 Gyr. The corresponding sound crossing time is of the order of 2.8 Gyr. In the 300:300 merger the gained entropy would be radiated away in 48 Gyr, while the gas expands in approximately 1 Gyr. Cooling is very important in the PL:PL case while does not affect at all the 300:300 case. The effect of cooling is to decrease the entropy further. This means that in the PL:PL case gas would mix even less efficiently that our estimate, so strengthening our conclusions.

We have then now a clear picture of what drives the mixing in a merger process. This can be resumed in a simple scheme:

- the atmospheres of the progenitors interact and a shock develops.
- as the cores collide, or go through their closest approach, they are shock heated. As the entropy increases, the shock heated gas expands. The efficiency of the expansion is set by the relative magnitudes of the sound crossing time, in which the gas expands, and the radiative cooling time, in which the gas radiates away the gained entropy.
- the heated gas is less dense than the surrounding and therefore it becomes buoyant. The

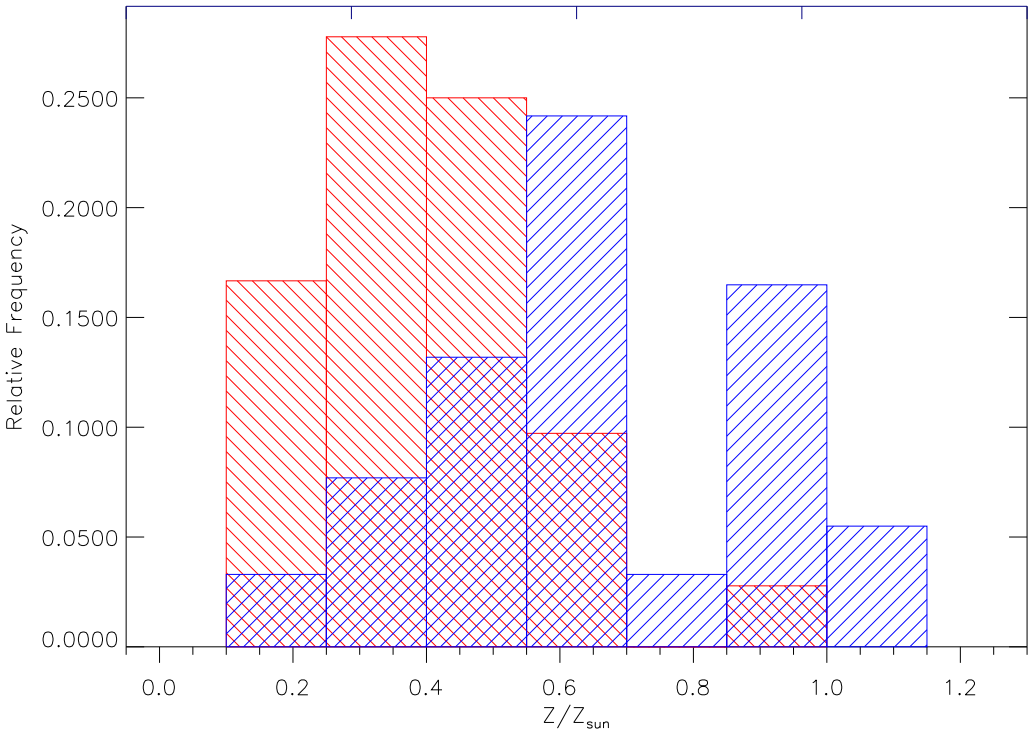

Figure 5.12: Distribution of core metallicities from the Cavagnolo et al. 2009 dataset. The colour code is: blue for low core entropy systems, red for high core entropy. The two classes populate two different areas in the plot. Low core entropy systematically corresponds to high core metallicity and vice versa.

entropy gradient acts against buoyancy, steeper gradients are more difficult to climb. Therefore, in an almost flat ambient entropy the heated gas can undergo wider oscillations and for longer.

5.6.2 Observational Signatures

The compelling evidence of strong merger influence over the thermodynamical and chemical state of the ICM is a source of major concern. Observations in fact require post mergers NCCs to show flat metallicity profiles (De Grandi & Molendi 2001; Leccardi & Molendi 2008; Leccardi, Rossetti, & Molendi 2010), and core entropy and core metallicity to be anti correlated (see Cavagnolo et al. 2009 or Fig. 5.12). Further evidence comes from the distribution of projected

offsets between the cluster X-ray centroid and the brightest cluster galaxy (BCG) (Sanderson, Edge, & Smith 2009b). There is a clear correlation between X-ray/BCG projected offset and the logarithmic slope of the cluster gas density profile at $0.04r_{500}$ and X-ray/BCG projected offset and BCG AGN activity. This implies that clusters without a cool core tend to be more dynamically disturbed and the corresponding BCGs tend to be in a quiescent state. BCG activity in fact is present only in those clusters whose central entropy is lower than ~ 30 kev·cm^2 (Rafferty, McNamara, & Nulsen 2008). At the same time two-body simulations of cluster mergers show the resilience of the CC and the impossibility of flattening the metal profiles by means of the merger alone (Poole et al. 2008). How to reconcile these opposing views? The results presented here suggest a simple way of understanding both the theoretical and observational issues and put them in a single consistent picture. We in fact considered mergers between CC-like systems, our PL case, *and* mergers between NCC-like systems, the 300 case. CC-like systems behaves exactly as expected from previous analogue work: their cool core is quickly re established after the merger event and the metal distribution is not significantly disrupted by the collision. NCC-like systems show instead very different features: because of their susceptibility to buoyancy, the core gas is mixed very efficiently by the merger, resulting in flat metallicity profiles in agreement with observations. So mergers can not transform CCs in NCCs, but given the existence of these two separate classes, mergers have significant different observational signatures in the two cases. On top of that, there is no need to transform a CC in a NCC if one accepts the preheating scenario (McCarthy et al. 2004). High resolution observations of merging and post-merging systems could be the most direct and efficient way to probe the state of the ICM of the progenitors because of the unique signatures left by the two classes of clusters.

Still our claim is somewhat unjustified, 1:1 mergers are currently very rare, so their influence over the evolution of the ICM is statistically marginal. Nevertheless, 3:1 and 10:1 mergers, that are much more common, show similar phenomena as the one we illustrated here using the 1:1 case. We defer an in depth study of these mass ratios to a future work.

5.7 Summary

In this chapter we studied a set of idealized two body merger simulations. In particular we concentrated on mergers between equal mass clusters and investigated the effects on the remnant of varying initial orbital configuration and initial core entropy. In particular we compared mergers between clusters whose entropy follow a pure power law profile similar to what observed in cool core (CC) clusters and clusters having a constant entropy floor in the core (NCC). This investigation is motivated the large scatter in core entropy observed in nature. We focused our analysis on the observational signatures in the metals distribution producing emission weighted maps as produced by X-ray satellites. In what follows the main results will be summarized:

- Mergers proceed through a set of common phases that are independent of the particular initial setup. Those phases were identified in Poole et al. (2006). After 4 Gyr since the beginning of the interaction, the surface brightness maps do not show any particular substructure. The PL:PL case clearly the presence of a well defined peak in the emission that can be identified with a cool core. In the 300:300 case the system requires longer to reach an equilibrium state compared to the PL:PL. The most cause for the slower time evolution in high core entropy clusters is the longer buoyancy timescales, resulting in slower and longer oscillations of shock heated gas.

- We investigated metals time evolution using emission weighted metal maps. The PL:PL metal maps trace closely the bulk of the gas evolution. In the 300:300 case the metals do not trace the bulk of the gas and a high metallicity core is never re established for the duration of our simulation. This results in flat metal profiles and complicated two dimensional morphologies. This confirms the merger scenario as an explanation for the observed metal profiles in NCC cluster of galaxies (De Grandi & Molendi 2001; Leccardi & Molendi 2008; Leccardi, Rossetti, & Molendi 2010). We also confirm the findings of Poole et al. (2008) that mergers between CC clusters do not destroy metal gradients.

- We quantified the amount of heating taking place during each simulation by studying entropy generation. Entropy is produced mainly during the first core interaction, approximately after 1 Gyr in simulation time, and in the core merger process after $\sim$ 4 Gyr. The amount of entropy generated is consistent with the self-similar expectation $S_{final} \propto M_{final}^{2/3} \approx 1.6 S_{init}$. The biggest deviations are observed when the merger is off-axis and in the very central regions of the remnant. In the PL:PL case the remnant core has a final entropy that is several factors higher than the progenitors, nevertheless the cool core reformed after few Gyr. Thus we confirm the findings in Gómez et al. (2002) and Poole et al. (2008).

- We investigated the amount of mixing taking place during a merger event. For this purpose we used enclosed mass plots. We found that in the PL:PL case only $\approx 1\%$ in mass is mixed. In contrast, up to $\approx 10\%$ is efficiently mixed in the 300:300 case. Mixing is driven by buoyancy that in turn is driven by shock heating. Shock heated gas expands and rises buoyantly. The buoyancy timescale is set by the entropy gradient, steeper gradients corresponding to shorter oscillations.

Bibliography

Agertz O., et al., 2007, MNRAS, 380, 963

Benson A. J., Bower R. G., Frenk C. S., Lacey C. G., Baugh C. M., Cole S., 2003, ApJ, 599, 38

Benson A. J., 2005, MNRAS, 358, 551

Bower R. G., Benson A. J., Malbon R., Helly J. C., Frenk C. S., Baugh C. M., Cole S., Lacey C. G., 2006, MNRAS, 370, 645

Bower R. G., McCarthy I. G., Benson A. J., 2008, MNRAS, 390, 1399

Cavagnolo K. W., Donahue M., Voit G. M., Sun M., 2009, ApJS, 182, 12

Cohn J. D., White M., 2005, APh, 24, 316

De Grandi S., Molendi S., 2001, ApJ, 551, 153

Gómez P. L., Loken C., Roettiger K., Burns J. O., 2002, ApJ, 569, 122

Kapferer W., et al., 2006, A&A, 447, 827

Leccardi A., Molendi S., 2008, A&A, 487, 461

Leccardi A., Rossetti M., Molendi S., 2010, A&A, 510, A82

Liedahl D. A., Osterheld A. L., Goldstein W. H., 1995, ApJ, 438, L115

Loewenstein M., 2001, ApJ, 557, 573

Lovisari L., Kapferer W., Schindler S., Ferrari C., 2009, A&A, 508, 191

Markevitch M., et al., 2000, ApJ, 541, 542

Markevitch M., Vikhlinin A., 2001, ApJ, 563, 95

McCarthy I. G., Balogh M. L., Babul A., Poole G. B., Horner D. J., 2004, ApJ, 613, 811

McCarthy I. G., et al., 2007, MNRAS, 376, 497

McCarthy I. G., Babul A., Bower R. G., Balogh M. L., 2008, MNRAS, 386, 1309

McNamara B. R., Nulsen P. E. J., 2007, ARA&A, 45, 117

Mewe R., Gronenschild E. H. B. M., van den Oord G. H. J., 1985, A&AS, 62, 197

Mihalas D., Mihalas B. W., 1984, ”Foundations of Radiation Hydrodynamics”, Dover Publications, New York

Mitchell N. L., McCarthy I. G., Bower R. G., Theuns T., Crain R. A., 2009, MNRAS, 395, 180

Mori M., Burkert A., 2000, ApJ, 538, 559

Navarro J. F., Frenk C. S., White S. D. M., 1997, ApJ, 490, 493

Poole G. B., Fardal M. A., Babul A., McCarthy I. G., Quinn T., Wadsley J., 2006, MNRAS, 373, 881

Poole G. B., Babul A., McCarthy I. G., Fardal M. A., Bildfell C. J., Quinn T., Mahdavi A., 2007, MNRAS, 380, 437

Poole G. B., Babul A., McCarthy I. G., Sanderson A. J. R., Fardal M. A., 2008, MNRAS, 391, 1163

Rafferty D. A., McNamara B. R., Nulsen P. E. J., 2008, ApJ, 687, 899

Rasera Y., Lynch B., Srivastava K., Chandran B., 2008, ApJ, 689, 825

Ricker P. M., Sarazin C. L., 2001, ApJ, 561, 621

Sanderson A. J. R., O’Sullivan E., Ponman T. J., 2009, MNRAS, 395, 764

Sanderson A. J. R., Edge A. C., Smith G. P., 2009, MNRAS, 398, 1698

Sauvageot J. L., Belsole E., Pratt G. W., 2005, A&A, 444, 673

Sijacki D., Pfrommer C., Springel V., Enßlin T. A., 2008, MNRAS, 387, 1403

Sivanandam S., Zabludoff A. I., Zaritsky D., Gonzalez A. H., Kelson D. D., 2009, ApJ, 691, 1787

Springel V., 2010, MNRAS, 401, 791

Springel V., Yoshida N., White S. D. M., 2001, NewA, 6, 79

Springel, V., 2005, MNRAS, 364, 1105

Springel V., Hernquist L., 2002, MNRAS, 333, 649

Voit G. M., Kay S. T., Bryan G. L., 2005, MNRAS, 364, 909

White R. E., III, 1991, ApJ, 367, 69

Zaritsky D., Gonzalez A. H., Zabludoff A. I., 2004, ApJ, 613, L93

6. Future Developments

Abstract

In this chapter the main results of this thesis will be summarized. Prospects for future work will be presented.

6.1 Summary of the main results

In this thesis different aspects of modern astrophysical research have been investigated. In Chapter 3 we introduced a Bayesian framework for performing test of General Relativity using future gravitational waves observations. In Chapter 4 we calculated the distribution of super massive black holes (SMBHs) in the local Universe and investigated its environmental dependence as well as its relation to AGN activity. In Chapter 5 we investigated the evolution of idealized two body mergers. In the context of galaxy clusters, we focused on the evolution of metal abundance.

In what follows, the main results of each chapter will be summerized:

Chapter 3

- We have developed a rigorous framework to systematically compare alternative theories of gravity. It is based on the Bayesian model selection method. We are able to compute Bayes factors between alternativs and thus discriminate between their predictions.

- We applied our framework to the emission of gravitational waves from non-spinning compact binary systems inspiral in two competing theories: (i) 2nd order Post-Newtonian General Relativity (GR); (ii) 2nd order Post-Newtonian General Relativity plus the additional contribution of a massive graviton (MG). Advanced LIGO is expected to be able to detect an MG gravitational wave for Compton wavelengths $\lambda_g \leq 5 \times 10^{15}$m, of the order of Solar System bounds (Will 1998).

- We investigated the potential bias that might be introduced by using non correct models to analyse gravitational waves data (Yunes & Pretorius 2009). The analysis of MG gravitational waves data using the GR model results in biased measurements of the symmetric mass ratio η. The main factor governing the bias is the number of cycles of the neglected factor entering the detector band.

- We investigated the bounds that Advanced LIGO and the Einstein Telescope should be able to put on the Compton wavelength λ_g of the graviton. We deduce that, independent of the details of the sources , Advanced LIGO will produce a bound $\lambda_g \geq 10^{16}$m and the Einstein Telescope $\lambda_g \geq 10^{17}$m.

- We developed an algorithm to combine multiple datasets to maximise the information extracted from the data. We proved that it leads to an order of magnitude improvement on the 95% lower limit on λ_g compared to the best single observation.

Chapter 4

- We used SDSS DR6 in concert with 2MASS and FIRST to identify potential BH hosts using a colour based scheme (Sample A), a morphology based scheme (Sample B) and the width of the H_α line (Sample C). Investigating the colour and morphology properties of the samples, we discovered a substantial fraction of Sample A galaxies not classified morphologically as early types. At the same time, we identified an analogous fraction of Sample B galaxies not characterised by red colours. We interpreted these as ”red spirals” and ”blue ellipticals”.

- We constructed the SMBHMF for the whole SDSS DR6 galaxy catalogue both for the inactive and the optically active population of BHs. Our findings are consistent with previous studies.

- We constructed the SMBHMF in clusters and groups both for the inactive and the optically active population of BHs. We find an excess of massive BHs compared to the field. We interpret this as a manifestation of the hierarchical assembly of structures leading to enhanced accretion rates onto BHs living in high density environments. The optical active population in clusters is supressed by a factor ~ 100 compared to the field and to groups. This is likely an effect of ram pressure striping.

- Using FIRST radio power measurements, we calculated the radio-active fraction for field and group/cluster galaxies. In the first case, we find a dependence on $M_{\bullet}^{1.6}$ in agreement with Best et al. (2005). Field Sample C galaxies show a constant RAF with $M_{\bullet}$. Sample A group and cluster galaxies have a probability of being radio-loud that is a factor of two higher than their field counterparts. Sample B group and cluster galaxies do not show this increased probability. We interpret the RAF as evidence for increased accretion rates in dense environment, in accordance to cosmological simulations (Colberg & Di Matteo 2008). Sample B galaxies do not show increased probability because their are likely going through a star-forming phase that decreases the amount of fuel available for the central BH.

- As a result of ram pressure striping, satellite galaxies in clusters show a RAF that depends on $M_{\bullet}$ stronger than their field and group counterparts; $f_{radio-loud} \sim M_{\bullet}^{2.3}$. This predicts that satellite galaxies should obey to $L_X \sim \sigma_{\rm star}^{10}$ in contrast to isolated and central galaxies where $L_X \sim \sigma_{\rm star}^{7}$.

- Using the BH fundamental plane relation of Falcke et al. (2004), we obtain a X-ray Luminosity Functions (XLFs) in the soft and hard bands. We compare our predictions with Hasinger et al. (2005) and Aird et al. (2009) and find excellent agreement. We also infer the fraction X-ray bright AGNs in clusters and in groups. Our fractions agree very well with what found by Martini et al. (2006), Martini et al. (2007) and Sivakoff et al. (2008).

- We interpret the different modes of AGN activity as a direct manifestation of the accretion rate distribution. From the number of galaxies in our radio samples, we estimate the fraction of systems in each accretion state: (i) Sub-Eddington rate, 5%; (ii) Eddington rate, 0.3%; (iii) Super-Eddington rate, 0.01%.

Chapter 5

- We examined mergers between equal mass clusters of galaxies. We considered two initial orbital configurations and two initial entropy distributions. In particular we concentrated on a pure power law (PL) and on a pure power law plus an entropy floor in the core (300keV·cm^2). These two alternative entropy setups are to be considered representative of cool core clusters (CC) and non cool core clusters (NCC).

- Regardless of the initial conditions, all mergers proceed through a set of common phases. The atmospheres of the progenitors interact and a shock develops and, as the cores collide, they are shock heated and their entropy is boosted. In the PL:PL case, the shock heats the gas preferentially in the core resulting in an entropy boost of a factor $\sim$10. Outside the core the entropy is generated in a manner consistent with self-similarity. In the 300:300 case, entropy is generated consistently with the self-similar expectation. Shock heating decreases the gas density. Heated gas parcels become buoyant and undergo oscillations in the ambient atmosphere. The entropy gradient acts against buoyancy, flatter gradients result in wider and longer oscillations.

- Buoyancy drives gas mixing. As a result of the enhanced mixing in NCC mergers, final metallicity profiles appear flat and consistent with observations of NCC post merger remnants (Leccardi, Rossetti, & Molendi 2010).

- In agreement with previous numerical work (Poole et al. 2008), we find that mergers between CC systems do not destroy the progenitor's metallicity gradient.

6.2 Further Work

6.2.1 Post Einstein Formalism

The formalism presented in Chapter 3 can be easily extended to a network of multiple detectors (Veitch & Vecchio 2010) and to any gravitational wave model. In particular a study of the so-called "Post Einstein" formalism (PPE) (Yunes & Pretorius 2009) in being undertaken. The PPE is analogous to the Post Newtonian formalism (Blanchet 2009), but model waveforms are enhanced in a systematic and well-motivated manner by parameters that can measure deviations from General Relativity. For instance, in a compact binary system, the simplest form that a 2nd order PPE waveform assumes is (Yunes & Pretorius 2009):

$$h(f) = h_{GR}(f)(1 + \alpha u^a)e^{\imath\beta u^b} \tag{6.1}$$

where $u = \pi f \mathcal{M}$ is the inspiral reduced frequency and $\mathcal{M}$ is the chirp mass. The GW is described by a chirping complex exponential, consisting of the GR component h_{GR} corrected by PPE amplitude and phase functions with parameters (a, b, α, β). This PPE waveforms family employs the smallest number of ppE parameters necessary to reproduce corrections to the GW response function from well-known alternative theories of gravity in the inspiral phase. For instance:

- $(a, b, \alpha, \beta) = (a, b, 0, 0)$ reproduces GR;
- $(a, b, \alpha, \beta) = (a, -7/3, 0, \beta_{BD})$ reproduces Brans-Dicke theories;
- $(a, b, \alpha, \beta) = (a, -1, 0, \beta_{MG})$ reproduces Massive Graviton theories;
- $(a, b, \alpha, \beta) = (1, b, \alpha_{CS}, 0)$ reproduces Chern-Simmons modified gravity.

In Chapter 3, we showed that, when the effects of additional parameters in the data analysis template are neglected, parameter estimates are biased. In the future, we plan to extend our

simplistic study to the more realistic PPE family of waveforms. In fact, depending on whether the signal is a GR or non-GR one and whether the template is a GR or PPE one, one can attempt to answer several important questions that are critical to data analysis. For example, with a non-GR signal and a GR template, one can determine how much systematic error induced by fundamental bias might contaminate parameter estimation and perhaps even signal extraction (depending on SNR). Alternatively, given a non-GR signal and a ppE template, one can attempt to determine how well GW observations can truly constrain generic GR deviations.

6.2.2 Black Hole Mass Function and AGN time evolution

In Chapter 4, we use wide-field survey to investigate the influence of the environment on the distribution of SMBHs and radio-loud AGNs in the local Universe, $z < 0.1$. An analogous study could be performed using small area but deep surveys to investigate the redshift dependence of both the SMBH mass function and the Radio-Active Fractions ($f_{\rm radio-loud}$). For instance, very a deep study could allow, in principle, to understand when the $f_{\rm radio-loud} - - - M_\bullet$ relation was established and whether it evolves with cosmic time. If the suggestion in Best et al. (2005), and partly in 4.7.1, that $f_{\rm radio-loud} \sim M_\bullet^{1.5}$ is set by cooling is true, no evolution with z should be seen. Of course, this would require to be able to disentangle the dependence of $M_\bullet$ from z first.

Our classification of the environment can be considered quite shallow. We rely on third party catalogues to identify galaxy associations and then we only consider a richness criterion. The use of a better density estimator, such as Σ_5, would quantify exactly what the dependence of $f_{\rm radio-loud}$ and $M_\bullet$ on the local density is. In that case, we would be able to make exact, quantitative predictions about number density of BHs, of AGNs and their preferred mode, radio, optical or X-ray.

An issue that needs further clarification is the discrepancy between different $M_\bullet$ estimators, cfr. Fig.4.5. At the moment, no reasonable explaination is available. Probably, the Broad Line Region, where the emission lines are produced, is not in virial equilibrium, contrary to the

assumptions. This assumption is, in fact, the basis of methods similar to the one envisaged in Greene & Ho (2005).

6.2.3 Non Equal Mass Mergers

As shown in Table 5.1, we already have available a much larger set of merger simulations than the ones presented in Chapter 5. We plan to extend our analysis to all of them. In fact, we investigated the evolution of equal mass mergers whose initial entropy configurations are representative of the two extremes of the cluster populations, very cold and very hot cores. Those are not necessarily the best cases to consider given the wide scatter observed in core entropies (e.g. Cavagnolo et al. 2009). Furthermore, in a hierarchical Universe, structures grow mostly via mergers where the mass ratio is typically between 3:1 and 10:1 (Cohn & White 2005) rather than the 1:1 ration considered here. So the analysis of unequal mass mergers will allow to more easily put our results in a cosmological context and help to improve our understanding of structure formation.

As most galaxies live in groups (e.g. Merchán & Zandivarez 2005 or sec. 4.2.3) and groups as well show core characteristics similar to clusters (e.g. Rasmussen & Ponman 2007), it would be very interesting to undertake a study analogous to the one presented in Chapter 5. The impact of mergers in the group regime is, to date, yet an uncharted territory.

Bibliography

Aird, J., et al. 2009, arXiv:0910.1141

Best, P. N., Kauffmann, G., Heckman, T. M., Brinchmann, J., Charlot, S., Ivezić, Ž., & White, S. D. M. 2005, MNRAS, 362, 25

Blanchet L., 2009, arXiv, arXiv:0907.3596

Cavagnolo K. W., Donahue M., Voit G. M., Sun M., 2009, ApJS, 182, 12

Cohn J. D., White M., 2005, APh, 24, 316

Colberg, J. M., & Di Matteo, T. 2008, ArXiv e-prints, 804, arXiv:0804.1756

Falcke, H., Körding, E., & Markoff, S. 2004, A & A, 414, 895

Greene, J. E., & Ho, L. C. 2005, ApJ, 630, 122

Hasinger, G., Miyaji, T., & Schmidt, M. 2005, A & A, 441, 417

Leccardi A., Rossetti M., Molendi S., 2010, A&A, 510, A82

Martini, P., Kelson, D. D., Kim, E., Mulchaey, J. S., & Athey, A. A. 2006, ApJ, 644, 116

Martini, P., Mulchaey, J. S., & Kelson, D. D. 2007, ApJ, 664, 761

Mercha'n, M.E. & Zandivarez, A., 2005, ApJ, 630, 759

Poole G. B., Babul A., McCarthy I. G., Sanderson A. J. R., Fardal M. A., 2008, MNRAS, 391, 1163

Rasmussen J., Ponman T. J., 2007, MNRAS, 380, 1554

Sivakoff, G. R., Martini, P., Zabludoff, A. I., Kelson, D. D., & Mulchaey, J. S. 2008, ApJ, 682, 803

Veitch J., Vecchio A., 2010, PhRvD, 81, 062003

Will C. M., 1998, PhRvD, 57, 2061

Yunes N., Pretorius F., 2009, PhRvD, 80, 122003